ESA-QCA00147T-C

EUROPEAN SPACE AGENCY
CONTRACT REPORT

The work described in this report was done under ESA contract. Responsibility for the contents resides with the author or organisation that prepared it.

FINAL REPORT

CCD Radiation Damage Study

Author: G R Hopkinson

Rider 1 to
ESTEC CONTRACT No: 9557/91/NL/LC(SC)
SIRA CONTRACT No: A/9503/00

APRIL 1995

SIRA ELECTRO-OPTICS DIVISION

Sira ELECTRO-OPTICS

SIRA LTD Registered Address: SOUTH HILL · CHISLEHURST · KENT · BR7 5EH · UK
TELEPHONE: 081 467 2636 · INTERNATIONAL: +44 81 467 2636
TELEX: 896649 SIRA G · FACSIMILE: 081 467 6515 Registered in England No 150576

Sira Ltd is an independent organisation, incorporated in 1918, which operates internationally providing laboratory and engineering services for research, development, evaluation and applications of scientific and industrial instrumentation and control equipment.

The Electro-optics Division undertakes research, development, design applications and consultancy with multi-disciplinary teams of engineers and scientists. The Division also supplies contracting services to national and international procurement agencies and engineered equipment on a commercial basis for specialist applications.

EUROPEAN SPACE AGENCY CONTRACT REPORT

The work described in this report was done under ESA contract. Responsibility for the contents resides with the author or the organisation that prepared it.

The copyright in this document is vested in Sira Ltd. This document may only be reproduced in whole or in part, or stored in a retrieval system, or transmitted in any form, or by any means electronic, mechanical, photocopying or otherwise, either with the prior permission of Sira Ltd or in accordance with the terms of ESTEC/Contract No. 9557/NL/LC(SC)

FINAL REPORT ON CCD RADIATION DAMAGE STUDY

prepared for ESTEC
by Dr G R Hopkinson

rider 1 to ESTEC contract 9557/NL/LC(SC)
Sira Reference A/9503/00

April 1995

Copyright © Sira Ltd 1995

The contents of this document are subject to the terms and conditions of Sira Ltd available free on request

Sira ELECTRO-OPTICS

SIRA LTD Registered Address: SOUTH HILL · CHISLEHURST · KENT · BR7 5EH · UK
TELEPHONE: 081 467 2636 · INTERNATIONAL: +44 81 467 2636
TELEX: 896649 SIRA G · FACSIMILE: 081 467 6515 Registered in England No 150576

Sira Ltd is an independent organisation, incorporated in 1918, which operates internationally providing laboratory and engineering services for research, development, evaluation and applications of scientific and industrial instrumentation and control equipment.

The Electro-optics Division undertakes research, development, design applications and consultancy with multi-disciplinary teams of engineers and scientists. The Division also supplies contracting services to national and international procurement agencies and engineered equipment on a commercial basis for specialist applications.

Issue 1

Authorised

Date April 1995

FINAL REPORT ON CCD RADIATION DAMAGE STUDY

prepared for ESTEC
by Dr G R Hopkinson

rider 1 to ESTEC contract 9557/NL/LC(SC)
Sira Reference A/9503/00

April 1995

Copyright © Sira Ltd 1995

The contents of this document are subject
to the terms and conditions of Sira Ltd
available free on request

Contents

SECTION PAGE

SUMMARY S-1

1 INTRODUCTION 1-1

1.1 BACKGROUND 1-1

1.2 OVERVIEW OF CCD RADIATION EFFECTS 1-2

1.3 OVERVIEW OF THE TEST PROGRAMME 1-2

1.4 REFERENCE DOCUMENTS 1-3

2 EXPERIMENTAL DETAILS 2-1

2.1 RADIATION FACILITIES 2-1
2.1.1 Cobalt 60 Testing 2-1
2.1.2 10 MeV Proton Testing 2-1
2.1.3 46 MeV Proton Testing 2-1

2.2 TEST OBJECTS 2-2
2.2.1 CCD02 and CCD05 Devices From the Previous Study 2-2
2.2.2 CCD25-20 Devices 2-2
2.2.3 TH7895M Devices 2-2
2.2.4 TH7395M Devices 2-4
2.2.5 TH7863B Devices 2-4

2.4 TEST ELECTRONICS 2-6
2.3.1 Universal Camera and Software 2-7
2.3.2 Computer and Frame Grabber 2-11
2.3.3 Programmable Timing Generator (Version 3) 2-11
2.3.4 12-bit CDS Amplifiers 2-12
2.3.5 CCD Remote Head and Optical System 2-12
2.3.6 Multiple CCD Driver 2-12
2.3.7 Calibration 2-12
2.3.8 Temporal Noise 2-12

2.4 TEST SOFTWARE 2-13

2.5 OPERATING VOLTAGES 2-14

2.6 CLOCKING WAVEFORMS 2-16

2.7 TEST METHODS 2-20

2.8 RADIATION TEST HISTORIES 2-21

3 MEASUREMENTS OF CHARGE TO VOLTAGE CONVERSION FACTOR 3-1

4 DARK CURRENT MEASUREMENTS 4-1

4.1 CCD02 DEVICES 4-1
4.1.1 Dither Clocking 4-1
4.1.2 Dither Clocking Results for CCD02 Devices 4-2

4.2 CCD25-20 DEVICES 4-5
4.2.1 Average Dark Current 4-5
4.2.2 Dark Current Non-uniformity 4-13
4.2.3 Dark Charge Spikes 4-19
4.2.4 Dark Signal and its Non-uniformity for the Readout Register 4-20
4.2.5 Effect of Dither Clocking 4-23

4.3 TH7895M DEVICES 4-27

4.4 TH7395M DEVICES 4-35

4.5 RESULTS FOR TH7863B DEVICES 4-37

4.6 DARK CURRENT NON-UNIFORMITY: GENERAL 4-40

4.7 RANDOM TELEGRAPH SIGNALS 4-41

5 LINEARITY AND FULL WELL CAPACITY 5-1

5.1 CCD25-20 DEVICES 5-1

5.2 TH7863B DEVICES 5-5

5.3 TH7895M DEVICES 5-7

5.4 TH7395M DEVICES 5-8

5.5 BLOOMING CHARACTERISTICS 5-9

6 BRIGHT FIELD MEASUREMENTS 6-1

7 CTE MEASUREMENTS 7-1

7.1 MEASUREMENT METHOD 7-1
7.1.1 Theory 7-3

7.2 RESULTS FOR CCD02 DEVICES 7-4
7.2.1. Measurements of Emission Time Constant 7-5
7.2.2. Effect of Signal Size and Background on CTI 7-6
7.2.3. Effect of Line Move Rate on the Trapped Charge 7-9
7.2.4. CTI Versus Proton Fluence (or Total Dose) 7-11
7.2.4. Change in CTI With Clock Waveform 7-12

7.3 RESULTS FOR CCD25-20 AND TH7895M DEVICES 7-13

7.4 CONCLUSIONS 7-16

8 OUTPUT WAVEFORM FEATURES 8-1

9 THRESHOLD VOLTAGE SHIFTS 9-1

9.1 DC OUTPUT VOLTAGE 9-1

9.2 OTHER MEASUREMENTS OF THRESHOLD SHIFTS 9-2
9.2.1 CCD25-20 Devices 9-2
9.2.2 TH7895M Devices 9-8
9.2.3 TH7395N Devices 9-14
9.2.4 TH7863B Devices 9-16

10 OUTPOUT AMPLIFIER SUPPLY CURRENTS 10-1

11 DISCUSSION 11-1

11.1 EXAMPLES FOR MISSION ANALYSES 11-1

11.2 IMPACT REVIEW 11-3

Sira

SUMMARY

This study was concerned with the effects of space radiation on CCDs manufactured by two European suppliers: EEV Ltd (Chelmsford, UK) and Thomson-CSF (St Egreve, France). The main emphasis was to obtain data relevant to the CCDs to be used on ESA's Envisat-1 Satellite and other low Earth orbit (LEO) missions. In these applications the main effects come from particles in the Earth's trapped radiation belts and from solar flares.

The following commercial devices were irradiated with Co-60 gamma rays and proton beams.

Device type	Number studied
TH7895M	8 (1 - UV coated)
TH7395M	2 (1 - UV coated)
TH7863B	5
CCD25-20	3

The EEV CCD25-20 devices are 780x1152 pixel back illuminated CCDs, specially developed for ESA's MERIS instrument. The TH7863B will be used as the startracker (SATU) instrument as part of ESA's GOMOS experiment.

In addition, a proton-irradiated CCD02 device from a previous study was subjected to further measurements of CTE and dark current.

A special CCD camera was constructed to drive the above devices. This had programmable bias voltages and clock levels (set to 12-bit accuracy) and could be configured to drive any of the CCDs by computer control. Also developed during the course of the project was a multiple CCD driver (capable of driving up to six CCDs in parallel for biased radiation tests or annealing) and a CCD gain calibrator.

The CCDs were operated in the range 20 to -20°C with pixel readout times of approximately 1μs. These conditions are appropriate for the Envisat-1 instruments as well as many other spaceborne payload instruments and startrackers.

The main results of the study are summarised below:

- A detailed study of the effects on charge transfer efficiency (CTE) was made, principally using a proton irradiated EEV CCD02 but also confirmed by measurements on CCD25-20 and TH7895M devices. It was found that the CTE is strongly dependent on signal size and the amount of background charge (whether from the imaged scene or from accumulated dark signal). The presence of background charge was found to be very beneficial in reducing the amount of CTE degradation. The dwell time for which charge resides within a pixel was also found to be important. An empirical model was derived which was found to be in good agreement with the data.

  A test of CTE was made for a representative MERIS operational mode. The results were in agreement with expectations. Tests with GOMOS operational modes on TH7895M and TH7395 devices showed no unusual effects.

Copyright © Sira Ltd 1995

- An investigation into the effects of dither clocking with EEV devices was made. This is a technique to periodically swap the clock phases used during integration so as to achieve inversion of the CCD surface and thence suppression of the ionization-induced dark current. Measurements were made of the time constant of the hole trapping process (which is responsible for the surface inversion) as a function of temperature and of the dark current nonuniformity (black/white pairs of pixels) which can be induced if the clock waveforms are not optimal. Also the effect of dither clocking on dark current suppression was measured for temperatures in the range 20 to -20°C. The findings of the investigation were in good agreement with theoretical expectations.

- An optimisation of the clock voltages was performed in order to achieve good full well capacity and CTE. The manufacturer's quoted levels were not always found to be optimum.

- Full well capacity measurements for spot illumination are in line with manufacturers data - but only after optimisation of clock levels. The need for changes in clock voltages was discovered late in the programme and necessitated repeat measurements to be made on several devices. For CCD25-20 devices this optimisation results in a reduced substrate voltage (relative to the clock low level) and a higher dark current. There is a small, but significant, reduction in full well capacity after irradiation (~5% after 4 krad) for the CCD25-20 devices, and larger for the TH7863B. This is consistent with previous results. Uniform illumination measurements were found to give artificially high values for full well capacity.

- Blooming characteristics (i.e. the effects of over-saturation) was studied for CCD25-20 and TH7895 devices. Dither clocking (on EEV devices) was found to give an antiblooming effect - as expected. This antiblooming effect is not found with MPP devices (such as the TH7895M).

- No changes in the effectiveness in dump gate operation for CCD25-20s was seen with radiation. At -20 °C an upper limit of residual charge (after 8 krad, compared with 0 krad) after dump gate operation is 0.9 electrons for a signal of 2.8E4 electrons.

- Dark current measurements on CCD25-20 devices are in line with previous measurements. The normal temperature law (dark current = const. exp(-E/kT), with E~0.64 eV) has been verified over the range 20 to -20 °C for both mean level and proton-induced DSNU, though there is an indication that the change in mean level when using dither clocking is somewhat faster (E ~0.7 eV) as expected from the changes in the time constants involved. Note that none of the three 25-20 devices studied showed strong transitions into inversion so that dither clocking was not particularly effective in this case, the more so since a high substrate voltage could not be used if good full well performance was to be maintained .

- Measurement on TH7863B devices indicated that the radiation-induced mean dark current is less than for the A version (particularly for the image region).

Copyright © Sira Ltd 1995

- Measurements on TH7895M devices showed that the MPP mode completely suppresses ionization-induced dark current (at least at the low, 4krad, total dose used here). However, for proton-irradiated devices there is still an important contribution from bulk dark current.

- Measurements on thinned MPP TH7395 devices showed high dark current, the reasons for this are not fully understood.

- It was found that random telegraph signals (with time constants of several hours) were present in proton-irradiated devices at -20°C. It had previously been expected that the time constants would be longer than a day at that temperature. Possible explanations have been considered.

- Charge to voltage conversion factors (CVFs) were found to be in line with manufacturers values. A problem was encountered early in the programme which was eventually identified as being due to too low a bandwidth in the CDS amplifier used. This resulted in a reduced signal (the reduction being dependent on device type and clocking waveform) and hence a changed ADC unit to voltage calibration for the off-chip electronics. However the appropriate calibrations were performed and consistent values of CVF obtained for all devices. There was found to be no change in CVF with irradiation (for a measurement accuracy of ~5%).

- There were no unusual effects which could be attributed to the UV coating of some of the CCDs. As predicted, the pixel response nonuniformity (PRNU) of thinned devices (CCD25-20 and TH7395) in the near infrared (~900nm) was found to be dominated by fringe patterns (not affected by irradiation). The thinned CCD25-20 devices also showed response nonuniformities (again not affected by irradiation). At other wavelengths the PRNU was as expected (though some excess nonuniformity was found for the un-irradiated part a UV coated TH7895 device - though the reasons for this are not fully understood).

- Measurements of threshold voltage shifts and output amplifier power supply current were in line with the results of previous studies.

Copyright © Sira Ltd 1995

1 INTRODUCTION

1.1 BACKGROUND

This report is concerned with the effects of space radiation on CCDs manufactured by two European suppliers: EEV Ltd (Chelmsford, UK) and Thomson-CSF (St Egreve, France). The main emphasis was to obtain data relevant to the CCDs to be used on ESAs ENVISAT-1 Satellite and other low Earth orbit (LEO) missions. In these applications the main effects come from particles in the Earth's trapped radiation belts and from solar flares.

This study follows on from previous test campaigns performed for ESA and reported as follows:

- CO^{60} irradiation testing of THX31160 and TH7863 CCDs for the Silex programme
- Proton radiation testing of CCDs for the Silex programme
- Radiation testing of EEV CCDs for the MERIS programme

The first two studies were concerned with standard devices from Thomson-CSF, in particular the TH7863A. In this study the TH7863B version has been tested. This has a changed channel stop technology so as to reduce the radiation induced surface dark charge. These devices are to be used, for example, in the star tracker (SATU) for the GOMOS (Global Ozone Monitoringby Occultation of Stars) instrument on ENVISAT-1. Surface dark current in CCDs can be appreciably reduced using the multiphase pinned (MPP) technology. The other devices from Thomson-CSF considered here are the TH7895M and TH7395M - which are both MPP CCDs (front and back illuminated, respectively, 512x512 pixels). The DMS-A and DMS-B instruments on GOMOS will use MPP technology (though from EEV Ltd) and MPP devices are also of interest for other ESA missions.

The third study listed above looked at standard EEV devices in relation to the MERIS (Medium REsolution Imaging Spectrometer) instrument on ENVISAT-1. In this report we investigate CCD25-20 devices which were specially developed for the MERIS application (being back illuminated and having a dump-gate).

The previous studies investigated dark current effects (both surface and bulk) for temperatures around 20 °C. In this work the temperature range was extended down to -20 °C. Other topics not previously studied in detail were:

- the variation of CTE with signal size and background level
- the effectiveness of dither clocking in non-MPP EEV devices in reducing surface dark current

In this (as in previous) radiation campaigns, Co^{60} gamma rays were used to simulate ionization damage and protons (10 and 46 MeV) were used to study displacement damage effects. The maximum total dose used was 4 krad - a level which is appropriate for ENVISAT-1 and other LEO applications. The clocking rate used was ~1 μs/pixel, which is appropriate for a wide range of instruments, including star trackers.

Copyright © Sira Ltd 1995

1.2 OVERVIEW OF CCD RADIATION EFFECTS

Basic radiation effects in buried channel CCDs have been widely discussed in the literature, we can summarise the effects as follows:

i) ionization damage

This produces charge build-up in the gate oxide layers of the CCD and shifts in the flatband voltage - and hence in the operating point of the output amplifier. This can produce changes in charge to voltage conversion factor, offset voltage and amplifier power supply current.

Build-up of interface traps leads to increased surface dark current generation and is also likely to produce a decrease in full well capacity (though it is possible that this is due to flatband voltage shifts).

ii) bulk displacement damage

Particles such as protons can displace silicon atoms from their lattice sites in the bulk of the silicon layer and produce trapping and dark current generation states. These, in turn, give a reduction in charge transfer efficiency and the production of dark current spikes, some of which show RTS (random telegraph signal) behaviour.

iii) transient effects

These result from the ionization-induced generation of spurious charge in the silicon by the passage of charged particles or the absorption/Compton scattering of bremsstrahlung photons (x-rays and gamma rays) in turn produced by the slowing down of charged particles (protons and electrons) in the spacecraft material. Unlike i) and ii) above, the effects are not permanent since the charge is swept out during readout. These effects are not device specific and were considered in the previous MERIS study.

1.3 OVERVIEW OF THE TEST PROGRAMME

In this study the following commercial devices were irradiated with Co^{60} gamma rays and proton beams.

Device type	Number studied
TH7895M	8 (1 - UV coated)
TH7395M	2 (1 - UV coated)
TH7863B	5
CCD25-20	3

In addition, a CCD02 device from the previous MERIS study was subjected to further measurements of CTE and dark current. A special CCD camera was constructed to drive these devices. This had programmable bias voltages and clock levels (set to 12-bit accuracy) and could be configured to drive any of these devices. Also developed during the course of the project was a multiple CCD driver (capable of driving up to six CCDs in parallel for biased radiation tests or annealing) and a CCD gain calibrator.

Copyright © Sira Ltd 1995

During the construction phase of the above equipment the previously used MERIS test camera (for EEV CCD02 and CCD05 devices) was modified to allow testing down to -25 °C and detailed measurements were made of CTE and the effect of dither clocking. There then followed a programme of pre-irradiation measurements using the new Universal camera and irradiations at AEA Technology, Harwell (Co^{60} and 10 MeV protons) and Louvain la Neuve (46 MeV protons). Post-irradiation measurements and annealing studies were then carried out. Measurements of the following parameters were made:

dark current and dark current nonuniformity
CTE
threshold voltage shifts
output waveform shape
temporal noise
linearity and full well capacity
offset voltage
pixel response nonuniformity
output amplifier power supply current

For annealing, devices were placed in an oven at 83 ±2 °C for 168 hours.

1.4 REFERENCE DOCUMENTS

RD1 ESA/SCC Basic Specification No. 22900, issue 1. 'Total dose steady-state irradiation test method.

RD2 ESA/SCC Basic Specification No. 25000, issue 1. 'Electro-optical test methods for charge coupled devices'.

RD3 Final Report on ESA contract number 7787/88/NL/DG, March 1991. 'Co^{60} irradiation testing of THX31160 and TH7863 CCDs for the Silex programme'.

RD4 Final Report on ESA contract number 103607, August 1991. 'Proton radiation testing of CCDs for the Silex programme'.

RD5 Final Report on ESA contract number 9557/91/NL/LC(SC), August 1992. 'Radiation testing of EEV CCDs for the MERIS programme'.

RD6 Paper published in IEEE Transactions on Nuclear Science, NS-41(6), pp1984-1991, Dec 1994, I H Hopkins, G R Hopkinson and B Johlander, 'Proton-induced charge transfer degradation in CCDs for near-room temperature applications'.

RD7 Paper published in IEEE Transactions on Nuclear Science, NS-40(6), pp 1567-1574, Dec 1993, I H Hopkins, G R Hopkinson, 'Random telegraph signals from proton-irradiated CCDs'.

RD8 Thomson TCS CCD Products Databook, 1992/1993.

Copyright © Sira Ltd 1995

2 EXPERIMENTAL DETAILS

2.1 RADIATION FACILITIES

2.1.1 Cobalt60 Testing

Cobalt 60 testing was performed at AEA Technology, Harwell, UK, in one of the Hi-Rad Cells, at a dose rate of 2.7 krad/hour. Dosimetry was obtained using an Ionex Monitor mounted adjacent to the arrays and was performed by the staff at AEA Technology (who also keep the facility in routine calibration). The accuracy of dosimetry is assumed to be better than ±5%. The CCDs were irradiated through their glass windows (~1mm thick), with no other shielding material. Interface dose enhancement was considered to be negligible because: i) for Co-60 gamma ray energies (1.17 and 1.33 MeV) the effects are small, and ii) . the materials overlying the CCDs (SiO_2, polysilicon, aluminium and the glass window) have a similar atomic number to silicon.

2.1.2 10 MeV Proton Testing

10 MeV proton testing was carried out at the Tandem Van de Graaff accelerator at AEA Technology, Harwell, UK. A dedicated beam line was used. This employs scatter foils (100 micrometers of gold) to produce a uniform beam (better than ± 5%) over the sample area. The devices under test were mounted in shorted zero insertion pressure sockets on a test board which was placed inside an evacuated test chamber. This chamber was originally set up by DRA (Farnborough) for testing solar cells and allows rotation and cooling (to 80K) of test samples, though these facilities were not used in this case (the irradiations being at normal incidence at room temperature).

The beam was monitored using a surface barrier detector positioned at an angle of 45 degrees to the beam axis, in a side-arm of the beam line, adjacent to the scatter foil. Before the test run, this was calibrated against a similar detector at the sample position in the test chamber and against a Faraday cup (placed upstream from the sample chamber). Fluence measurements are considered to be accurate to better than ±5%. The beam flux was such that a typical exposure time of 1 minute was needed for a fluence ~2E9 p/cm^2.

2.1.3 46 MeV Proton Testing

This was performed by ESA personnel at the CYCLONE cyclotron accelerator at Louvain-la-Neuve, Belgium. An 85MeV proton beam was used with lead (250µm) and brass (150µm) foils. Just in front of the samples was an energy degrader consisting of 31mm polystyrene which produced a beam of 46MeV protons at the CCDs (mounted at the collimator position).

Beam monitoring was performed using a transmission ionisation chamber, calibrated against a Faraday cup. The total ionising dose was also checked against packs (of 9) TLDs (thermoluminescent dosimeters).

Copyright © Sira Ltd 1995

2.2 TEST OBJECTS

The devices tested in this report were two dimensional CCD imaging arrays manufactured by EEV, UK and Thomson TCS, France. The devices consist of an epitaxial layer of silicon over which are overlapping polysilicon gates (with ~100nm oxide isolations) forming an array of MOS capacitors. Photo-generated charge is collected on each capacitor and is first readout down each column in parallel and then serially along a readout register to an output amplifier.

All devices were in ceramic packages with glass windows. Apart from the two devices (one TH7895M, one TH7395M) which were phosphor coated, all the windows were removable. The devices were procured to commercial specifications. Brief descriptions of the devices are as follows:

2.2.1 CCD02 and CCD05 Devices From the Previous Study

These are, respectively, 385(H)x576(V) and 770(H)x1152(V) pixel devices, in this case operated in frame transfer mode so that the effective number of pixels in the vertical (column) direction is halved. The pixel dimensions are 22μm x 22μm for the smaller format CCD02 and 22.5μm x 22.5μm for the CCD05. All clocks are 3-phase. Two of the CCD02 devices studied previously were thinned and back-illuminated (though these will not be discussed in this report). The remainder and all CCD05 devices were front illuminated. It is possible to operate these devices with increased substrate voltage so that clock low phases are inverted (from n-type to p-type) so that surface dark current generation is reduced. During the integration time, the clock high phase (under which charge is collected) can be swapped with one of the other two phases so as to achieve inversion of the whole surface. This technique is known as dither clocking. The devices were irradiated at AEA Technology, Harwell, UK in December 1991.

The principal device given further testing in this study was CCD02-06-5-019 serial no.(batch-wafer-device) 8218-13-27, Sira no. 08 . This was a standard CCD02 device with a store shield.

2.2.2 CCD25-20 Devices

These are a version of the CCD05 device which is thinned and back illuminated (the full part number is CCD25-20-4-841). The CCDs have been specially developed for the MERIS (Medium Resolution Imaging Spectrometer) project and have the additional feature of a dump gate, running parallel with the readout register. This allows fast dumping of charge (to a dump drain) when the dump gate is pulsed high. Three early engineering samples were availlable for this study. These were mounted in ceramic CCD05 packages (i.e. standard commercial packages rather than flight packages). The number of useful pixels (in frame transfer mode) is 780(H)x576(V). The pixel size is 22.5μm x 22.5μm. The devices did not have any metallized store shield or dark reference regions and had removable glass windows.

The parts were marked as follows:

device marking	Sira number
2023-3-12	01
2023-3-7	02
2023-3-5	03

Copyright © Sira Ltd 1995

2.2.3 TH7895M Devices

These are front illuminated 512x512 devices with 19μm x 19μm pixels, manufactured by Thomson TCS, St Egreve, France. They can (as in this study) be operated in frame transfer mode, in which case the format is 512(H)x256(V) useful pixels. The CCD is designed for operation in the Multi Pinned Phase (or MPP) mode, where the surface of the silicon is inverted (from n-type to p-type) by the accumulation of holes from the channel stop regions (attracted to the surface by biasing the electrodes negative with respect to the substrate). In this mode the generation of dark current at the surface is reduced. An implant beneath one electrode phase ensures that charge is confined within a pixel even when all electrodes are biased negative during integration. Note however that during readout at least one phase must be taken out of inversion. A device schematic is given in figure 2.2.3-1. Although there are four output amplifiers, only one was operated in this study (shown with bold lines in figure 2.2.3-1). Note that all registers are operated with 4-phase clocks. There was no storeshield.

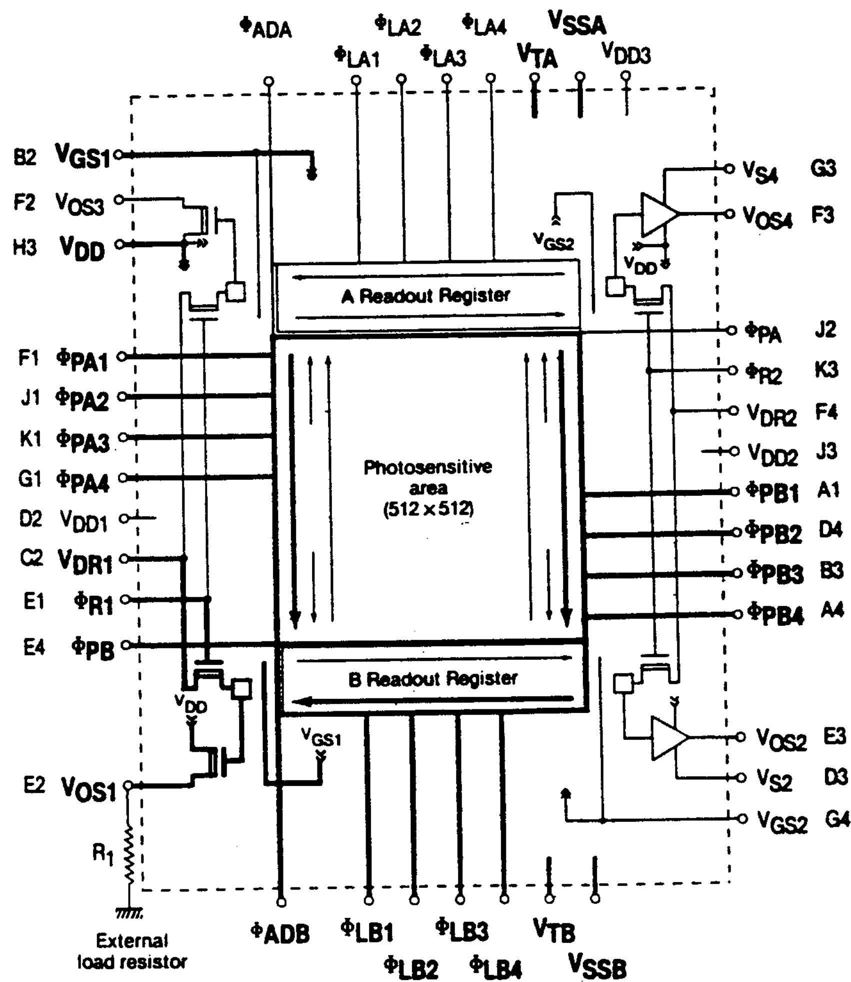

Figure 2.2.3-1 Device schematic for the TH7895M CCD (from RD8)

Six TH7895M devices were provided for this study, with details as follows:

Copyright © Sira Ltd 1995

Part number: TH7895MVRLN
Lot: M351J01A
Code: 9403
Marking: handwritten on underside of chip:

device marking	Sira number
4	04
3	05
2	06
6	07
5	08
1	09

In addition, results from a sample device (Sira number 11) are also included in this report. A phosphor coated device was also provided:

Part number: TH7895MGRPNQA
Lot: M327J03
Code: 9403
Marking: hand-written on underside of chip:

device marking	Sira number
4	uv

2.2.4 TH7395 Devices

These CCDs are identical in construction to the TH7895 devices except that the silicon substrate is thinned and the die is mounted for back illumination. This gives improved UV response. As for the TH7895M, operation in MPP mode is possible (for the TH7395M).

Two devices were tested in this study. One was a standard device provided by the manufacturer as a sample:

Part number: THX7395N
Lot: unknown
Code: 412-6-15
Marking: hand-written on underside of chip:

device marking	Sira number
412	01

The other was a phosphor coated device:

Part number: TH7395NVRXN
Lot: 395N407
Code: 13-4
Marking: hand-written on underside of chip:

device marking	Sira number
13-4	02

Copyright © Sira Ltd 1995

2.2.5 TH7863B Devices

These are front illuminated 384(H)x576(V) devices with 23µm x 23µm pixels. They can (as in this study) be operated in frame transfer mode, in which case the format is 384(H)x288(V) useful pixels. The CCD is identical to the TH7863A version previously tested for the SILEX programme (c.f. RD3 and RD4) with the exception that the channel stop isolation is changed so as to give a lower ionization-induced dark current A device schematic is given in figure 2.2.5-1. Note that image and storage registers are operated with 4-phase clocks and the readout register with 2-phase clocks.

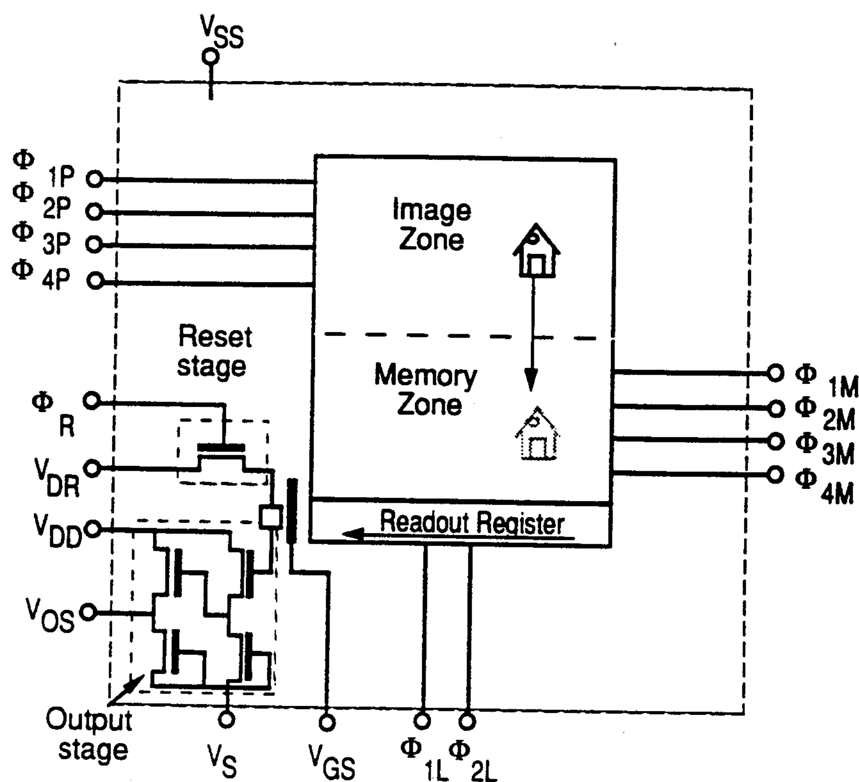

Figure 2.2.5-1 Device schematic for the TH7863A CCD (from RD8)

Four devices were procured for this study:

Part number: TH7863B
Lot: M350J01
Code: 9401
Marking: hand-written on underside of chip:

device marking	Sira number
1	12
5	13
8	14
4	15

In addition a sample device (provided by the manufacturer) was tested. This had code 9401, but an unknown lot number. It was given Sira number 04 (TCS device number, handwritten, was 7).

Copyright © Sira Ltd 1995

2.3 TEST ELECTRONICS

Figure 2.3-1 is a block diagram of the CCD test electronics, this was used for all device testing, with the exception that testing in between dose steps (at Harwell) was carried out at 20 °C with a simplified optical set-up (a 50 mm lens and ambient room lighting) - the hermetic box and test bench was not used. The separate components of the test equipment are described below.

Figure 2.3-2 shows the set up as used in the Co60 cell at Harwell (for operation of devices biased during irradiation). A wall of lead bricks was used to shield the drive electronics for those devices which were irradiated in a biased (and clocked) condition. This electronics consisted of a Multiple CCD Driver (for TH7863B devices) and a Universal CCD Camera for the other types (biased irradiation taking place one CCD at a time). The Multiple CCD Driver generated its own continuous clocking waveforms. The timing waveforms for the Universal camera were provided by a programmable timing generator mounted inside a portable 286 computer located in the entrance corridor to the cell, and shielded from the source by a concrete wall. Also positioned in the corridor were a set of bench power supplies for powering the CCD electronics.

Figure 2.3-3 shows the test electronics as used at Sira

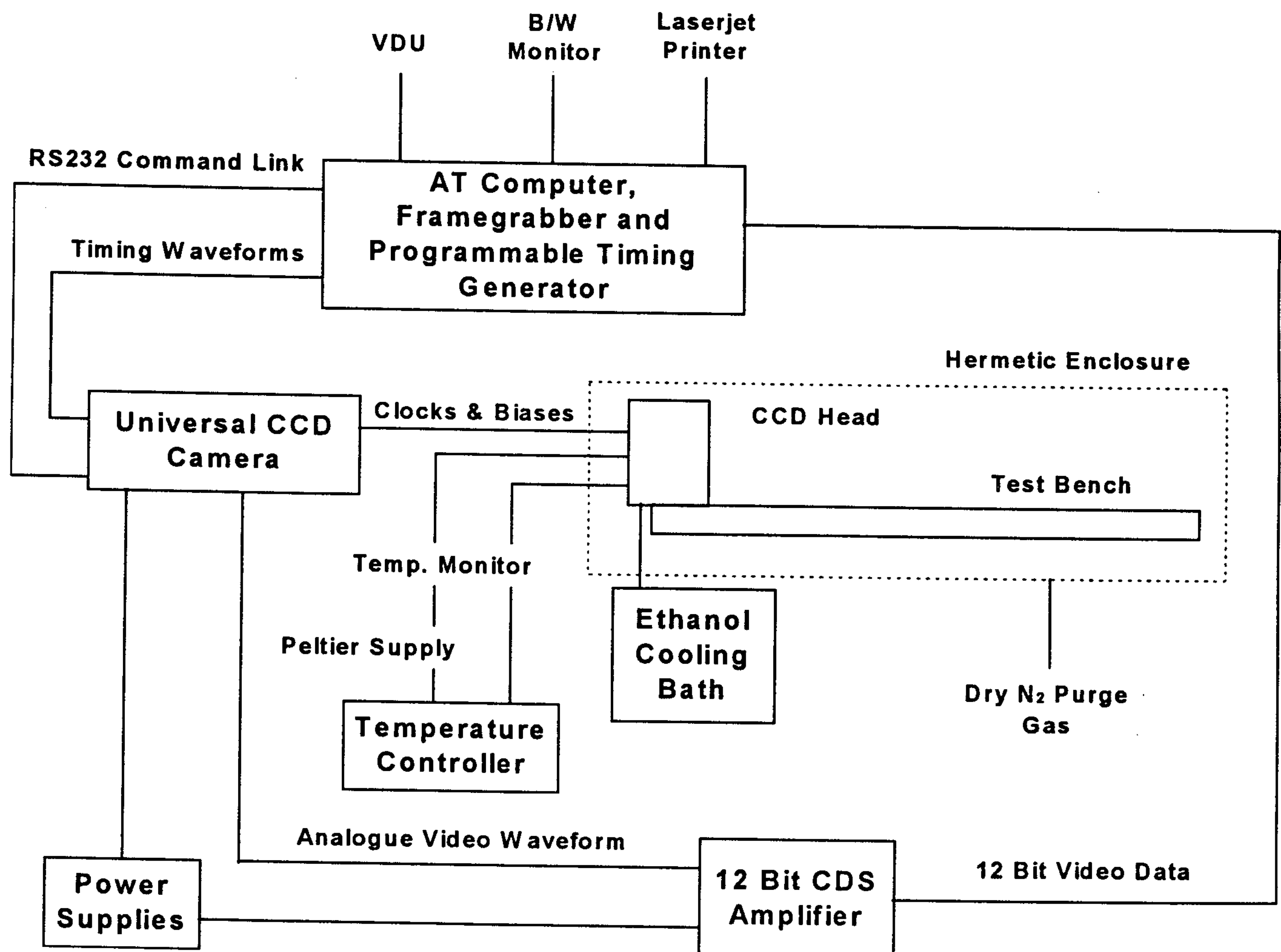

Figure 2.3-1 Block diagram of the test system

Copyright © Sira Ltd 1995

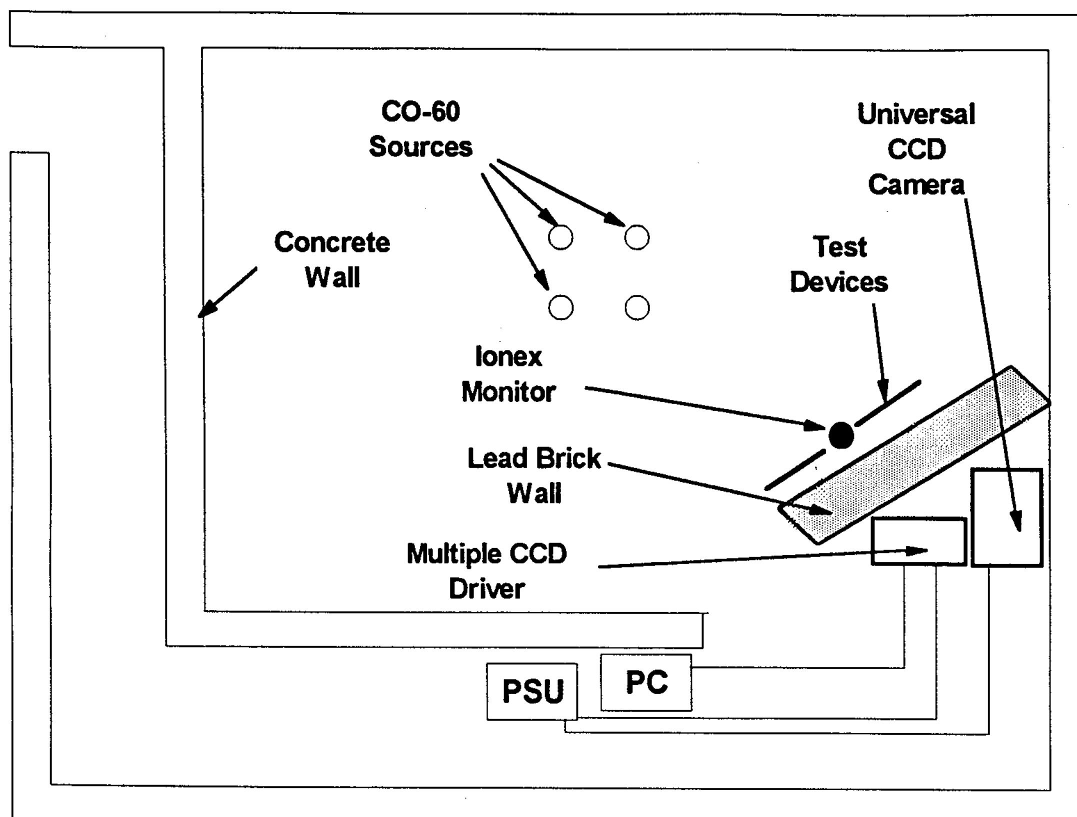

Figure 2.3-2 Test set up for the Hi-Rad cell at Harwell

2.3.1 Universal Camera and Software

The first part of this study was concerned with further investigation of CCD02 and CCD05 devices irradiated in the course of a previous study (c.f. RD5)> To this end the camera electronics used in that study was modified so as to allow cooling (and temperature control) at temperatures down to -25 °C with one other exception. The exception was that a new version of the programmable timing generator (para 2.3.3) was used so as to give extra flexibility in CCD clocking. The electronics system was as described in RD5.

In the second part of the study, four types of CCDs needed to be tested (CCD25-20, TH7863B, TH7895M and TH7395M). Rather than have separate drive electronics for each CCD, it was decided to design and construct programmable bias and clock drivers, cable of operating all known CCD types and to accommodate specific devices by using plug-in personality boards. Figure 2.3-4 shows the camera electronics box and two personality boards, plus a selection of CCDs (not all used in this study) and figure 2.3-5 shows a CCD in its personality board being illuminated by a spot of light.

The personality (or daughter) boards interfaced to the camera via two 37-way D-types (for clocks, biases and video outputs) and a 9-way D-type connector (for temperature monitoring and Peltier cooler supply).

Copyright © Sira Ltd 1995

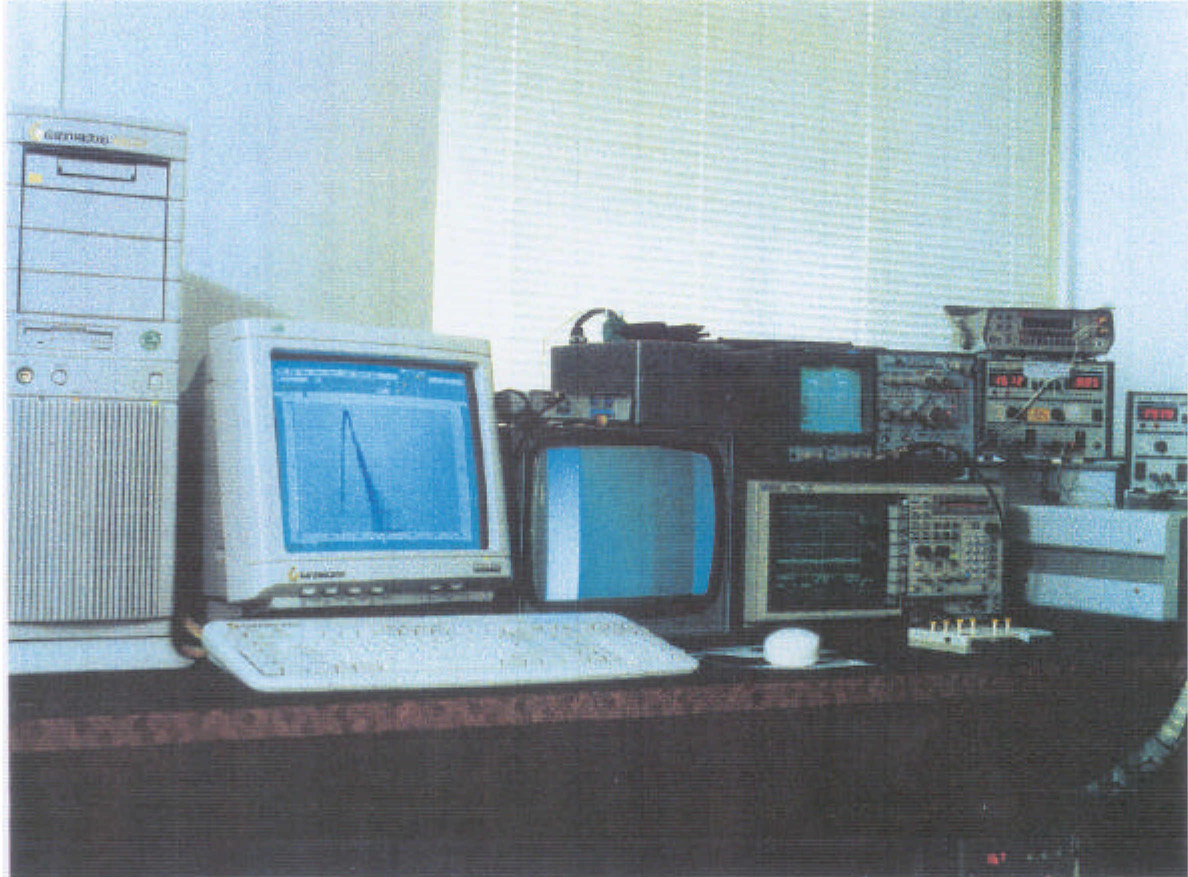

Figure 2.3-3 Photograph of the CCD test electronics at Sira

Copyright Sira Ltd 1995

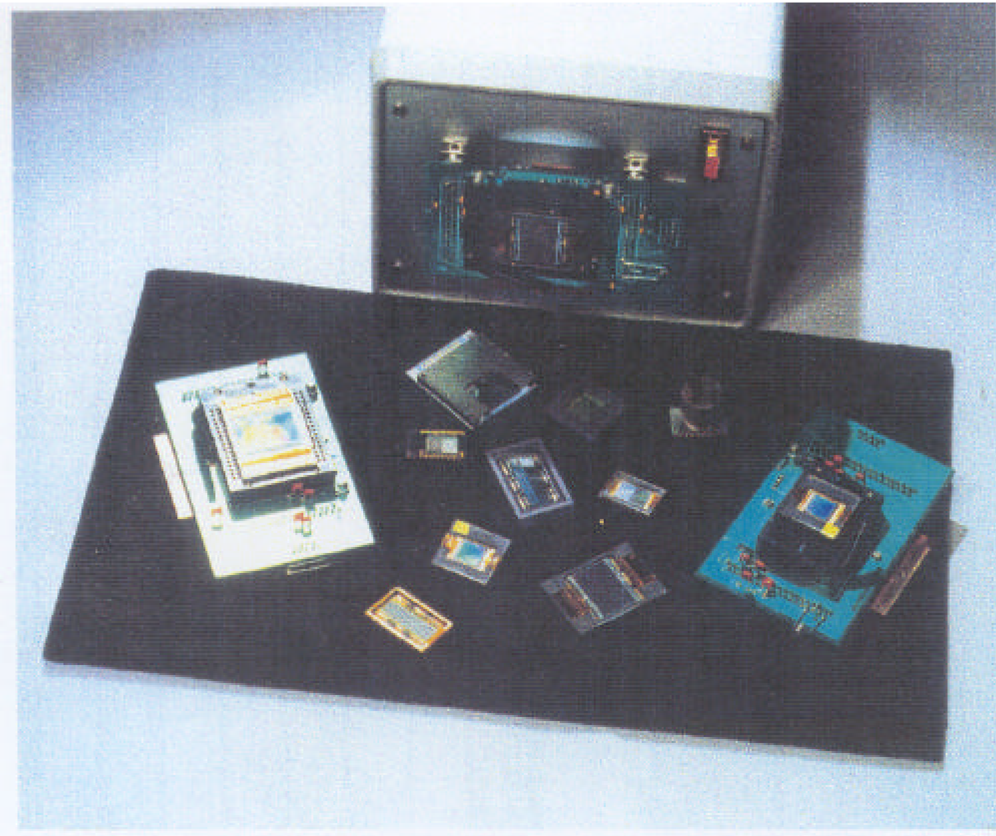

Figure 2.3-A The Sira universal CCD camera and a selection of CCDs

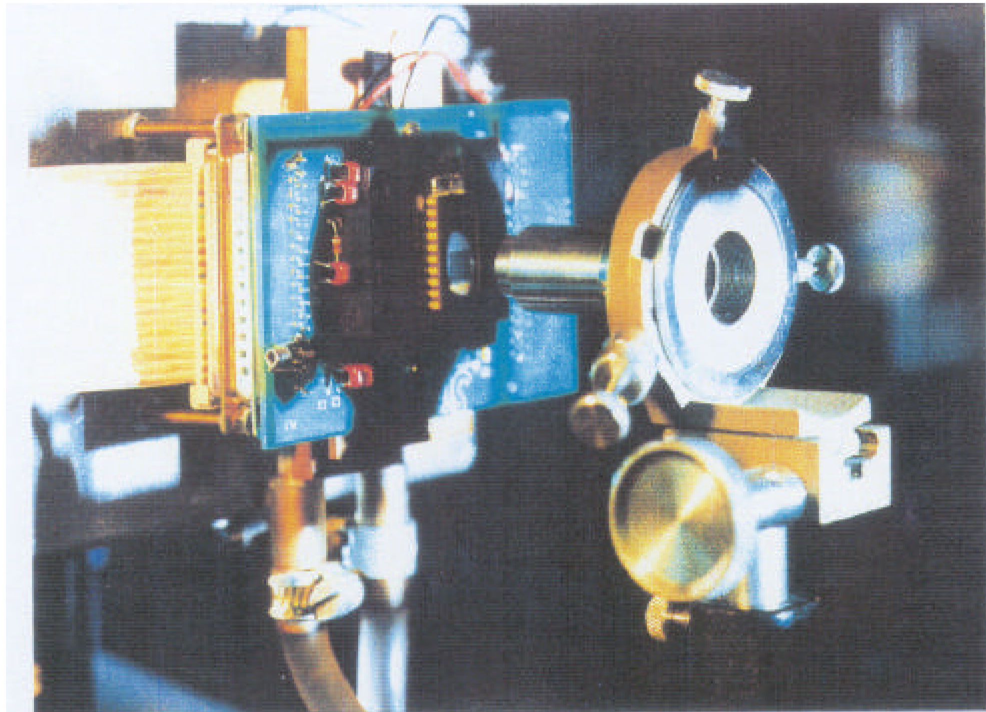

Figure 2.3-5 A CCD mounted on its personality board being given spot illumination, cooling tubes can be seen at the bottom of the photograph. Mounted behind the CCD is a Peltier cooler.

Each personality board also contained:

- a zero insertion pressure socket
- copper heatsink with two thermistors (one used in the temperature control loop and one as a monitor)
- an emitter follower transistor for each CCD output amplifier
- decoupling capacitors

The camera takes ECL waveforms from the programmable timing generator (para 2.3.3) It contains the following PCBs:

- video board with a high speed video amplifier and relays for switching between CCD outputs (there was also a 0 V channel for offset voltage calibration). This board also contained a Dallas DS5000 microcontroller for interfacing the camera to an AT computer. There were 9 programmable gain settings : x0.5, 1, 1.5, 2, 2.5, 3, 3.5, 4 and 8.
- bias board, with 8 12-bit programmable supplies (one of them negative). 4 of the biases have a high current capability (10 mA). All can have their currents monitored.
- clock boards (2 off) for image and storage region (i.e. area) clocks. Each of the two boards had 4 clock drivers with separately programmable high and low levels. These could be set anywhere in the range -20 V to +20 V with 12-bit precision, provided that the clock swing (difference between high and low levels) is no more than 20 V. Each clock level could also be switched to an alternate voltage during the clock sequence. The slopes of the clock waveforms were also programmable.
- (2 off) for readout register clock boards. Each of the two boards had 4 clock drivers with separately programmable high and low levels, slopes and falling edge delays. These could be set with 12-bit precision.

The Dallas microcontroller (on the Video board) was used to load values into the 12-bit DACs and was then sent into 'sleep mode' with its internal clock tuned off, so as to reduce pick-up. For each type of CCD there are two set-up files resident in the AT computer. The configuration file (*.cfg, e.g. 2520.cfg, 7895.cfg etc) defines which driver channels (and hence pins on the personality board) correspond to which clock name (for example Iϕ3 might correspond to area board 3, channel 4) and whether the DACs are to be bipolar or unipolar. The configuration file also specifies which biases are to be used. The default voltage file (normal.* e.g. normal.63, normal.78 etc) defines the default voltages to be used for the various clocks and biases.

During operation the 'unicam' program can be used to change voltages and to perform other operations. For example:-

Command:-

unicam vod 12.5	sets the V voltage to be 12.5 V
unicam on/off	turns the camera on and off (with biases switched in a controlled sequence)
unicam mon vrd	allows current monitoring on the Vrd line
unicam gain 3	sets the gain of the camera to setting 3 (corresponding to x2)
unicam video 3	sets the output video channel (out of maximum choice of 4, channel 2 being 0 V)

Copyright © Sira Ltd 1995

2.3.2 Computer and Framegrabber

A Gateway 2000 66 MHz 486DX2 computer was used with a 500 MByte hard disk and 250 Mbyte tape cartridge drive. It was operated under MS-DOS. Slotted into the AT-bus was a VS100 framegrabber/image memory card manufactured by Imaging Technology Inc. This is capable of capturing normal CCIR video signals or non-CCIR variable scan rate pictures up to a pixel rate of 10 MHz. The image memory is 1024 x 1024 x 12 bits deep. A 512 x 512 window in this memory can be output to the display at any one time. The variable scan rate pictures can be input either as digital data up to 12 bits deep (as in this case), or as an analogue signal to be digitised with an internal ADC. The internal ADC digitises to 8 bits.

2.3.3 Programmable Timing Generator (Version 3)

Also slotted into the AT-bus was a purpose-built programmable Timing Generator

The Timing Generator produces both TTL and ECL level clock waveforms for the camera unit. It consists of a series of RAM-controlled sequencers. The number and frequency of pulses in a train and the grouping together of different trains to form the overall pulse sequence for the multiplexer are variable. Sequences are generated by typing user-friendly high level statements on the host computer to generate a file containing the sequence information. This file is then down-loaded to the RAM via the AT-bus.

Because the pulse trains are variable, it is simple to generate the sequences necessary for driving a variety of arrays and for variation of stare time etc. In the latest version there are the additional features of:

- extended memory for the location of sequences
- cycle and group repeat commands to allow sequences to be repeated indefinitely or up to a predefined integration time
- master clock frequency defined by crystal oscillators or variable frequency phase locked loop.

The Timing Generator operates at clock rates of up to 64 MHz. There are 23 separate output lines. thus allowing for control of external circuitry such as clamps, sample and holds and ADCs, as well as clocking the multiplexer.

In general it is possible to store several different complete sequences in the timing generator at any one time, though the number depends on their complexity. Hence the operator can switch sequences without reloading from the host computer. This is particularly useful, for example, when changing integration times.

Copyright © Sira Ltd 1995

2.3.4 12-bit CDS Amplifiers

This contains a switchable gain amplifier (with gains of 1, 2.9 and 9.7). DAC controlled offset stage, correlated double sampling circuit and 12 bit ADC (which can convert at rates up to 10 MHz/pixel). ADC timing is under control from the programmable timing generator.

2.3.5 CCD Remote Head and Optical System

The Universal CCD camera is connected via two 37-way D-type connectors and twisted ribbon cables to a remote head. This remote unit is housed inside a light-tight hermetic enclosure which can be purged with dry nitrogen gas. The CCD can be cooled to ~-25 °C using an ethanol bath and refrigeration unit. Temperature control to ±0.05 °C is achieved with a Peltier cooler. Temperature is sensed with two thermistors, one in the control loop and one for monitoring. The CCD head was placed on an xyz translation stage mounted on an optical bench. The light source was a Xe arc lamp placed outside the enclosure. A fibre optic cable was used to transmit light into the box (to a pinhole).

2.3.6 Multiple CCD Driver

To enable several CCDs to be operated in a biased condition whilst irradiated or annealed, a multiple driver board was designed and built. This has high current drivers to enable several CCDs to be driven in parallel. During this study the board was only used for TH7863B devices but the board is configurable for either 2/4 or 3-phase devices and for a variety of clock and bias voltages. A simple continuous clocking scheme (implemented via a PAL) can be used, or inputs can be taken from the programmable timing generator (para 2.3.3).

2.3.7 Calibration

The combination of CCD daughter board, universal camera and CDS amplifier - i.e. the complete chain from CCD output to ADC output was calibrated using a specially designed calibration unit. This uses a variable potential divider to scale down the $R\phi_3$ (or, if appropriate, $R\phi_2$) clock waveform and superimpose it on a variable DC offset voltage so as to produce an artificial CCD output waveform. The variable reference voltages used to define the simulated 'reset' and 'video' levels can be measured using a digital voltmeter. The calibration was performed for each CCD type for a selection of camera gain settings and for the three CDS amplifier gain settings. Figure 2.3.7-1 gives example data for a TH7895M waveform.

2.3.8 Temporal Noise

With the current configuration of the test electronics,the temporal readout noise was dominated by pick-up in the CCD camera and was in all cases ~150electrons rms. It is not expected that the readout noise will be affected by irradiation (for the present conditions) - though displacement damage has been reported to affect the noise for low noise, slow scan conditions. Temporal noise will not be discussed further in this report.

Copyright © Sira Ltd 1995

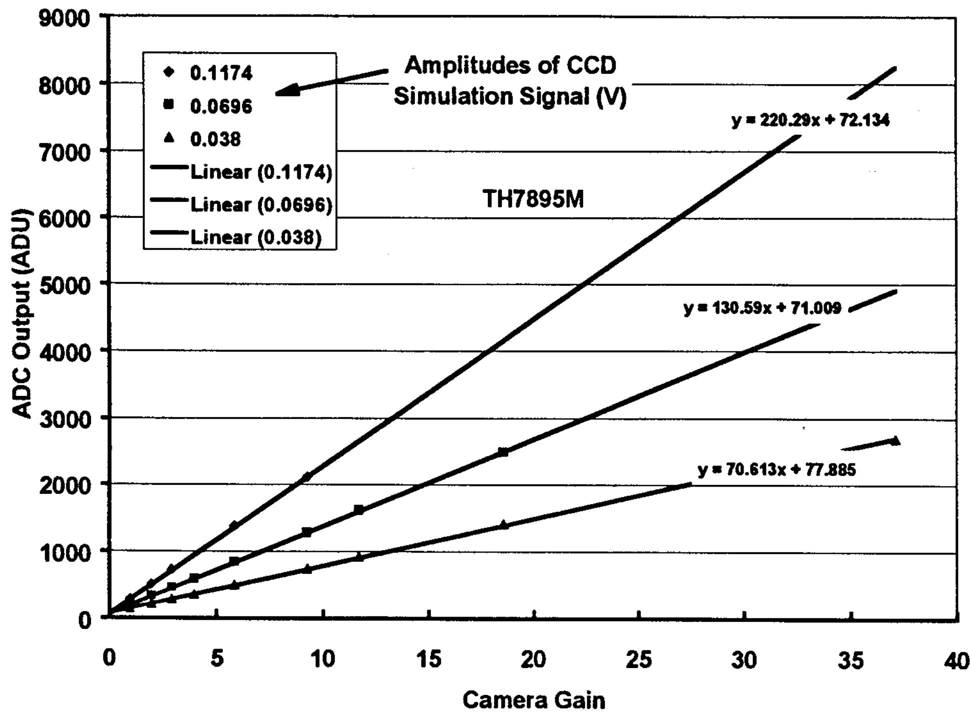

Figure 2.3.7-1 Calibration plots for the Universal camera used with TH7895 devices

2.4 TEST SOFTWARE

Sira has written system level software which acts as an interpreter for the VS100 image memory board functions and allows these to be selected in a user-friendly manner and assembled together to form sequences for automated testing or data analysis. Examples of functions available within simple commands are:

- image acquisition (either continuously or as single frames)
- pan and zoom
- image scaling and off-setting
- display of a cursor on the image display and readout of a 14x14 matrix of pixel values on the computer console
- cursor movement from keyboard or mouse
- selection of points, lines, columns or areas of interest by keyed commands or by mouse
- calculation of mean and standard deviation of areas of interest and display of histograms. Also dumping of this data to a file
- recording of intensity profiles across slices through images
- detection of pixels above or below a set threshold (e.g. for analysis of image non-uniformity)
- adding or averaging successive images to reduce random noise
- addition, subtraction, division or multiplication by previously stored images

Copyright © Sira Ltd 1995

- Statistical analysis of values from one pixel (or a group of pixels) from successive frames for noise analysis
- saving of image data, either in VS100 or standard TIFF (tagged image file) format
- operations on input and output look-up tables (LUTs)
- control of Unidex mirror drives
- control of Bentham Instruments monochromator
- loading of bias and clock supply voltages into the microcontroller memory in the universal CCD camera.

Examples of operation are:

- definition of sequences of regions of interest and recording of mean, standard deviations etc.
- measurement of output signal as a function of bias or clock voltages
- interaction with the programmable timing generator so as to form linearity plots by successive changes in integration time and recording of image values from a specified section of interest.

Data files (such as histograms) can be analysed and plotted using standard spreadsheet or graphics packages. This is made easy since it is possible to flip in and out of the command program without reloading any parameters or losing the screen display.

Built into the command program are safeguards to ensure that files cannot be overwritten by giving two files the same name. The database is organised by giving each device a unique directory. All files relating to a device are stored in its directory. To keep track of the current directory the directory name appears as the prompt from the command program.

2.5 OPERATING VOLTAGES

All devices were operated in frame transfer mode at an output rate of 1 μs/pixel (with the exception of CCD25-20 devices which were operated at 0.875 μs/pixel). Line move times were 2 μs. In cases where the dark current was low (e.g. at low temperatures and/or with surface inversion) the integration time was extended by repeating the readout sequence for the required number of 'overscanned' lines. The voltages used were 'typical' values as specified by the manufacturers:

Copyright © Sira Ltd 1995

CCD25-20 devices:

Parameter	Symbol	Voltage (V)
Output drain voltage	V_{od}	27.0
Reset drain voltage	Vrd	17.0
Substrate voltage	Vss	7.8
Output gate voltage	V_{og}	2.0
Diode drain voltage	V_{dd}	22.0
All clock high voltages		11.0
All clock low voltages		0.0
dump gate high voltage	V_{dgh}	variable
Load resistor :	10 K	

TH7863B devices

Parameter	Symbol	Voltage (V)
Output drain voltage	V_{od}	15.0
Reset drain voltage	Vrd	12.8
Substrate voltage	V_{ss}	0.0
V_1 bias	V_1	0.0
Output gate voltage	V_{og}	2.5
All clock high voltages		10.0
All clock low voltages		0.0

TH7895M devices

Parameter	Symbol	Voltage (V)
Output drain voltage	V_{od}	19.0
Reset drain voltage	Vrd	12.5
Substrate voltage	V_{ss}	0.0
Output gate voltage	V_{og}	1.5
V_1 bias	V_1	15.0
V_2 bias	V_2	10.0
V_3 bias	V_3	0.0
V_4 bias	V_4	-10.0
Image zone clock voltages during integration		-10.0
Image & storage zone clock high voltages during transfer		+5.0
Image zone clock low voltages during transfer		-7.0
Storage zone clock low voltages during transfer		-5.0
Output register clock high voltages		11.0
Output register clock low voltages		0.0
Load resistor :	15 K	

Copyright © Sira Ltd 1995

TH7395M devices

Output drain voltage	V_{od}	19.0
Reset drain voltage	V_{rd}	13.0
Substrate voltage	V_{ss}	0.0
Output gate voltage	V_{og}	1.0
V_1 Bias	V_1	15.0
V_2 Bias	V_2	10.0
V_3 Bias	V_3	0.0
Image zone clock voltages during integration		-8.0
Image & storage zone clock high voltages during transfer		5.0
Image zone clock low voltages during transfer		-7.0
Storage zone clock low voltages during transfer		-5.0
Output register clock high voltages		11.0
Output register clock low voltages		0.0
Load resistor :	15 K	

2.6 CLOCKING WAVEFORMS

As discussed in para 2.5, all devices were operated in frame transfer mode at an output rate of 1 µs/pixel (with the exception of CCD25-20 devices which were operated at 0.875 µs/pixel). Line move times were 2 µs. In cases where the dark current was low (e.g. at low temperatures and/or with surface inversion) the integration time was extended by repeating the readout sequence for the required number of 'overscanned' lines. Timing diagrams for the CCD25-20, THX7895 and TH7863B are given in figures 2.6-1 to 2.6-3 (note: the TH7395 was clocked in the same way as the TH7895).

In order to achieve frame transfer operation with the TH7895M and THX7395 devices, the M clock line moves during readout were performed in an identical fashion to the P and M line moves during frame transfer (i.e. the clock low level was always -5V). This resulted in the storage region not being inverted. In a more complex clocking scheme (not used here) the M clocks would have -5/+5V levels during the line move and the clock low voltage would switch to -10V during pixel readout of each line.

For the TH7863B, the integration was performed with 3 P clock phases high - as for the GOMOS SATU instrument. For the CCD25-20, a 2-phase dither clocking scheme was used (as in the MERIS instrument).

Measurements were normally performed on all image area pixels, however dumping of pixels (to simulate GOMOS and MERIS) operational modes was performed for some measurements. During irradiation the devices were clocked as follows:

CCD25-20	representative MERIS mode with dumping and binning of pixels
TH7895	normal frame transfer mode
TH7863B	simplified full frame mode with 256 pixels per line. Line move rate 1MHz, pixel rate 2MHz

Copyright © Sira Ltd 1995

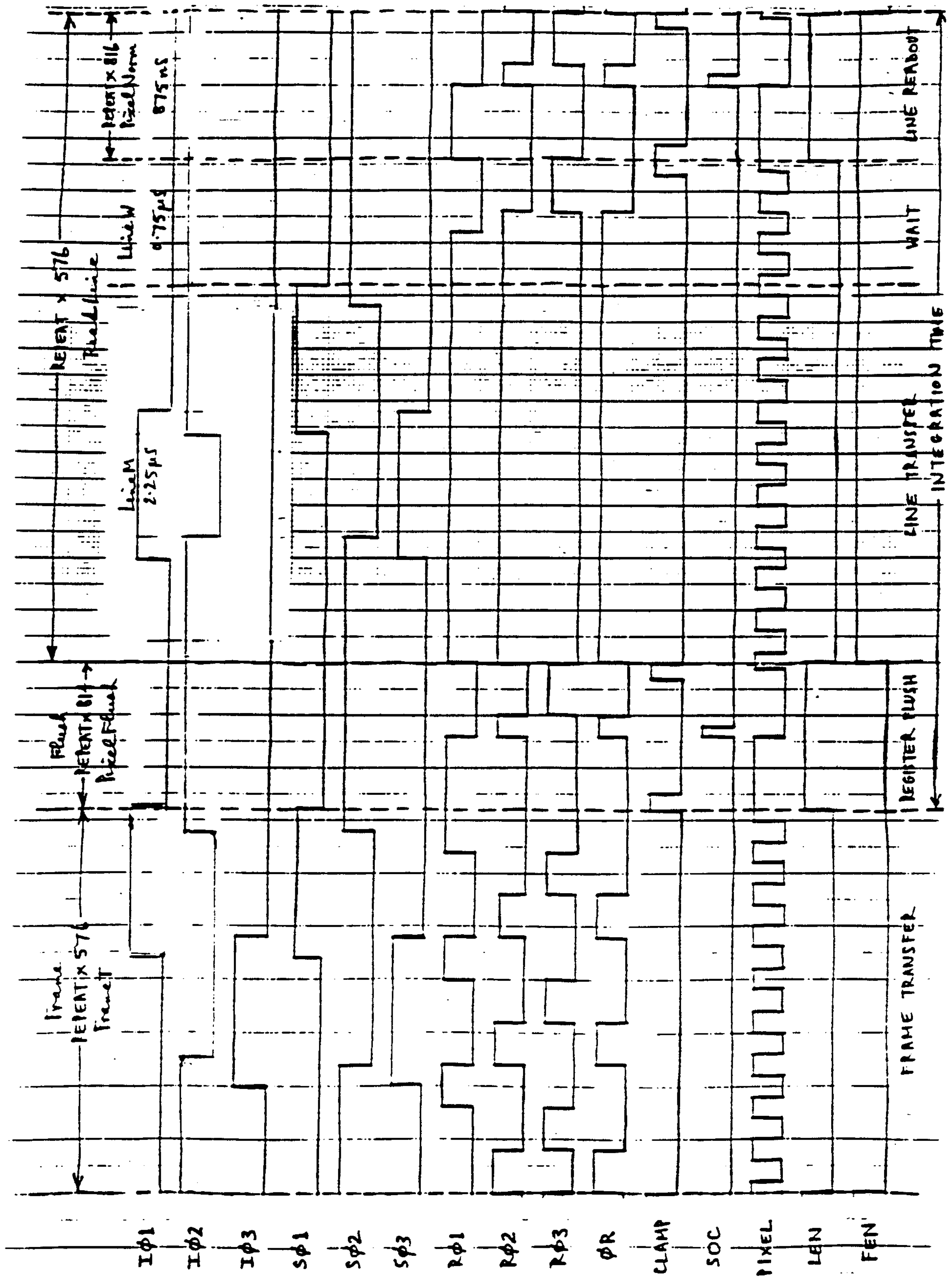

Figure 2.6-1 Timing diagram for CCD25-20 CCDs

Copyright © Sira Ltd 1995

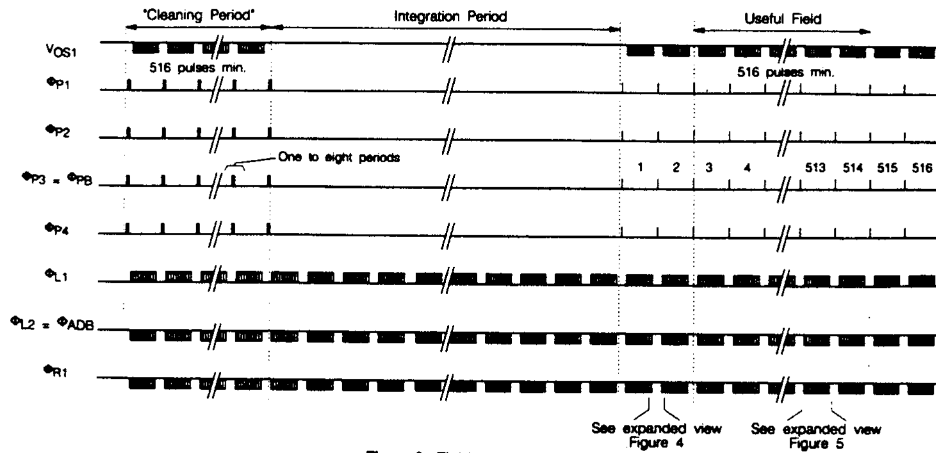

Figure 3 : Field timing diagram.

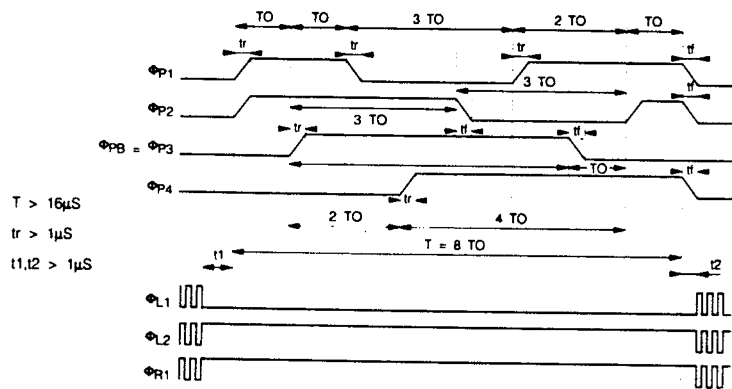

Figure 2.6-2 Timing diagram for TH7895 CCDs

Copyright © Sira Ltd 1995

FRAME TIMING DIAGRAM

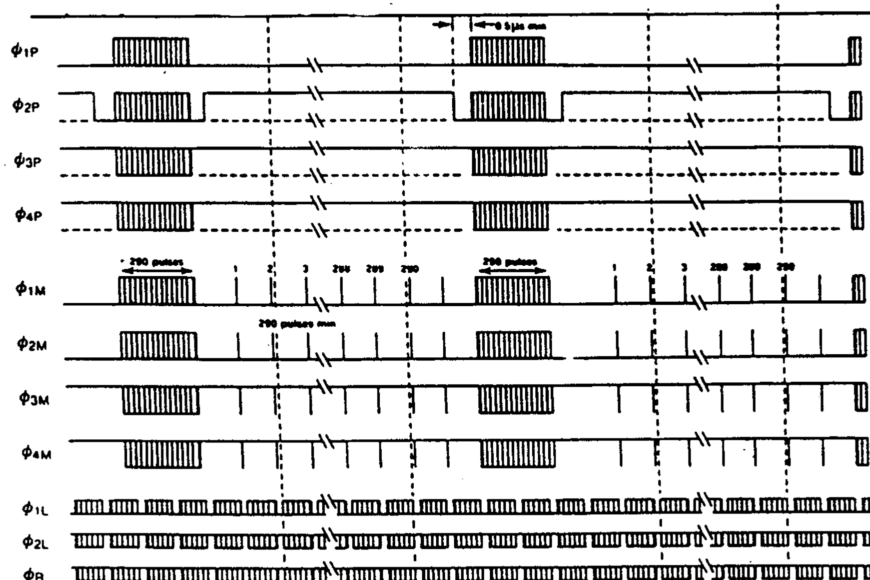

NOTES
1. Repartition of lines: First : shielded.
2nd : partially shielded.
3 to 288 : useful lines.
289 : partially shielded.
290 : shielded.

OUTPUT TIMING DIAGRAM FOR ϕ_P AND ϕ_M CLOCKS DURING TRANSFER

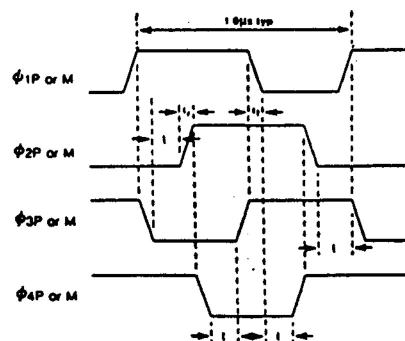

VERTICAL TRANSFERS TIMING DIAGRAM

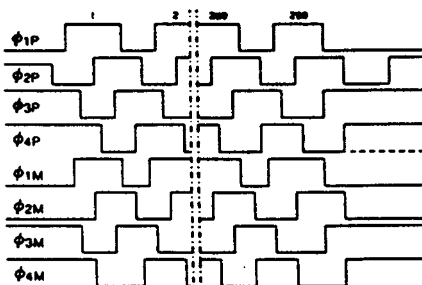

NOTES
1. $30ns \le t_r \le 80ns$; $30ns \le t_f \le 80ns$; $t \ge 50ns$.
2. Crossover of complementary clocks (ϕ_1 and ϕ_3, ϕ_2 and ϕ_4) in the high state (above 90% of max. amplitude).

NOTES
1. Fl = 1.0MHz; FL = 1.0MHz; Typical Ti = 1.25 ms

OUTPUT TIMING DIAGRAM FOR READOUT REGISTER AND RESET CLOCKS

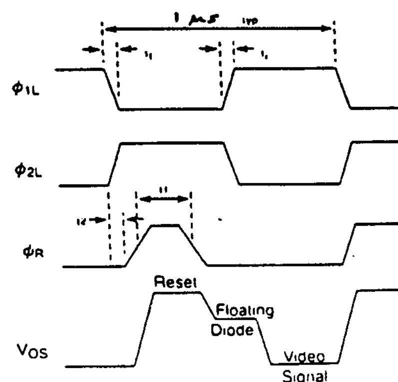

LINE TIMING DIAGRAM

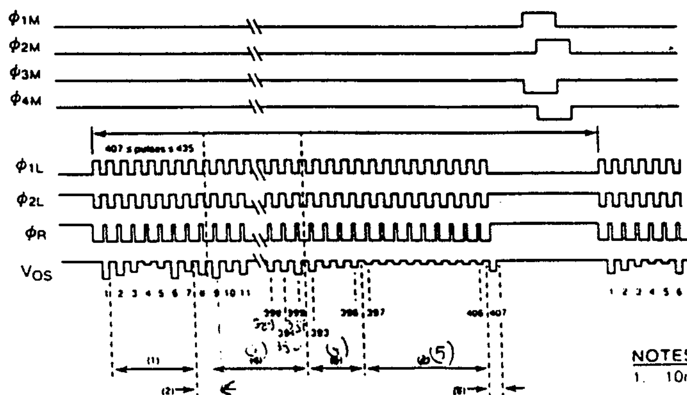

NOTES
1. $10ns \le t_r \le 30ns$; $10ns \le t_f \le 30ns$; $t_1 \ge 30ns$; $t_2 \ge 0ns$

Figure 2.6-13 Timing diagram for TH7863B CCDs

2.7 TEST METHODS

The following measurement equipment was used:

Measurement		Equipment
Output amplifier and reset drain currents:	-	calibrated 4½ digit DVM
Output waveform:	-	calibrated HP digital oscilloscope
All other measurements:	-	recording of images using the CDS amplifier and framegrabber (as discussed in para 2.3)

Test methods were as discussed in RD2. In particular we list the relevant paragraphs of RD2 below. Measurements were made with the CCD at 20°C and at lower temperatures (particularly -20°C) as discussed in the results sections.

Parameter	Para in ESA/SCC 25000	Comment
Power supply current	5.3	In darkness, some tests at Vsat/2
DC output level	5.4	Relative changes measured, so no separate measurement of buffer amplifier offset
Output signal waveform features	6.3	Changes in delay time ($t_{D\text{-signal}}$) and slew rate measured by superimposing waveforms
Temporal noise	6.4.2b	Measurement of post-scan pixels
Offset voltage	6.5	measured from the absolute value (after CDS) of post-scan pixels
Saturation voltage for image area	6.7	Uniform and spot illumination as discussed in the text, λ=540nm
Saturation voltage for readout register	6.8	Defocussed spot and x4 binning along a column. CCD25-20 only
Blooming characteristics	6.10	CCD25-20 only
Charge transfer efficiency	6.12	Optical spot measurement as discussed in section 7
Photoresponse non-uniformity	6.14	
Charge to voltage conversion factor	6.18	
Average dark signal	6.20	
Dark signal non-uniformity	6.21	
Threshold voltages	6.22	

Values of CCD signal in ADU were converted to voltages using the electronics system calibration and to electrons/pixel using the charge to voltage conversion factor (para 3). Dark currents in electrons/pixel/s were converted to nA/cm^2 using the total pixel area and the electron charge.

Image and storage region dark currents were usually separated by measuring the signals in the first and last lines readout and subtracting (as in method of RD2), however this method gives significant errors when the image region dark current is nonuniform. Hence another technique

Copyright © Sira Ltd 1995

was used which involved recording two images, one with a short integration time and high gain, the other with a longer integration time and lower gain. The gains and integration times were arranged so that the image area dark signals were approximately the same for each image. Hence the difference image gave a uniform slope, whose measurement yields the difference in storage region dark currents. These components are independent of integration time and only depend on gain. So if the ratio of the two gains used is G then the difference image gives the storage region dark current multiplied by (1-1/G).

For measurements requiring illumination a Xenon arc lamp plus neutral density and/or interference filters was used.

2.8 RADIATION TEST HISTORIES

The irradiations conducted as part of the original study on EEV CCD02 and CCD05 devices were performed as follows (c.f. para 2.1):

Irradiation	Facility	date
10 MeV protons	Tandem Van de Graaff, Harwell, UK	December 10 & 11 1991
Co-60	Hirad, Harwell, UK (dose rate 2.7 krad/hr)	December 12 & 13 1991

The irradiations conducted as part of this study were performed at the following facilities (c.f. para 2.1):

Irradiation	Facility	date
10 MeV protons	Tandem Van de Graaff, Harwell, UK	August 10 & 11 1994
Co-60	Hirad, Harwell, UK (dose rate 2.7 krad/hr)	August 15-17 1994
46 MeV protons	CYCLONE, Louvain la Neuve, Belgium	4 October 1994

The proton fluences used were 1.7, 3.4 and 5.3 x 10^9 p/cm^2 at 10MeV; 3.5 and 7.0 x 10^9 p/cm^2 at 46MeV. The proton fluxes were ~10^7 p/cm^2/s.

The irradiations were carried out at ambient room temperature (20 ±5°C). Devices irradiated unbiased had their pins shorted. Those irradiated biased were operated as follows (paras 2.5 and 2.6 give details of the bias voltages and clock waveforms):

Device type	Bias Circuit (all Sira designed)	Clocking Scheme
EEV CCD02 and CCD05	MERIS Radiation Camera	standard frame transfer
EEV CCD25-20	Universal Camera	MERIS sequence
TH7863B	Multiple CCD Driver	full frame
TH7895M	Universal Camera	standard frame transfer
TH7395M	Universal Camera	standard frame transfer

The irradiation steps were as follows:

Device number	Sira number	Irradiation	Dose steps (krad)
TH7895M	04	Co-60, biased	2, 4
	05	Co-60, biased	4
	06	Co-60, unbiased	2, 4
	07	46 MeV, protons †	0.6*,1.2*
	08	10 MeV, protons †	0.1, 0.4, 2
	09	10 MeV, protons †	1, 2, 4
	10	Spare	-
	11	10 MeV, protons †	0.1, 0.4, 2
	UV	46 MeV, protons	1*, 2*
TH7395NVRXN	01	Co-60, biased	2, 4
	02	46 MeV protons	0.6*,1.2*
TH7863B	12	Co-60, biased	2, 4
	13	Co-60, biased	2, 4
	14	Co-60, unbiased	2, 4
	15	10 MeV protons †	0.1, 0.4, 2
	16	10 MeV protons	1, 2, 4
CCD25-20-4-841	01	Co-60 biased **	2, 4
	02	10 MeV protons †	0.1, 1, 2, 4
	03	10 MeV protons	0.4, 1, 1.4, 2, 4, 8, 9

† proton irradiations were unbiased

* corresponding to fluences of 3.5E9 and 7.0E9 p/cm^2. Equivalent to NIEL of 1.8E9 and 3.6E9 p/cm^2 (1 krad and 2 krad) at 10 MeV.

** last ~0.8 krad was unbiased

The proton irradiated devices were masked to form the various fluence regions using plates of 1 mm Al (10 MeV) and 5 mm stainless steel (45 MeV) the edges of the plates were parallel to the column direction. It was usually arranged that the output amplifier received the highest fluence.

3 MEASUREMENTS OF CHARGE TO VOLTAGE CONVERSION FACTOR

The charge to voltage conversion factor for each CCD was measured using method 6.18 of RD2. That is, the CCD was uniformly illuminated and the average current in the reset drain bias line (I_{RD}) was measured. This was done by monitoring the voltage across a resistor. The resistor was calibrated using a Keithley 206 Source Measure Unit as a variable current source. It was found that 1 mV across the resistor was equivalent to 0.917 nA (that is the resistance was 1.08 M). If the off-chip electronics provides a conversion of K(μV/ADU) then:

$$\underset{(\mu V/\text{electron})}{CVF} = \underset{(\mu V/ADU)}{K} \times \underset{(ADU)}{\text{CCD signal per pixel}} \times \frac{\text{number of pixels} \times e(\text{Coulomb})}{I_{RD}(A) \times T_{int}(s)} \qquad (3\ 1)$$

where T_{int} is the integration time (in seconds) and e the electronic charge.

For devices which showed large dark currents after irradiation (and so a fluctuating I_{RD} current) it was found advantageous to use a continuous clocking (rather than frame transfer) waveform which gives a constant signal (and current) throughout the readout time.

The gain calibration, K, (in μV/ADU) of the off-chip electronics was significantly changed after returning to Sira after the irradiations, since it was noticed that the bandwidth of the correlated double sampling amplifier (para2.3.4) had been too low and was causing significant attenuation of the CCD signal. This also caused the μV/ADU calibration to be dependent on device type and clocking frequency. The majority of post-irradiation measurements were carried out with a higher amplifier bandwidth.

Table 3-1 below gives the CVF values for all devices (calculated using the appropriate μV/ADU calibration in each case). The measurement accuracy is estimated to be ±3%. It is seen that CVF values are similar for each device type (and are consistent with manufacturers values) and that there is no significant change in CVF (within the measurement tolerance) during irradiation (the maximum dose being 4 krad (Si)).

Copyright © Sira Ltd 1995

Table 3-1 CVF values (in μV/electron)
- means measurements not performed

TH7895M devices						
Device No	**Irradiation**			**immediate**	**after 2 months**	
		0 krad	**half-dose**	**full dose**	**full dose**	**average**
04	4 krad Co-60, biased	1.47	1.26	1.43	1.35	1.39
05	4 krad Co-60, biased	1.37	-	-	1.50	1.42
06	4 krad Co-60, unbiased	1.29	1.32	1.34	1.26	1.30
07	46 MeV protons	1.20	-	-	1.51	1.36
08	2krad 10 MeV protons	1.39	-	1.36	1.34	1.36
09	2krad 10 MeV protons	1.28	-	1.40	1.40	1.36
11	2krad 10 MeV protons	1.35	-	1.39	1.45	1.38
UV	2krad 46 MeV protons	1.36	-	-	1.33	1.35

TH7395M devices						
Device No	**Irradiation**			**immediate**	**after 2 months**	
		0 krad	**half-dose**	**full dose**	**full dose**	**average**
01	4 krad Co60 biased	1.10	1.16	1.11	1.13	1.13
02	46 MeV protons	1.13	-	-	1.14	1.13

TH7863B devices						
Device No	**Irradiation**			**immediate**	**after 2 months**	
		0 krad	**half-dose**	**full dose**	**full dose**	**average**
12	4 krad Co-60, biased	1.74	1.66	1.73	1.68	1.71
13	4 krad Co-60, biased	1.80	-	1.78	1.81	1.80
14	4 krad Co-60, unbiased	1.67	-	1.65	1.65	1.66
15	2krad 10MeV protons	1.74	-	1.72	1.70	1.72
16	2krad 10MeV protons	1.72	-	-	1.76	1.73

Copyright © Sira Ltd 1995

CCD25-20 devices						
Device No	**Irradiation**			**immediate**	**after 2 months**	
		0 krad	**half-dose**	**full dose**	**full dose**	**average**
01	4 krad Co-60, unbiased	0.81	0.85	0.83	0.82	0.83
02	2krad 10MeV protons	0.77	0.77	0.84	0.81	0.80
03	2krad 10MeV protons	0.77	-	-	0.79	0.78

With unity gain in the CCD camera (gain normally used for dark current measurements was 37.14) the final gain calibration for each device type was:

	Electronics conversion gain µV/ADU
TH 7895	530
TH 7395	754
TH 7863B	505
CCD25-20	638

Copyright © Sira Ltd 1995

4 DARK CURRENT MEASUREMENTS

The results in this section were obtained from recorded dark images, each the average of 16 frames.

4.1 CCD02 DEVICES

Measurements of dark current and dark current non-uniformity were reported in RD5 for CCD02 and CCD05 devices in the range 40 °C to 6 °C. In this study, the temperature range has been extended down to -23 °C with a particular emphasis on investigating the effectiveness of dither clocking at the lower temperatures. The theory of dither clocking will be briefly discussed in the next section. The effect is, in principal, to achieve inversion of the CCD surface (from n type to p type) so that interface traps are filled (by holes from the channel stops) and dark current generation is suppressed. In practice it was found in RD5 that there was considerable variability in the amount of reduction in dark current that was achievable, with the best devices only showing a factor ~4 reduction in radiation-induced dark current (from ~2 nA/cm^2 to ~0.5 nA/cm^2 at 20 °C for the image regions). However it was noticed that a greater reduction in dark current was possible at temperatures below 20 °C.

4.1.1 Dither Clocking

The theory of dither clocking has been discussed by Burke and Gajar (B. E. Burke and S. A. Gajar, 'Dynamic suppression of interface - state dark current in buried channel CCD's, IEEE trans. on Electron Devices, 38(2), pp285-290, 1991). They define a characteristic time constant $t_i = 1/(n_i v_{th} \sigma)$, where n_i is the intrinsic carrier concentration = $3.10 \times 10^{16} T^{3/2} e^{-0.603/kT}$ cm^{-3}, v_{th} is the thermal velocity = $1.0 \times 10^7 (T/300)^{1/2}$ cm/s and σ is the electron capture cross section, with T the temperature and k, Boltzmann's constant.

Burke and Gajar then give the instantaneous current density (in nA/cm^2) as:

$$J_D(t) = \frac{2}{\pi} \cdot J_D(\infty) \int_0^\infty \frac{\exp(t[x + 1/x]/t_i)}{1 + x^2} dx \qquad (4.1)$$

where $x = (E - E_i)/kT$

In order to obtain the total dark current, the above equation must be integrated over time t. If t^- is the time that the electrodes are high and t_o-t^- the time that they are low then the dark current is given by

$$I = \alpha I_{bulk} + \beta I_{surface} \qquad (4.2)$$

with

$$\alpha = 1 - t^-/t_o \qquad (4.3)$$

Copyright © Sira Ltd 1995

and $$\beta = \alpha - \frac{t_i}{\pi \cdot t_o}\left(1 - \int_0^{\infty} \frac{\exp\left[-2(t_o - t^-)\cosh x / t_i\right]}{\cosh^2 x}\right) dx \qquad (4.4)$$

Note that similar equations have been given by W. Van Toren and J. Bisschop, ('Complete characterization of dark current in frame transfer image sensors', Philips J.Res. 48 pp207-231, 1994). In our case t^- is typically ~1-2 μs which is much shorter than the time between dithers (several hundred μs), hence t^- ~0 and α ~1, so that

$$I = I_{bulk} + \beta I_{surface} \qquad (4.5)$$

with $$\beta = 1 - \frac{t_i}{\pi \cdot t_o}\left(1 - \int_0^{\infty} \frac{\exp\left[-2 t_o \cosh x / t_i\right]}{\cosh^2 x}\right) dx \qquad (4.6)$$

This integral was evaluated using the Microsoft Excel software and the results are given in the next section.

4.1.2 Dither Clocking Results for CCD02 Devices

Figure 4.1-1 shows normalized dark current as a function of t_o/t_i for the theory of para 4.1.1 and experimental data for a CCD02 device. The device chosen was discussed in RD5 (#08) and showed good inversion characteristics (figure 4.1-2 shows a plot of dark current versus substrate voltage, Vss). This device had been irradiated by 10 MeV protons in 4 fluence regions (equivalent to 0, 1, 2 and 4 krad).

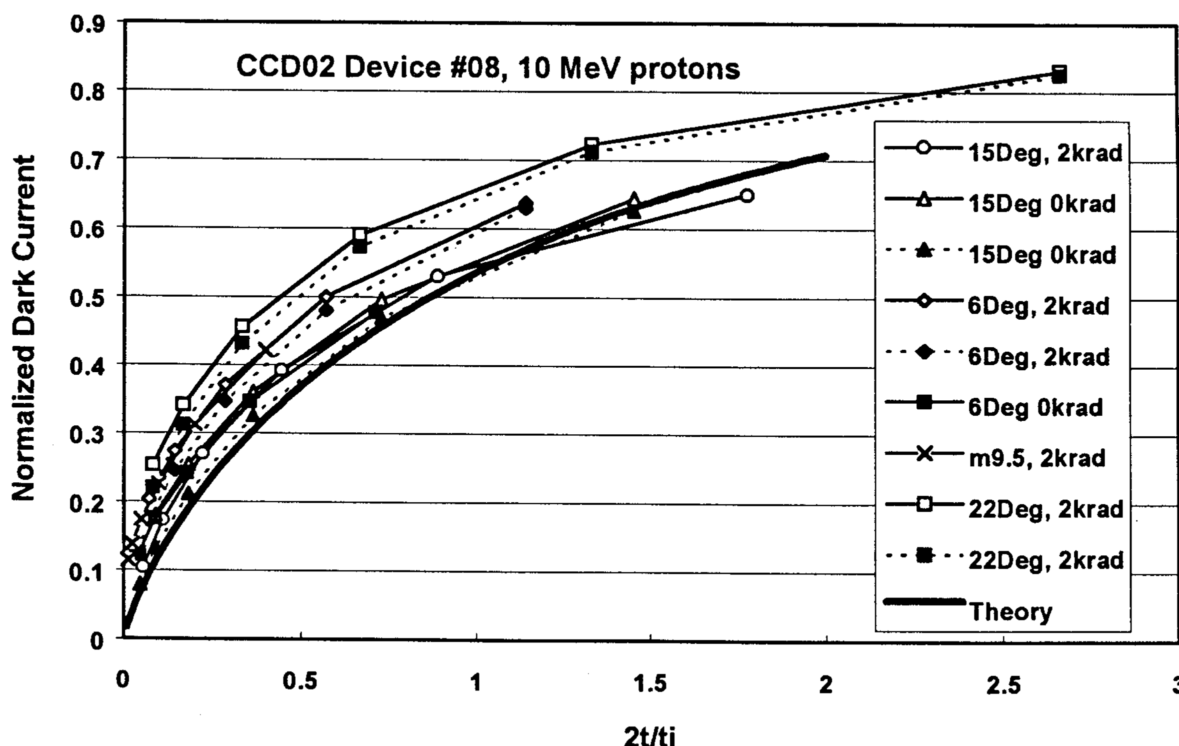

Figure 4.1-1 Dark current as a function of time between dithers for 2-phase (solid) and 3-phase (dotted) dither clocking

Copyright © Sira Ltd 1995

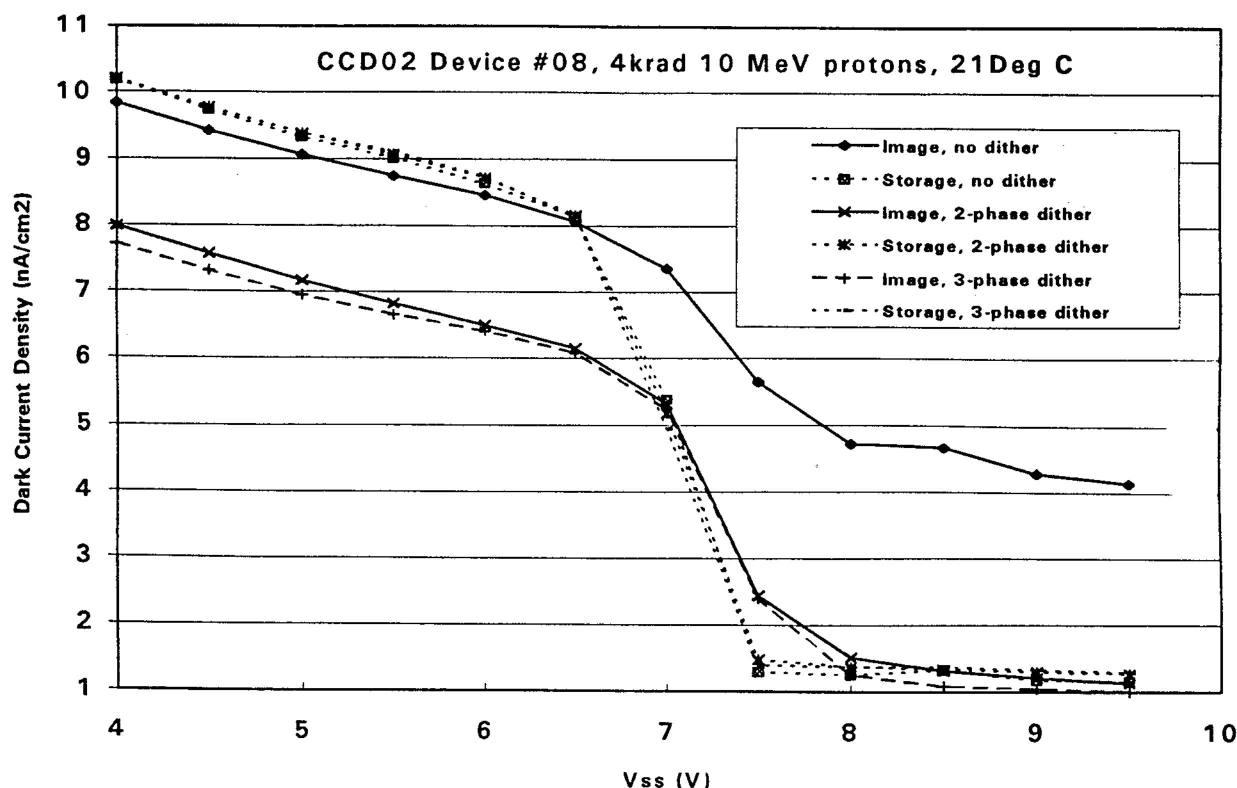

Figure 4.1-2 Dark current density versus substrate voltage for the CCD02 device studied

The data in figure 4.1-1 are for the 2 krad and 0 krad regions. The value of t_i has been adjusted for each temperature so as to achieve a best fit (judged by eye) - note that the curves are offset vertically because of the constant bulk dark current term. The derived values of t_i are plotted in figure 4.1-3 for the 2 krad and 0 krad regions, along with theoretical values calculated from $t_i = 1/(n_i v_{th} \sigma)$. It is seen that the agreement with theory is good near 20 °C but the curves tend to diverge at lower temperatures - with the time constants for 2 krad always being longer than at 0 krad (ie. not irradiated). Note that there will be significant errors in the experimental determination of t_i arising from errors in separation of the bulk and surface components and from temperature changes in the CCD caused by the varying power dissipation (due, in turn, to the changes in clock duty cycles for the different dither clocking regimes). It is however probably significant that t_i after irradiation is increased.

Dither clocking, in effect, shifts charge from one phase to another whilst the signal integration is taking place. Traps which are present at the edge of a pixel (e.g. those that have been produced by bulk displacement damage) will lead to the effect known as pocket pumping, where charge is shifted from one pixel to an adjacent one (in the column direction) so as to produce a 'black and white pair'. this is discussed further in para 4.2.5.

The data shown in figure 4.1-1 includes data for 1-phase dither clocking (where charge is temporarily shifted from phase 2 to phase 1, and back again) and for a 3-phase scheme (or 'super-dither' - dashed lines) which moves charge across all three phases (c.f. figure 4.1-4). A problem with the simple 1-phase dither is that the boundary between phases is never fully inverted; this is one of the reasons why the surface component is not fully suppressed. This problem is largely overcome with the 3-phase scheme, the effect being particularly noticeable for

Copyright © Sira Ltd 1995

data taken in the unirradiated (0 krad) region where at -23 °C a factor 47 improvement in dark current was achievable with 3-phase dither clocking every 425 μs (i.e. once per line) in contrast to a factor 16 for 1-phase dither. Note that because t_i increases as T is reduced, these improvement factors will increase at lower temperatures and factors of >100 improvement can be expected for temperatures below ~ -30 °C.

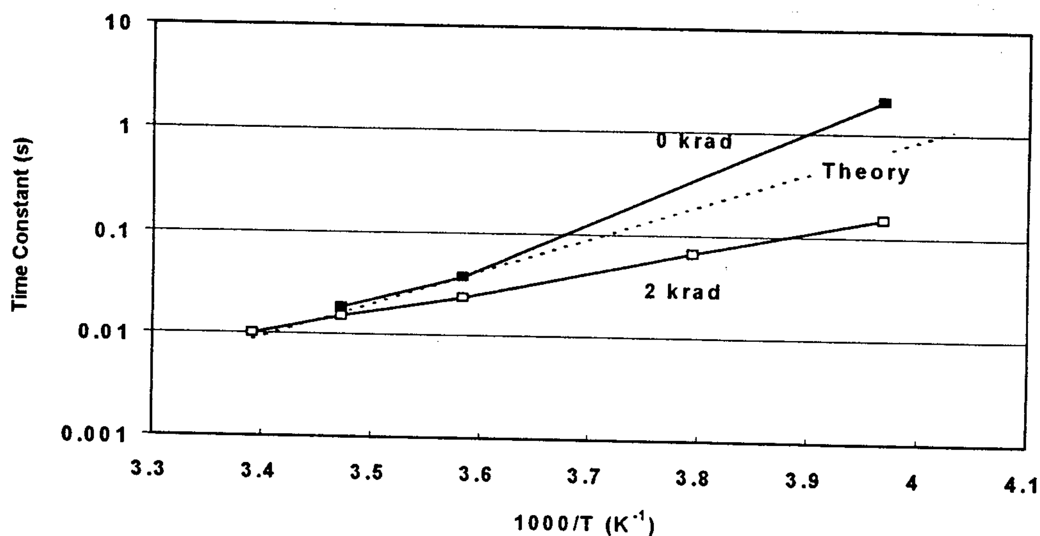

Figure 4.1-3 Values of the time constant for dither clocking

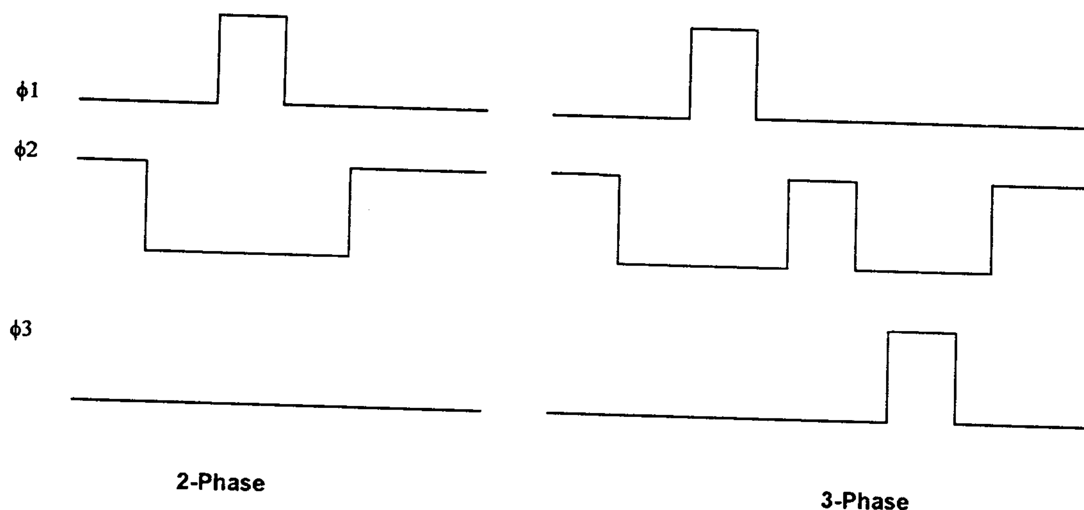

Figure 4.1-4 Illustration of 2-phase and 3-phase dither clocking

Values for the image area dark current as a function of temperature are given in figure 4.1-5 for the 2 krad region of CCD02 device #08. Also shown is a theoretical line, calculated using an Arrhenius relation with an activation energy of 0.63 eV. It is seen that the data is in reasonable

Copyright © Sira Ltd 1995

agreement with this function, with the fall in dark current being faster when dither clocking (as expected since t_i increases as T falls). 0 krad data is included in figure 4.1-3 for comparison.

Note that the 2 krad data tends to be dominated by the bulk component at low temperature (this component is ~0.1 nA/cm^2 at 20 °C and again falls with an activation energy of 0.63 eV). In other words in a space environment a point is rapidly reached where bulk displacement damage limits the dark current and improvements in dither clocking efficiency (because of t_i increases) are not of great benefit. As a rough guideline it is likely that with efficient dither clocking (as occurs with device #08), bulk dark current is dominant for temperatures below 0 °C. Note that the storage region component is always effectively dithered because of the readout process.

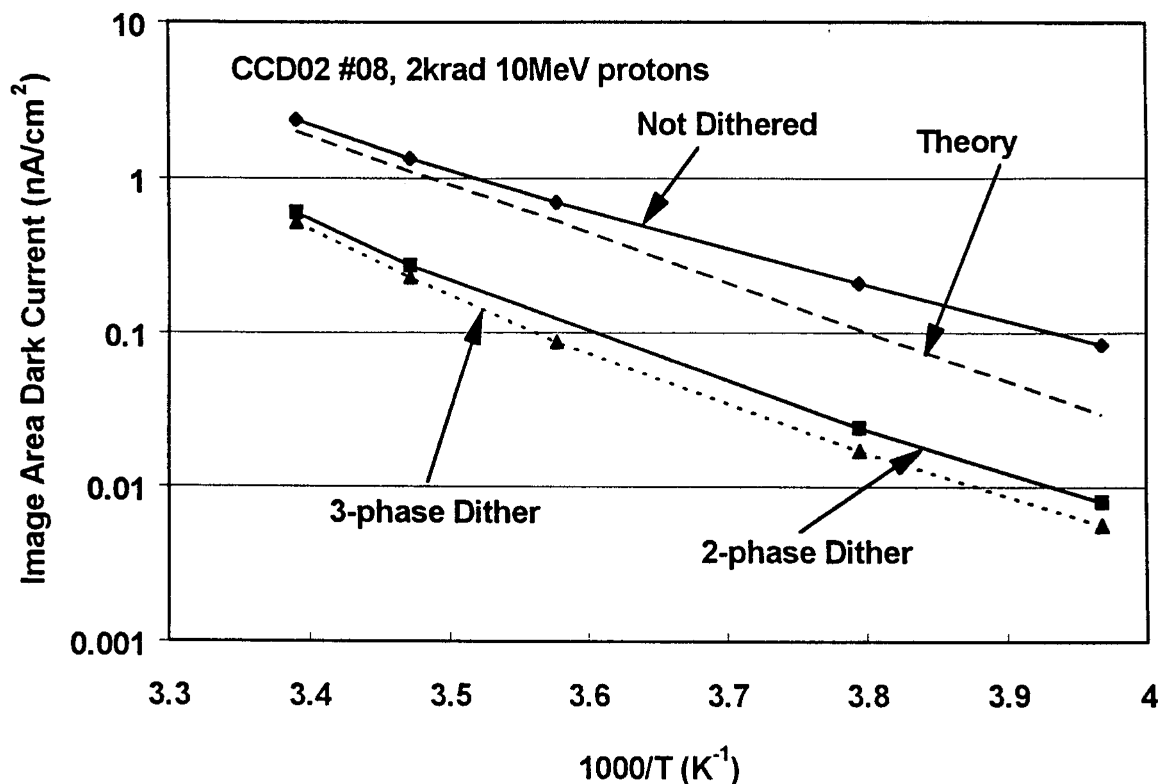

Figure 4.1-5 Image region dark current versus 1000/T

4.2 CCD25-20 DEVICES

4.2.1 Average Dark Current

The three back-illuminated CCD25-20 devices measured in this study showed a variation of dark current with substrate voltage similar to typical devices measured in the previous study (RD5) (i.e. not such a sharp transition into inversion as the CCD02 #08 studied above, but not as slow a transition as some of the CCD02 devices). Plots of dark current versus Vss are shown in figures 4.2-1 to 4.2-5, with and without dither clocking. Typically the reduction in dark current is a factor 2-4 (pre- and post-irradiation). The present results apply for a substrate voltage of 7.8 V. A further reduction in dark current might be expected for higher values of v_{SS} but, as will be seen in para 5, this leads to a loss in full well capacity. With these devices the highest v_{SS} that could practically be used was 7.8 V.

Copyright © Sira Ltd 1995

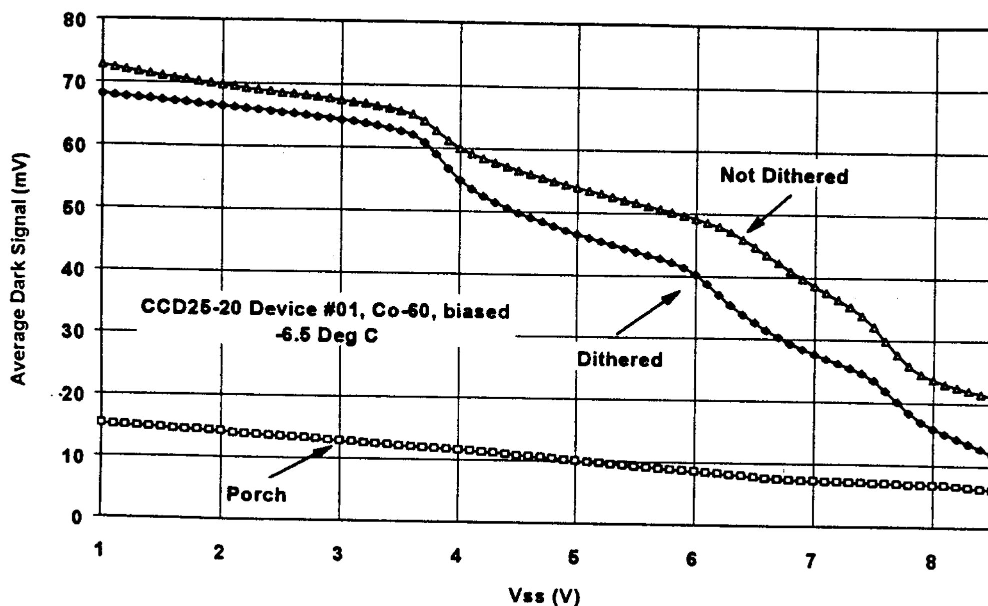

Figure 4.2-1a Average image region dark signal at -6.5°C versus substrate voltage for CCD25-20 #01. Operating point was Vss = 7.8V

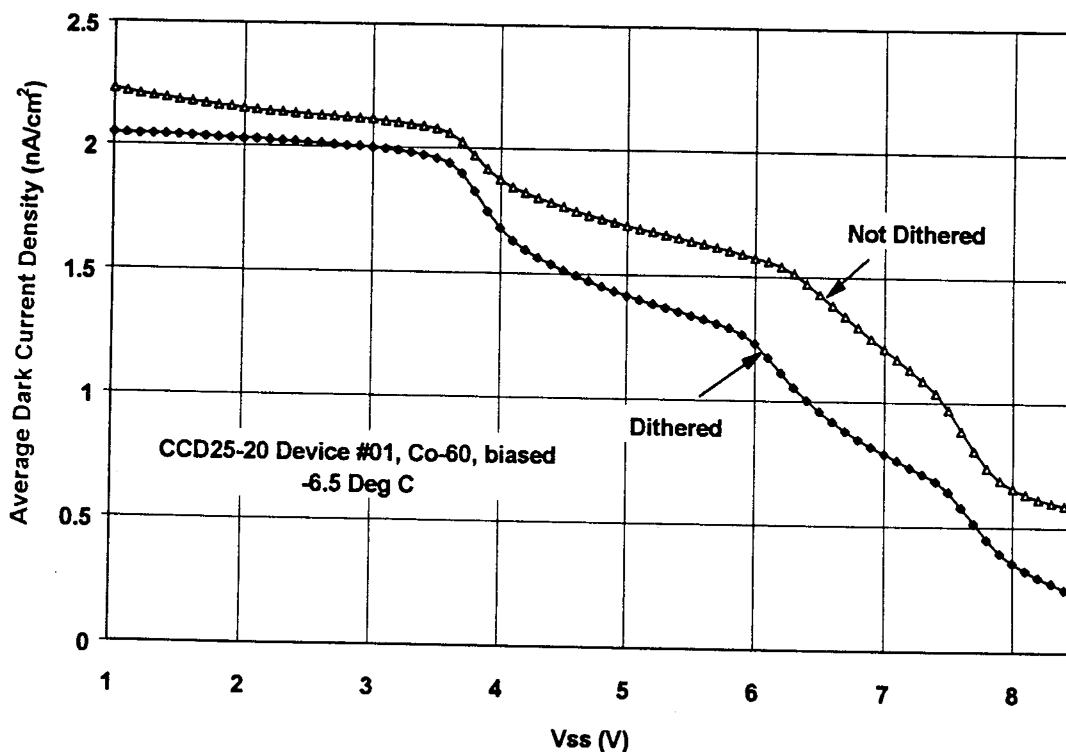

Figure 4.2-1b Average image region dark current density at -6.5°C versus substrate voltage for CCD25-20 #01. Operating point was Vss = 7.8V

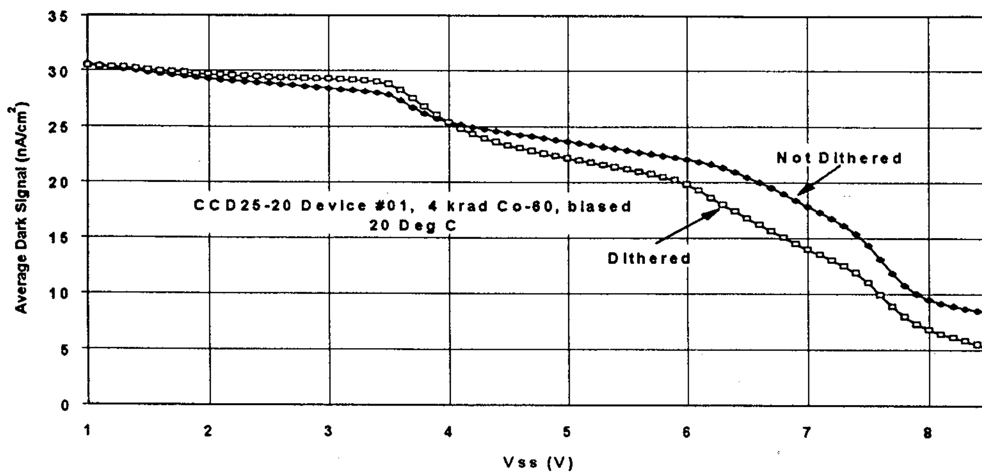

Figure 4.2-1c Average image region dark current density at 20°C versus substrate voltage for CCD25-20 #01. Operating point was Vss = 7.8V

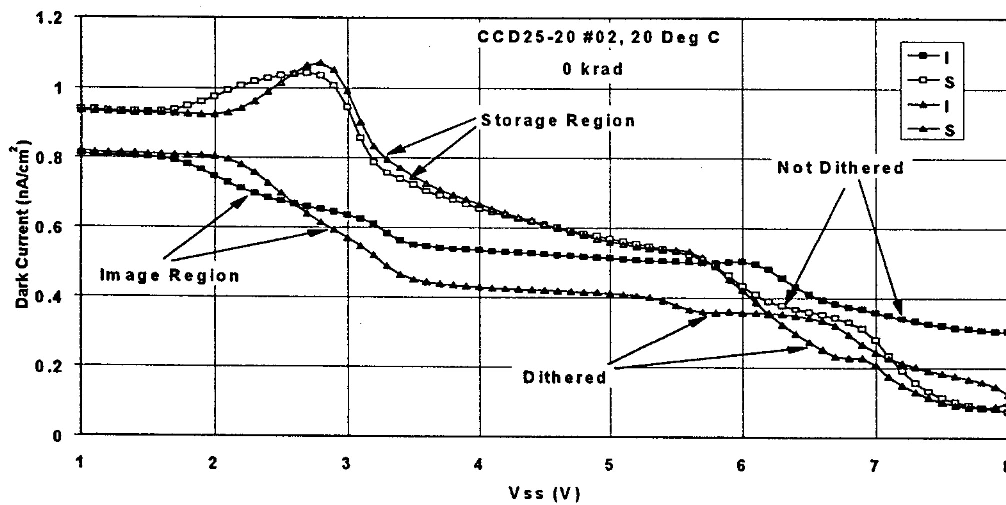

Figure 4.2-2a Average image region dark current density at 20°C versus substrate voltage for CCD25-20 #02 pre-irradiation. Operating point was Vss = 7.8V

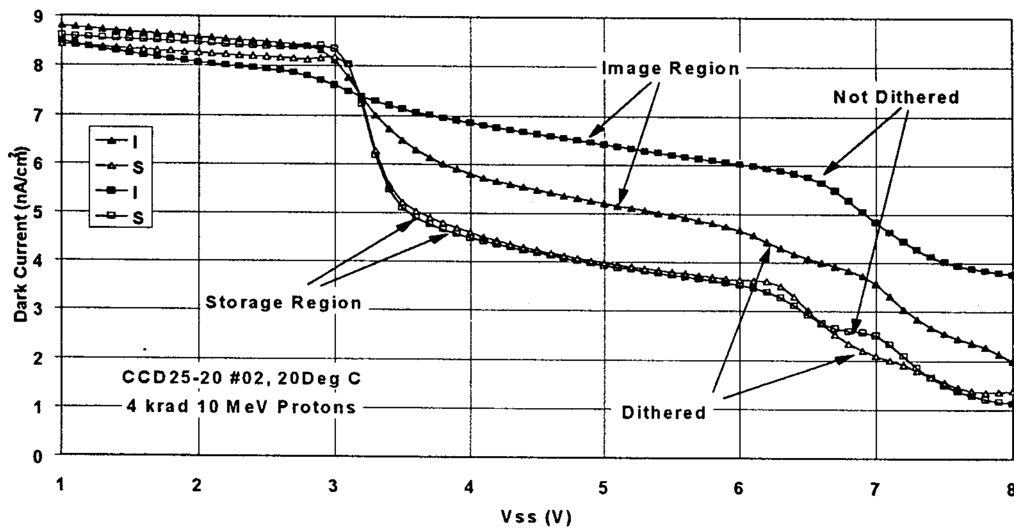

Figure 4.2-3 Average image region dark current density at 20°C versus substrate voltage for CCD25-20 #02 4krad 10MeV protons. Operating point was Vss = 7.8V

Copyright © Sira Ltd 1995

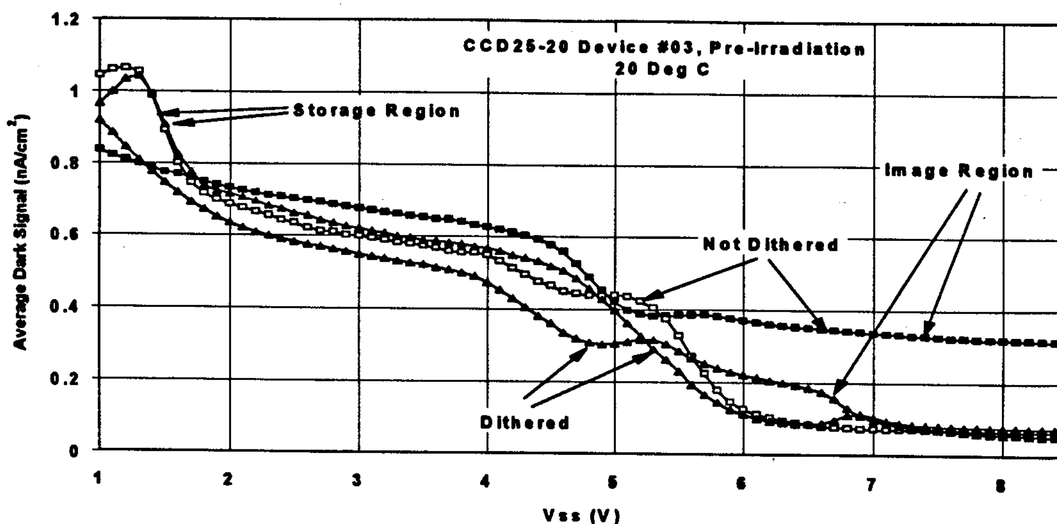

Figure 4.2-4 Average image region dark current density at 20°C versus substrate voltage for CCD25-20 #03 pre-irradiation. Operating point was Vss = 7.8V

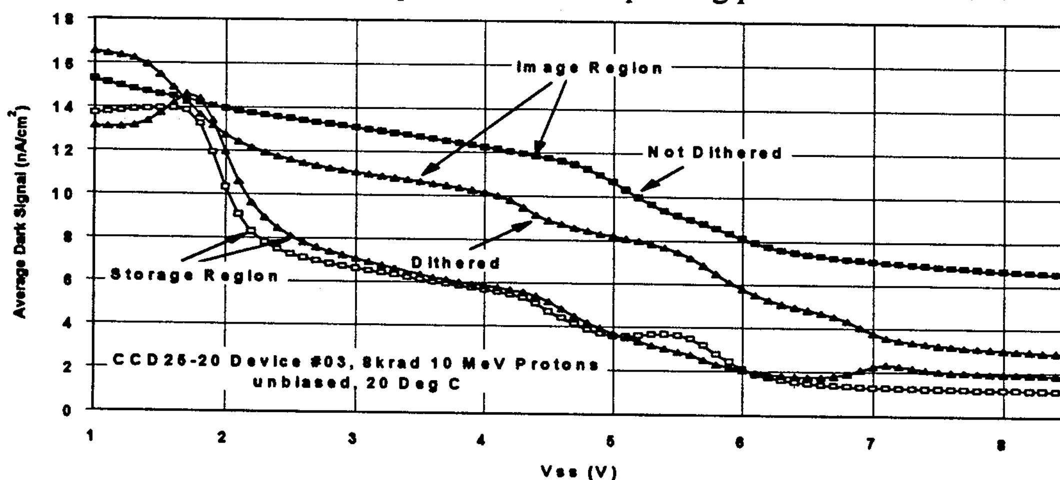

Figure 4.2-5 Average image region dark current density at 20°C versus substrate voltage for CCD25-20 #03 8krad 10MeV protons. Operating point was Vss = 7.8V

At 20 °C we have the following results:

Table 4.2-1 Dark current density in nA/cm^2 (20 °C) - means data not available

Device		Pre-irradiation	Immediate 2 krad	Immediate 4 krad	after 2 months 4 krad
#01 (Co-60,p)	image region	0.93	0.81	1.84	7.13
	image dithered	0.25	0.40	-	4.24
	storage region	0.35	0.49	0.52	-
	storage dithered	0.30	0.38	0.29	-
#02 (proton)	image region	0.32	0.92	2.02	3.8
	image dithered	0.10	-	-	2.2
	storage region	0.09	0.74	1.59	1.1
	storage dithered	0.09	-	-	1.0
#03 (proton)	image region	0.30	1.21	1.98	3.5
	image dithered	0.08	-	-	1.5
	storage region	0.05	0.90	1.51	0.66
	storage dithered	0.07	-	-	0.90

The dark current in these devices was somewhat non-uniform (especially when dither clocking) and this occasionally made the determination of the storage region component difficult. Such cases are marked with a dashed line in the table

The two proton-irradiated devices (#s 02 and 03) were masked into several fluence regions and plots of dark current density are shown in figure 4.2-6. these data were obtained after 2 months storage at room temperature, unbiased and it is seen that the dark current is linear with equivalent dose of 10 MeV protons (1 krad ≡ 1.79E9p/cm^2). Table 4.2-1 shows that data taken immediately after irradiation have only a small dark current increase, but the dark current reverse anneals (i.e. increases) with storage after irradiation (as has been found in previous studies)

Further measurements were made on the Co-60 irradiated device (#01), in particular **after a** 168hr bake at 83°C. At this time the storage region dark current was estimated by taking two exposures at different gains and integration times as discussed in para 2.7. The results are given in the following table. Note that there is little further reverse annealing (which has largely taken place during the first 2 months)

Table 4.2-2 Dark current density in nA/cm^2 (20 °C), Vss = 7.8V
Device #01 after 4krad Co-60

Region	after 2 months	after 4 months	4 days bake at 80°C	2 days bake at 80°C	2 weeks after bake
Image	7.13	7.17	9.17	8.11	8.78
Image, dithered	4.24	4.38	6.93	6.23	7.04
Storage	-	-	-	-	2.2
Storage, dithered	-	-	-	-	2.2

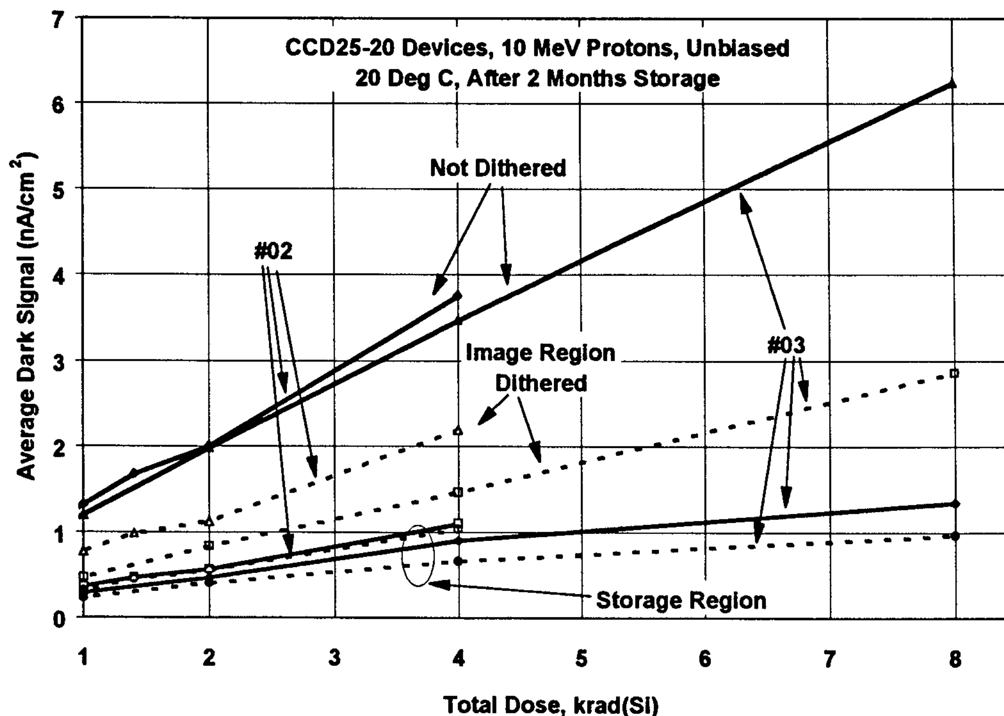

Figure 4.2-6 Dark current density at 20°C for proton irradiated devices (unbiased).

Copyright © Sira Ltd 1995

Looking at all the devices, there is some variability in pre-irradiation dark currents at 20 °C but the image region is in the range 0.3-0.9 nA/cm^2 (not dithered) and ~0.1 to 0.2 nA/cm^2 (dithered), with the increase/krad being as follows.

	Δ dark current density at 20 °C (nA/cm^2 per krad) Vss = 7.8V	
	Co-60 (powered) after anneal	10 MeV proton (not powered)
image region	2.2	0.8
image region dithered	1.7	0.4
storage region storage region dithered	0.55	0.2

The increases for proton irradiated devices are very similar to values found previously (RD5) but in contrast to the earlier result (which showed little difference), the Co-60 powered irradiation gives twice the increase.

Note that we cannot make a strong conclusion about the effectiveness of dither clocking for the CCD25-20 devices studied here because of the weak inversion characteristics.

The change of average dark current density with temperature was studied for the Co-60 irradiated device #01 and the proton-irradiated device #03. Figures 4.2-7 and 4.2-8 show results for the various dose regions. It is seen that, apart from inaccuracies in estimating the storage component (because of non-uniformities and the fact that the readout time was fixed), the agreement with an Arrhenius relation with an activation energy of 0.63 to 0.65 eV is good. This means that the above results at 20 °C should be scaled by a factor ~60 to get corresponding values at -20 °C. Results for the variation in activation energy with Vss were obtained for device #01 and are shown in figure 4.2-9. For completeness, figure 4.2-10 gives the dark current versus Vss for #03 at -20°C. The storage region component at -20 °C was too small to measure accurately. We note that for unbinned pixels and an integration time ~40 ms at -20 °C (as for the MERIS instrument) the average dark signal (image plus storage regions components) is estimated to be 50 electrons after 2 krad - assuming the extra factor 2 discussed above for a device biased during irradiation.

Copyright © Sira Ltd 1995

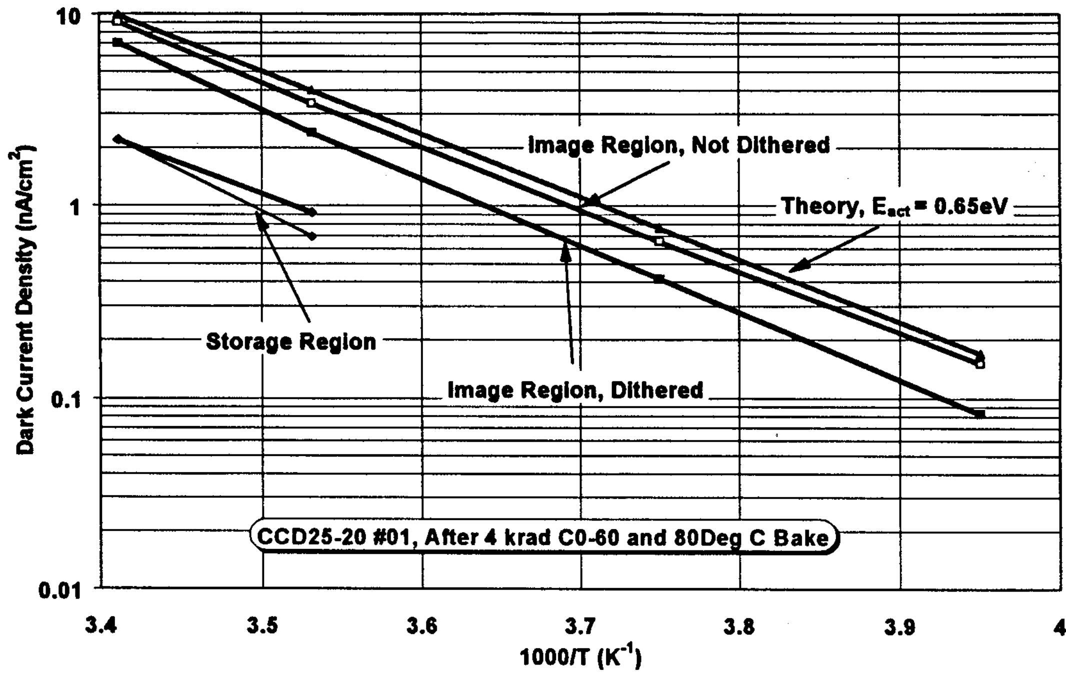

Figure 4.2-7 Dark current density variation with temperature for #01

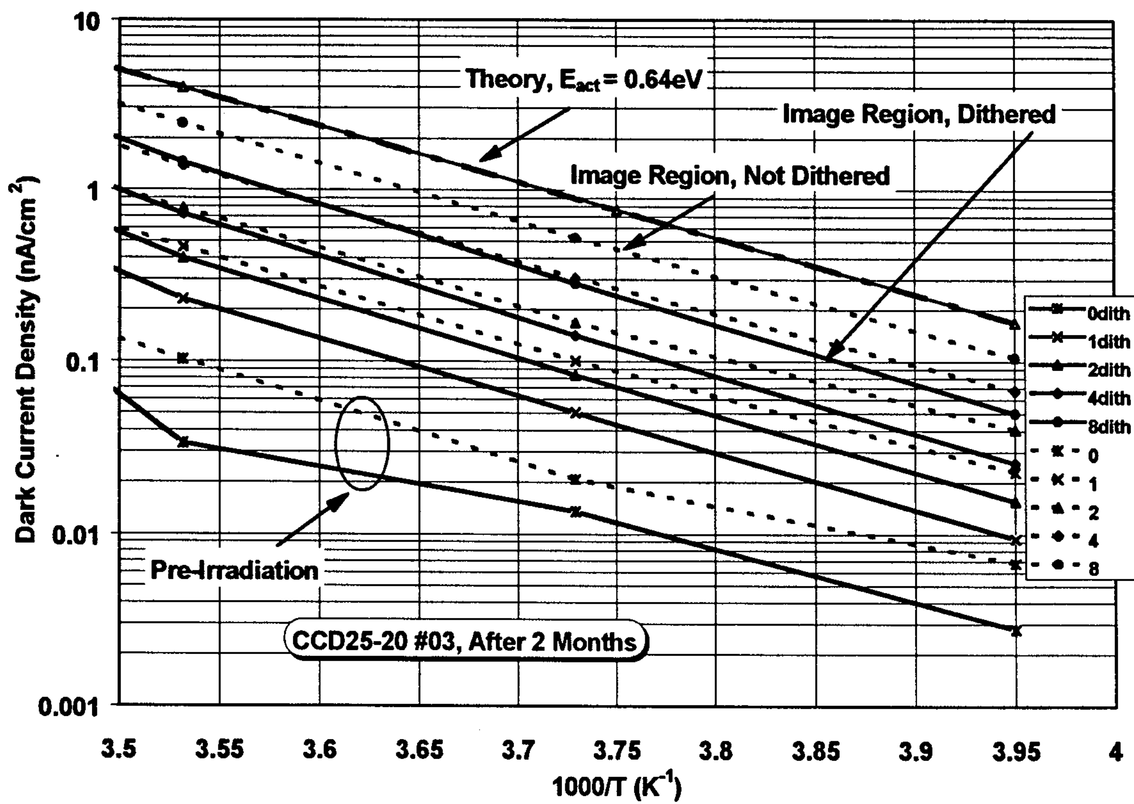

Figure 4.2-8 Image region dark current density variation with temperature for #03 for total doses (10 MeV protons) increasing from 0 to 8 krad. Results for dither clocking are shown dotted. Storage region data showed the same slope but are omitted for clarity.

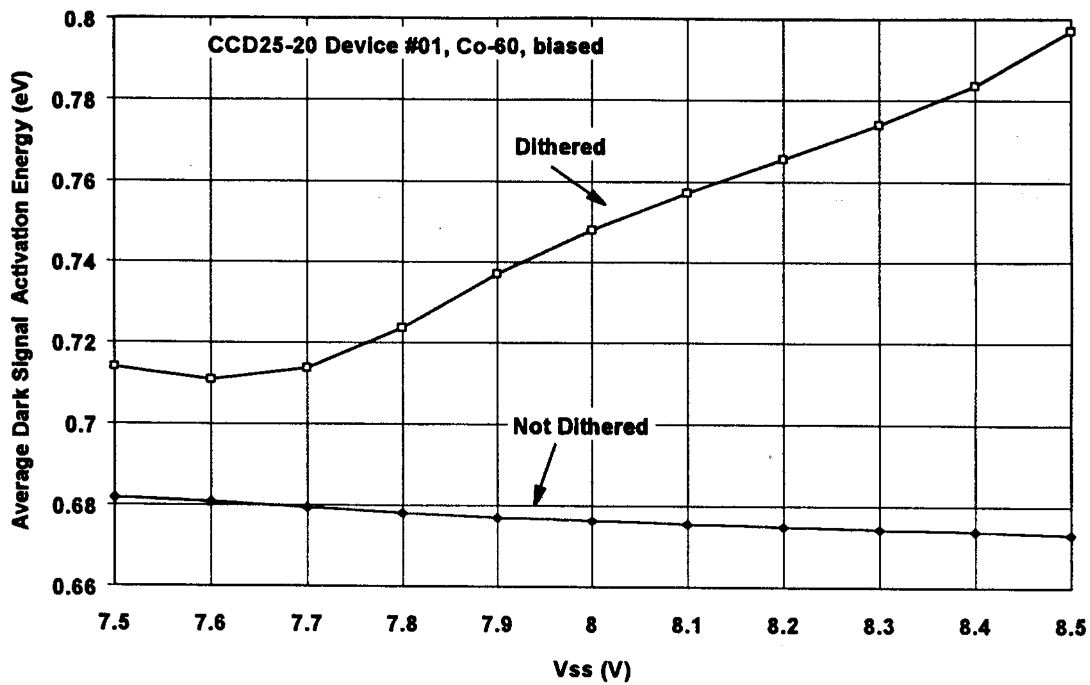

Figure 4.2-9 Dark current activation energy (-20°C to 20°C) versus Vss for the Co-60 irradiated CCD25-20. Dither clocking becomes more efficient at lower temperatures and E_{act} increases.

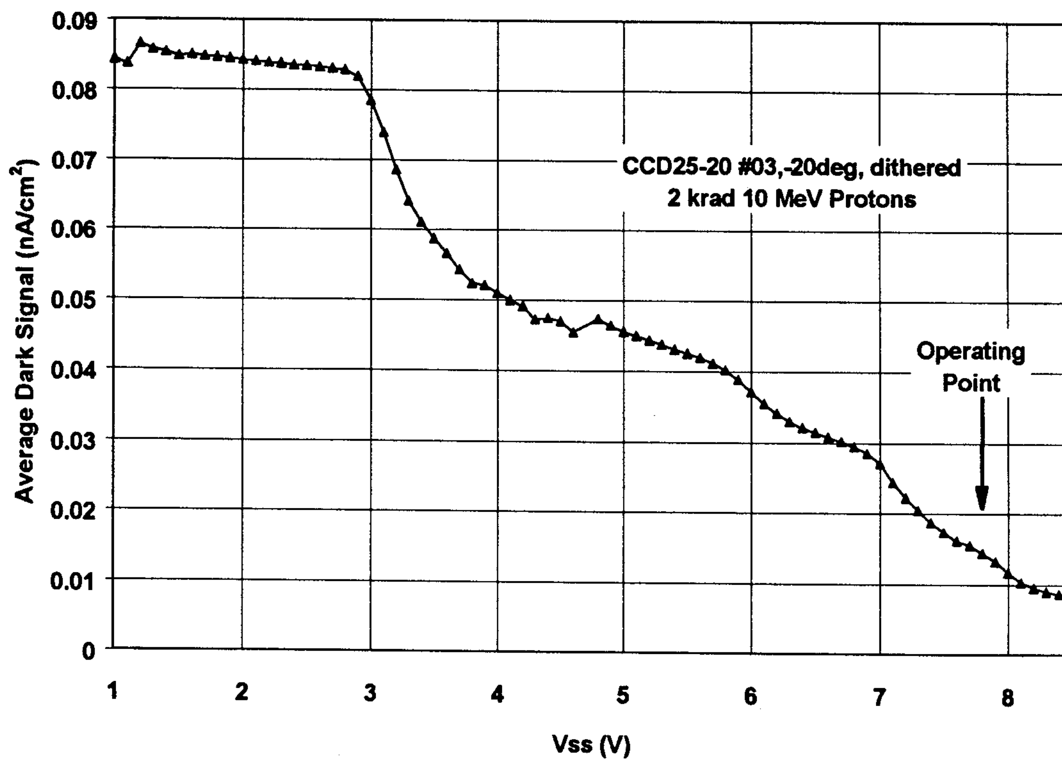

Figure 4.2-10 Dark current density at -20°C for a proton irradiated device.

Copyright © Sira Ltd 1995

Figure 4.2-11 shows plots of normalized dark current versus the time between dithers. These plots are analogous to those of para 4.1 and show the decrease in dark current as the dither rate is increased and the increase in characteristic time constant as the temperature is lowered. Note, however, that the results are affected by temperature changes within the CCD as the dither rate is changed; so that the results are not as clear-cut as for the smaller CCD02 (figure 4.1-1) for which clock-induced power dissipation is not so large.

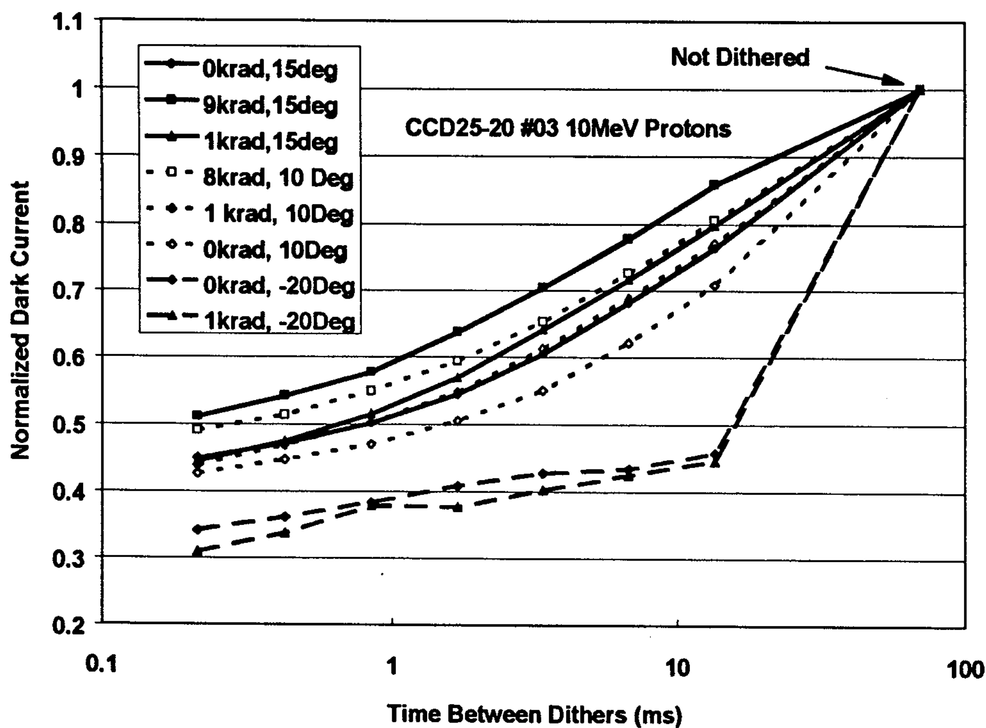

Figure 4.2-11 Plots of normalized dark current versus the time between dithers for device #03.

4.2.2 Dark Current Non-uniformity

This is dominated by the effects of bulk displacement damage caused by proton irradiation. Figures 4.2.2-1 and 4.2.2-2 show dark current histograms for the two 10 MeV proton irradiated devices (including the average dark current discussed in para 4.2.1, but with the slope - i.e. storage region component subtracted).

The plots are scaled so as to have a total count (i.e. the area under each plot) of 10^5. the histograms are similar in appearance to those found for previous studies. Also shown in figure 4.2.2-2 are histograms for -20 °C but scaled by a factor 57; this being the factor decrease in dark current for an activation energy of 0.63 eV. The plots for 20 °C and -20 °C are exactly superposed - indicating that (as found in previous studies, e.g. RD5),on average, the bulk dark current scales in the same way as the mean level (which is caused by both bulk and surface generation).

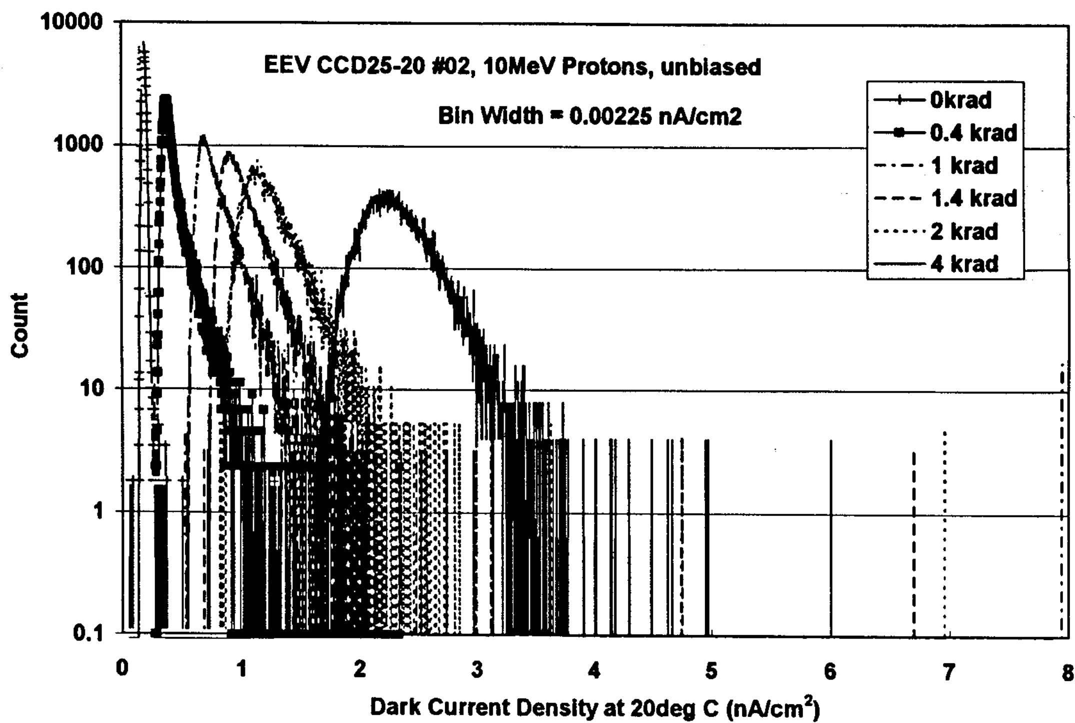

Figure 4.2.2-1a Dark current histograms at 20°C for device #02

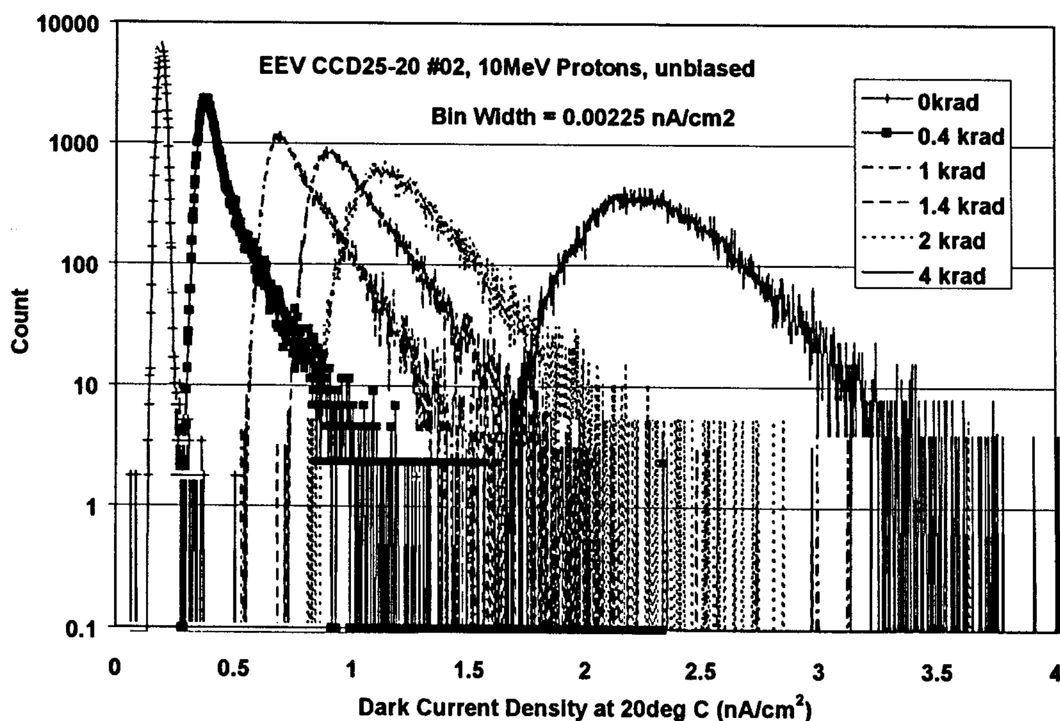

Figure 4.2.2-1b Dark current histograms at 20°C for device #02, increased scale.

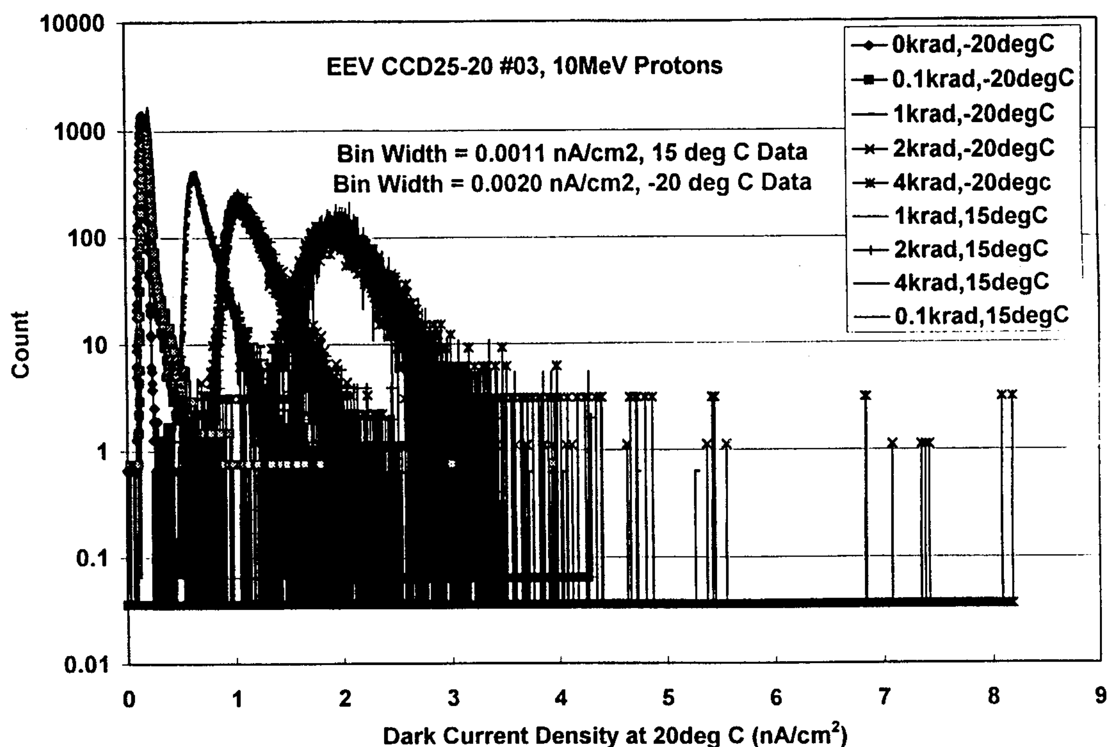

Figure 4.2.2-2a Dark current histograms at 15 and -20°C for device #03. The dark current density values have been scaled (according to Eact = 0.63eV) so as to give equivalent values at 20°C.

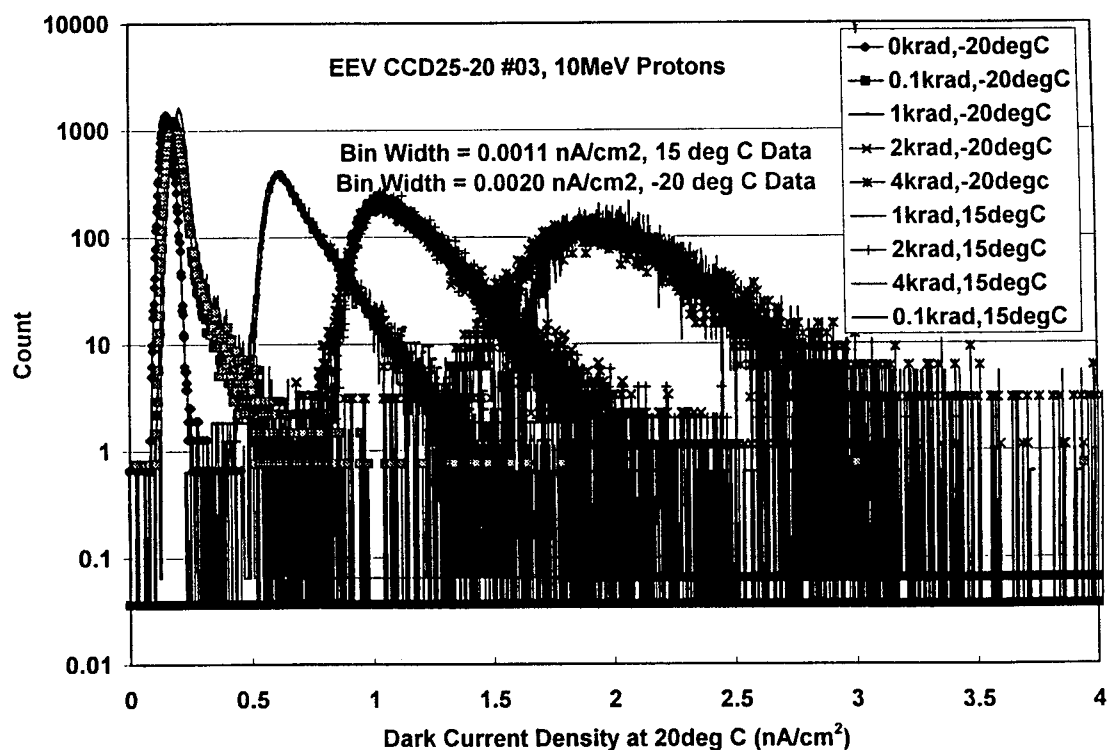

Figure 4.2.2-2b As above but showing the main peaks in more detail

Copyright © Sira Ltd 1995

An important question is how the non-uniformity changes when pixels are binned together. At first glance it might be expected that with 2x2 binning the non-uniformity would increase by the square root of 4 (i.e. 2). This should certainly be true if the dark current varies randomly from pixel to pixel with a gaussian distribution. However the dark current distributions are skewed, since there are many dark current spikes. Dale et al [C. J. Dale., P. W. Marshall, E. A. Burke, G. P. Summers and G. E. Bender "The generation lifetime damage factor and its variance in Si", IEEE Trans. on Nuclear Science, NS-36, pp 1872-1881(1989)] have shown that the variance of the dark current should be proportional to fluence and increasing the pixel size might be expected to be equivalent to increasing the proton fluence by the same factor (since the number of proton interactions, and hence dark charge generating states, should be the same). However there are other factors to be considered:

i) the effect of recoil tracks which cross pixel boundaries

ii) large scale (i.e. low spatial frequency) non-uniformities (i.e. correlation between dark current values) - especially as with the devices studied here the surface dark currents not fully suppressed

iii) the effect of large dark current spikes due to field enhanced emission

The effect of ii) or iii) above might be expected to be to reduce the averaging effect of binning N pixels together so that the rms should increase by more than $\sqrt{N}$. This can be seen in figure 4.2.2-3 where the variance of the dark current increases with the fluence (and with total dose) but there is a factor ~6 increase (rather than 4) when 4 pixels are binned. In fact the effect is more pronounced if, instead of looking at the rms (which is very much influenced by the outlying dark current spikes) we consider the half width of the main peak of the distribution. Figure 4.2.2-4 shows dark current distributions (on a linear scale) for 1 krad and 4 krad regions of a CCD25-20 at -20 °C for unbinned and 4x1 binned pixels, the unbinned case having been scaled by a factor 4 (not 2 as might have been expected). It can be seen that the main peak is nearly the same shape - so it could be argued that the non-uniformity has increased by 4 as a result of the binning (naturally the mean has also increased by 4). This is not unreasonable considering that the dark current spikes are sparse - and more than 4 pixels apart, hence a 4x1 'super pixel' is not likely to include more than one large spike and so there is no averaging effect. Note however that the distribution after binning is less skewed (as we expect from the central limit theorem) and so the rms will increase by less than 4 (as we found above - since the increase was $\sqrt{6}$). The basic conclusion is that non-uniformity is not significantly reduced by 2x2 binning this is perhaps plausible, though the exact reasons are not fully clear.

Note that the above results have also been checked by performing the binning off-chip (i.e. in computer memory) and it has been verified that on chip binning does produce a simple addition of pixel signals (c.f. figure 4.2.2-5).

The dark images from CCD25-20 devices show an additional nonuniformity in that the first and last few columns are bright (i.e. near full scale). This is thought to be due to charge diffusing in from surrounding parts of the wafer. This effect may be reduced for MERIS flight devices, depending on the guard ring structures used and the definition of the useful pixel area (there will be a light shield to define dark reference and smear regions). The effect is illustrated in figure 4.2.4-3 (in the section on readout register dark current). At temperatures above -20°C blooming can occur and several columns can be affected. Only pixels in the first and last columns were affected and not the first and last lines. This is not unreasonable since the top and

Copyright © Sira Ltd 1995

bottom of the CCD are shielded from the rest of the wafer by the readout registers and dump gate. Note that the additional charge decreases with temperature. Since this charge is distributed along columns, rather than being confined to localized areas (such as the vicinity of an output amplifier), the cause is not thought to be due to voltage-induced charge injection - though further work (e.g. a detailed investigation of temperature and voltage behaviour).

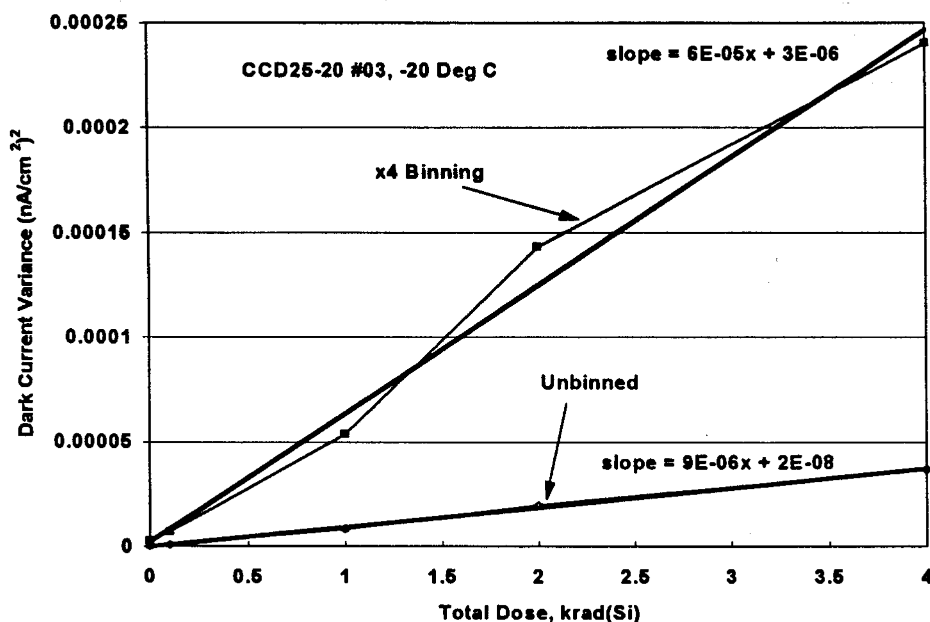

Figure 4.2.2-3 Variance of the dark signal versus total dose, with and without binning

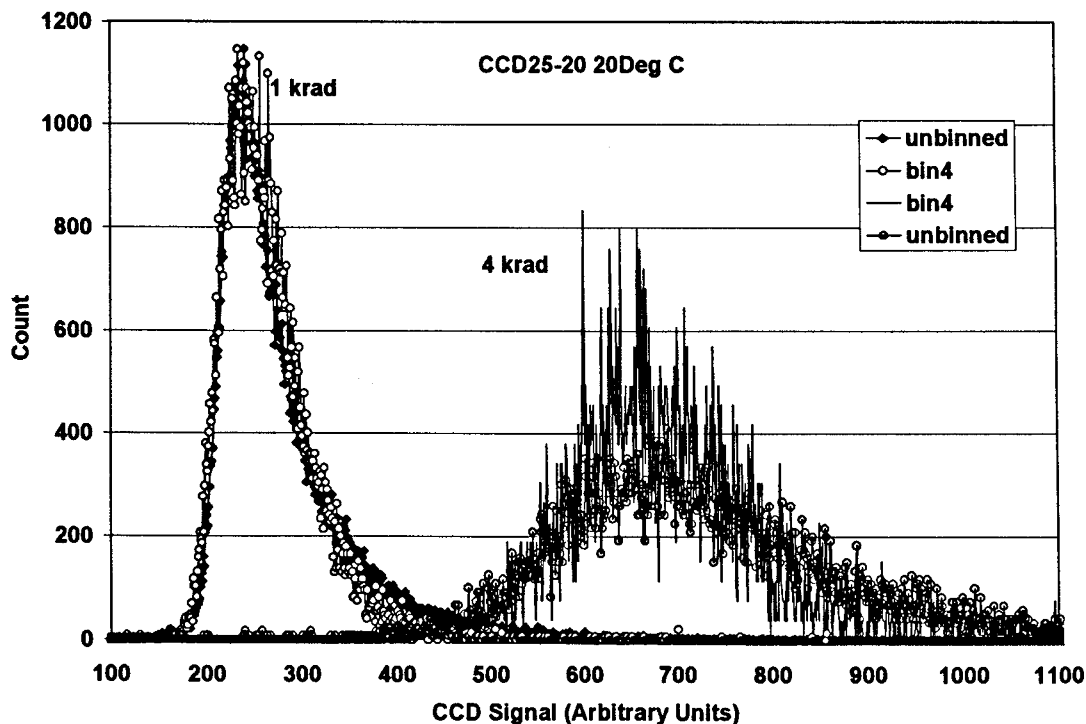

Figure 4.2.2-4 Dark current histograms with and without binning - linear scale

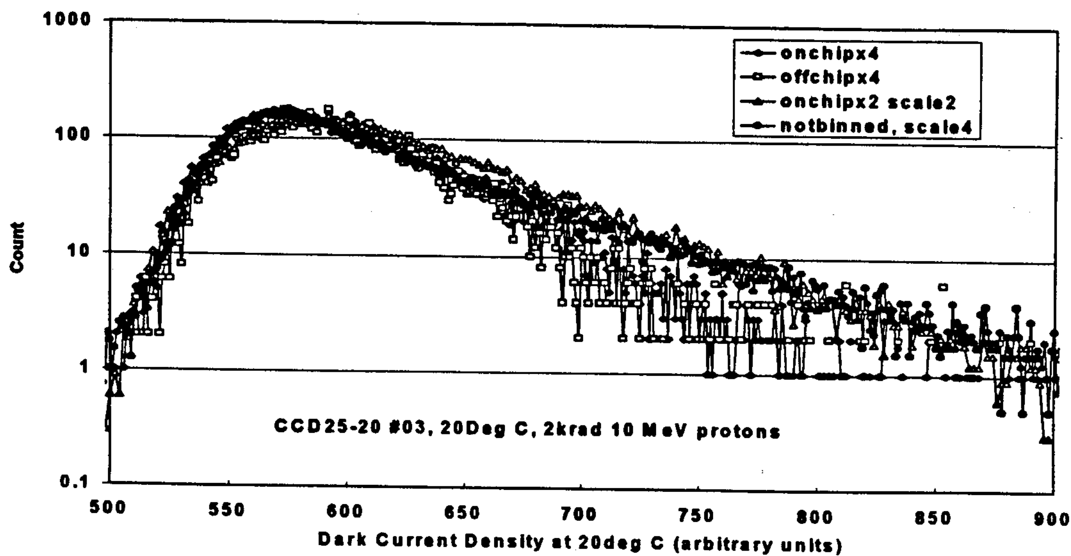

Figure 4.2.2-5 Dark current histograms with and without binning - logarithmic scale

Figure 4.2.2-6 shows cumulative dark current histograms for device #03, i.e. plots of the percentage of pixel with dark current density above a given value.

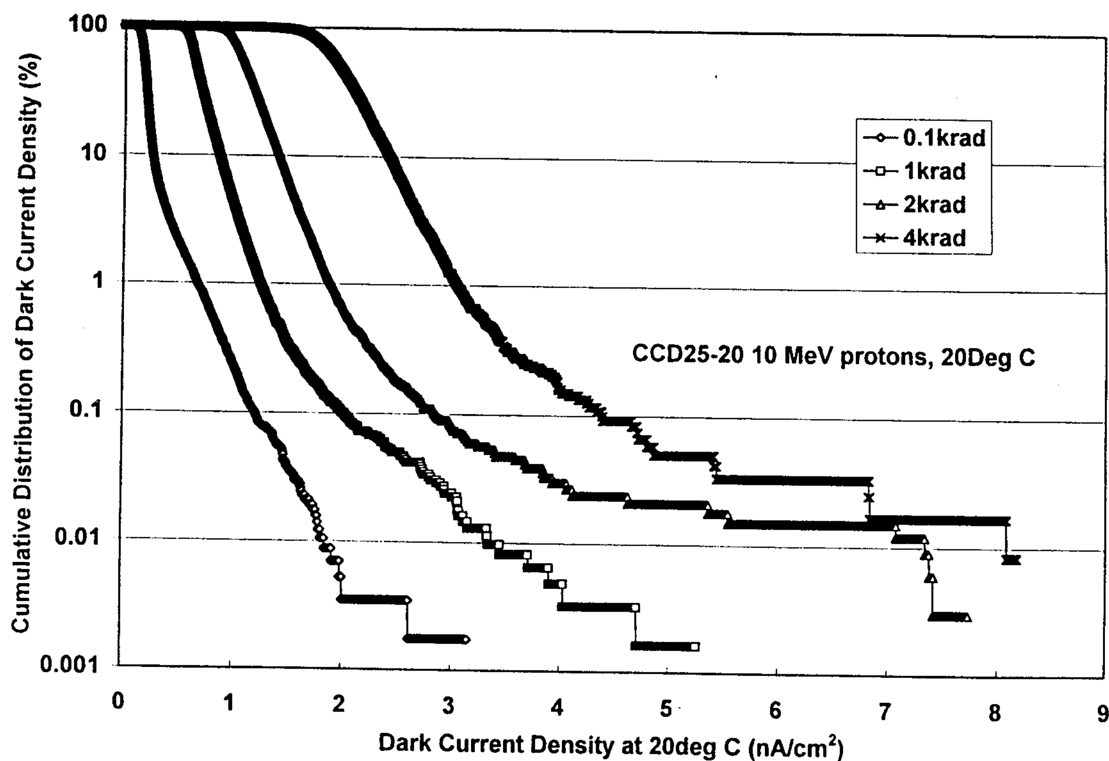

Figure 4.2.2-6 Cumulative dark current histograms

Copyright © Sira Ltd 1995

4.2.3 Dark Charge Spikes

It has been demonstrated in previous studies that the largest dark current spikes are due to field enhanced emission. Note that approximately 1% of pixels have dark currents significantly outside the main peak. It can be seen from figures 4.2.3-1 and 4.2.3-2 that, as expected, there is a trend for the largest spikes to have a reduced activation energy (i.e. they cool out slower).

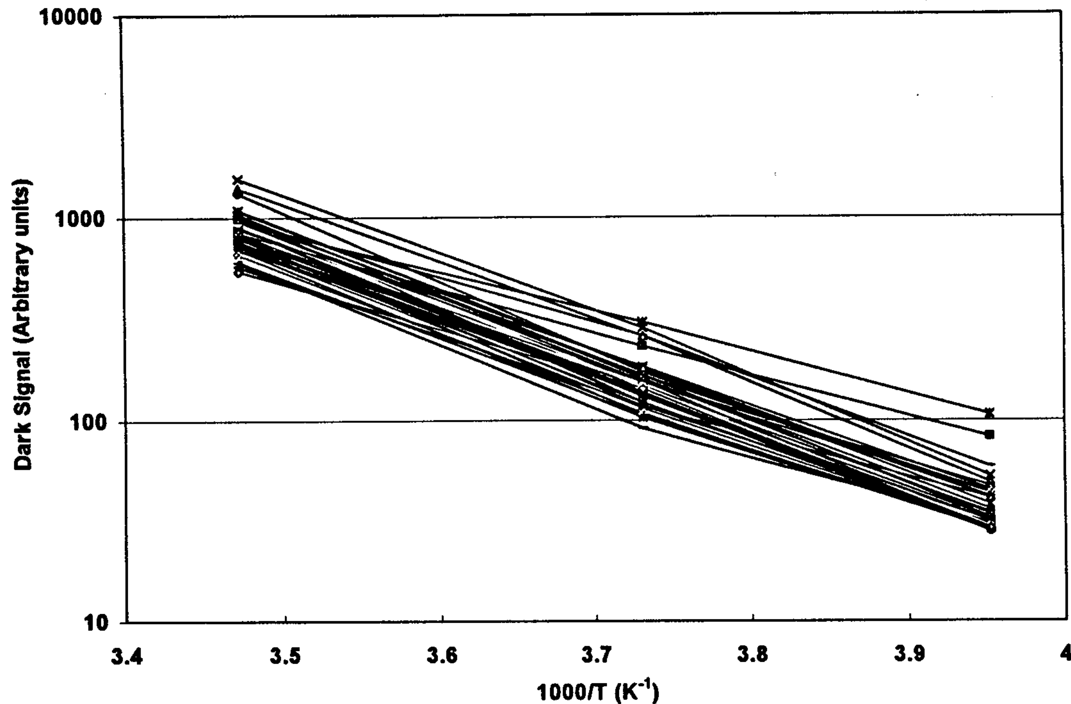

Figure 4.2.3-1 Typical variation of spike amplitude with temperature

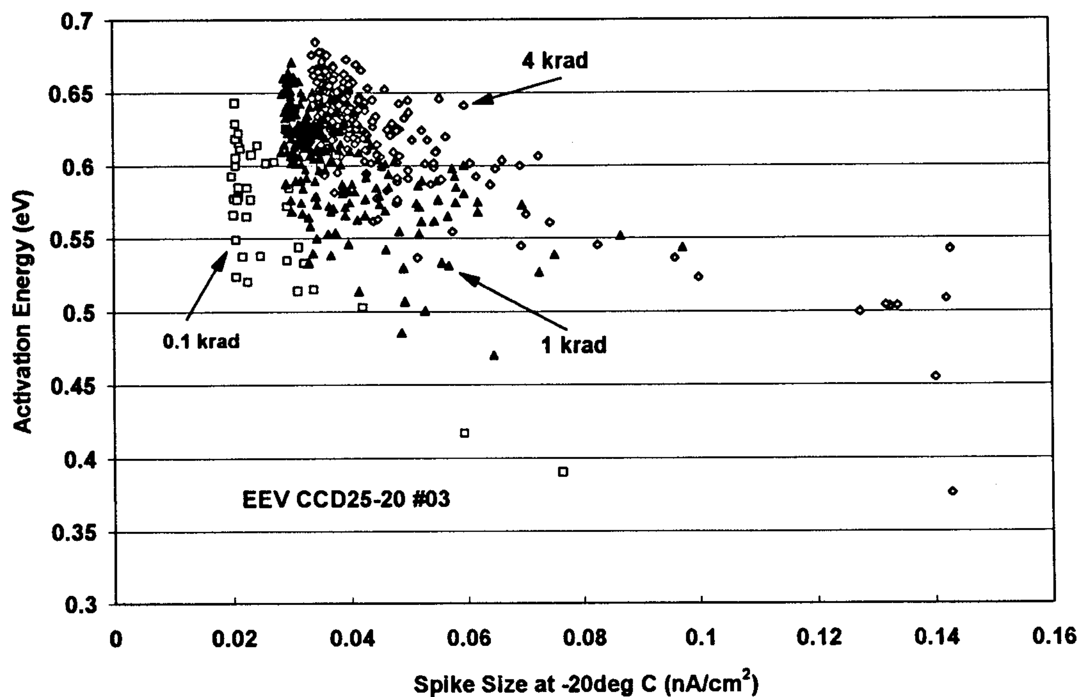

Figure 4.2.3-2 Activation energy for spike size versus spike size at -20°C

Copyright © Sira Ltd 1995

4.2.4 Dark Signal and its Non-uniformity for the Readout Register

This was measured, on return from Harwell, by allowing the readout register to act as a linear CCD and accumulate charge (typically for 1 second) before reading out. In normal operation the readout clocks would normally be pulsed frequently, so giving a dither clocking effect. Hence measurements were made for dithered and undithered integrations. For the dither clocked situation the effect of having either one or two R clocks high for most of the time was investigated. In normal operation two R clocks are high during transfer from the storage to the readout register so the two clocks high case should be the most representative. Results for the average readout register dark current are shown as a function of total dose (10 MeV protons) and clocking conditions for device #03 in figure 4.2.4-1, and for all 3 devices (dither clocking, two phases high case) in figure 4.2.4-2. It can be seen that, in contrast to the image area case, the dark current is higher for the proton-irradiated devices than for the Co-60. The reason for this is unknown but may be due to differences in dither clocking efficiency for the readout register. Also the dark currents expressed in nA/cm^2 are larger than for the image and storage regions. However this is a somewhat artificial result since the values were calculated assuming 22.5 μm pixels and it is known that the readout register pixels are about a factor 4 larger in area. The effect is illustrated further in figure 4.2.4-3 which shows dark current densities for both readout register and image area (both dithered) for device #01 (again assuming identical pixel areas).

Also shown in figure 4.2.4-3 are the bright pixels at the start and end of each line, discussed in para 4.2.2 above. Figures 4.2.4-4 to 4.2.4-6 show plots of dark signal non-uniformity for the three devices. The various dose regions can be seen in the proton-irradiated devices. There are also several large spikes. Some of these occur in un-irradiated regions and so were presumably always present.

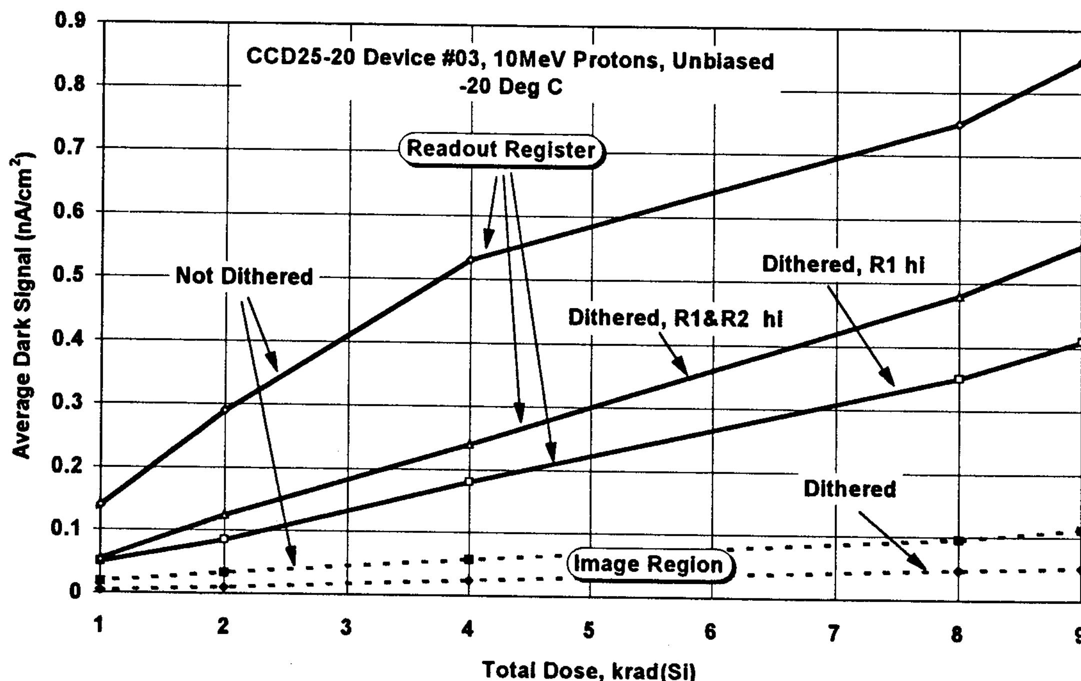

Figure 4.2.4-1 Dark current density for various clocking modes :dark signal converted to nA/cm^2 assuming a notional pixel area of 22.5μm x 22.5μm.

Copyright © Sira Ltd 1995

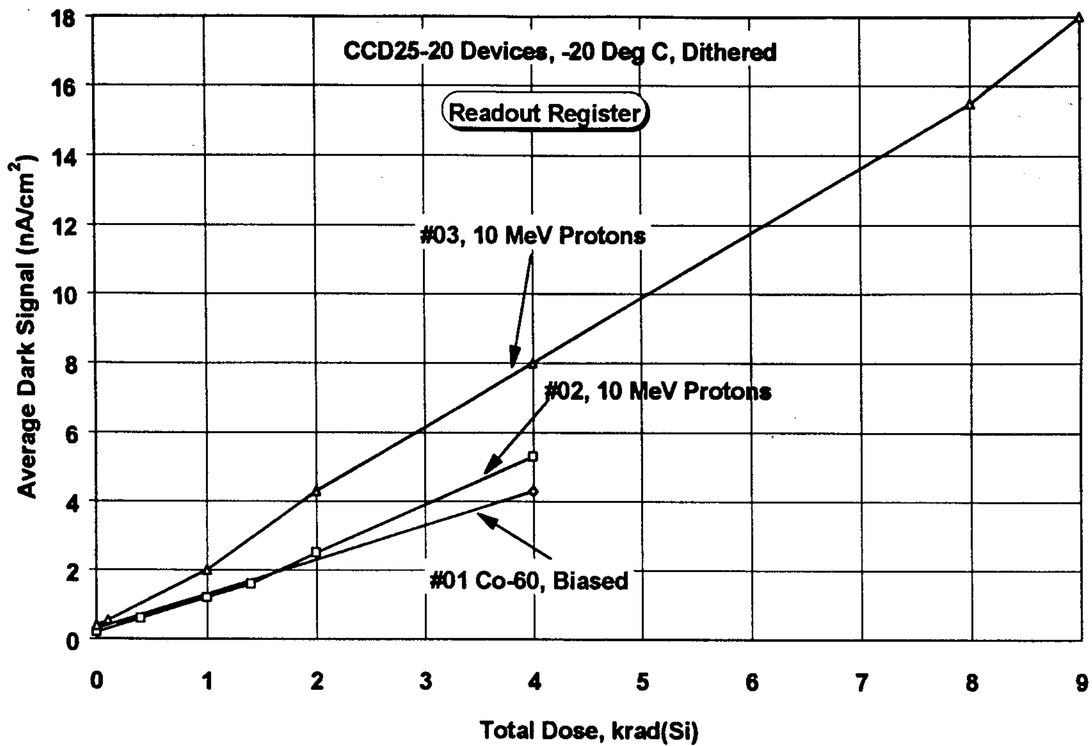

Figure 4.2.4-2 Readout register dark current density v. total dose for the three CCD25-20s

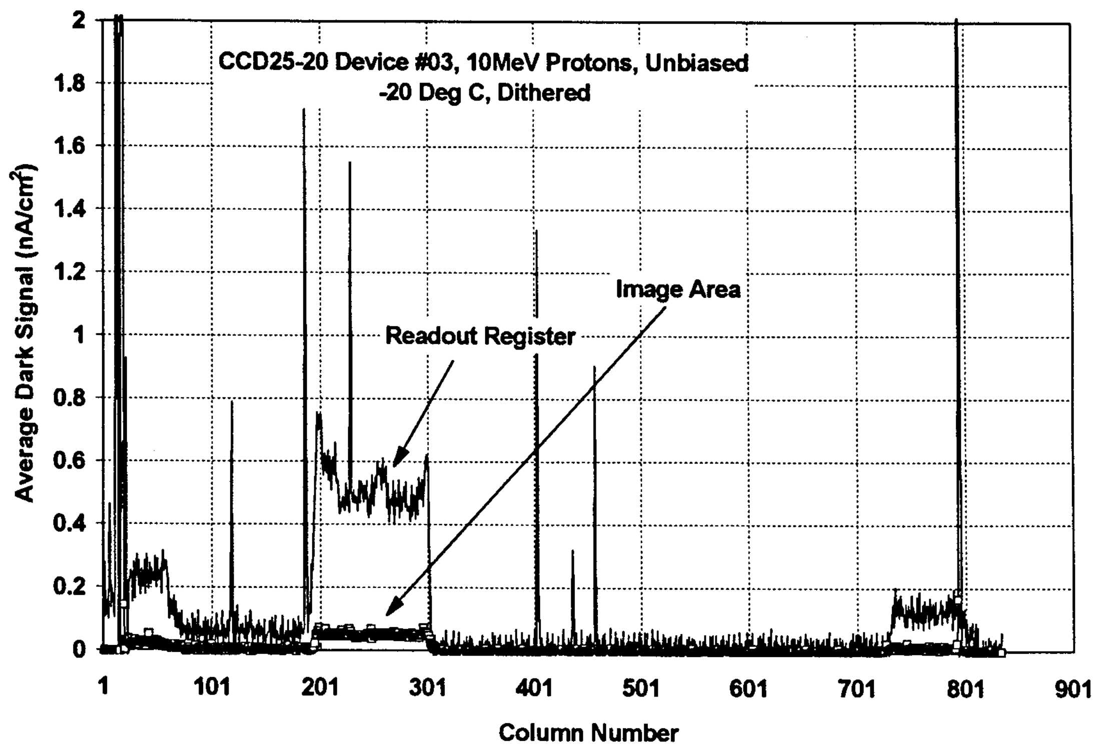

Figure 4.2.4-3 Dark current density for image and readout regions (device #03), :dark signal converted to nA/cm^2 assuming a notional pixel area of 22.5µm x 22.5µm.

Copyright © Sira Ltd 1995

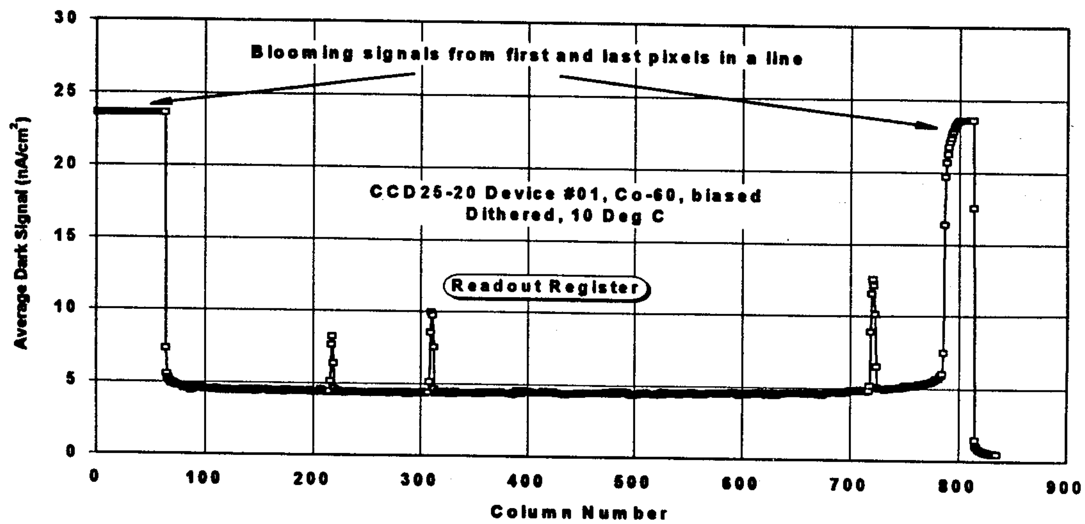

Figure 4.2.4-4 Dark current density for device #01, dark signal converted to nA/cm^2 assuming a notional pixel area of 22.5μm x 22.5μm.

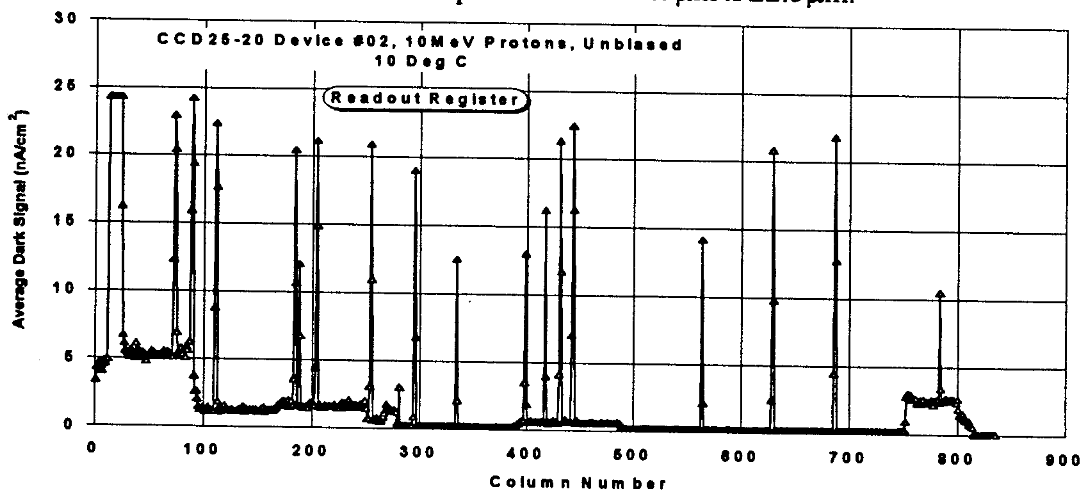

Figure 4.2.4-5 As figure 4.3.4-5, but for device #02.

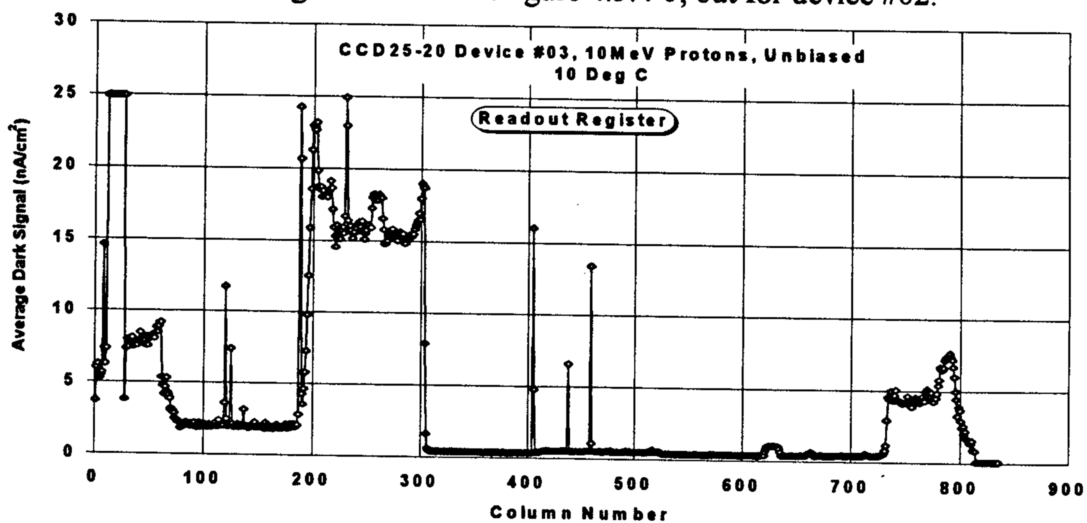

Figure 4.2.4-6 As figure 4.3.4-5, but for device #03

Copyright © Sira Ltd 1995

4.2.5 Effect of Dither Clocking

It was noted in para 4.2.1 that dither clocking produces black/white pixel pairs because of 'pocket pumping'. Figure 4.2.5-1 shows the effect of varying the number of dither cycles (for a 16s integration at -20 °C). The data is plotted for 17 black/white pairs as a function of the number of line times between dithers and the black/white pair amplitude). The pixels were taken from a 1 krad region of a CCD02. Also shown is the expected amplitude for one electron traps. For dither rates >400 μs the black/white pair amplitude increases as the total number of dithers increases, however at faster dither rates the increase is not so marked. This is to be expected since (as will be shown in section 7) the trap emission time, τ_e at -20 °C is ~400 μs. To understand the theory behind pocket pumping it is advantageous for the reader to refer to the theory of charge trapping given in section 7. A model for the processes occurring during pocket pumping is illustrated in figure 4.2.5-2. It is necessary for a trap to be located at a pixel boundary. Charge is integrated most of the time under one phase ($\phi 2$ in our case). When charge in dither clocked it temporarily is transferred to an adjacent phase ($\phi 1$ in our case) at which point it can become trapped (if the trap is in a location within the buried channel where it can 'see' the charge pocket). In 2-phase dither clocking, the main charge pocket is then transferred back under $\phi 2$ and the trap will emit its charge. The probability of emission to pixel B will depend on the exact location of the trap but will be ~50%, so for every dither clock cycle the difference will increase by 1 electron.

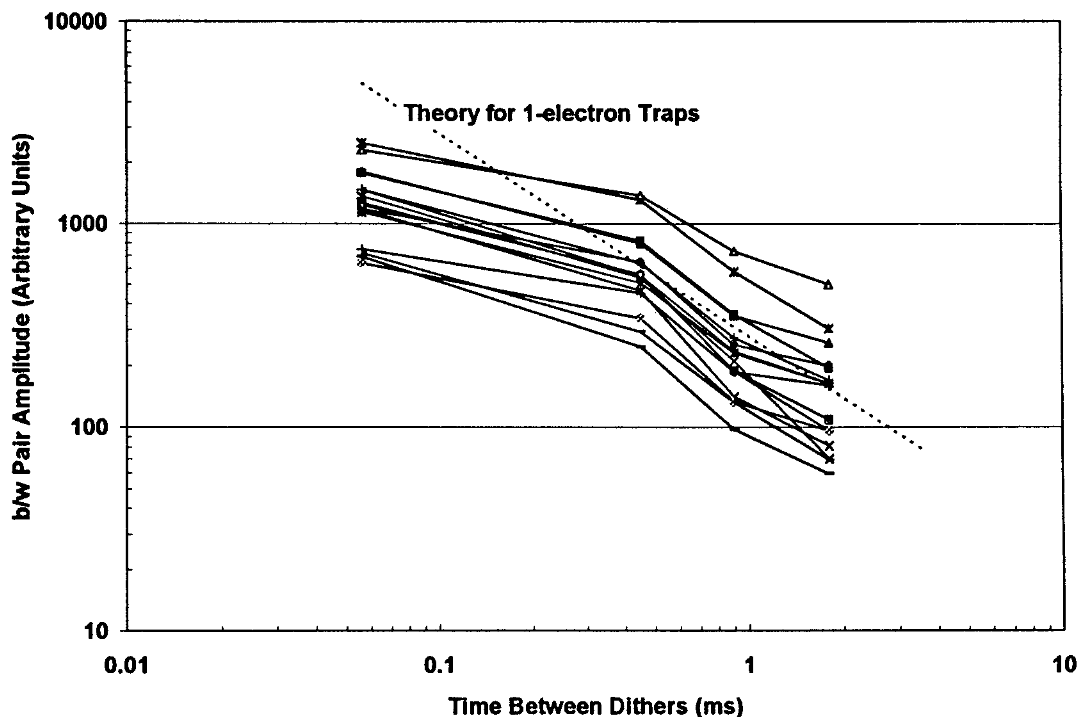

Figure 4.2.5-1 Amplitude of b/w pairs as the dither rate is changed

Copyright © Sira Ltd 1995

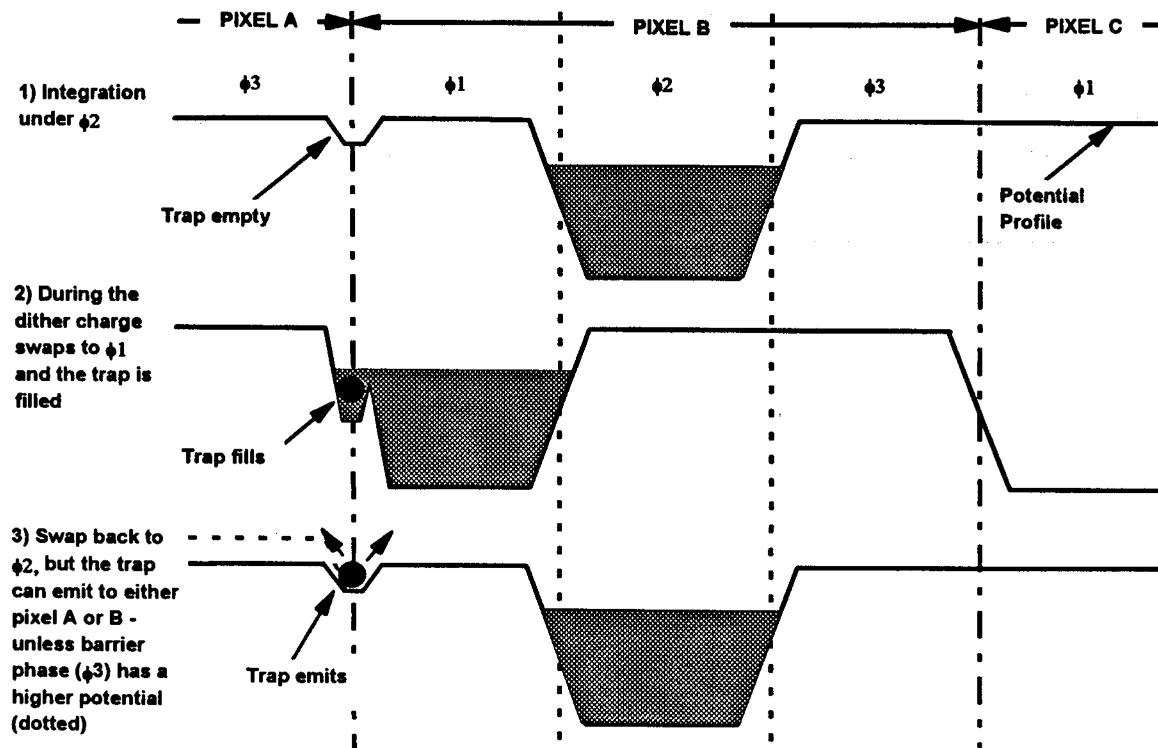

Figure 4.2.5-2 Model for black/white pairs created during pocket pumping

Note that in this model, 2-phase dither clocking will always result in transferring charge in the direction ϕ2 to ϕ1, so the black and white pairs always have the same orientation. It has been verified that when the dither clock sequence is changed to dithering between Iϕ2 and Iϕ3 the black/white pairs have the opposite orientation. Also increasing the potential under the 'barrier phase' - Iϕ3 in the figure, prevents charge from migrating to the next pixel and can completely suppress the effect. It has been verified that lowering Iϕ3 by 1 V (from 0 V to -1 V) has this effect. Also lowering Iϕ1 when dithering between Iϕ2 and Iϕ3 suppresses the pocket pumping. Note that it was found that in the two devices studied in detail (a CCD02 and a CCD25-20) there was an asymmetry in the clock potentials - so that, with Iϕ2 to Iϕ3 dithering, a voltage of 0 V on barrier phase Iϕ1 was sufficient to suppress dithering (which occurs if Iϕ1 clock low >1 V. However the reason for this behaviour is not understood at present so it may be unwise to assume that Iϕ2 to Iϕ3 dithering is always preferable.

The number of black/white pairs will depend on the signal size, since this affects the volume of silicon occupied by a charge pocket and hence the probability of a trap being filled. Also the number of pairs for a given fluence seems to depend on the CCD. Figure 4.2.5-2a shows estimates of the number of black/white pairs for a CCD25-20 (#03)and a CCD02 (similar numbers were observed for the other proton-irradiated CCD25-20 - #02). Note that the black white pairs were counted by eye (since it was found to be very difficult to descrininate them numerically because of their varying amplitude and the dark current non-uniformity) and the estimates are probably only accurate to a factor 2. For 1 krad of 10 MeV protons, the CCD02 gave roughly 1 in 20 pixels affected, whereas for the two CCD25-20s the number was ~1 in 200, either way it is likely that several pixels will be affected per line.

Copyright © Sira Ltd 1995

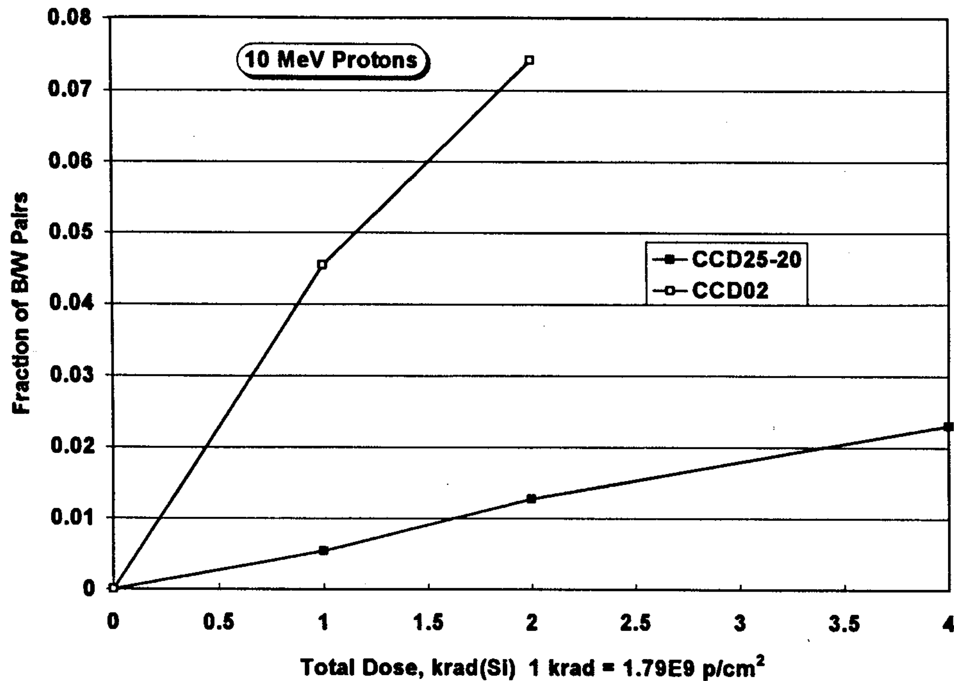

Figure 4.2.5-2a Fraction of black/white pairs for two dither clocked CCDs

Figure 4.2.5-3 shows the effect of emission time on dither clocking. In this case a variable delay time was inserted in the dither sequence and this is plotted against the black/white pair amplitude. It is seen that the plate has an exponential form with time constant ~8μs.

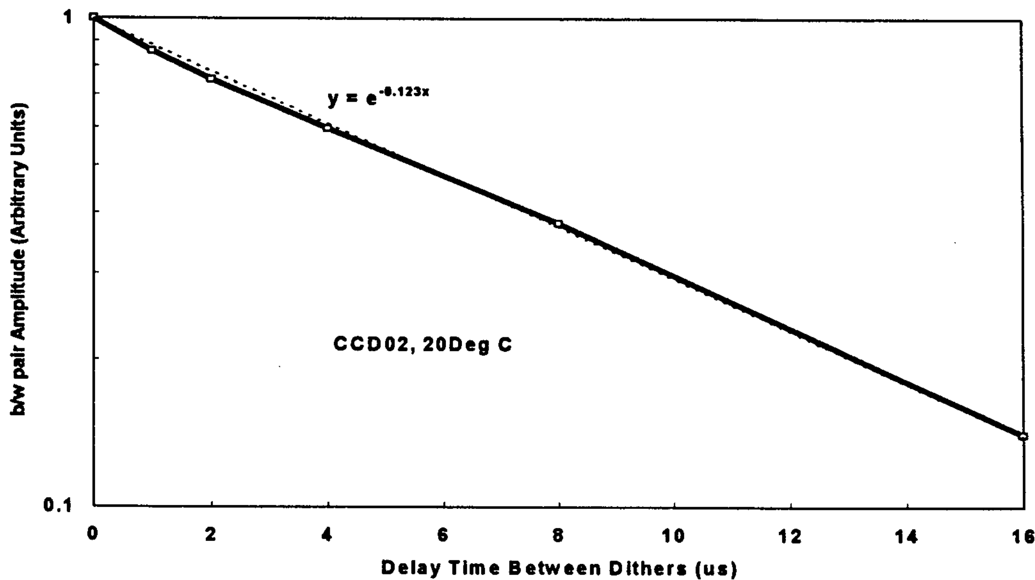

Figure 4.2.5-3 Amplitude of b/w pairs as a function of the delay time between dithers

For an instrument such as MERIS the effective number of dithers will be close to the number of useful lines readout, i.e. ~40. Hence the black/white pair amplitude will be 40 electrons (assuming, as for the majority of pixels, that we have only one trap per pixel). The effect of pixel binning will be to average the signals (and so give zero non-uniformity) if both halves of the pair fall within a 'super pixel'. For 4 line binning this will occur for 3/4 of the time but for the remaining 1/4 of the time (and so probably at least one pixel per line) a pair will not be averaged and a 20 electron (i.e. 1/2 amplitude) DSNU will be produced in that line. Figure

Copyright © Sira Ltd 1995

4.2.5-4 shows the 4krad, 1krad and 8/9krad regions of a CCD25-20 (#03) with dither clocking at -20°C for a 20s integration. Numerous b/w pairs can be seen. As discussed above, the density of b/w pairs was higher for the CCD02 device studied (figure 4.2.3-5).

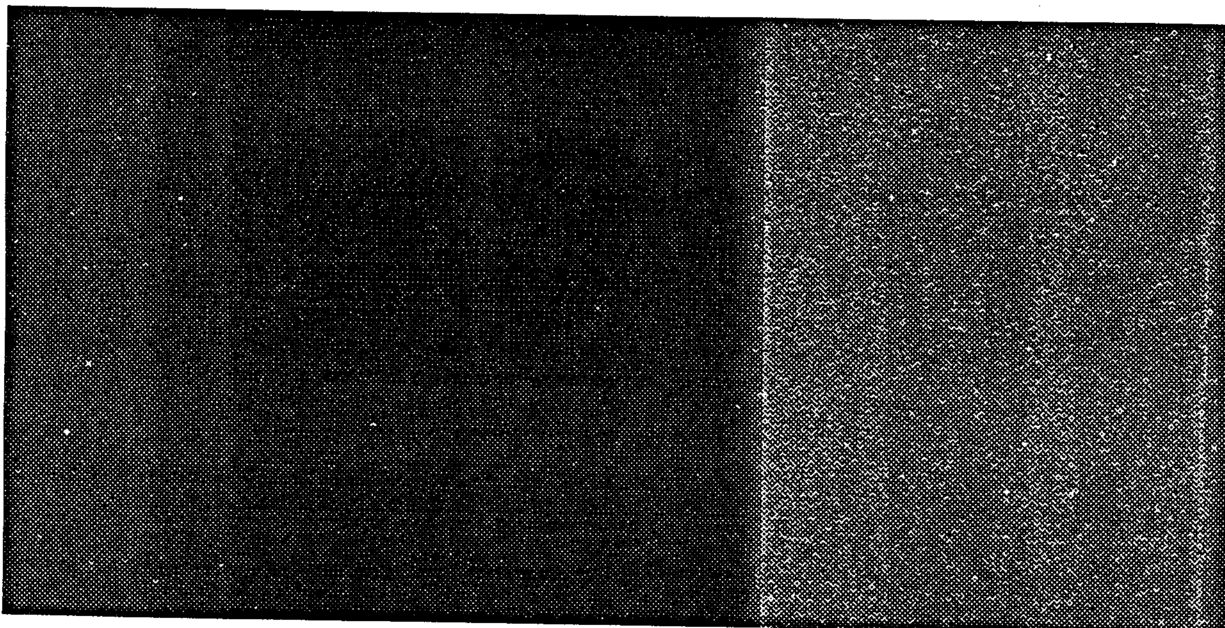

Figure 4.2.5-4 shows the 4krad, 1krad and 8/9krad regions of a CCD25-20 (#03) with dither clocking at -20°C for a 20s integration. Numerous b/w pairs can be seen.

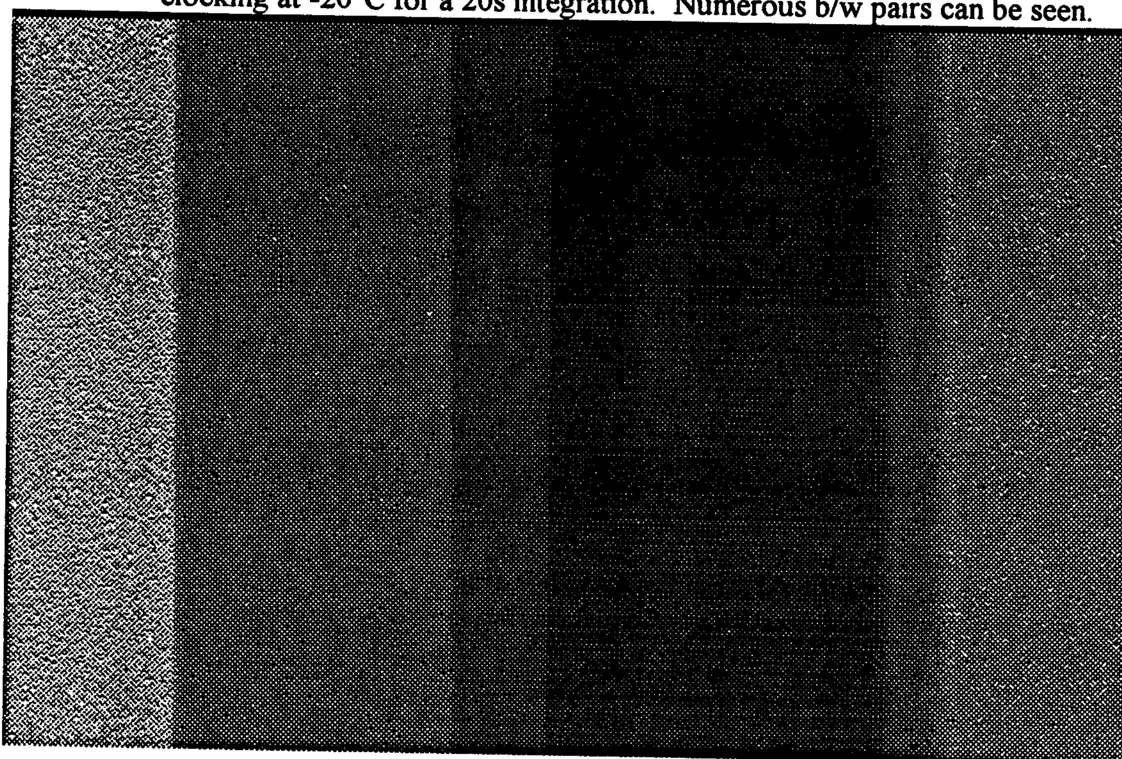

Figure 4.2.5-5 shows the 4krad, 1krad and 2krad regions of a CCD02 (#09) with dither clocking at -23°C for a 16s integration. Numerous b/w pairs can be seen.

Copyright © Sira Ltd 1995

4.3 TH7895M DEVICES

For most of the measurements these CCDs were operated with the image region in MPP mode (clock low = -10V) but with the storage region in normal mode (clock low = -5V). This results in suppression of the ionization-induced dark charge for the image region (leaving only the bulk component (which is appreciable for proton-irradiated devices) for the image region and a substantial surface component (which is not suppressed) for the storage region (giving a large dark current slope). At the end of the project it was checked that setting the storage region clock low voltage to -10V (which gave good charge transfer provided the signal was low) gave suppression of the storage component also. Figure 4.3-9 shows the transition into inversion.

Figures 4.3-1a and b (for image and storage region dark currents) show the relatively large increase in image region dark current for proton rather than Co-60 irradiated devices. For Co-60 irradiation the dark current (from the surface) is well suppressed and the dark current stays at the ~10 pA/cm^2 level (at 20 °C) - at least until the devices were annealed. At that point the dark current increased to ~0.25nA/cm^2 - though we noted above that this is for conditions where the storage region is not inverted and there may be errors in estimating the image component because of the signal build-up during frame transfer and line clear operations. When the storage region clock lows were put at -10V the Co-60 devices showed image region components returning to the 10 pA/cm^2 level (0.0122, 0.0119 and 0.0133 nA/cm^2 for devices #04,05 and 06, respectively) and the storage component being too small to measure accurately. Hence we conclude that the MPP mode is, in principle, very efficient in suppressing surface dark current in these devices. The image region results for the proton-irradiated devices were not significantly affected by the storage region inversion.

Note that, because of displacement damage-induced dark spikes, the 10 MeV proton-irradiated devices showed an increase in image area dark current of ~0.06 nA/cm^2/krad. This is consistent with what would be predicted theoretically (~0.1 nA/cm^2/krad at 20 °C - RD5) and leads to a damage constant of 1.44 nA/cm^2/krad at 20 °C for each MeV of energy deposited.

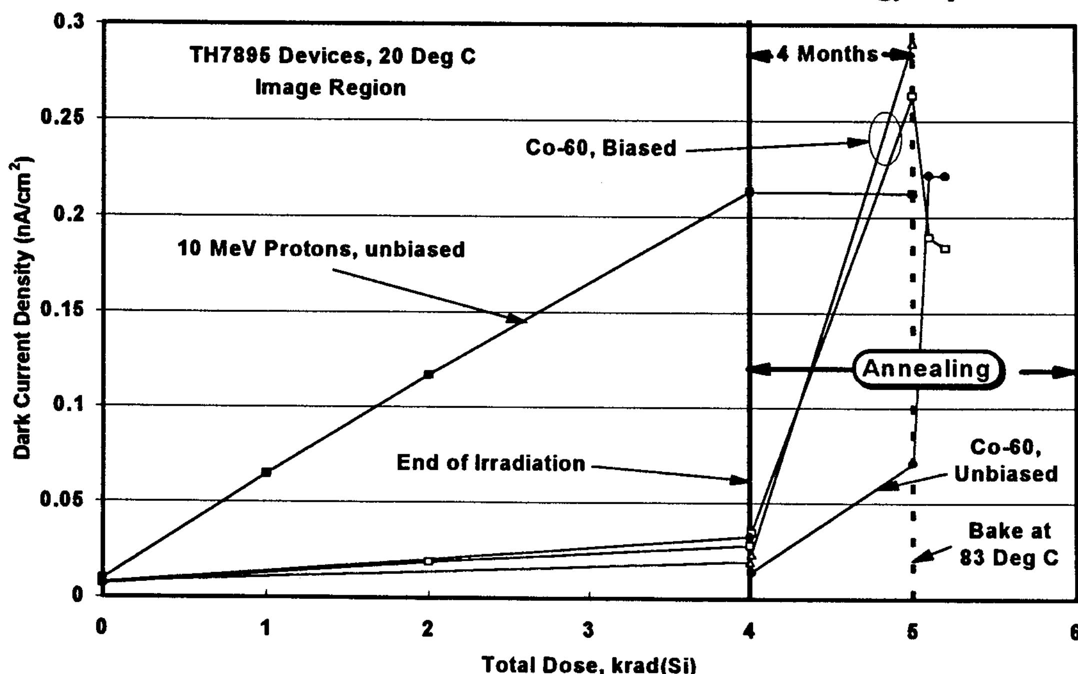

Figure 4.3-1a Image region dark currents for TH7895 devices (storage region not inverted).

Copyright © Sira Ltd 1995

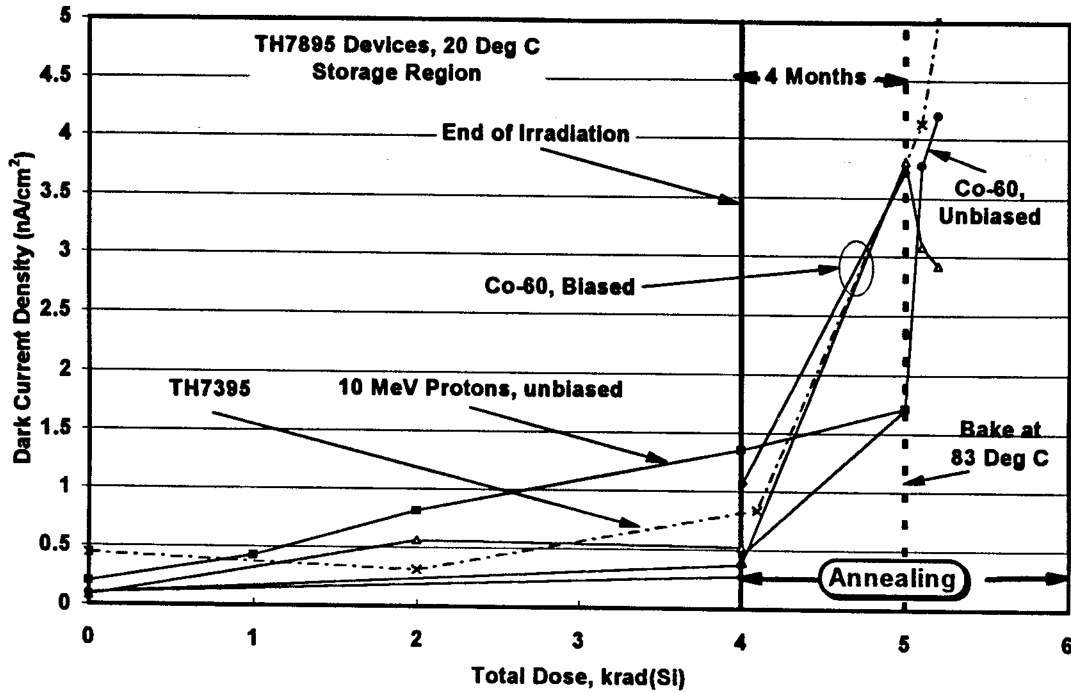

Figure 4.3-1b Storage region dark currents for TH7895 devices (storage region not inverted).

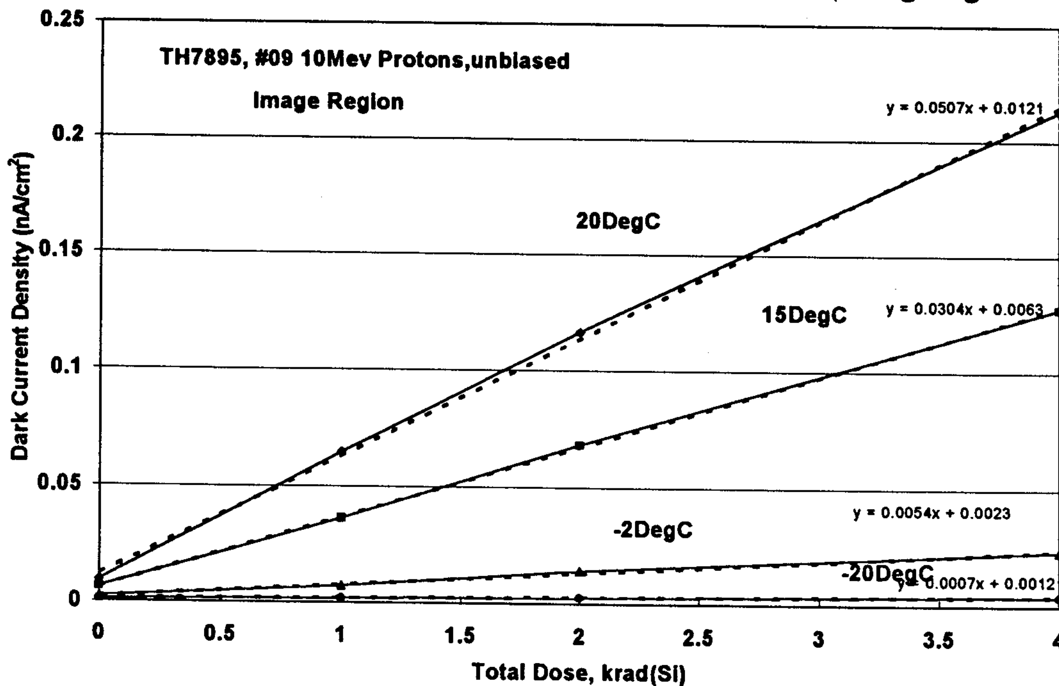

Figure 4.3-2 Image region dark currents for device #09

Figure 4.3-2 shows the behaviour of the image and storage region dark currents as a function of dose and temperature and figure 4.3-3 shows that the activation energy for the dark current is 0.65 eV as expected.

Copyright © Sira Ltd 1995

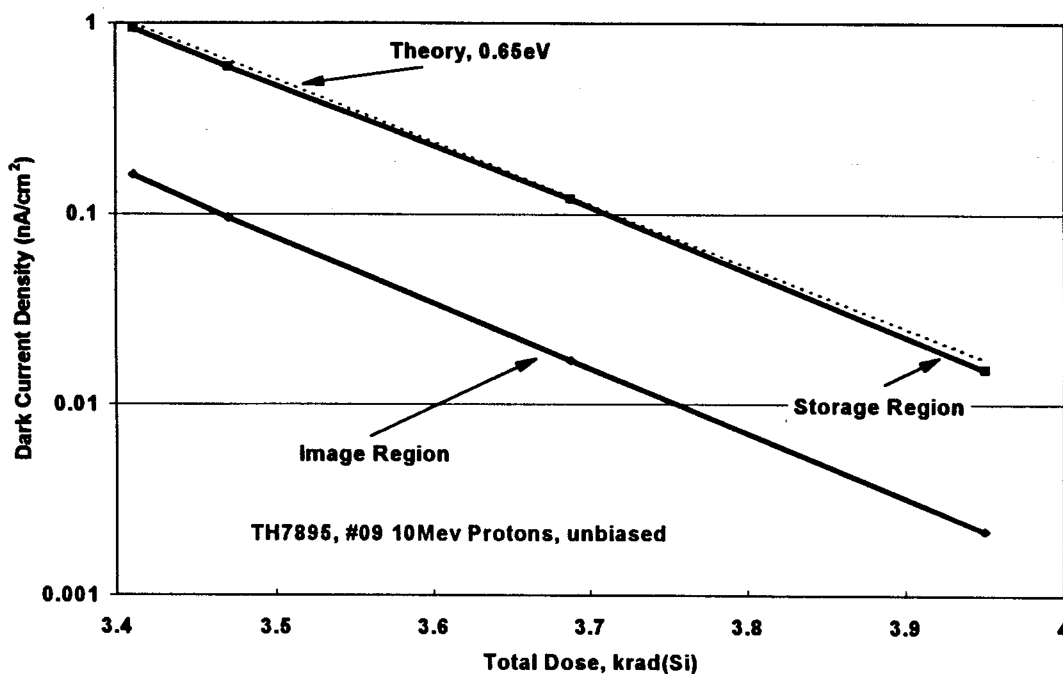

Figure 4.3-3 Dark current density versus 1000/T

Figure 4.3-4 shows total dark current histograms for 2krad and 4krad dose regions of 10 MeV proton-irradiated device #09 at 20°C, -2 and -20 °C, with the dark current in the latter cases scaled (by factors ~8 and 50) according to an Arrhenius relation with E=0.65 eV. It is seen that the histograms are well superposed and also that the surface component is small.

In fact though, the surface dark current does have an effect, as shown in figures 4.3-5 and 4.3-6. These shows histograms for long and short integration times (figure 4.3-5 for device #09 and figure 4.3-6 for a variety of devices). The storage region was not inverted and the short exposure will have a larger contribution from the dark current accumulated during readout. Even though the slope (mean storage region component) has been subtracted, there is a difference in shape - with the long exposure (i.e. predominantly bulk dark current) histogram having a much narrower main peak. This would be of somewhat academic interest (we could only consider the long exposure histograms) if it were not for the fact that this may have a bearing on the interpretation of previous (and present) results for EEV devices: these may also be broadened because of statistical fluctuations in the surface dark current.

The long exposure TH7895M histograms are not easily fitted to the theory of Marshall et al (IEEE Trans. Nuclear Science, NS-37(6),pp1776-1783(1990)). Figure 4.3-7 shows TH7895M data along with some attempts at a theoretical fit. The main peak can be fitted quite well assuming an active volume depth of 1-4μm (it is not very sensitive) but only if we assume a damage factor ~1nA/cm^2 at 20°C for 1MeV energy deposited. This is a factor 2 to 3 lower than found previously. Also the tails of the histograms are not fit at all well. This may be because the tails are showing significant field enhancement. We do not have good MPP data for EEV devices. It may be that these would have a similar appearance, in which case the modeling would need to be re-examined.

Figures 4.3-5 and 4.3-6 indicate that the histograms for the various TH7895M devices are very similar - including the UV coated CCD and device #07, both of which were irradiated with 46MeV protons (to a fluence giving the same NIEL as 2krad 10MeV protons). Since the higher

Copyright © Sira Ltd 1995

proton energy would be expected to give an increased probability for inelastic reactions and hence a more pronounced tail, the fact that the plots are similar is consistent with the shape of the tail being due largely to field enhancement. (though part of the discrepancy will be due to departure from radiation equilibrium - and the effect of long range recoil tracks- at the higher proton energy).

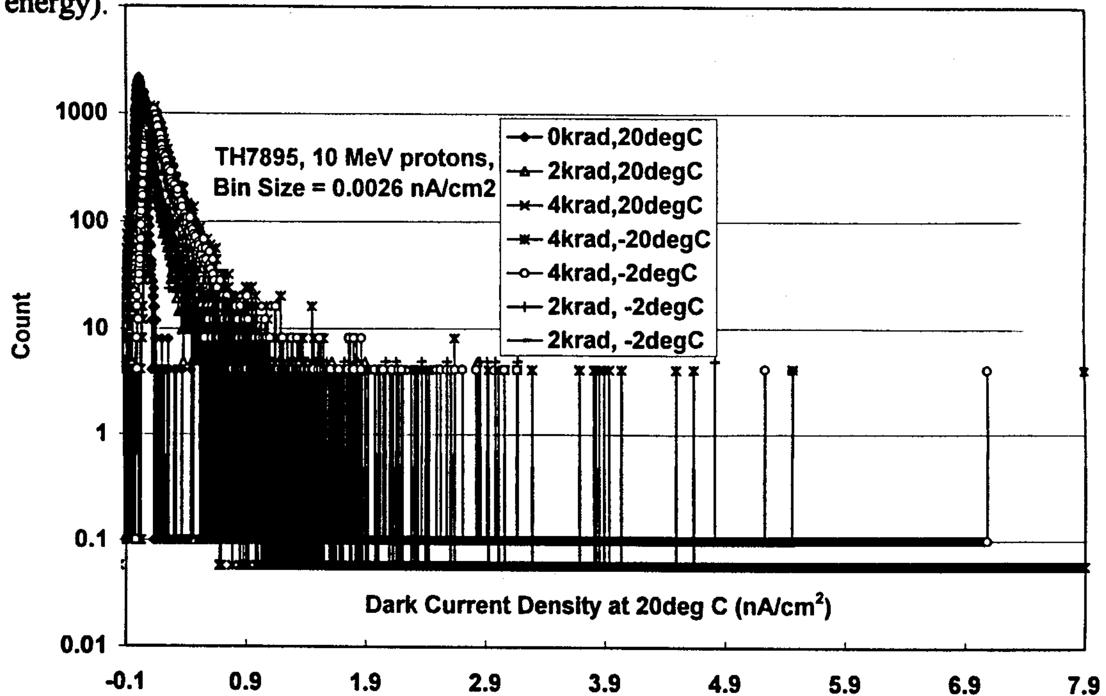

Figure 4.3-4a Dark current histograms at 20, -2, and -20°C for device #09. The storage region was not inverted. The -2 and -20°C data were scaled by multiplying the dark current density values by 8 and 50 (respectively), so as to get an equivalent dark current at 20°C.

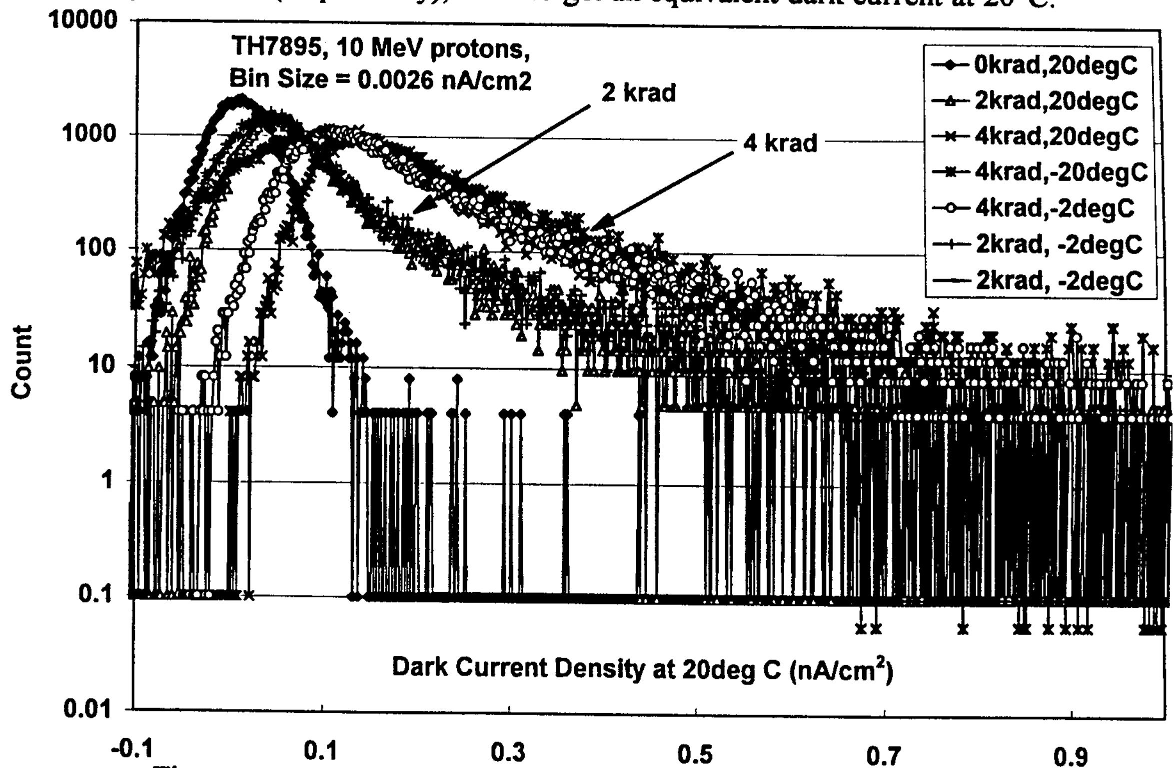

Figure 4.3-4b As above but with a reduced horizontal scale

Copyright © Sira Ltd 1995

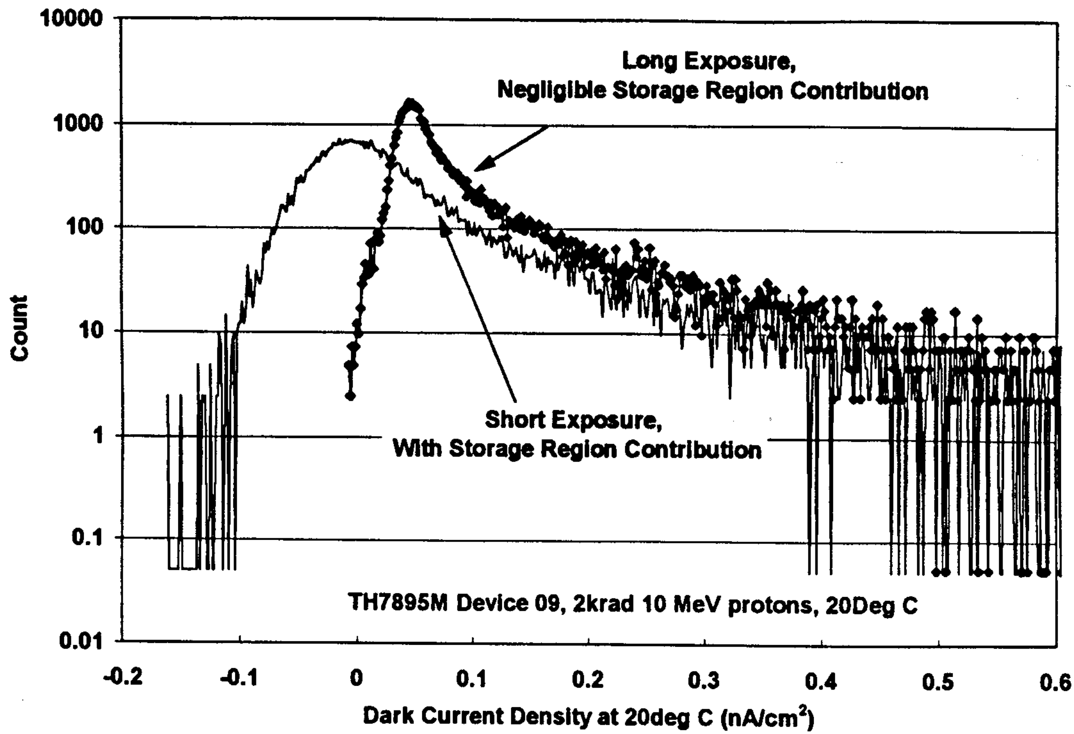

Figure 4.3-5 Dark current histograms with and without broadening due to fluctuations in surface dark current.

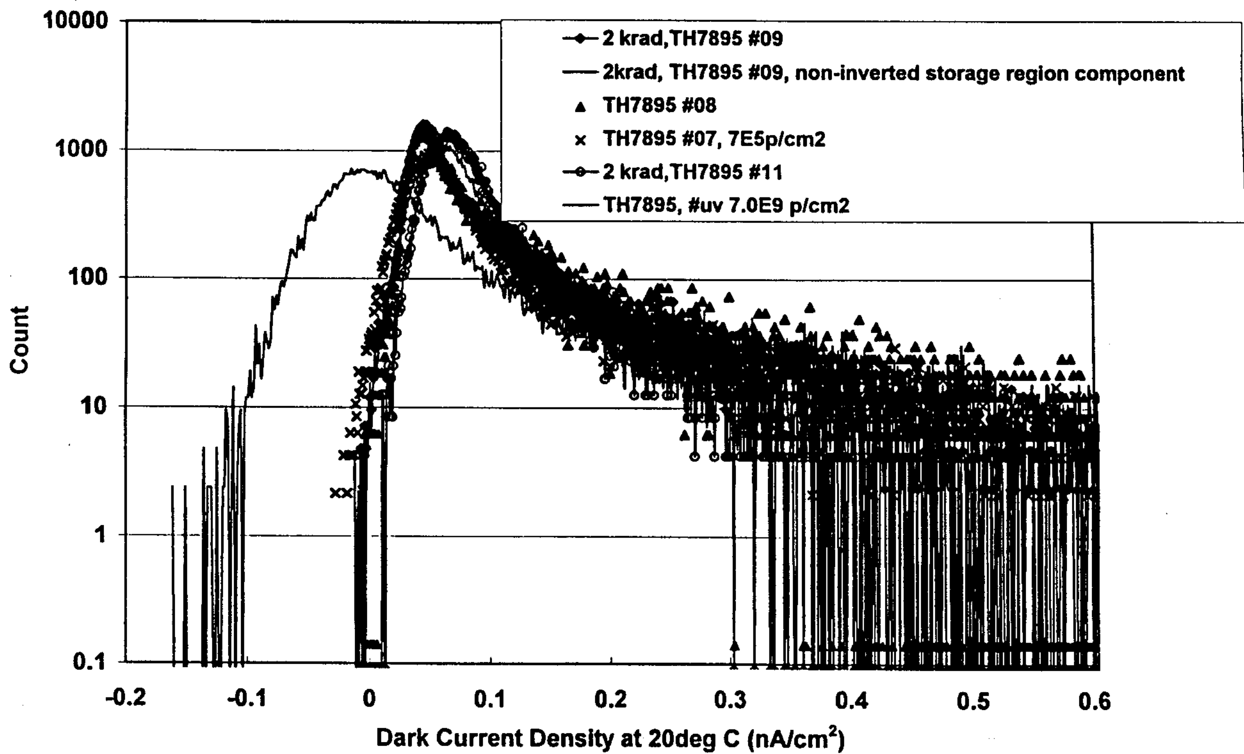

Figure 4.3-6 Dark current histograms for a variety of TH7895M devices, #s 07 and uv were irradiated with 46MeV protons.

Copyright © Sira Ltd 1995

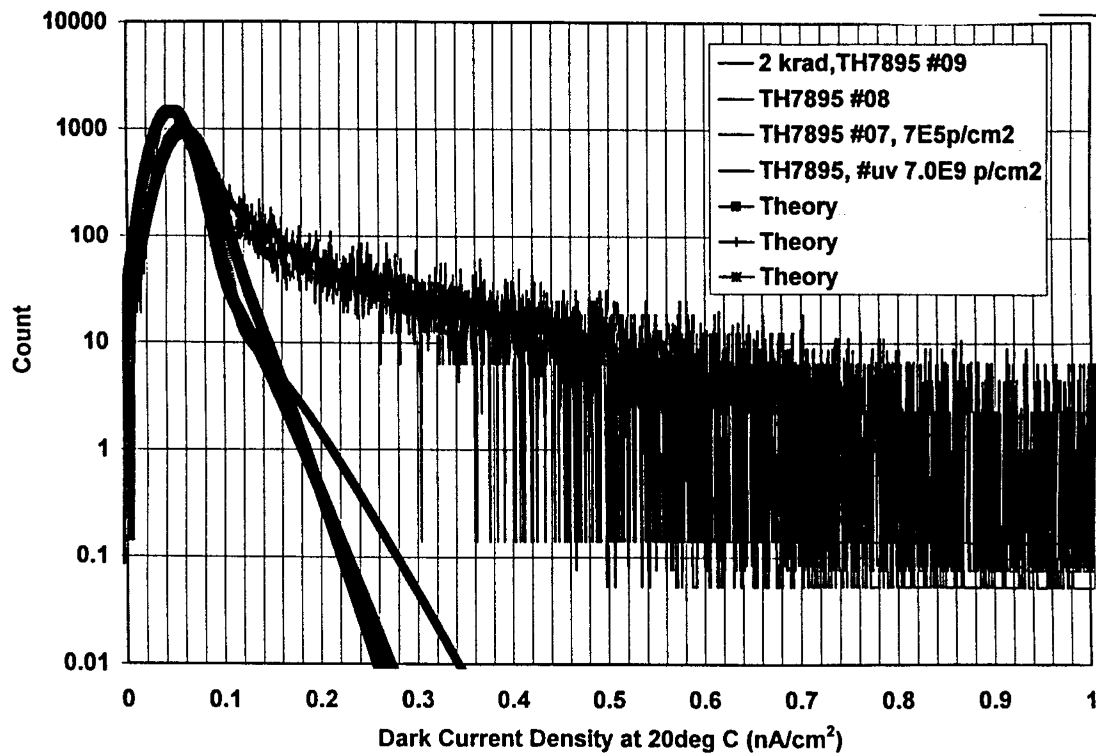

Figure 4.3-7 As figure 4.3-6 but showing trial theoretical fits.

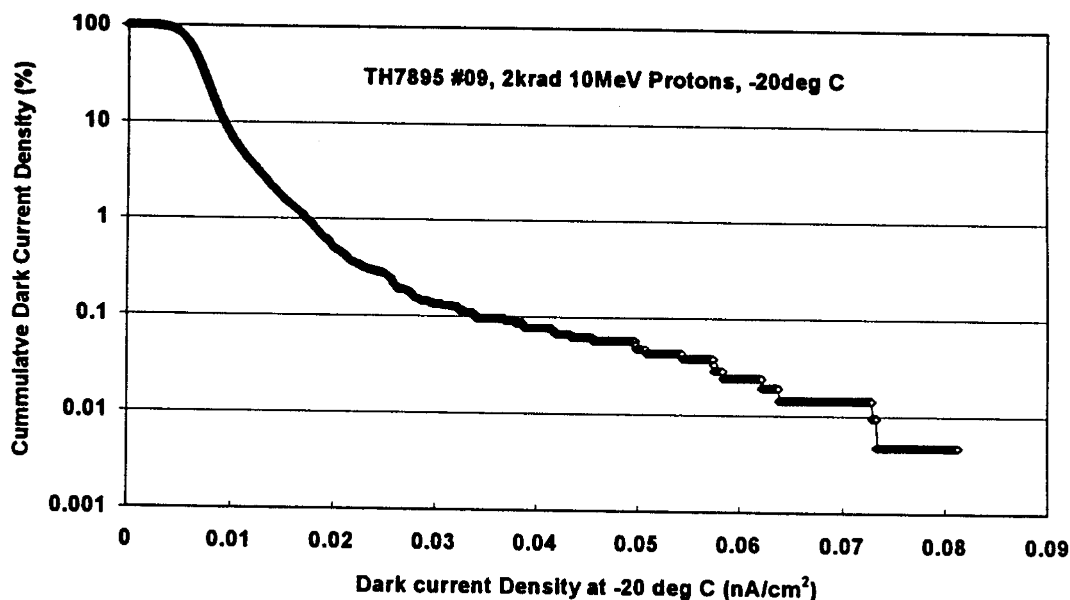

Figure 4.3-8 Cumulative dark current histogram

For completeness, figure 4.3-8 shows a cumulative dark current histogram, i.e. the percentage of pixels with dark current density higher than a given value. Figure 4.3-8a shows dark current histograms for 1, 2 and 4krad fluence regions of device #09. An empirical fit to this data is discussed in section 11. Figure 4.3-9 shows dark current as a function of the image area clock voltage during integration, showing inversion occurring between -6 and -7V.

Copyright © Sira Ltd 1995

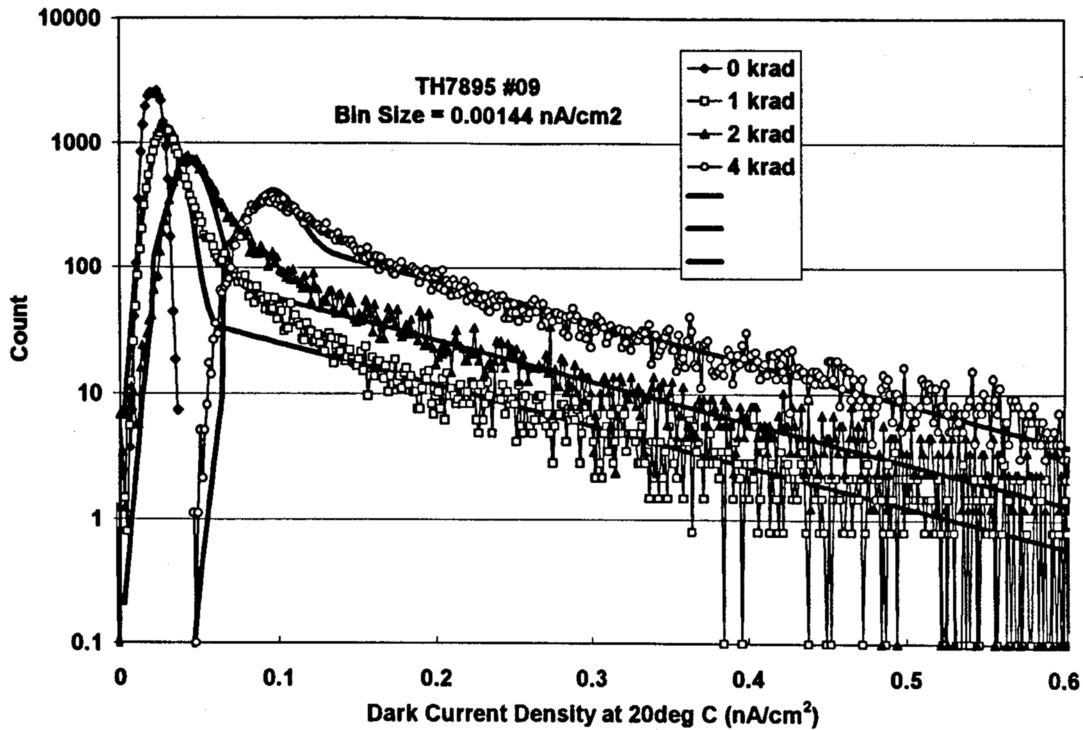

Figure 4.3-8a Dark current histograms for device #09, negligible storage region component

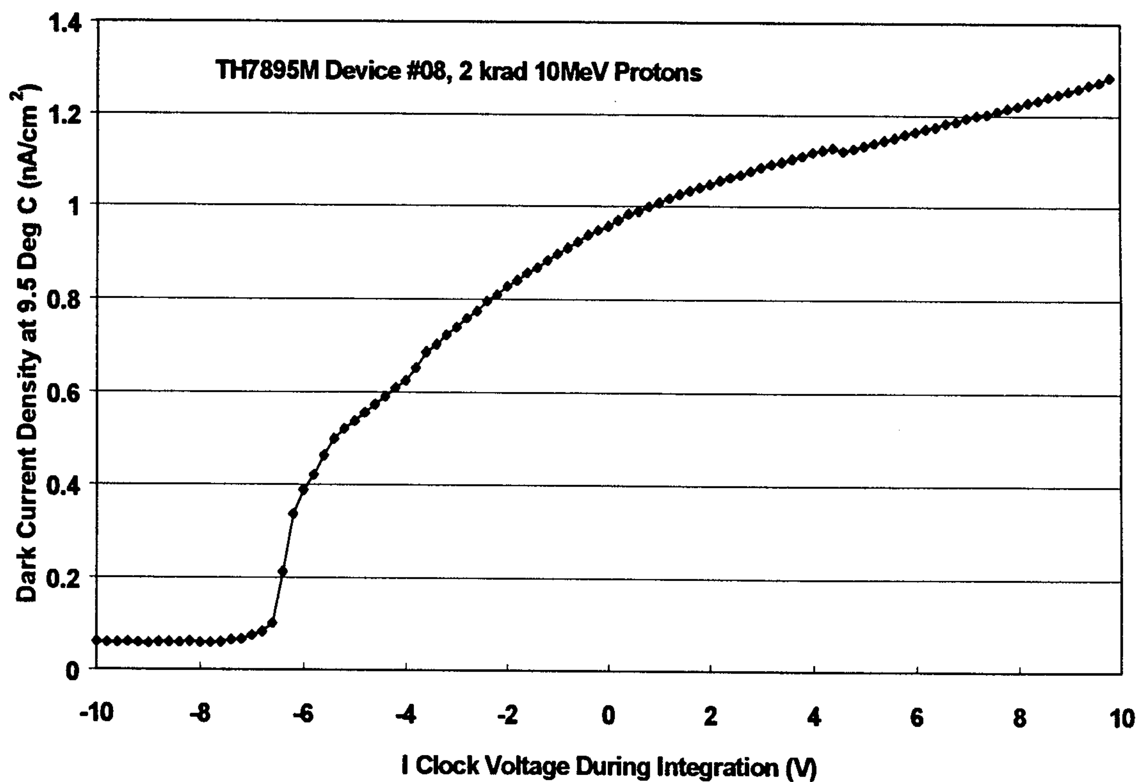

Figure 4.3-9 Dark current density versus image area clock voltage during integration for a TH7895M device, note that this is after 2 krad 10MeV protons so there is a dark current component due to bulk damage (amounting to $0.06nA/cm^2/krad$ at 20°C)

Copyright © Sira Ltd 1995

Figure 4.3-10 shows the activation energy for the proton-induced dark spikes. As for the CCD25-20, there is evidence for field enhancement. Note that spikes showing departures from a uniform temperature law (e.g. because of RTS effects) have been removed from the data set. Figure 4.3-11 shows an extreme value statistics plot (see RD4 for an explanation of this technique). The plot should give a straight line if dark current spikes arise from a single statistical process. The fact that the plot is curved gives evidence for field enhancement.

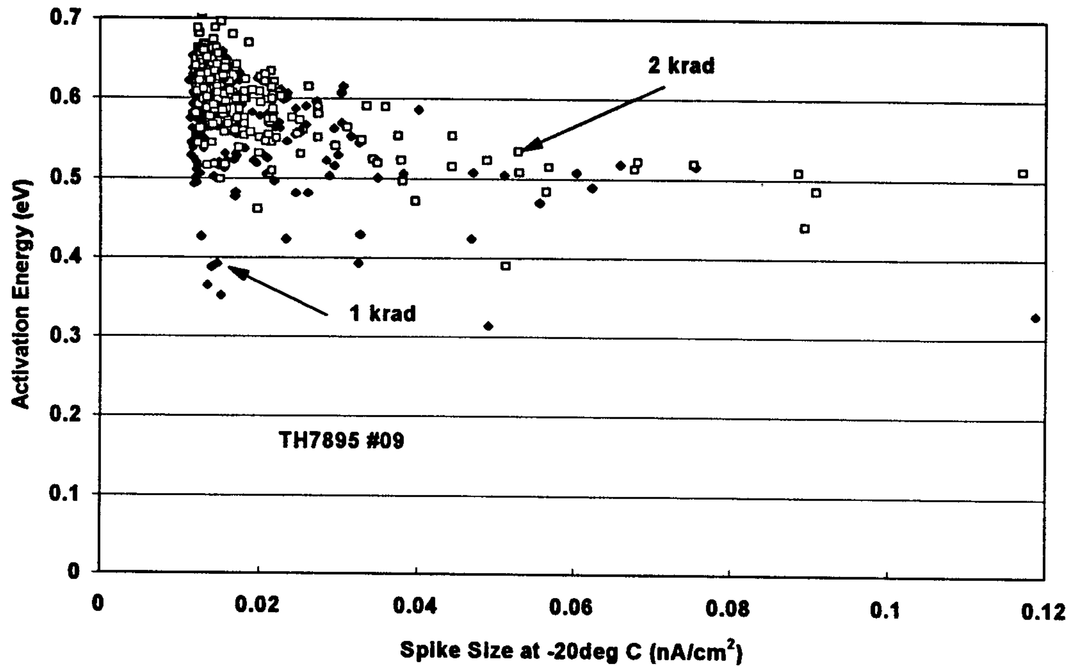

Figure 4.3-10 Activation energy for dark current spikes in a proton-irradiated TH7895M device

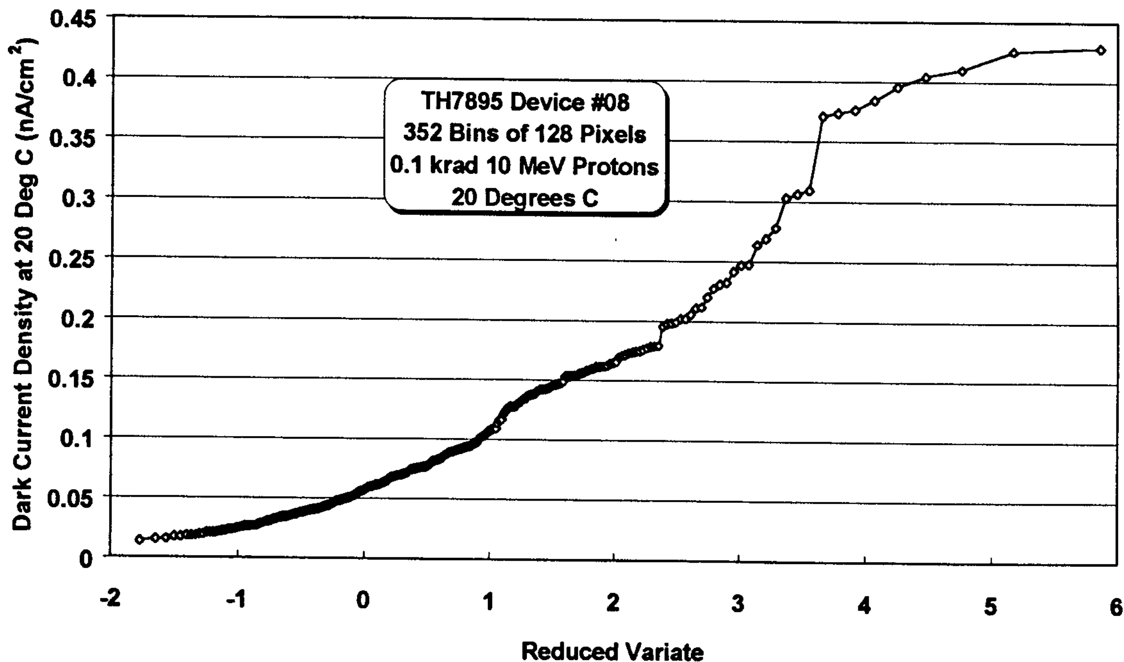

Figure 4.3-11 Extreme value statistics plot for dark current density in a TH7895M device

Copyright © Sira Ltd 1995

4.4 TH7395M DEVICES

Pre-irradiation values of dark current density for the two devices studied are given below

Table 4.4-1 Pre- irradiation dark current density at 20 °C (nA/cm^2)

	#01, later C0-60 irradiated	#02 UV coated, later 46MeV proton irradiated
image region	0.29	0.55
storage region	0.44	0.44

The pre-irradiation dark current is much higher than for the TH7895M, this is thought to be due to the fact that these devices are thinned and back illuminated. Though the exact causes are not known, this is generally thought to give additional dark current generating states. The above data is for the storage region non-inverted (clock low at -5V). Lower values for the storage region inverted might be expected with -10V clock lows.

After irradiation it was found that the dark current was non-uniform (particularly for the Co-60 irradiated device- which perhaps coincidentally was a set-up grade sample), even though the incident irradiation was uniform (to ~5%). The radiation induced dark currents were also much higher for the TH7395 devices. Figures 4.4-1 and 4.4-2 show dark current data for the image and storage (non-inverted) regions. For the 46 MeV proton irradiated device there was little effect of storage at room temperature and the dark current increased approximately linearly with dose at a rate of 0.49 nA/cm^2 /krad at 20°C. If -10V clock low voltages were used so as to invert the storage region (as discussed for the TH7895M devices above) then this increased to 0.80 nA/cm^2 /krad at 20°C. The maximum fluence used ($7.0x10^9$ p/cm^2) corresponds to an ionizing total dose of 1.2krad(Si) and has the same NIEL as 2krad of 10MeV protons, thus if the damage factor were the same as for the TH7895 (0.06 nA/cm^2 /krad at 20°C was given above), then we would have expected 1.2krad of the 46MeV protons to give 0.12 nA/cm^2 at 20°C (or 1krad to give 0.1 nA/cm^2). The actual value (0.5-0.8 nA/cm^2) is much higher. The dark current for the Co-60 irradiated device was also high, particularly after the 80°C bake - though the storage region component was reduced somewhat when operating with -10V clock lows, as shown in the table below:

Table 4.4-2 Dark current density for the 46 MeV proton irradiated device, 5 months after irradiation. The values in parentheses are for the storage region operated with -10V clock low voltages, values are in nA/cm^2 at 20°C.

	0.6 krad ionizing total dose	1.2 krad ionizing total dose
Image region	0.81 (1.05)	1.14 (1.51)
Storage region	0.844 (0.18)	1.20 (0.76)

The reasons for this behaviour are not known and it should be noted that we only have a sample of 2 devices. However it may be that the back-illuminated architecture is giving a high surface component which increases on irradiation and becomes more non-uniform.

Copyright © Sira Ltd 1995

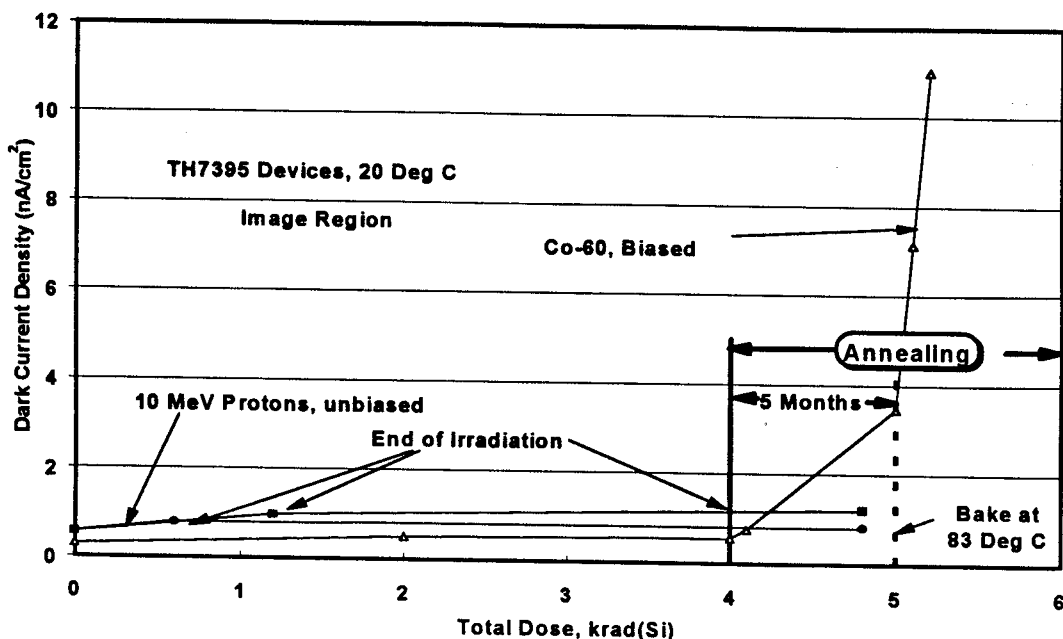

Figure 4.4-1 Image region dark current density at 20°C for TH7395 devices with the storage region non-inverted.

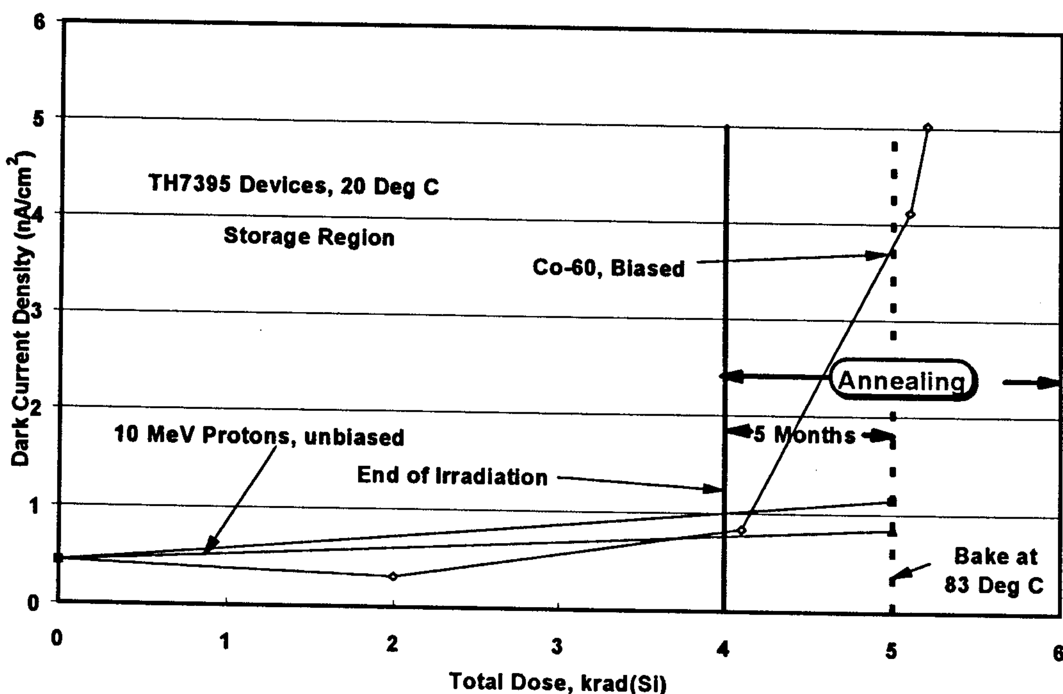

Figure 4.4-2 Storage region dark current density at 20°C for TH7395 devices with the storage region non-inverted.

Figure 4.4-3 shows dark current histograms for the 0.6 and 1.2 krad regions on the 46MeV proton irradiated device. The plot for 1.2 krad is broader than that for 1.2krad 46MeV protons on a TH7895M device (#07, also shown) - this would be expected from the increased non-uniformity and the higher mean level of the thinned TH7395 device.

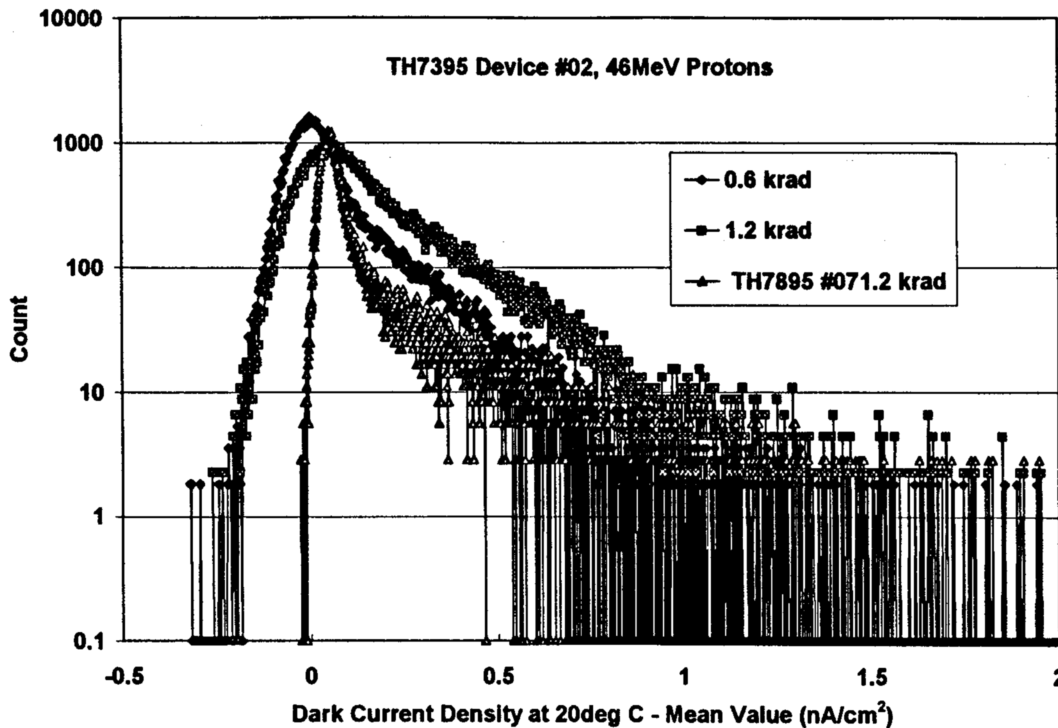

Figure 4.4-3 Dark current histograms for the 0.6 and 1.2 krad regions on the 46MeV proton irradiated TH7395 device. Data for a 46 MeV proton irradiated TH7895M CCD is shown for comparison.

4.5 RESULTS FOR TH7863B DEVICES

Results for the TH7863B devices which were Co-60 irradiated are given in table 4.5-1 below.

Table 4.5-1 Dark current density at 20 degC, nA/cm² After Co-60 irradiation

image region	**0 krad**	**immediate 2 krad**	**immediate 4 krad**	**after 35 days 4 krad**	**3.5 days at 80 4 krad**	**7 days at 80 degC 4 krad**	
powered irrdn.	0.52		1.45	1.12	2.13	1.70	
powered irrdn.	0.59	1.19	1.30	1.37	3.86	3.24	powered bake
unpowered irrdn.	0.57	1.18	1.02	1.53	3.78	5.09	unpowere d bake
storage region	**0 krad**	**immediate 2 krad**	**immediate 4 krad**	**after 35 days 4 krad**	**3.5 days at 80 4 krad**	**7 days at 80 degC 4 krad**	
powered irrdn.	0.14		6.00	9.05	19.19	21.39	
powered irrdn.	0.15	1.97	6.17	9.60	27.08	32.25	powered bake
unpowered irrdn.	0.19	1.30	4.52	7.53	14.73	13.34	unpowere d bake

It is seen that the pre-irradiation dark current was ~0.6nA/cm² for the image region and

~0.15nA/cm^2 for the storage region. The dark current shows considerable reverse annealing after which the image region shows an increase of approximately 1 nA/cm^2 at 20°C. This is much less than previous results for the A version and is comparable with the increase for EEV devices. The storage region, however, shows a larger increase of ~8 nA/cm^2 for the powered device and 3 nA/cm^2 for the unpowered (after the bake). The dark current increases for the unpowered devices are comparable, though somewhat larger than, for the 10 MeV proton-irradiated devices, for which data is given in figures 4.5-1and 4.5-2 (but note that these devices were not baked at 80°C).

Figure 4.5-3 shows histograms for the various fluence regions on one of the 10MeV proton irradiated devices and figure 4.5-3 shows data for the 2krad region on both devices. The results are similar to previous findings.

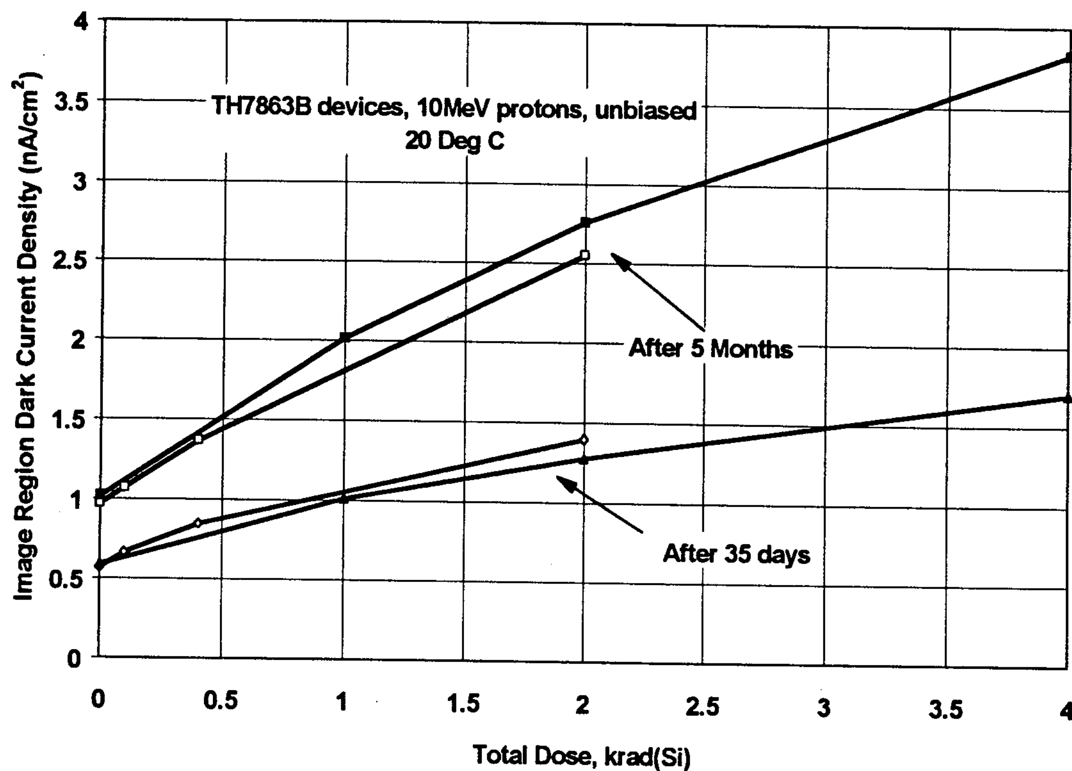

Figure 4.5-1 Image region dark current density for two TH7863B devices given an unbiased 10MeV irradiation to maximum doses of 2krad and 4krad.

Copyright © Sira Ltd 1995

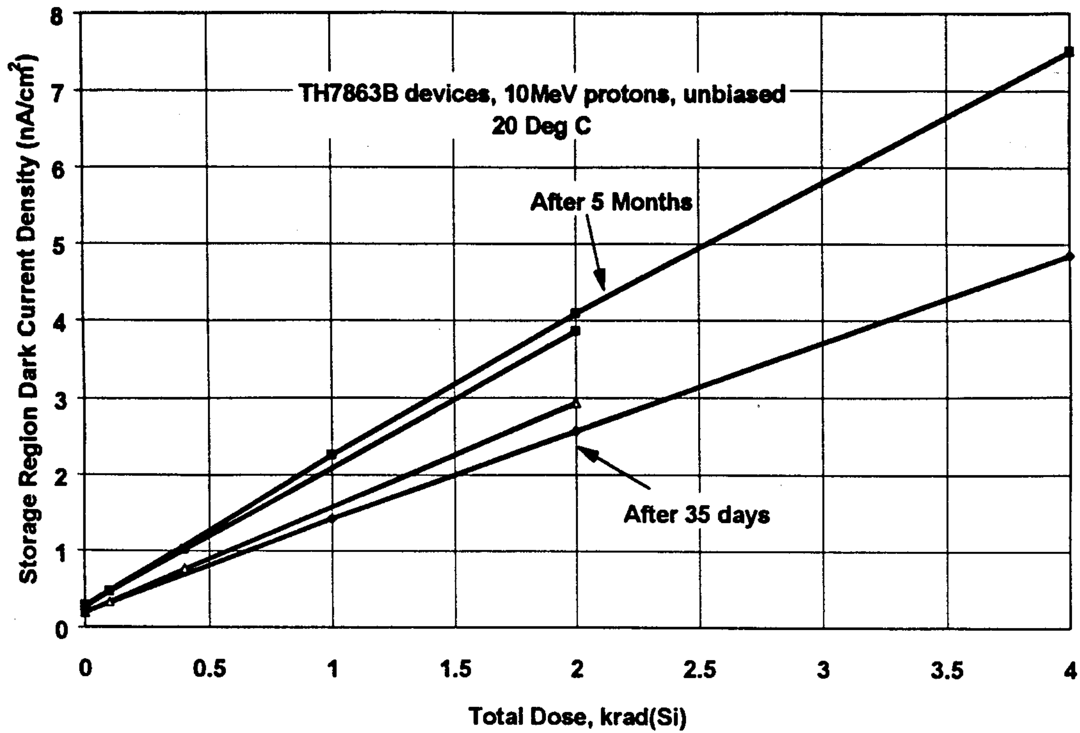

Figure 4.5-2 Storage region Dark current density for two TH7863B devices given an unbiased 10MeV irradiation to maximum doses of 2krad and 4krad.

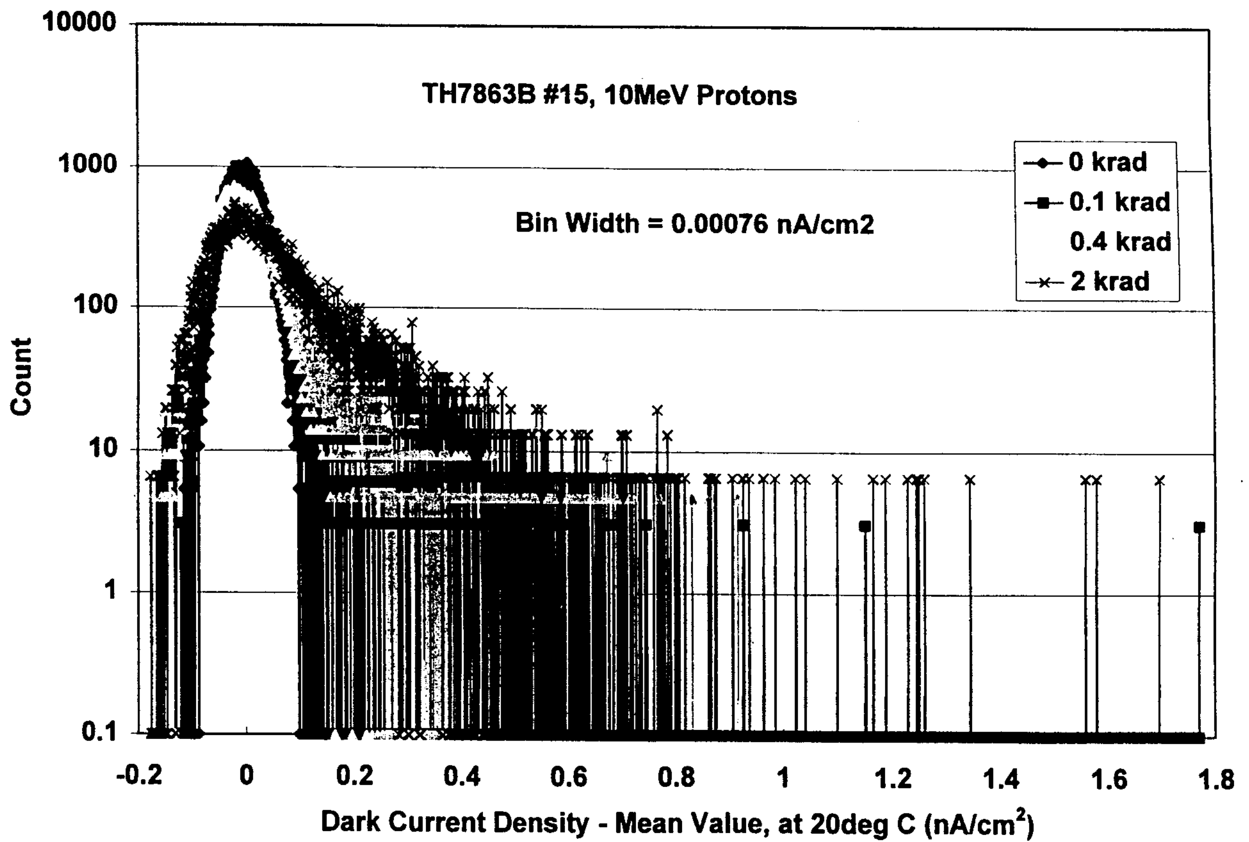

Figure 4.5-3 Dark current histograms for the various fluence regions on one of the 10MeV proton irradiated TH7863B devices

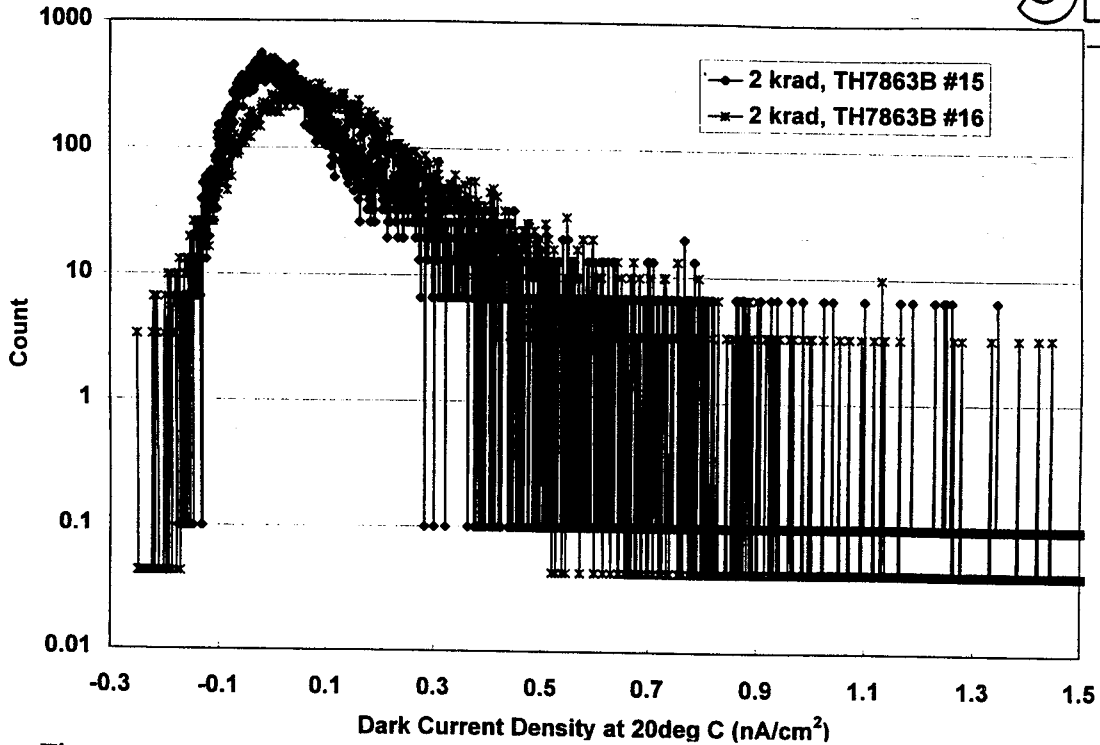

Figure 4.5-4 Dark current histograms for the 2krad region on both TH7863B devices

4.6 DARK CURRENT NON-UNIFORMITY: GENERAL

Figure 4.6-1 shows dark current histograms for the 2krad regions of 10 MeV proton-irradiated devices and the 7e9 p/cm^2 regions of 46 MeV proton-irradiated CCDs. It can be seen that the tails of the histograms are broadly similar.

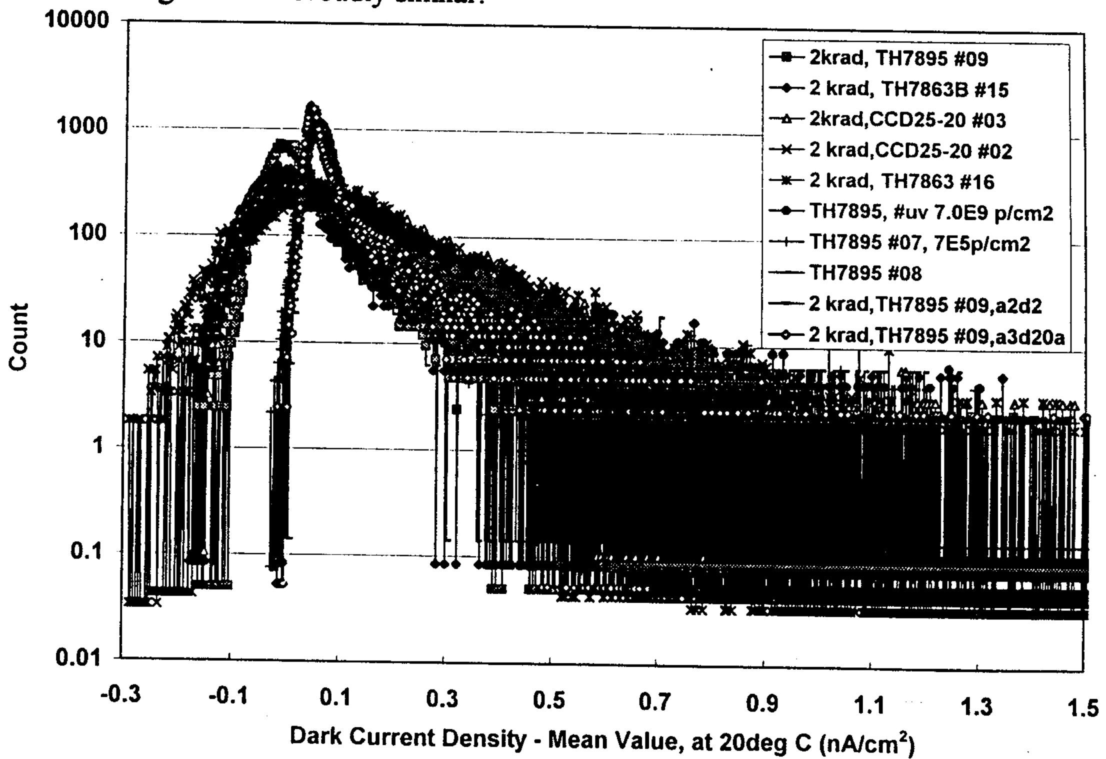

Figure 4.6-1 Dark current histograms for various proton-irradiated devices

Copyright © Sira Ltd 1995

4.7 RANDOM TELEGRAPH SIGNALS

These have been studied for CCD25-20 and TH7895M proton irradiated CCDs. Figure 4.7-1 shows signals for four pixels at 15 °C, -5 °C and -20 °C for a CCD25-20 (#03), three of these pixels show Random Telegraph Signal (RTS) behaviour (the lower being rather erratic) and the fourth shows a steady level. Based on earlier measurements of activation energy (values~0.9eV were found in RD7), it would be expected that the time constants at -20°C would be more than a day. However a few pixels still show some RTS behaviour at -20°C with time constants of the order of hours. Similar results were found for the TH7895M device.

There are three possible explanations for this behaviour:

i) These pixels have a lower activation energy (≤ 0.8 eV) than those previously studied. A spread of about 0.1eV in the activation energy was seen and this could represent the lower end of this spread. Another possibility is that these signals could be due to different defects.

ii) There could be differences in the rate constant (pre-exponential factor). This is determined by the jump frequency and by the efficiency in coupling thermal energy into vibrations in a particular direction (in this case over the potential barrier). It is plausible that the rate constant may depend on the local environment.

iii) At low temperatures, when the time constants become of the order of several hours, it may become more probable for energy to be supplied from non-thermal sources so as to achieve reconfiguration of the defect. One such source might be electron-hole recombination.

Further work (which is outside the scope of the present study) will be needed to find the mechanism responsible.

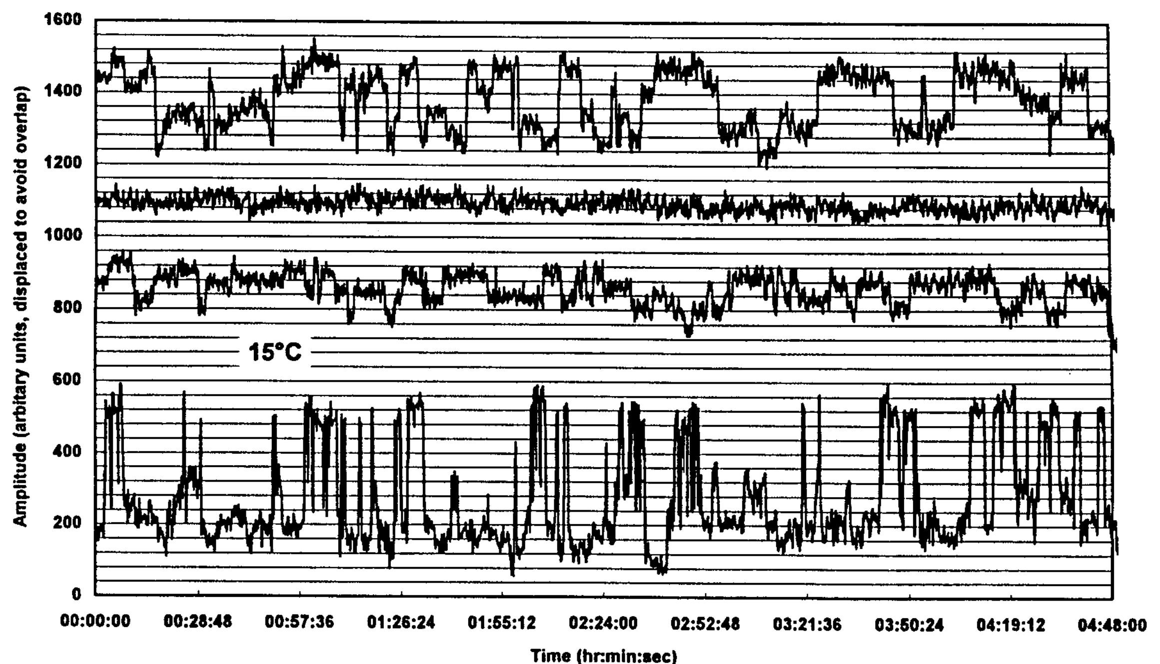

Figure 4.7-1a RTS plots for 4 pixels in CCD25-20 device #03 at 15°C

Copyright © Sira Ltd 1995

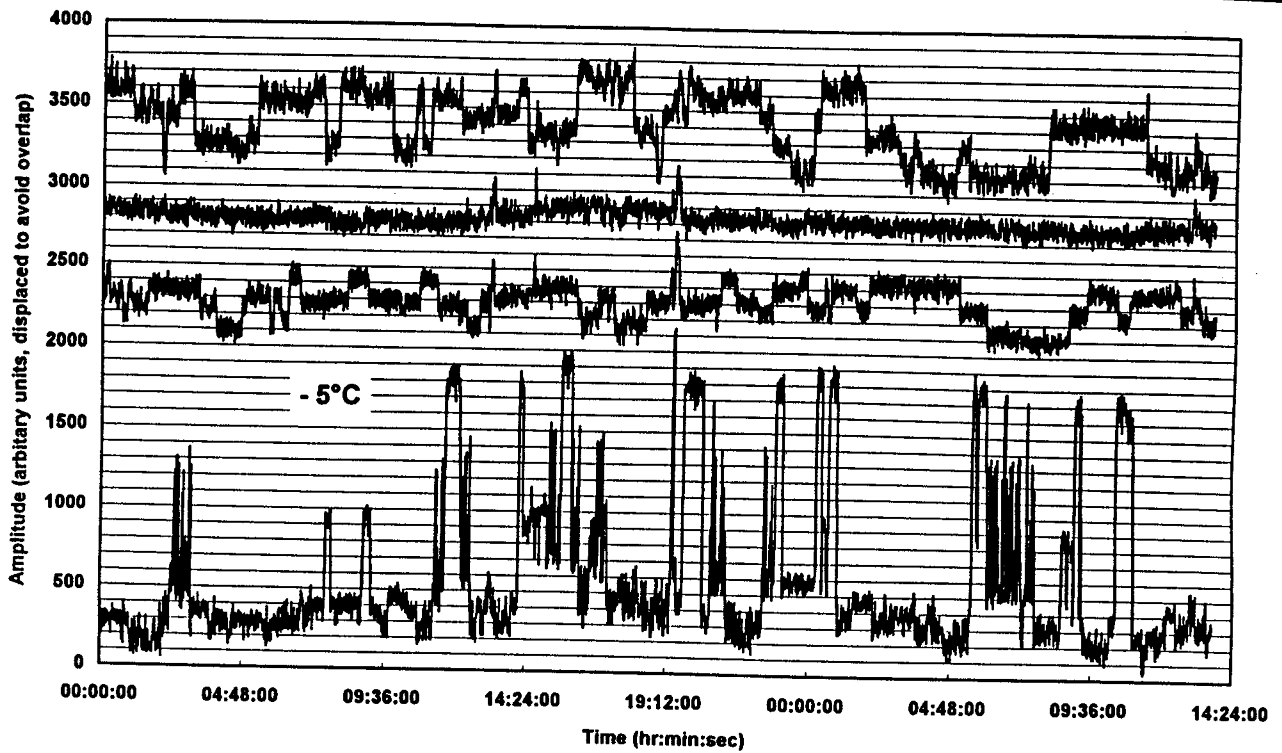

Figure 4.7-1b RTS plots for 4 pixels in CCD25-20 device #03 at -5°C

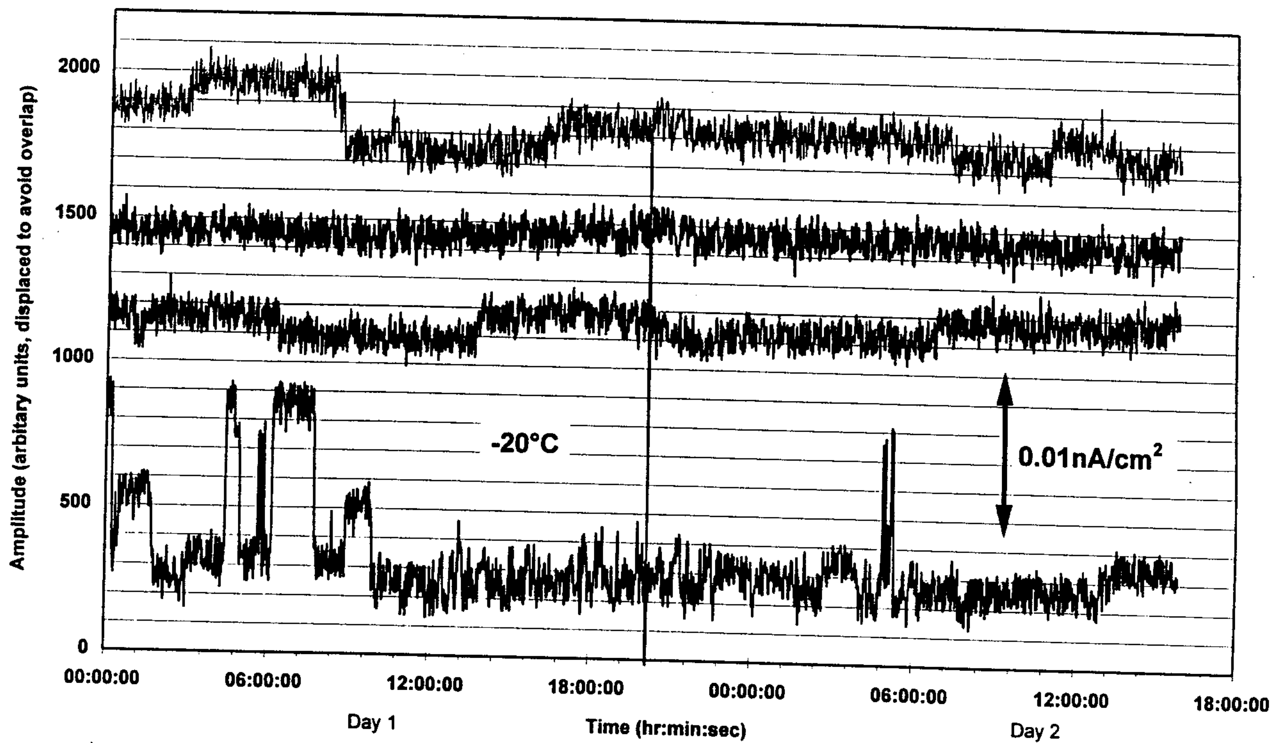

Figure 4.7-1c RTS plots for 4 pixels in CCD25-20 device #03 at -20°C

Copyright © Sira Ltd 1995

In RD7 it was reported that the cross-section for the production of an RTS defect, ~0.65 barns, was close to that for inelastic collisions given an interaction volume of 22×22×4 microns. However as the interaction volume is an unknown (e.g. if field-enhancement is essential then the interaction volume is only a small fraction of the total pixel volume), it is necessary to take measurements at several proton energies to determine if any trend exists. A survey of occurrence probabilities was undertaken in order to establish if the probability scales with elastic, inelastic or total NIEL.

Over two thousand pixels from CCDs irradiated with protons of energy 1.5, 10 and 46 MeV and various doses from 1-4 krad(Si) were examined. The occurrence frequencies were fitted to a Poisson distribution to yield a value that corresponds to the probability per incident proton of an RTS defect being created. This was plotted as a function of the elastic, inelastic and total NIEL. The results are shown in Figure 4.7-2

It is clear that the probability/proton goes down with increasing proton energy whereas the inelastic NIEL goes up. The cross-section for inelastic interaction does not vary significantly between 10 MeV and 46 MeV. This implies that nuclear interactions are not the cause of RTS defect production. In fact the probability/proton is proportional to the elastic NIEL (the fit to the total NIEL is not so good, as one expects the graph to go through zero). The line slope implies that ~1% of PV centres show RTS effects.

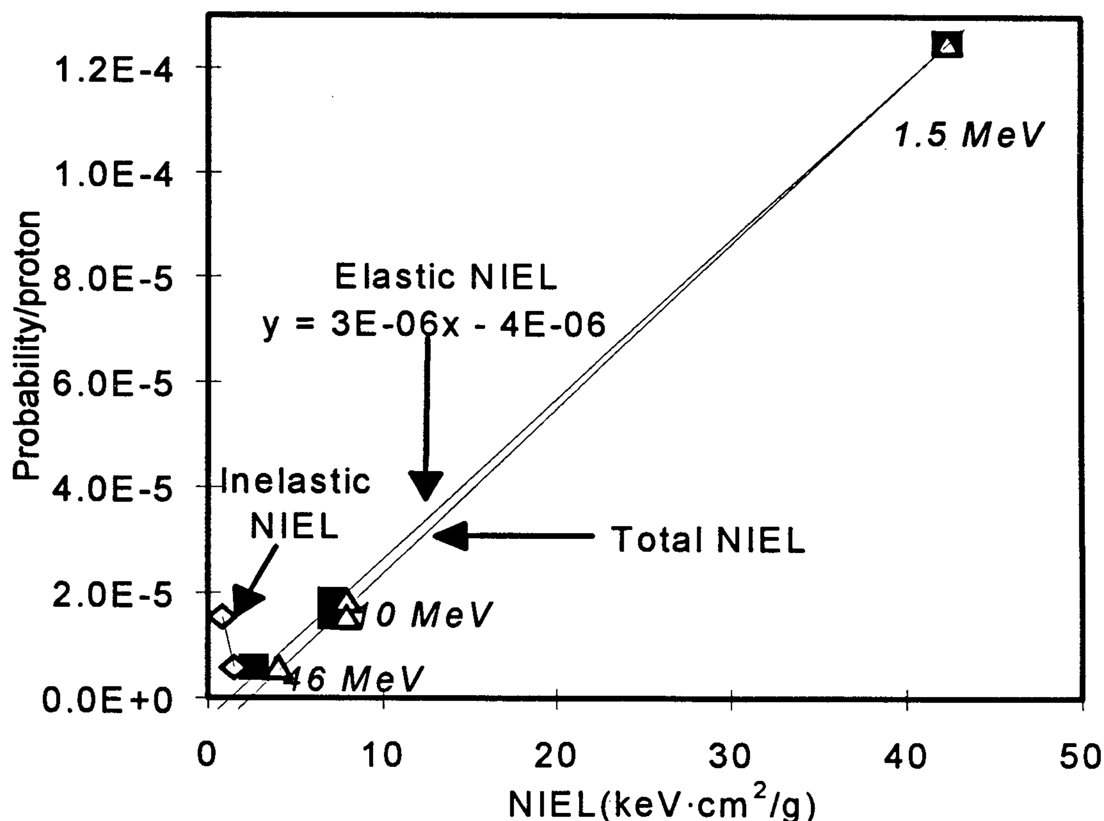

Figure 4.7-2 The probability/incident proton of creating an RTS defect as a function of the elastic, inelastic, and total NIEL.

Copyright © Sira Ltd 1995

Measurements were taken of the amplitude of the RTS transitions for 30 pixels in a TH7895M device at 15°C (#09) after 1krad(Si) of 10MeV protons. The histogram is plotted in Figure 4.7-3.

The occurrence frequency and the amplitudes of the RTS transitions were plotted as a function of the mean dark current within a pixel (dark current pedestal) for each pixel (Figure 4.7-4 and Figure 4.7-5). The results indicate that the probability of finding a pixel showing RTS switching increases with dark current pedestal but that the amplitude of the transitions is not correlated to that value. Note, though, that not all dark current spikes show RTS behaviour.

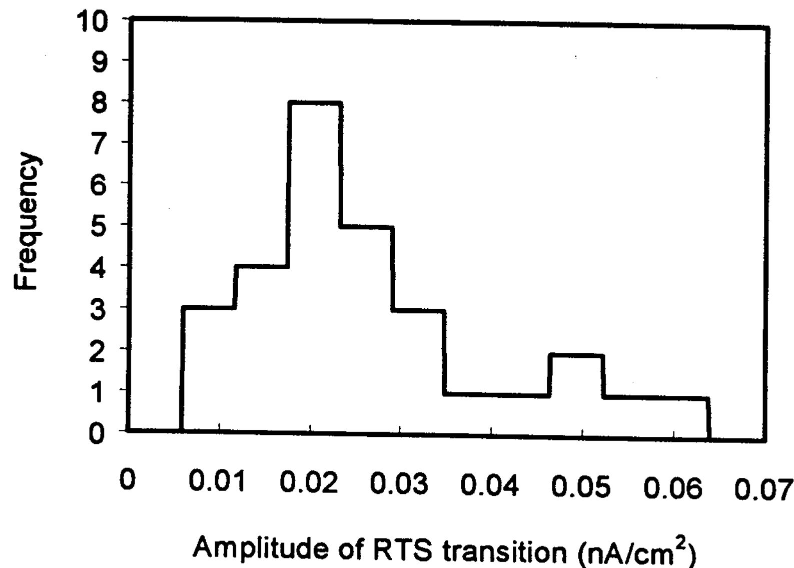

Figure 4.7-3. Histogram of RTS amplitudes for TH7895 device at 15°C after 1 krad of 10 MeV protons.

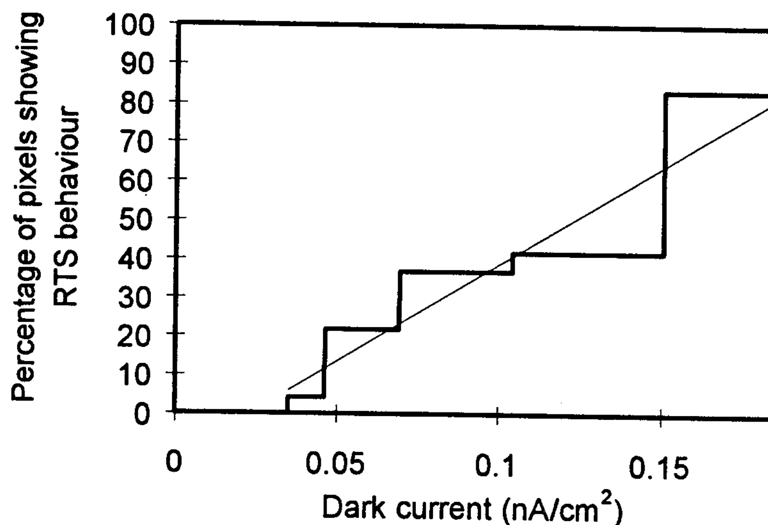

Figure 4.7-4. Occurrence frequency as a function of the dark current pedestal.

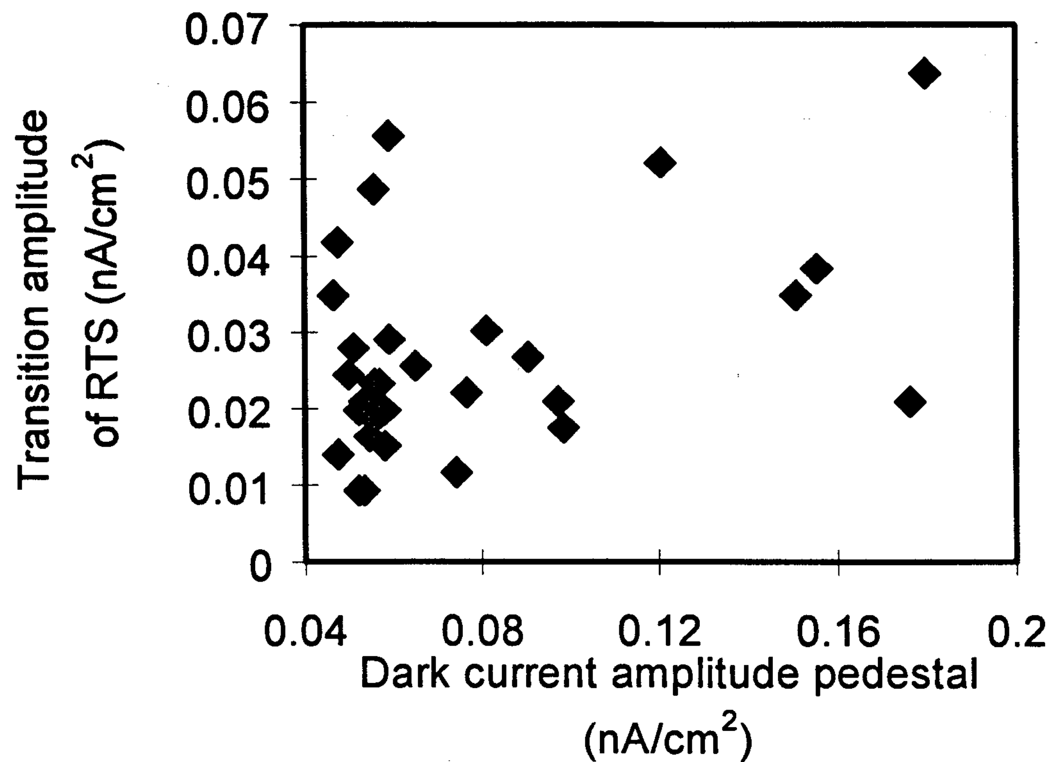

Figure 4.7-5. RTS amplitudes versus the dark current pedestal of that pixel.

Copyright © Sira Ltd 1995

5 LINEARITY AND FULL WELL CAPACITY

Measurements were made at constant irradiance and by changing the integration time. Both uniform and spot illumination were used. The test set-up for spot illumination was identical to that used for spot measurements of CTE and is described in section 7. Uniform illumination was achieved by allowing light emerging from a fibre optic cable (the end of which was ~20cm from the CCD) to reach the CCD surface with no intervening optics. The cable was in turn illuminated by a Xe arc lamp (placed outside the light-tight enclosure which housed the CCD)

5.1 CCD25-20 DEVICES

Figures 5.1-1 to 5.1-3 show linearity plots for CCD25-20 devices for both spot and uniform illumination at 20 °C. It can be seen that uniform illumination gives a ~20% increase in full well capacity. This can probably be explained by the fact that, as the uniform illumination is increased and full well is approached, charge starts to come in contact with interface traps. However with uniform illumination the traps are kept uniformly filled and little trapping can take place. Linearity is therefore preserved up to higher signal levels (at which the potential wells become collapsed and charge flows into the channel stop regions and the substrate). Uniform illumination is a somewhat unrealistic case since most scenes will have some regions brighter than others and this will allow interface traps enough time to emit during a line move time. Spot illumination measurements will normally give the worst case (lowest full well capacity) but the most relevant test method will depend on the application.

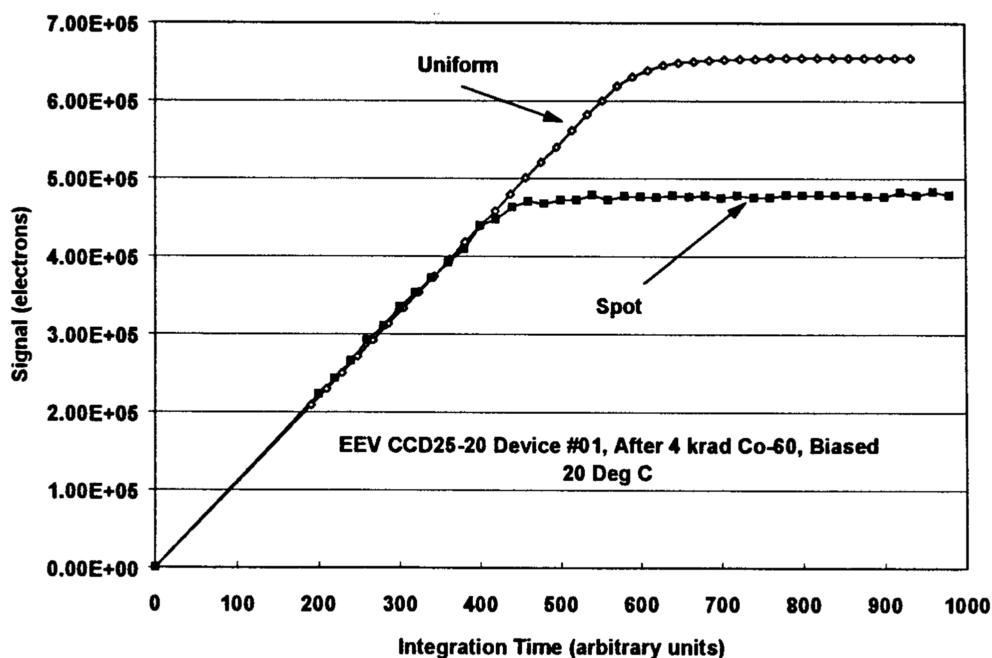

Figure 5.1-1 Linearity plots for CCD25-20 #01 after 4krad Co-60.

Copyright © Sira Ltd 1995

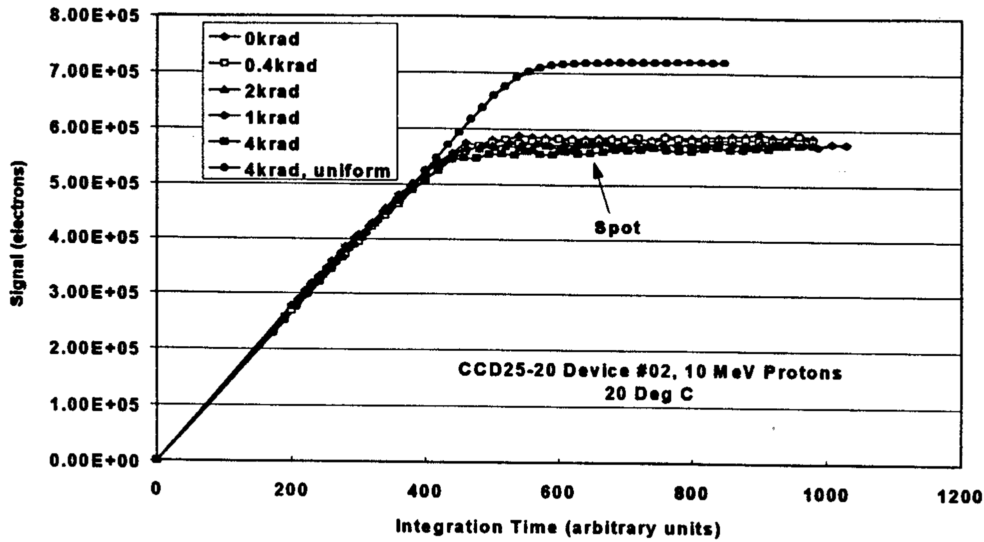

Figure 5.1-2a Linearity plots for CCD25-20 #02 after 10MeV proton irradiation.

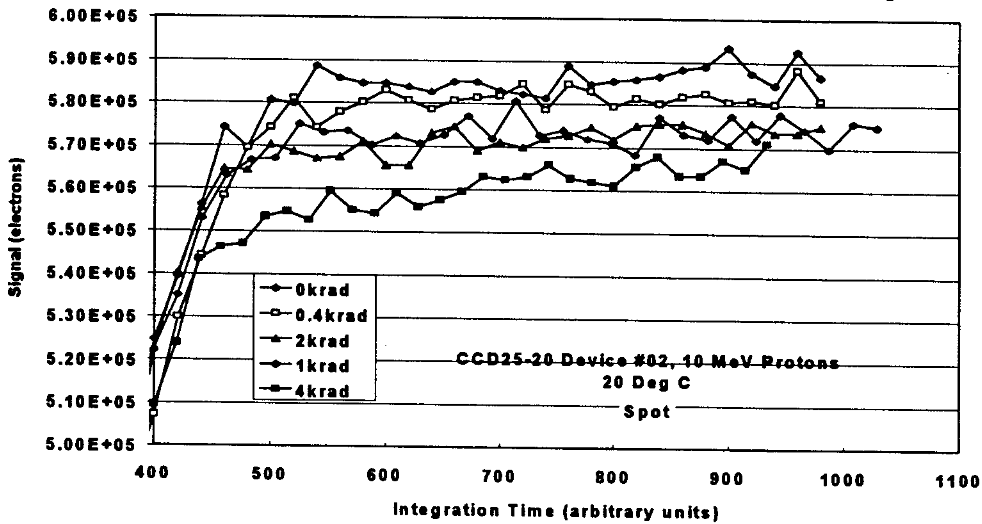

Figure 5.1-2b Linearity plots for CCD25-20 #02 after 10MeV proton irradiation - vertical scale expanded so as to see variation with proton fluence

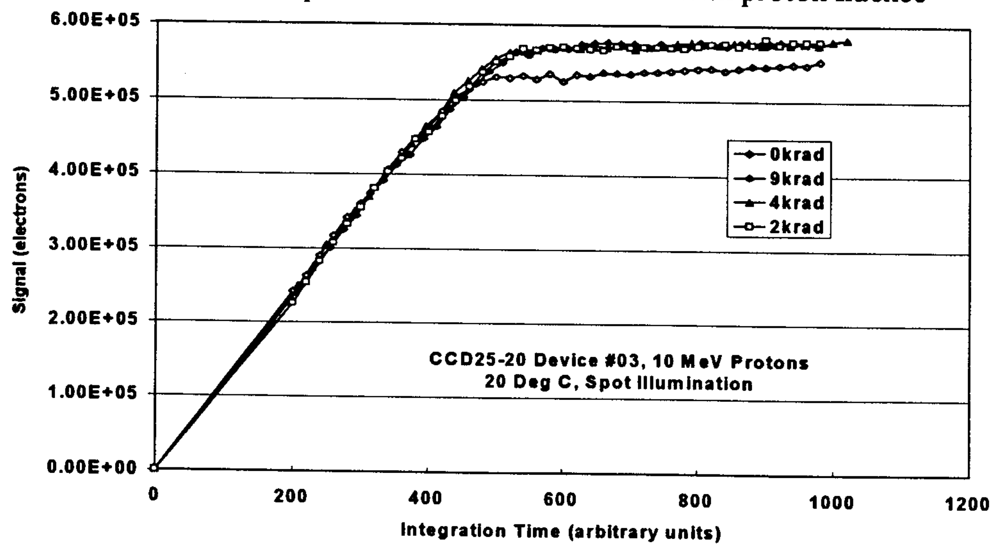

Figure 5.1-3 Linearity plots for CCD25-20 #03 after proton irradiation.

Copyright © Sira Ltd 1995

The following full well capacities were derived:

Table 5.1-1 CCD25-20 full well capacity
(10^5 electrons)
Manufacturers' data are given in brackets, - means measurements not performed

	Pre-irradiation	4 krad
#01 Co-60, powered (manufacturers data)	- (6.4)	4.7
~02, 10 MeV protons (manufacturers data)	5.7 (6.2)	5.2
#03, 10 MeV protons	5.7 (5.9)	5.2

The pre-irradiation values agree well with manufacturers' data but note that the clock amplitudes used were 11 V to 0 V rather than 11 V to -1.5 V as suggested by the manufacturer. The latter values were satisfactory at low values of Vss but this gives higher dark current. At high Vss 0V clock low voltages were needed for good linearity at high signal levels.

Note that the full well capacity is reduced after irradiation by ~5% for 4 k rad of 10 MeV protons. Unfortunately, pre-irradiation measurements on device #01 were obtained with uniform illumination, however the post-irradiation value is low and so it would appear that biased Co-60 irradiation has a more damaging effect (perhaps as much as 20% reduction after 4 krad).

Full well capacities for the readout registers were measured by using a defocused spot and using x4 binning in the vertical direction. Plots are given in figures 5.1-4 and 5.1-5. It can be seen that the full well capacity is again reduced after irradiation. The manufacturer's value was ~2.5E6 electrons. The value measured here is higher - in fact more than 4 times the capacity of the image area for spot illumination. It would appear that the results are closer to the uniform illumination case - as might be expected from the defocused nature of the spot.

Copyright © Sira Ltd 1995

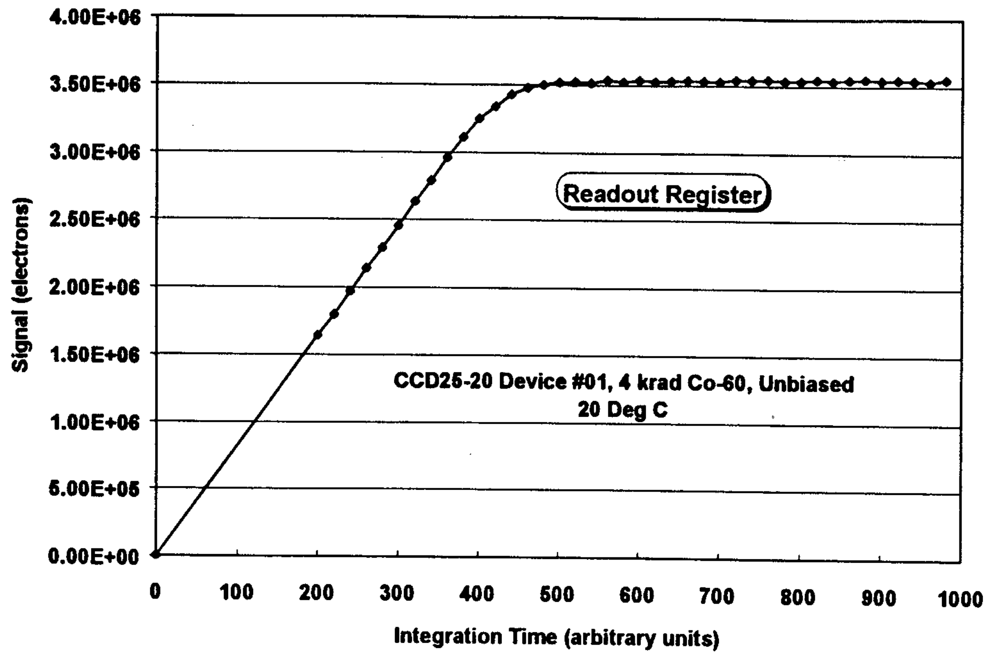

Figure 5.1-4 Linearity plots for CCD25-20 #01 (readout register) after 10MeV proton irradiation

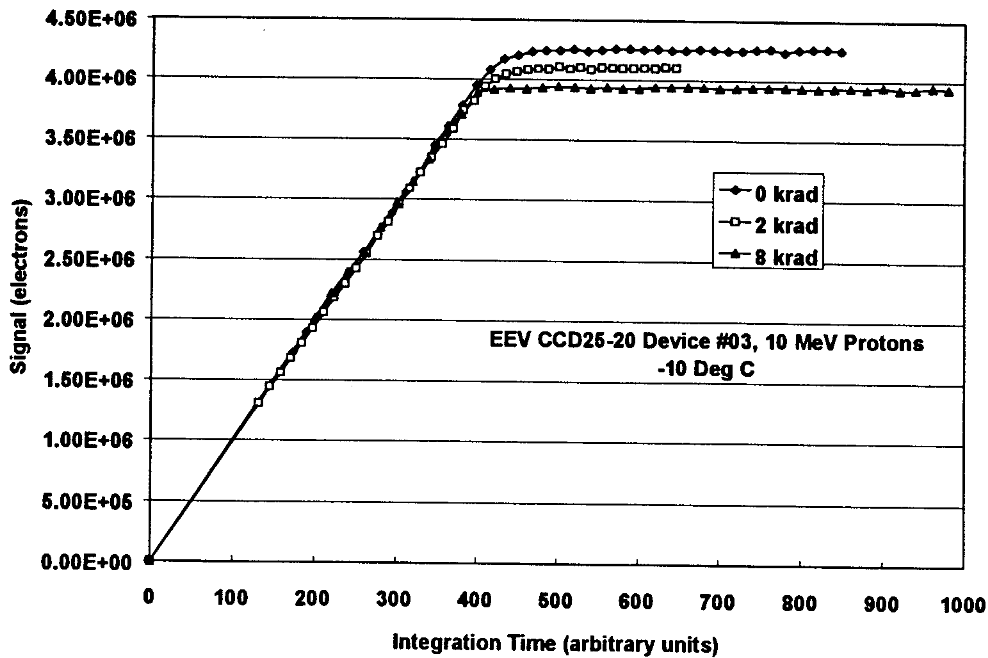

Figure 5.1-5 Linearity plots for CCD25-20 #03 (readout register) after 10MeV proton irradiation

Copyright © Sira Ltd 1995

5.2 TH7863B DEVICES

Figures 5.2-1 to 5.2-5 show linearity plots for TH7863B devices. It can be seen that, as for the CCD25-20, the full well capacity is increased (to ~1.2 E6 electrons) for uniform illumination, and this value is not changed much by the irradiations. For spot illumination the values of full well capacity are given below:-

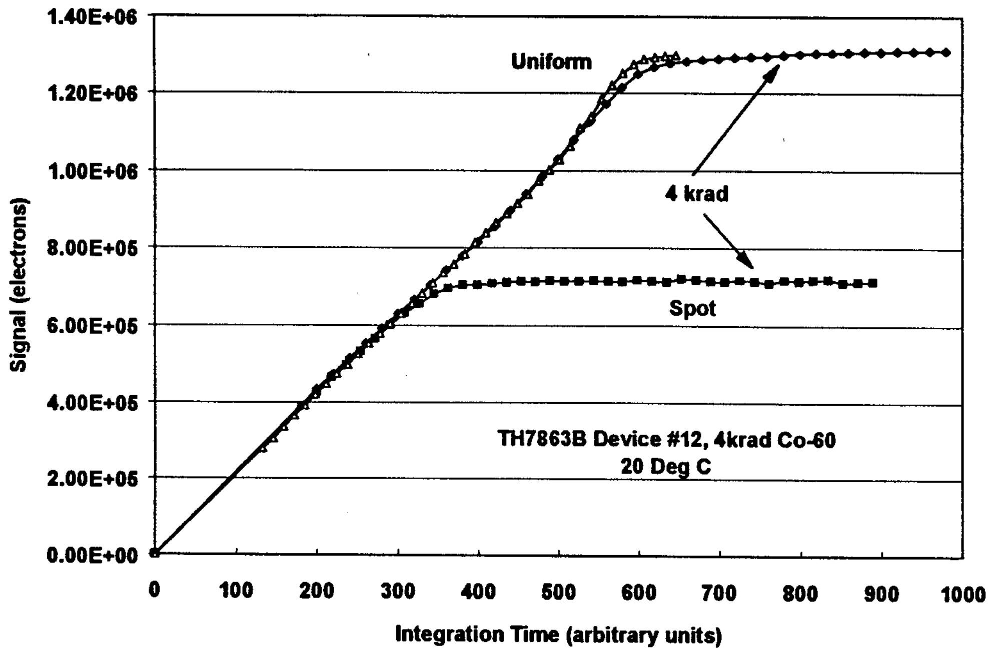

Figure 5.2-1 Linearity plots for TH7863B #12 after 4krad Co-60.

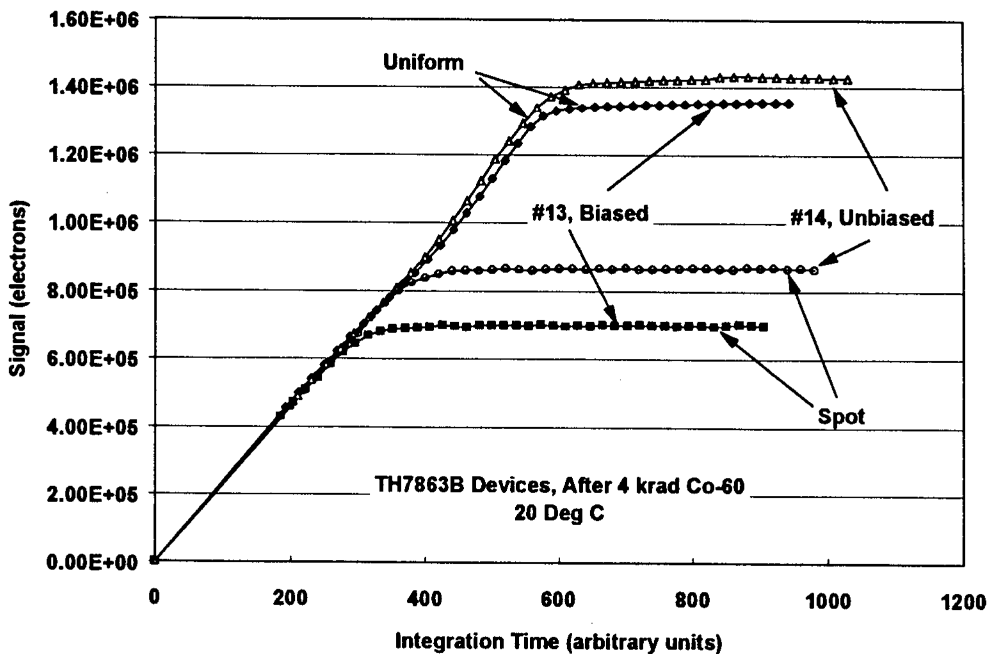

Figure 5.2-1 Linearity plots for TH7863Bs #s 13 and 14 after 4krad Co-60 irradiation

Copyright © Sira Ltd 1995

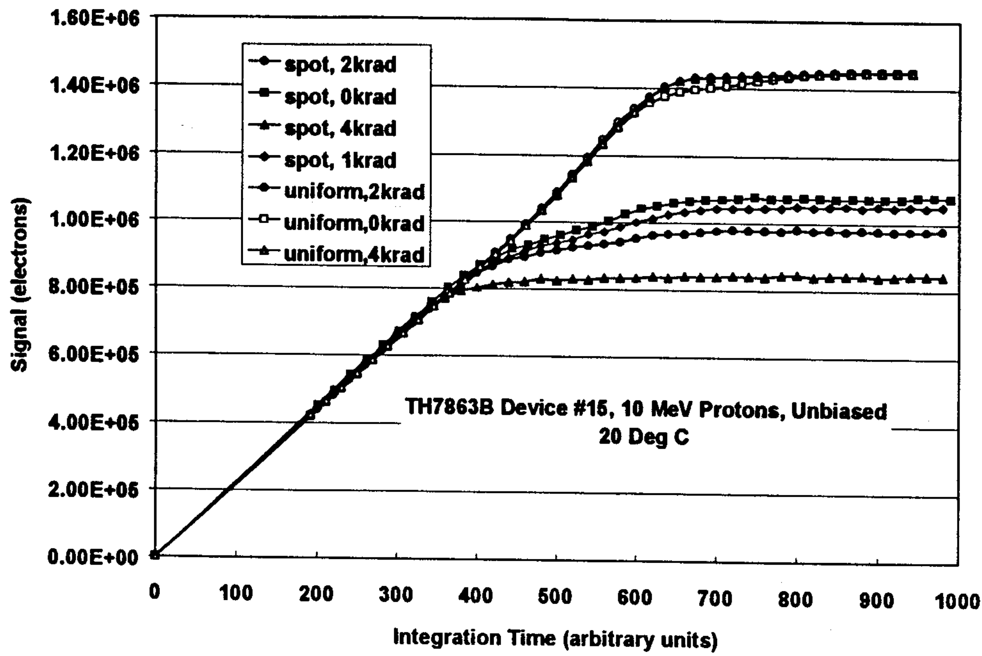

Figure 5.2-3 Linearity plots for TH7863B #15 after 10MeV proton irradiation

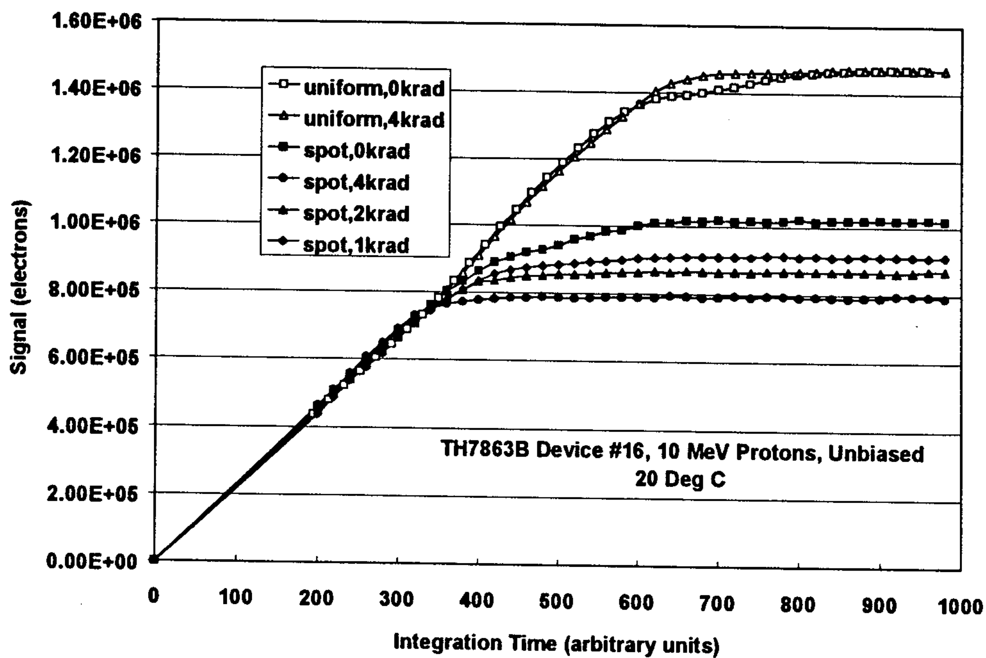

Figure 5.2-3 Linearity plots for TH7863B #16 after 10MeV proton irradiation

Copyright © Sira Ltd 1995

TH7863B, spot illumination
(10^5 electrons)
- means measurements not performed

device # and irradiation	Pre-irradiation	after 4 krad
12 Co-60, biased	-	7.0
13 Co-60, biased	-	7.0
14 Co-60 unbiased	-	8.6
15 10 MeV proton, unbiased	9.4	8.2
16 10 MeV proton, unbiased	9.4	8.0

It appears that the full well capacity is reduced by ~15% for unbiased devices, and probably ~30% for biased devices after 4 krad. These results are in line with previous measurements of the A version (RD4).

5.3 TH7895M DEVICES

Some difficulties were encountered in optimising the clock voltages in order to get good linearity and full well capacity. Most devices needed 5 to -7 V, image area clocks during frame transfer (compared with 5 V to -5 V as suggested in the manufacturers data book), with spot illumination the full well capacity did not seem to be largely affected by the irradiations (within a tolerance of 5%). A typical full well capacity was 4.2 E5 electrons. Data for two devices (proton irradiated) is shown in figures 5.3-1 and 5.3-2.

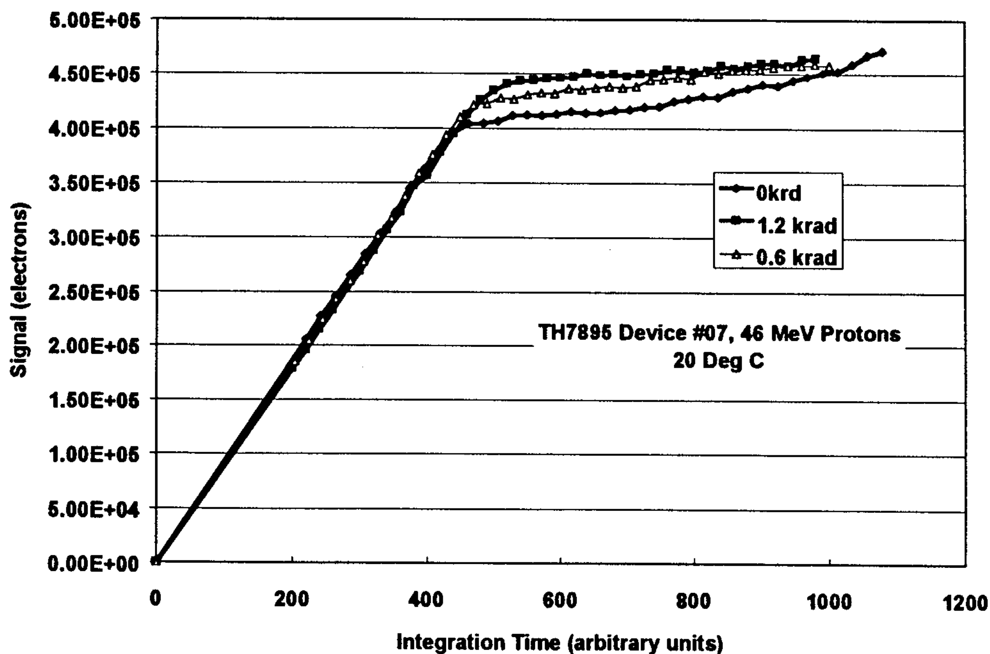

Figure 5.3-1 Linearity plots for TH7895M #07 after 10MeV proton irradiation

Copyright © Sira Ltd 1995

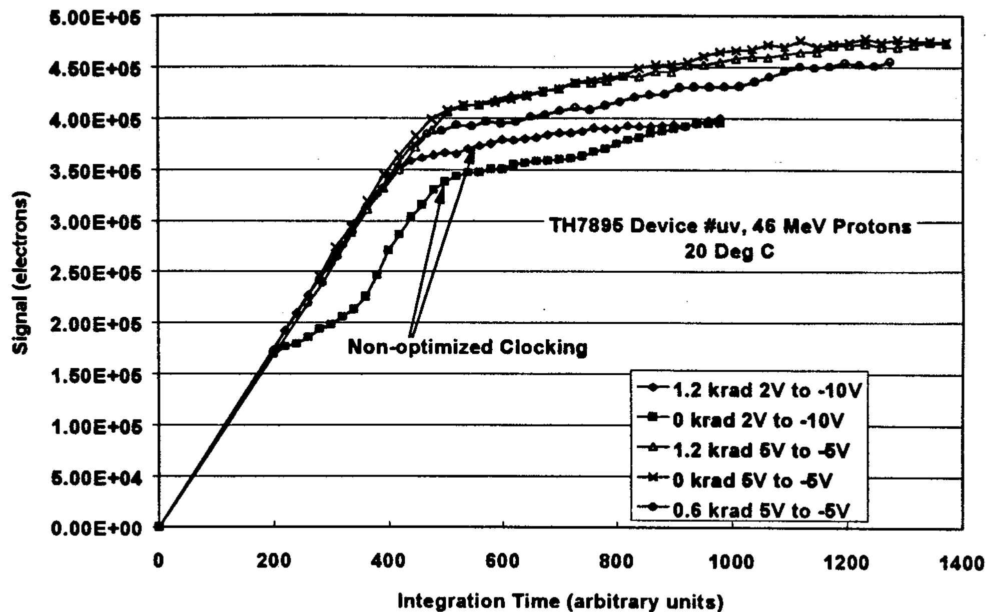

Figure 5.3-2 Linearity plots for TH7895M #UV after 46MeV proton irradiation

5.4 TH7395M DEVICES

As with the TH7895M devices, these CCDs needed 5 V to -7 V I clocks during frame transfer, and this was not discovered until late in the programme (because many early measurements were performed with uniform illumination, which is not so critical). Data for device #02 after irradiation with 46 MeV protons, the full well capacity was ~5.3 x 10^5 electrons. It appears that the full well capacity was larger at the edges of the device (co-incidentally, which received the proton irradiation) than in the middle. This may be due to a degradation in the clock waveform shape at the centre of the device because of the distributed resistance and capacitance of the electrode structure, though why this should occur for this device type and not the others studied is not clear. For the Co-60 device (after 4 krad) the full well capacity was 5.2 x 10^5 electrons.

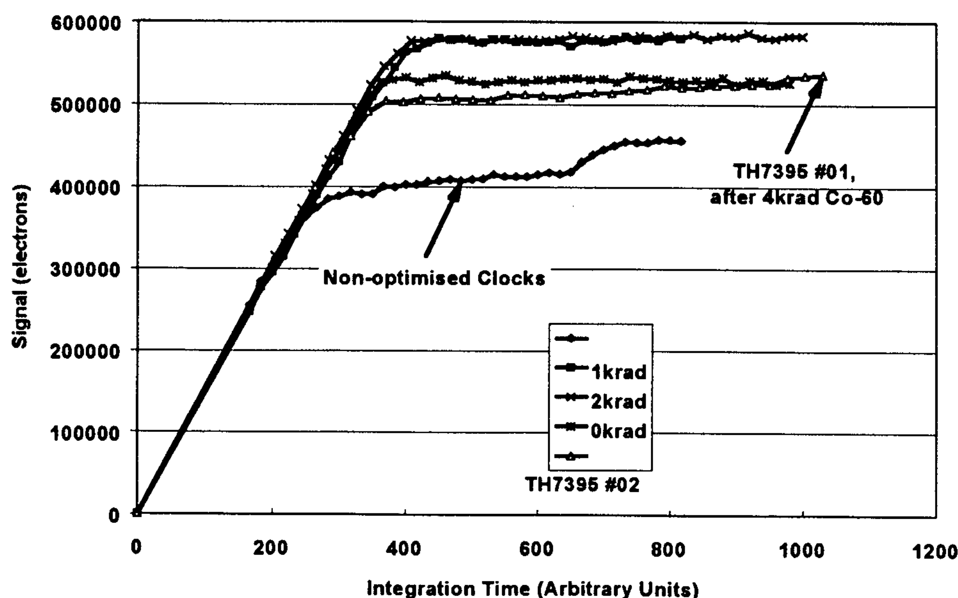

Figure 5.4-1 Linearity plots for TH7395 devices

5.5 BLOOMING CHARACTERISTICS

For the CCD25-20 the dither clocking mode gives an antiblooming effect. Even for images x300 above saturation there is no blooming down a column. If the dither clocking is switched off however blooming occurs. This is shown in figures 5.5-1 to 5.5-4. The CCDs were illuminated with a spot centred within a pixel and of such an intensity as to be just below saturation. The exposure was increased by lengthening the integration time. The figures show a slice down a column. Blooming is seen when not dithering. For the x1000 integration the dark charge became nearly as large as the full well capacity, but there was still no blooming (the width of the spot being determined by diffraction and charge diffusion effects)- this is shown in figure 5.5-2.

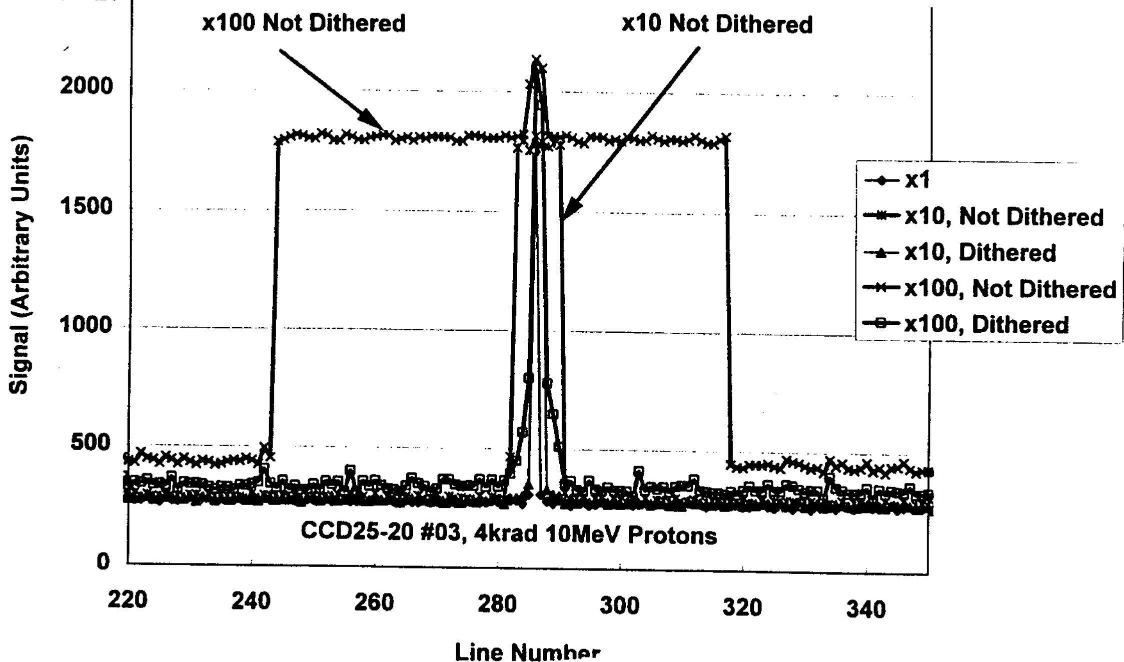

Figure 5.5-1 Column plots for a CCD25-20 after over exposure.

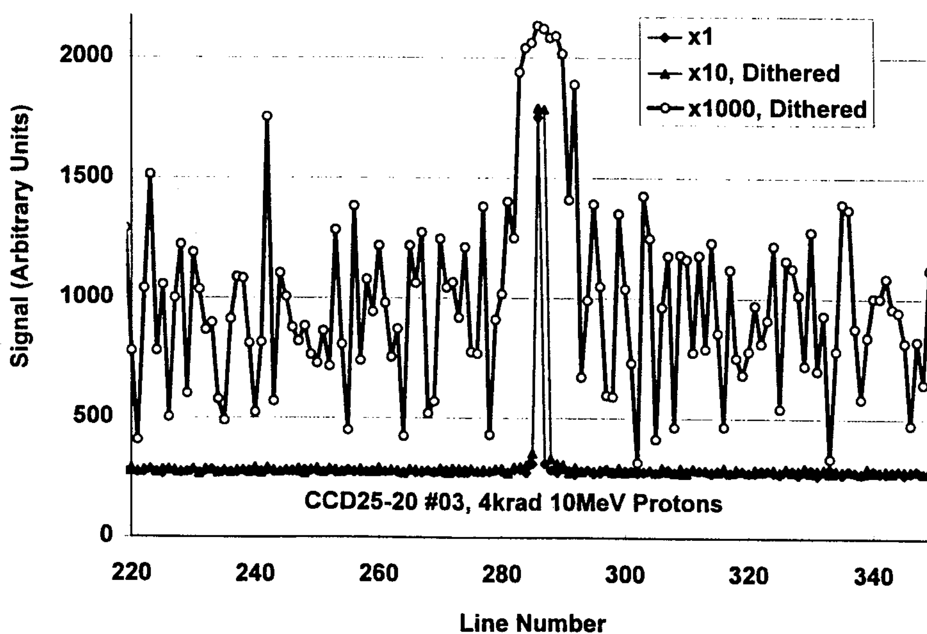

Figure 5.5-2 Column plots for a CCD25-20 after over exposure

Copyright © Sira Ltd 1995

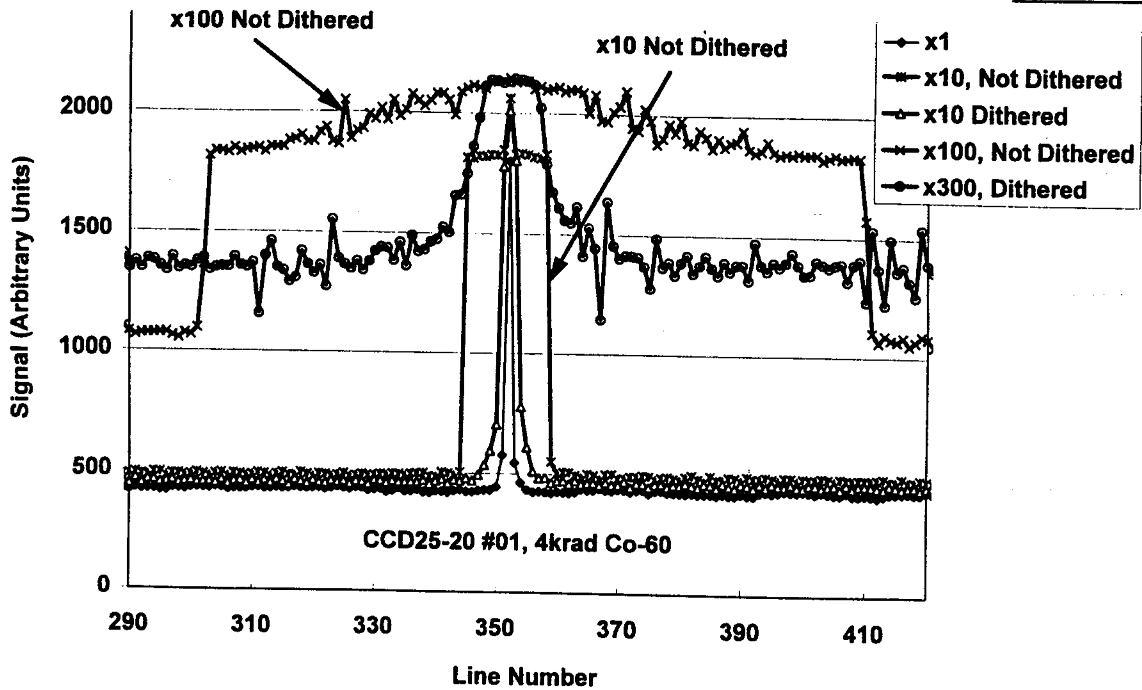

Figure 5.5-3 Column plots for a CCD25-20 after over exposure

For the TH7895M which suppresses dark charge using an MPP implant the effect is not the same and blooming occurs as normal. With dither clocking, overflow charge is allowed to come into contact with the inverted surface and the exess charge combines with the holes that have accumulated there. With MPP devices the surface is also inverted (in order to reduce dark current) but charge flows over the implanted barrier phase (i.e. blooms) before it comes into contact with holes at the surface.

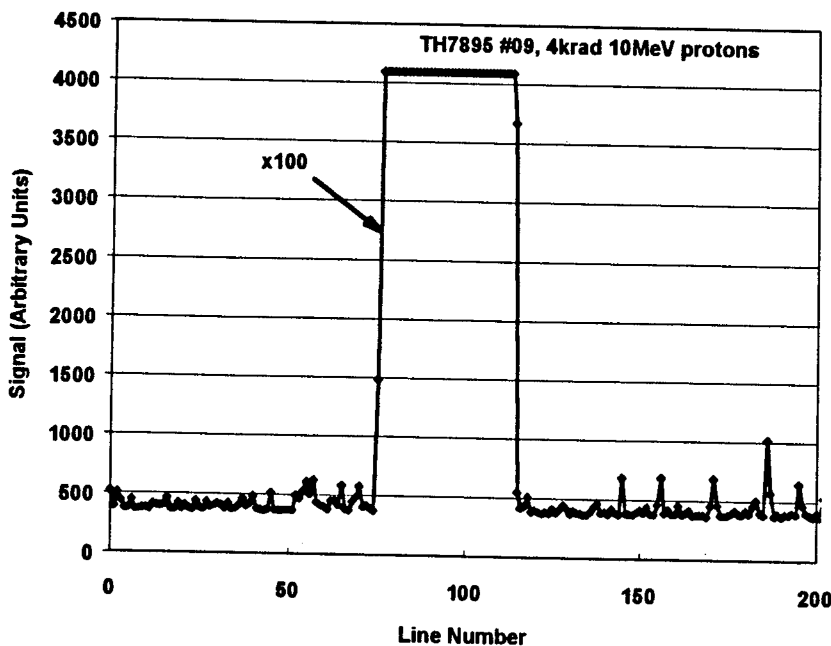

Figure 5.5-4 Column plots for a TH7895M device after over exposure

Copyright © Sira Ltd 1995

6 BRIGHT FIELD MEASUREMENTS

Bright field measurements were made using during the coarse of the study (pre-irradiation and post-irradiation) using broad band illumination from a Xe arc lamp. The optical set-up was as described in section 7, with the exception that the pinhole was large (about 1mm in diameter) and no objective lens was used. This was the same situation as used for uniform illumination measurements of full well capacity (section 5). These measurements were as a check that there were no unusual effects of the irradiations.

At the end of the study a more detailed examination was made using narrow band illumination. Since it was desired that this could be performed in the UV as well as the visible, the optical arrangement was simplified so that there was no glass in the optical path. Light from the arc lamp was passed to the entrance slit of an Oriel 77250 monochromator via a quartz condensing lens. The CCD under test was placed some distance away from the exit slit so as to get quasi-uniform illumination. The uniformity of the illumination that could be achieved was generally a few % but was occasionally larger (especially for the large CCD25-20 devices), in these cases the data was corrected for large scale non-uniformity before further analysis.

The slit width of the monochromator was 10nm and the wavelengths used were as follows

Back illuminated or UV coated devices:	320, 550, 765 and 900nm
Front illuminated devices	445, 765 and 900nm.

Proton illuminated devices were used for these measurements since with these the image area was divided up into several dose regions so enabling comparisons either by eye or by computer analysis (histogramming or image slicing). It was found that there was no discontinuity between the dose regions - and hence no detectable change in quantum efficiency. Also, there was no significant change in the pixel nonuniformity. Histograms are given in figures 6-1 to 6-17. The thinned devices (CCD25-20s and TH7395s) showed pronounced fringe patterns at 900nm and so the non-uniformity (and the width of the histograms) is large. Figures 6-18 to 6-20 show slices across the images. Also with the CCD25-20 devices at 320nm there was some structure in the images: mainly in the form of vertical lines (perhaps a feature of the laser scanning annealing process); there were also some isolated regions of increased responsivity. Image slices at 320nm are shown in figures 6-21 and 6-22. Figures 6-23 to 6-27 show images at 900 and 320nm.

Copyright © Sira Ltd 1995

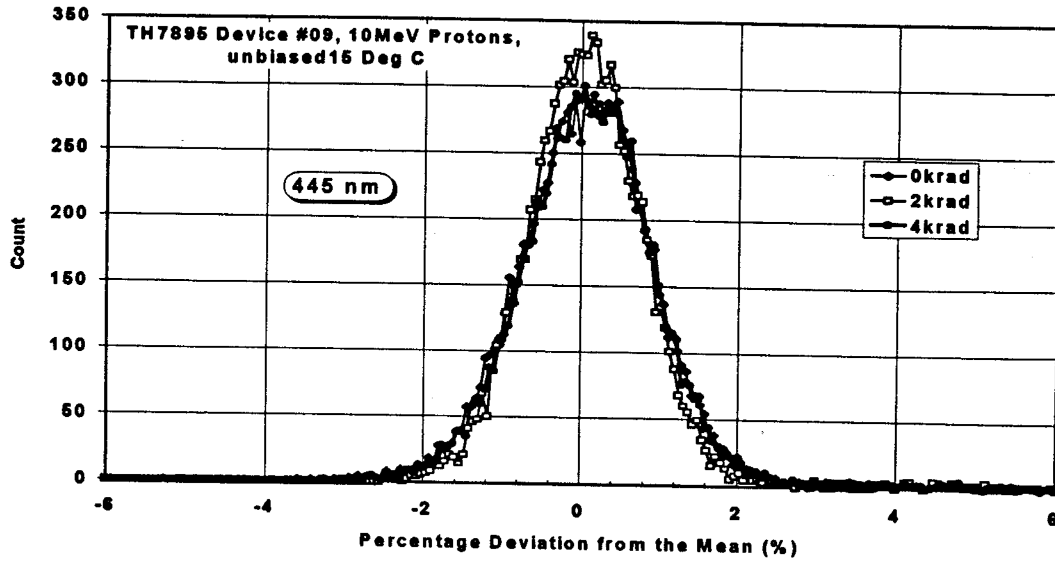

Figure 6-1 Bright field histograms for a TH7895M device at 445nm.

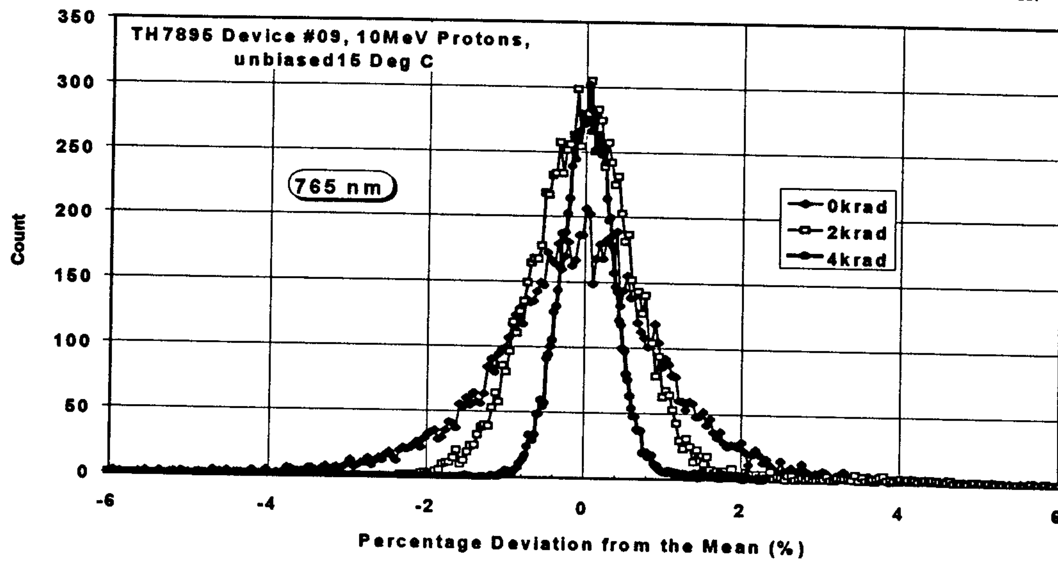

Figure 6-2 Bright field histograms for a TH7895M device at 765nm.

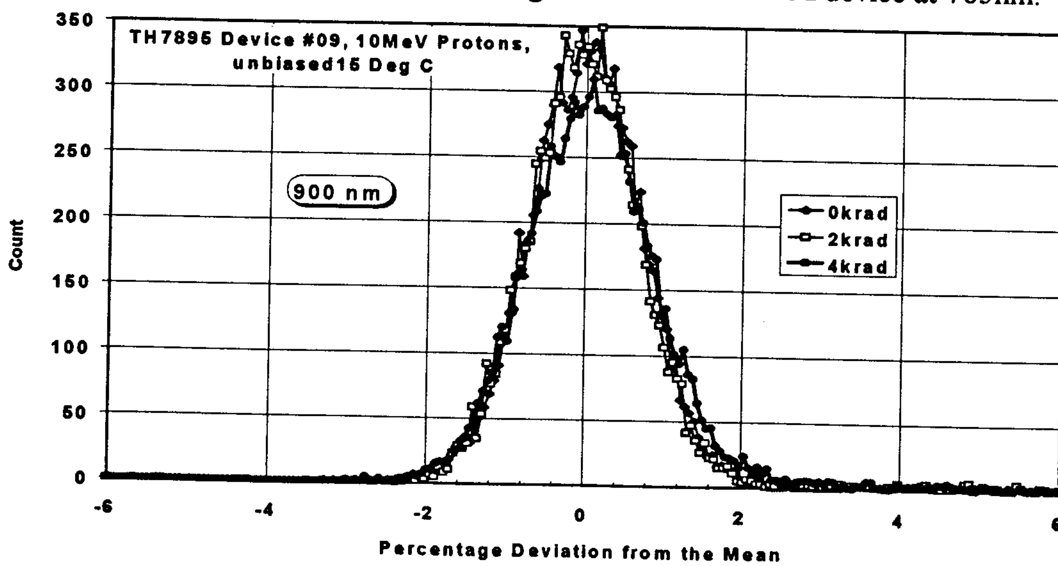

Figure 6-3 Bright field histograms for a TH7895M device at 900nm.

Copyright © Sira Ltd 1995

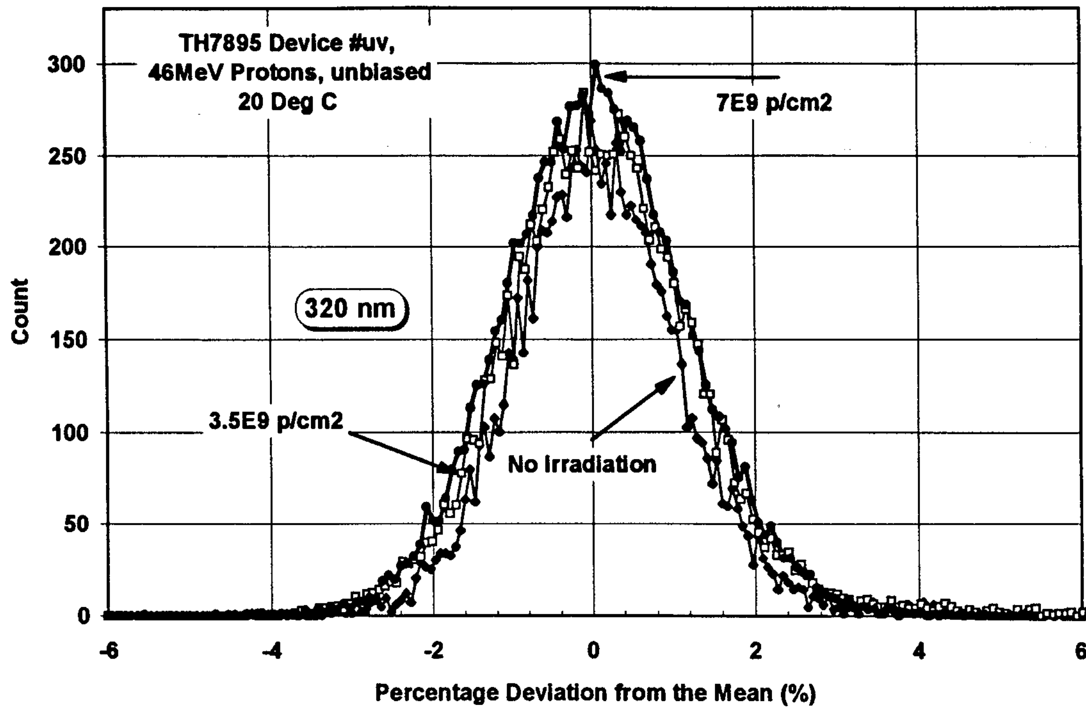

Figure 6-4 Bright field histograms for a TH7895 UV coated device at 320nm.

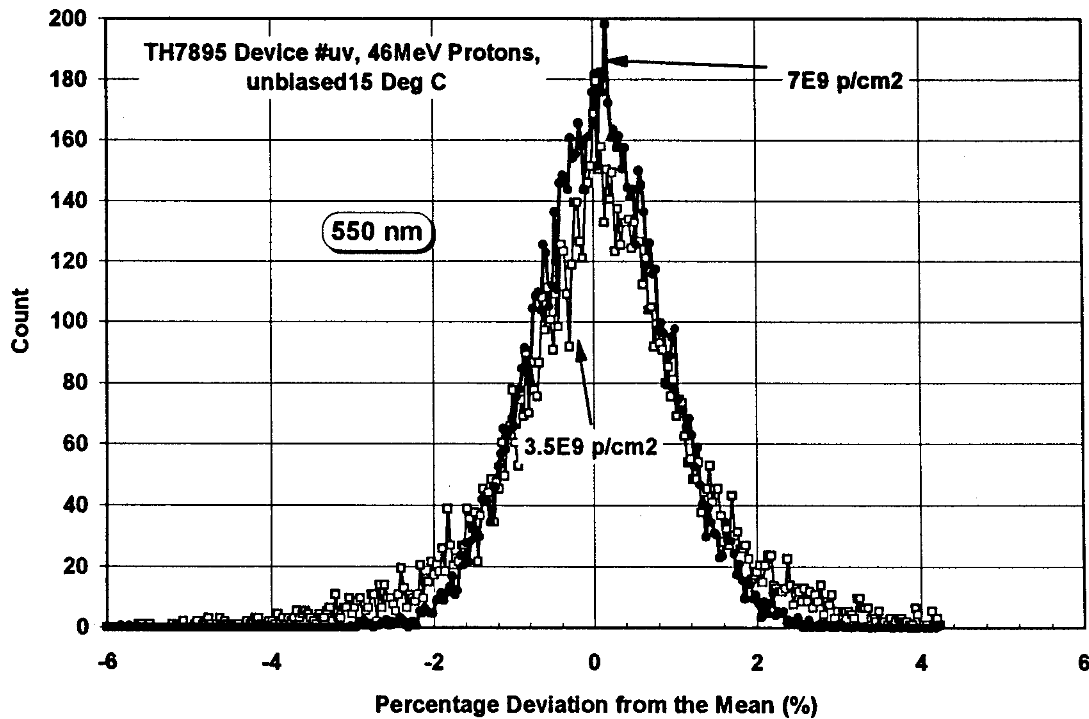

Figure 6-5 Bright field histograms for a TH7895 UV coated device at 550nm

Copyright © Sira Ltd 1995

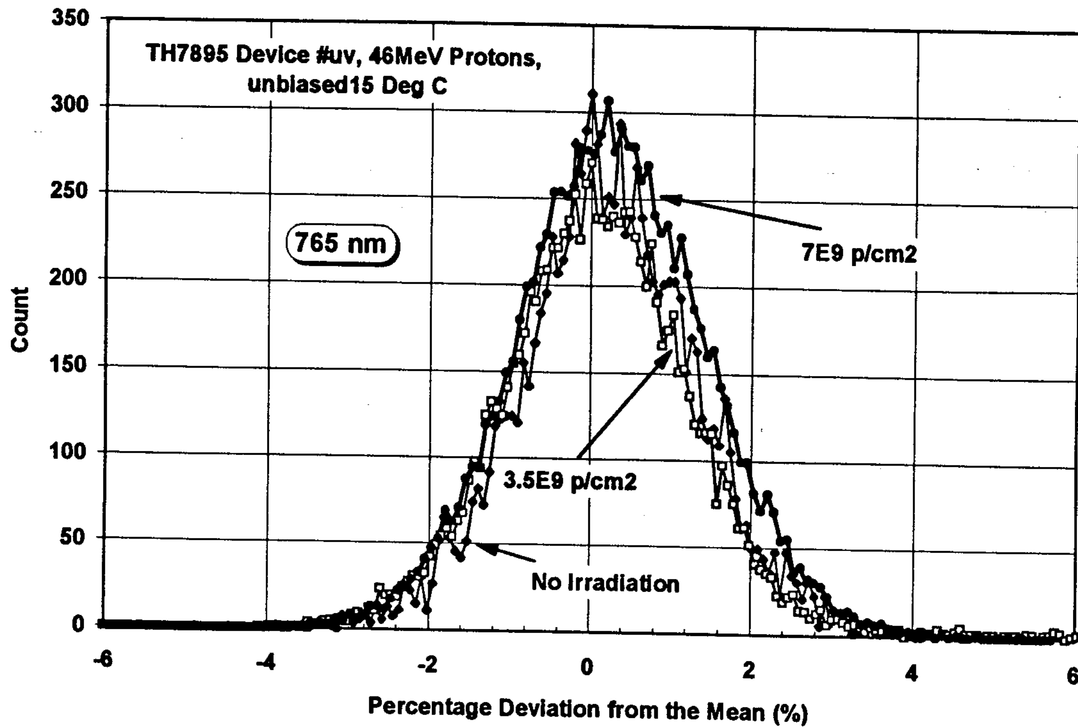

Figure 6-6 Bright field histograms for a TH7895 UV coated device at 765nm

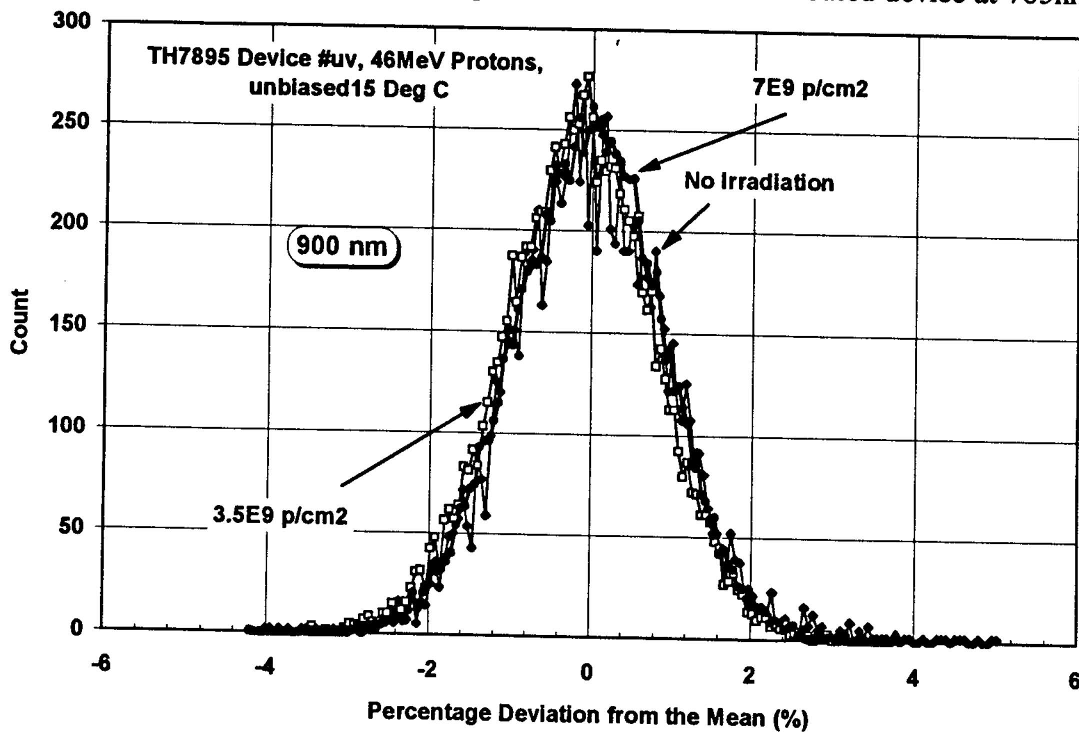

Figure 6-7 Bright field histograms for a TH7895 UV coated device at 900nm

Copyright © Sira Ltd 1995

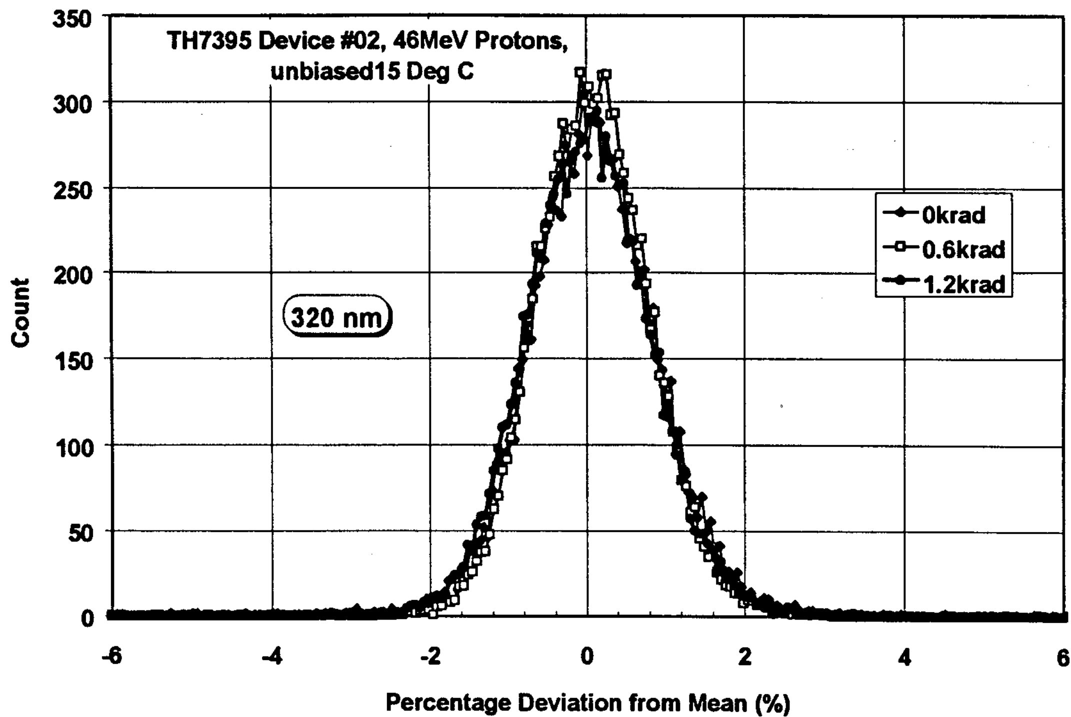

Figure 6-8 Bright field histograms for a TH7395 UV coated device at 320nm.

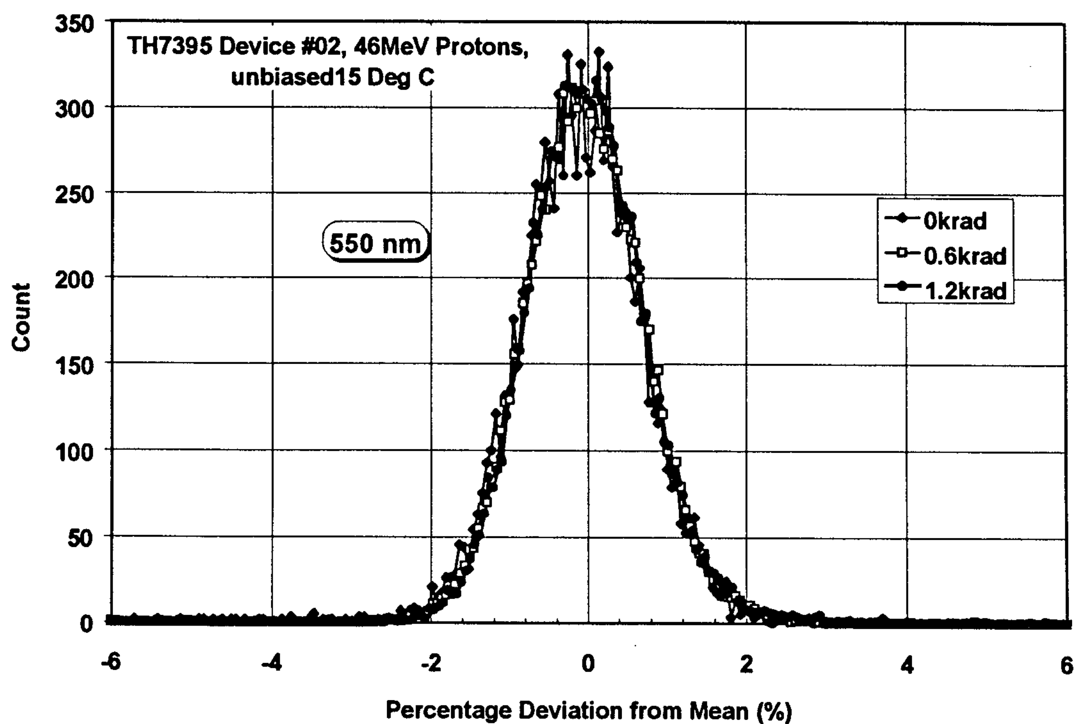

Figure 6-9 Bright field histograms for a TH7395 UV coated device at 550nm

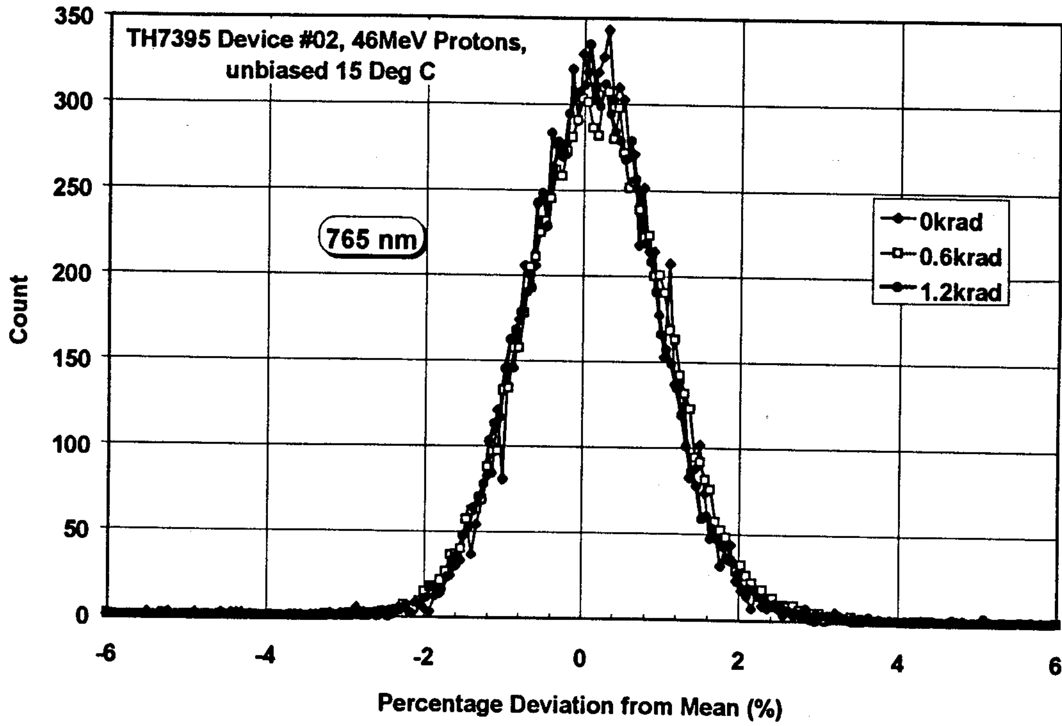

Figure 6-10 Bright field histograms for a TH7395 UV coated device at 765nm

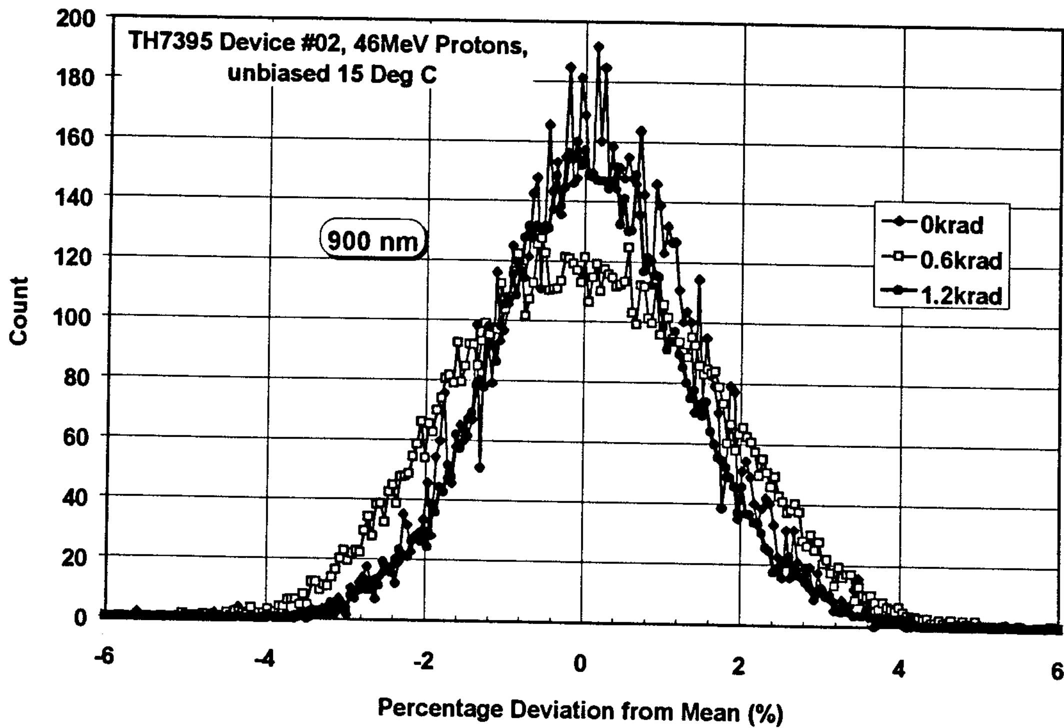

Figure 6-11 Bright field histograms for a TH7395 UV coated device at 900nm

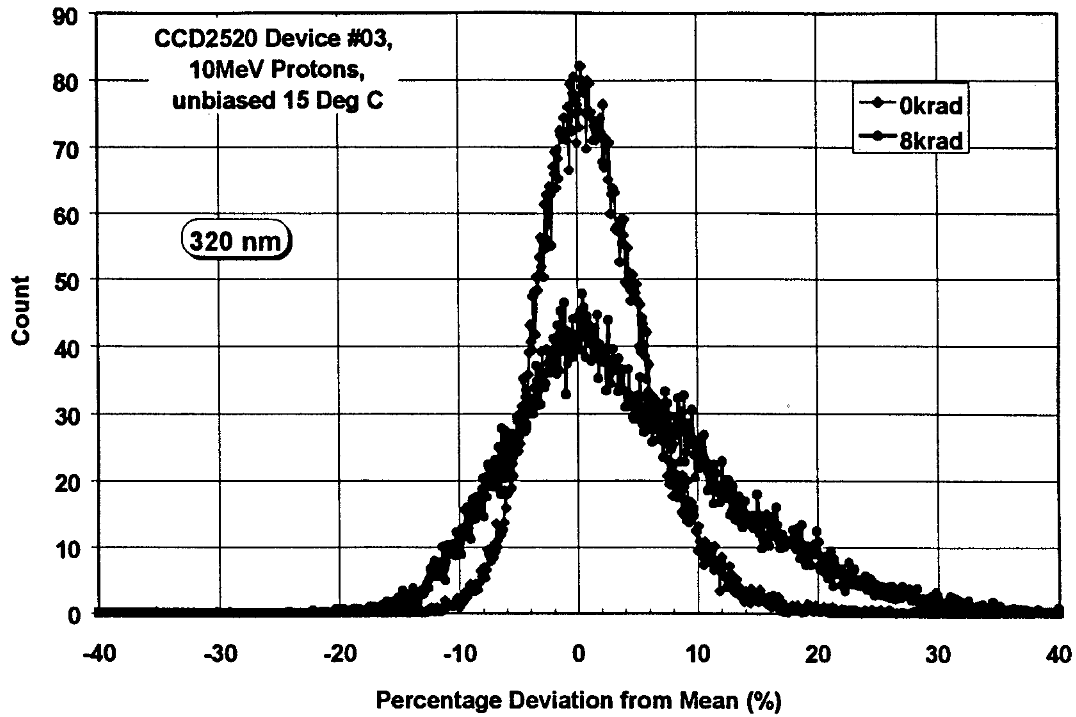

Figure 6-12 Bright field histograms for a CCD25-20 device at 320nm

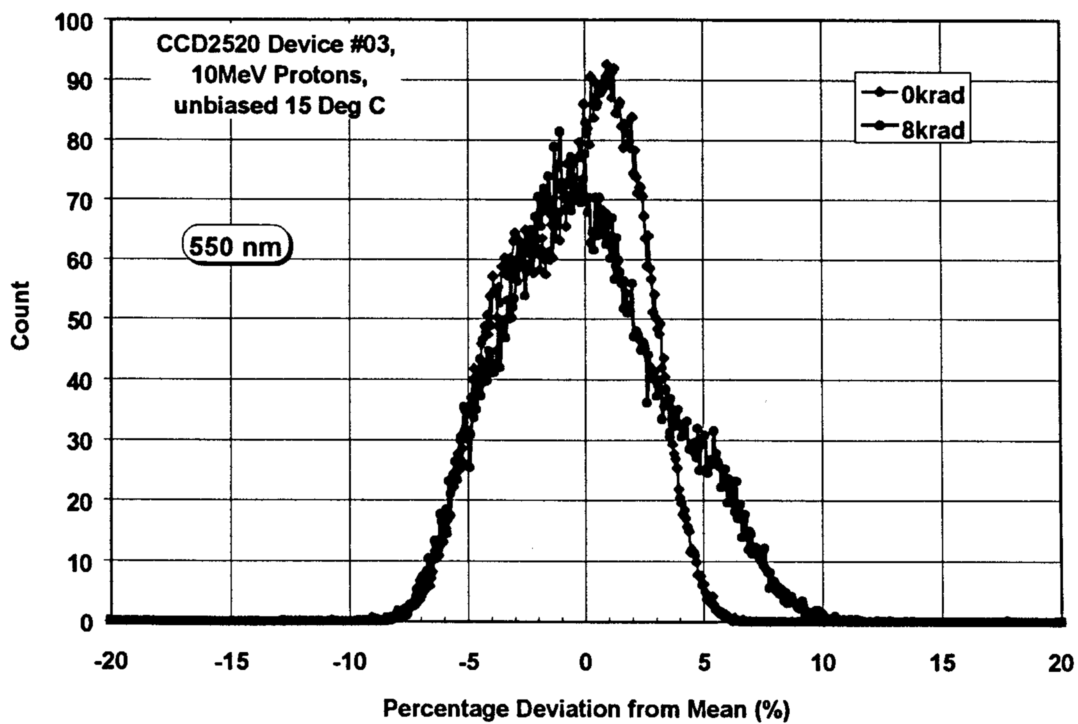

Figure 6-13 Bright field histograms for a CCD25-20 device at 550nm

Copyright © Sira Ltd 1995

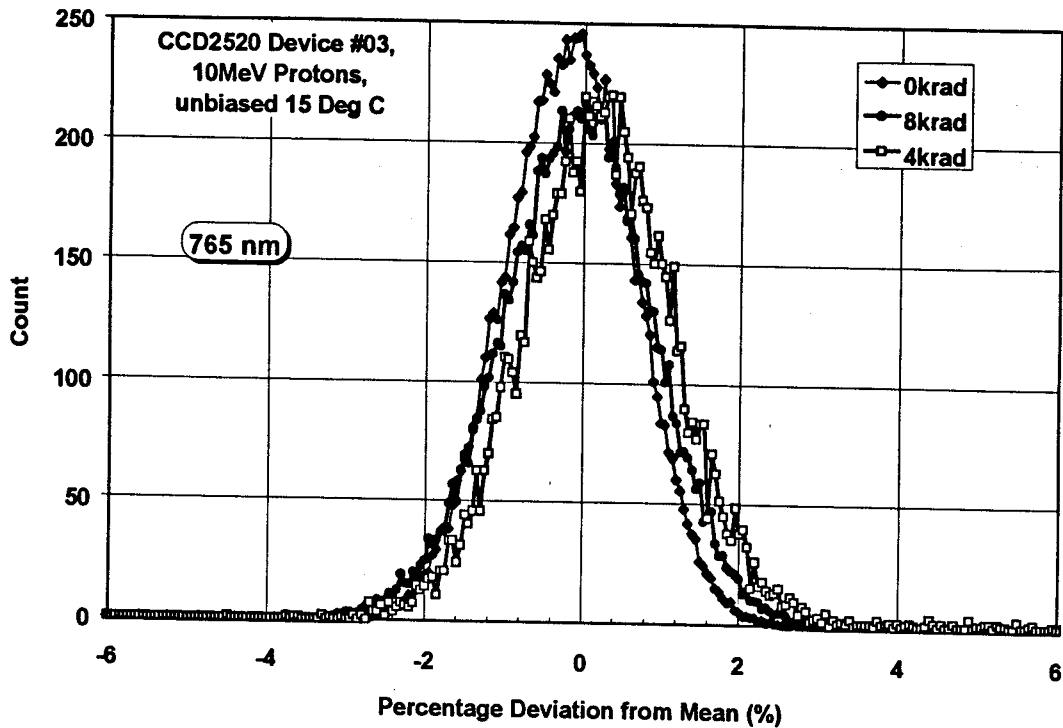

Figure 6-14 Bright field histograms for a CCD25-20 device at 765nm

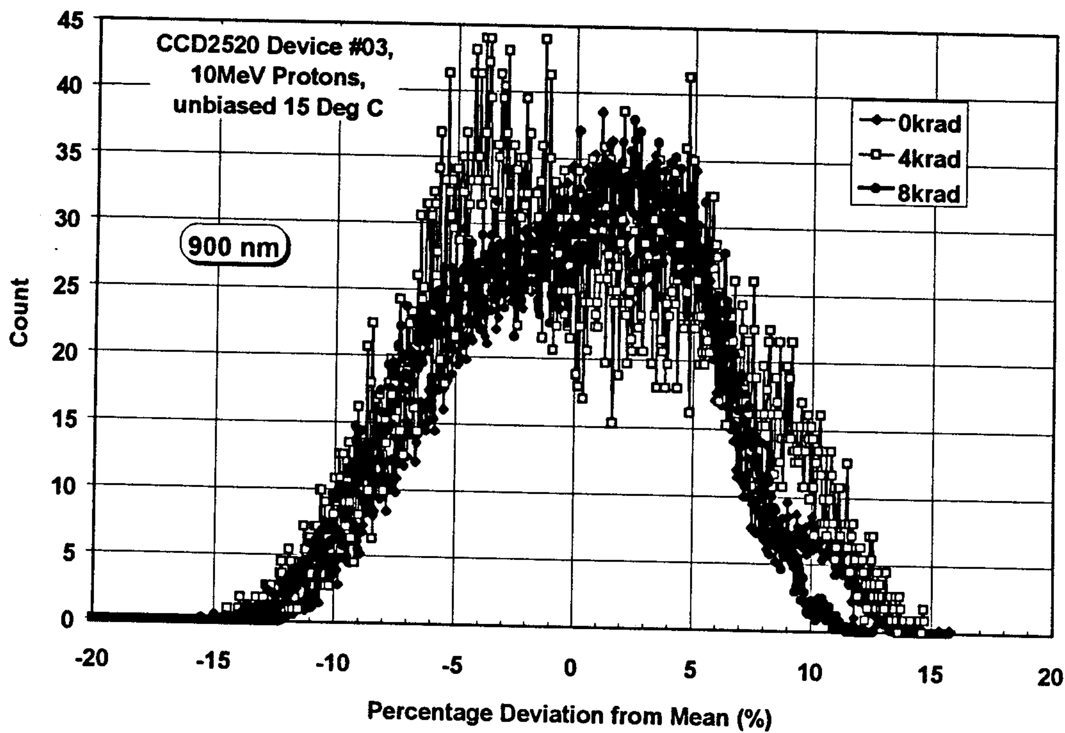

Figure 6-15 Bright field histograms for a CCD25-20 device at 900nm

Copyright © Sira Ltd 1995

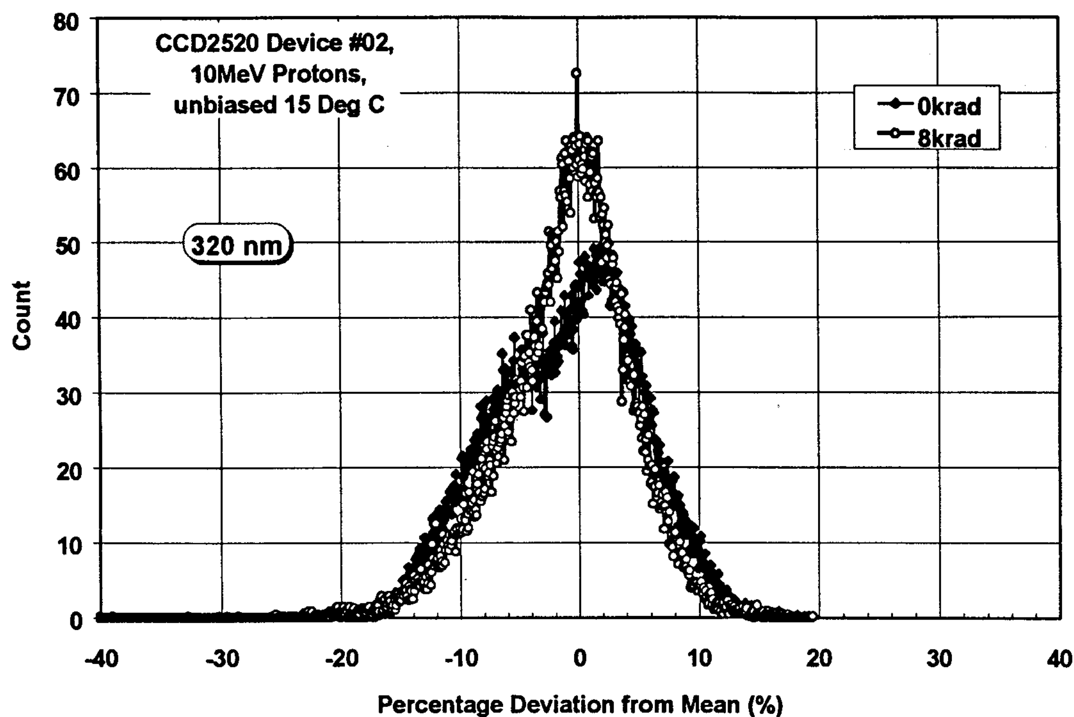

Figure 6-16 Bright field histograms for a CCD25-20 device at 320nm

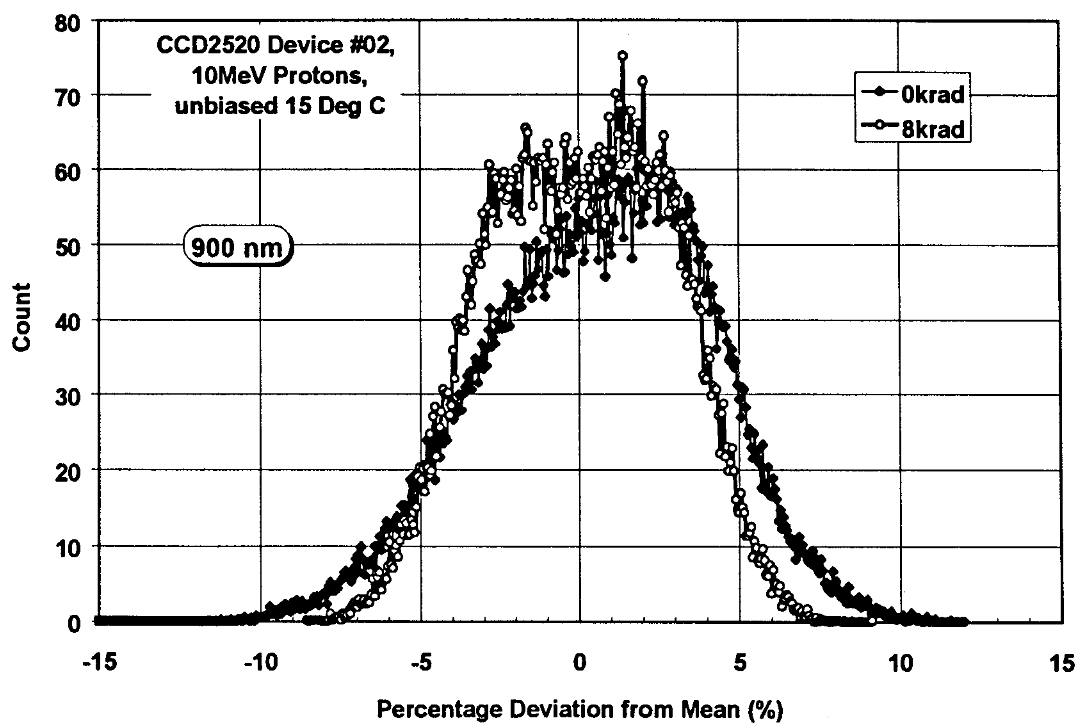

Figure 6-17 Bright field histograms for a CCD25-20 device at 900nm

Copyright © Sira Ltd 1995

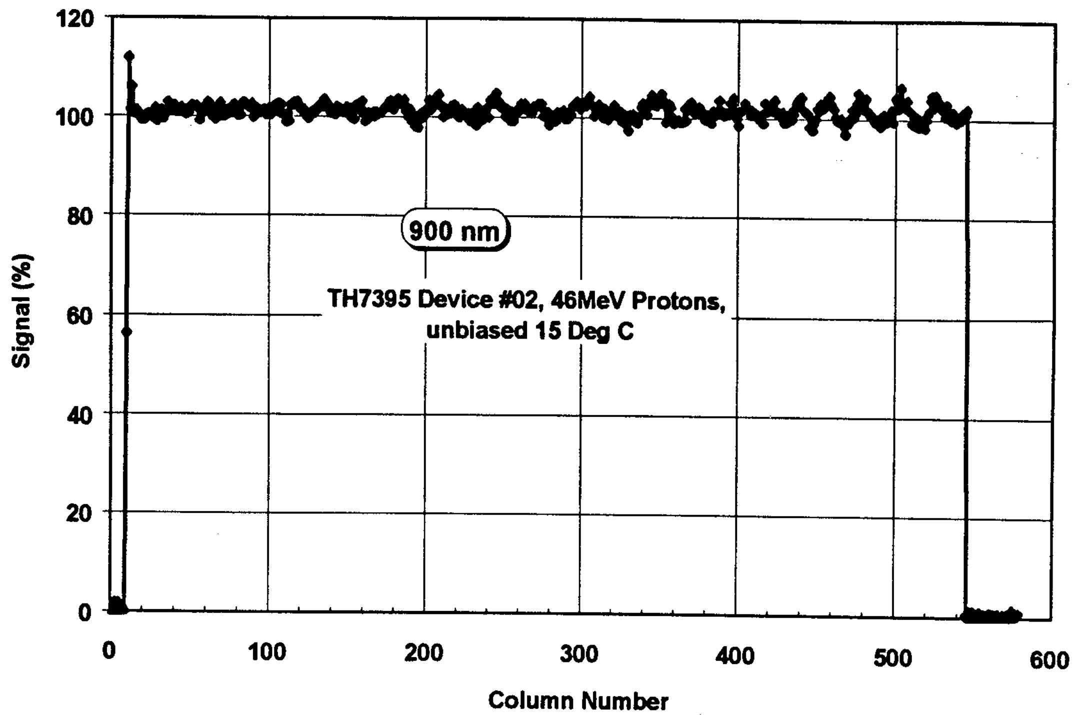

Figure 6-18 Image slice along the line direction for a TH7395 device at 900nm showing fringe patterns

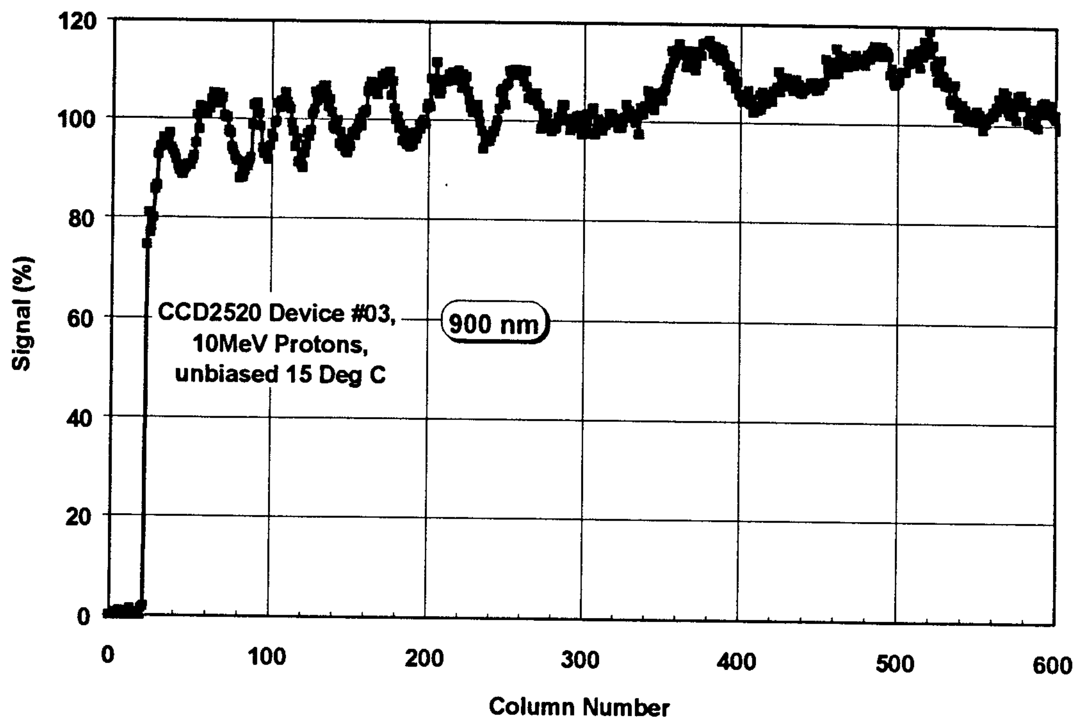

Figure 6-19 Image slice along the line direction for a CCD25-20 device at 900nm showing fringe patterns

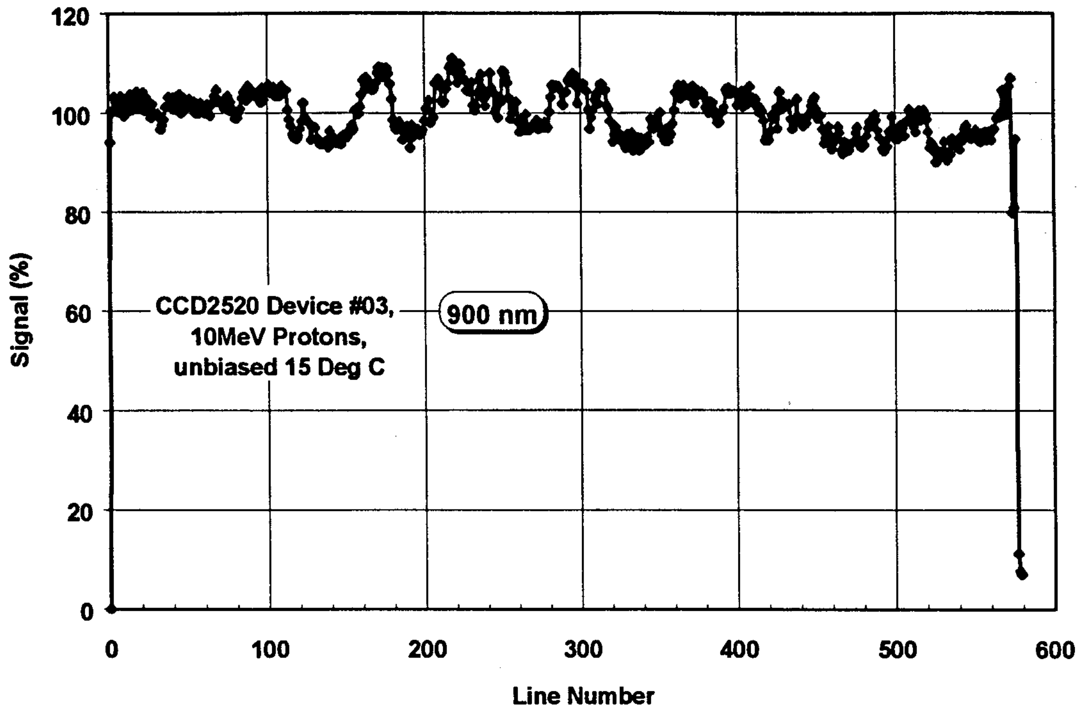

Figure 6-20 Image slice along the column direction for a CCD25-20 device at 900nm showing fringe patterns

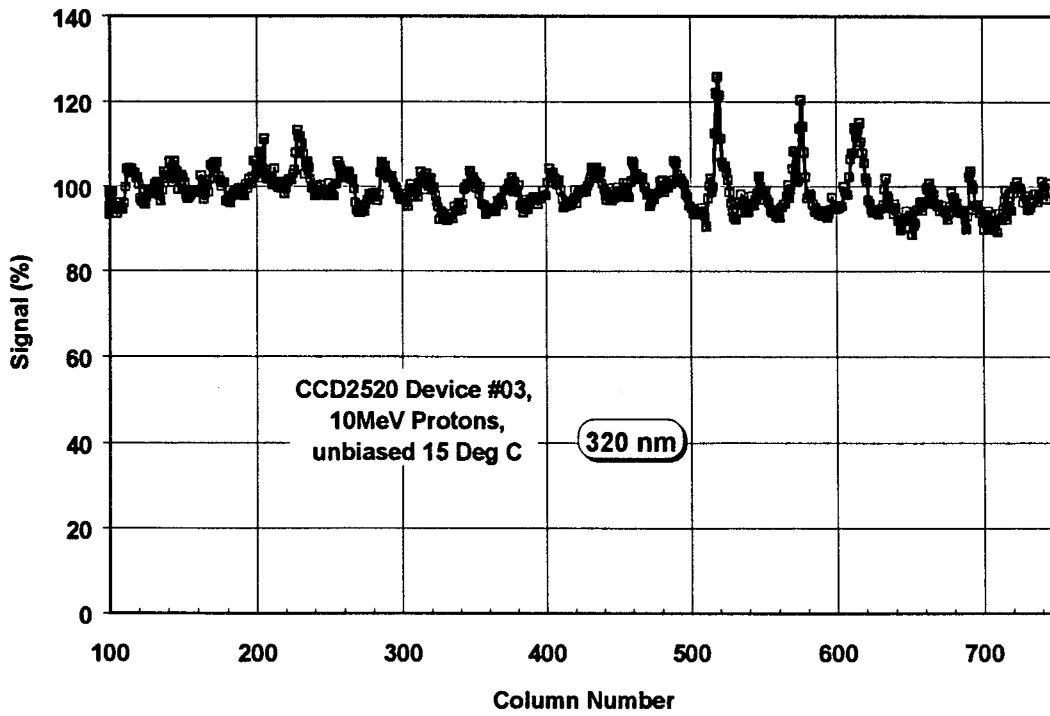

Figure 6-21 Image slice along the line direction for a CCD25-20 device at 320nm showing structure.

Copyright © Sira Ltd 1995

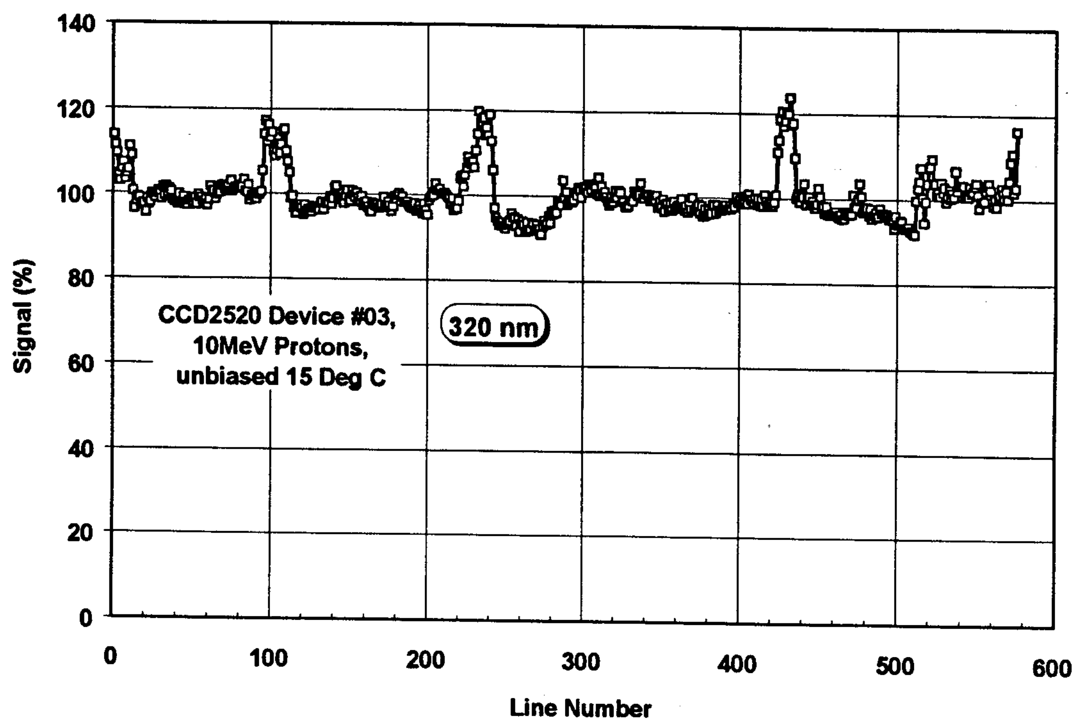

Figure 6-22 Image slice along the column direction for a CCD25-20 device at 320nm showing structure.

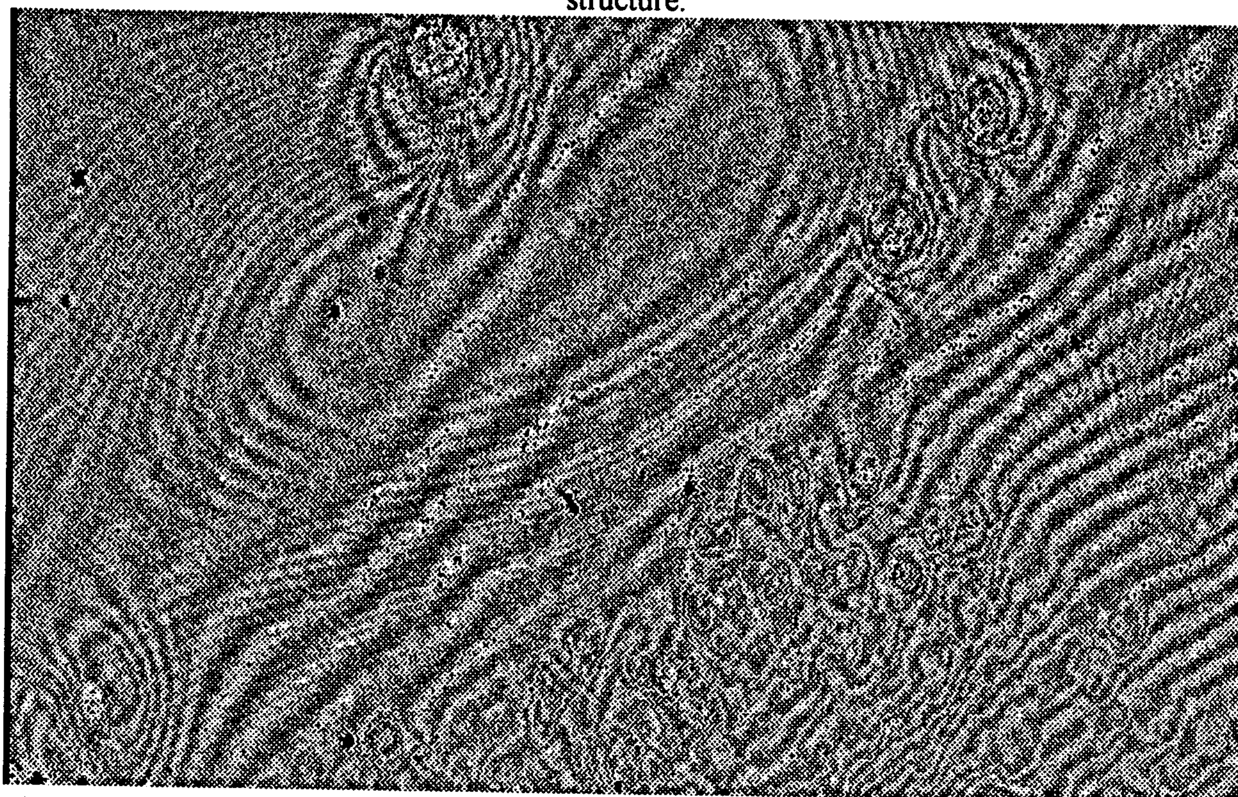

Figure 6-23 Bright field image at 900nm from a TH7395 device

Copyright © Sira Ltd 1995

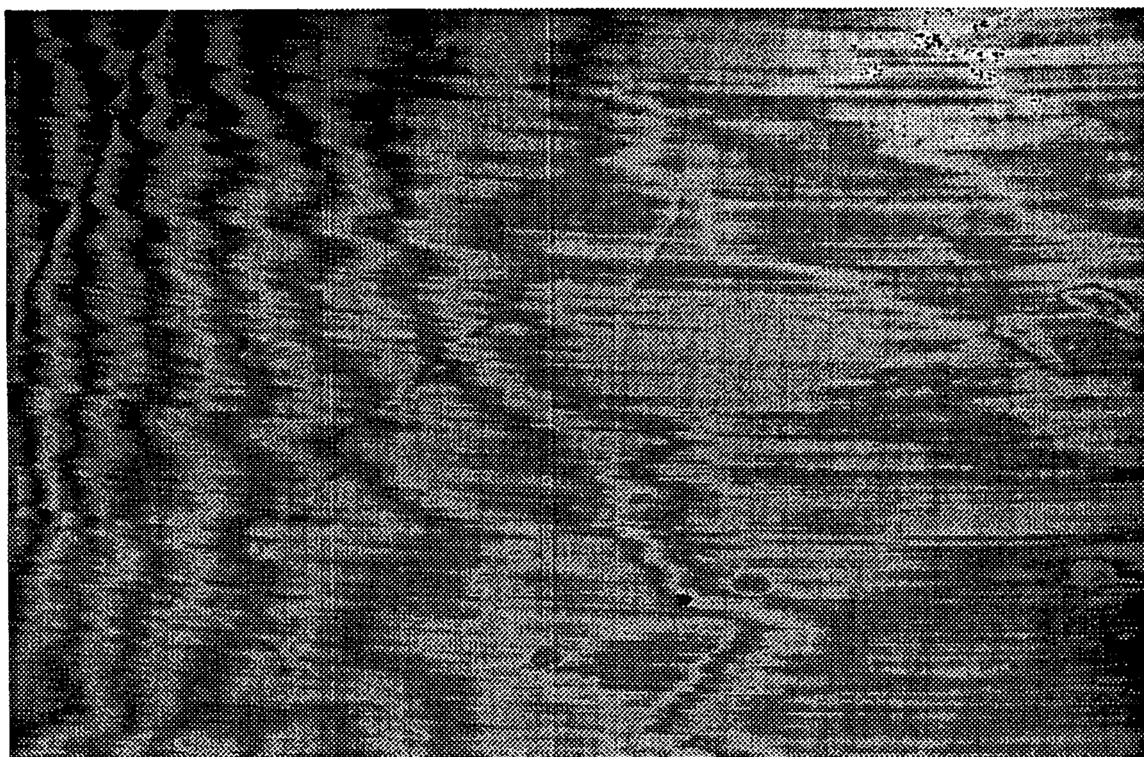

Figure 6-24 Bright field image at 900nm from a CCD25-20 device (#03)

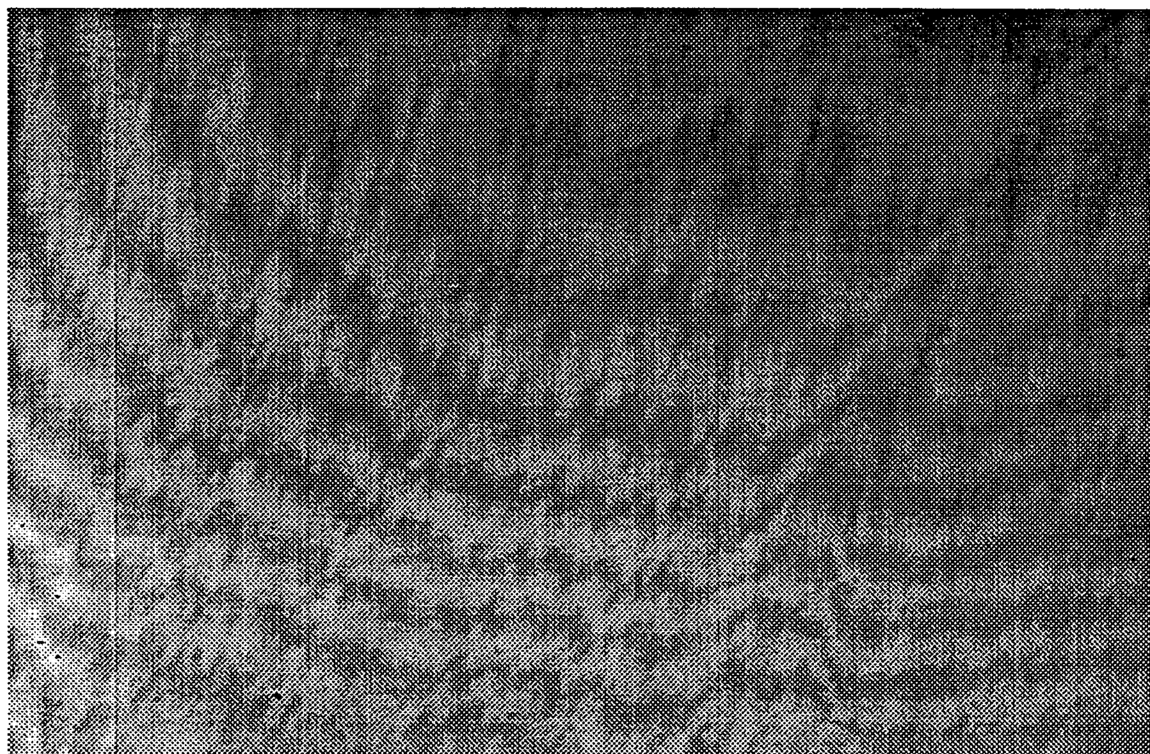

Figure 6-25 Bright field image at 900nm from a CCD25-20 device (#02)

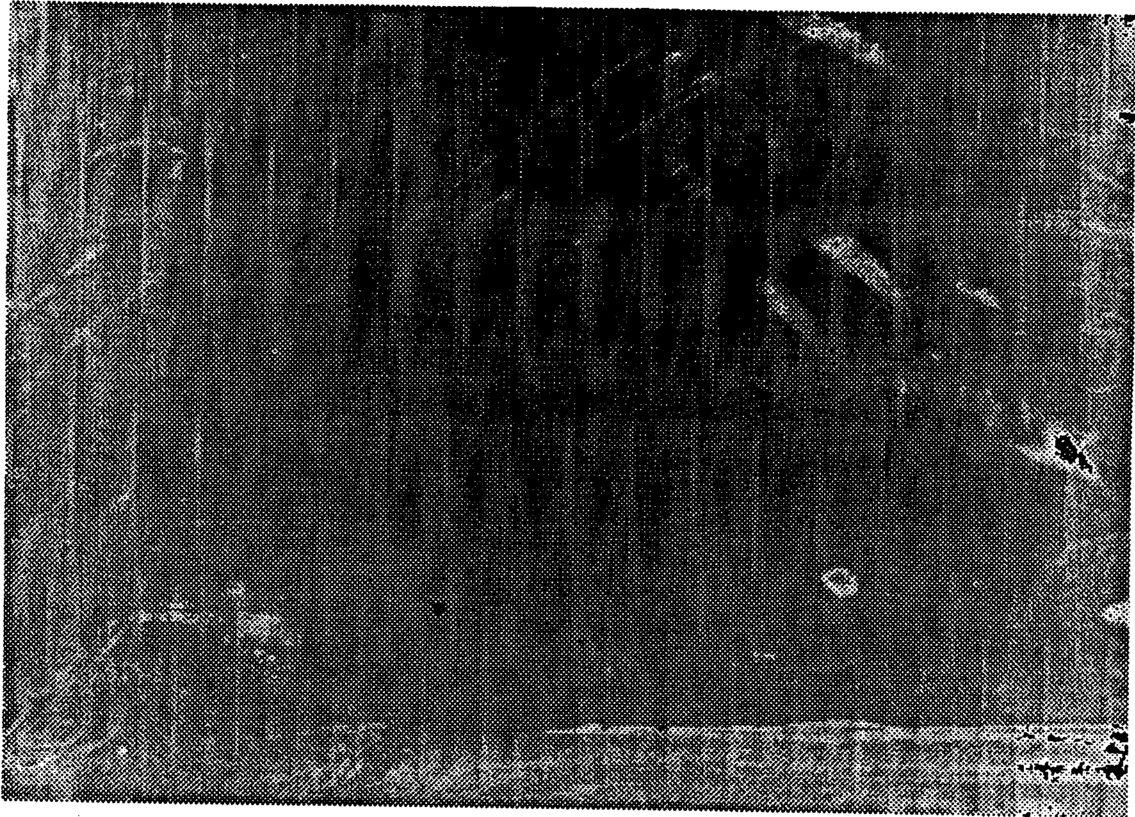

Figure 6-26 Bright field image at 320nm from a CCD25-20 device (#03)

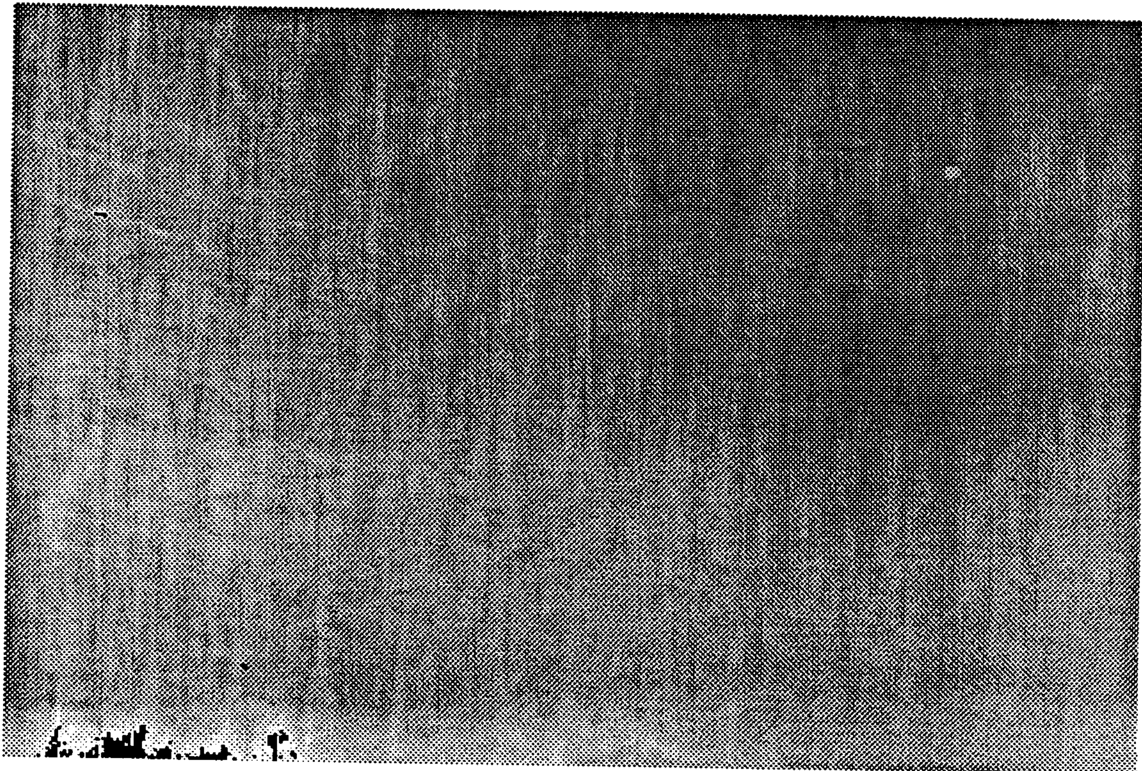

Figure 6-27 Bright field image at 320nm from a CCD25-20 device (#02)

Copyright © Sira Ltd 1995

7 CTE MEASUREMENTS

The Charge Transfer Efficiency (CTE) was studied in detail for an EEV CCD02 device previously irradiated. In particular the variation with signal size and background level were studied. Measurements were also made on an EEV CCD25-20 and a TH7895 CCD in order to confirm that the effects were similar for a given set of conditions.

In this section we will often refer to the Charge Transfer Inefficiency (= 1 - CTE).

An optical method employing spot illumination of the CCD was used. For comparable conditions (signal size, temperature and background signal), this gave comparable results to the x-ray method used in an earlier study on a CCD05 device (RD5).

7.1 MEASUREMENT METHOD

The optical set-up is shown in figure 7.1-1. Light from a Xenon arc passes through a green filter and is focused onto a fibre-optic cable. This routes the light to a 12.5μm pinhole, an image of which is projected onto the CCD by a x20 microscope objective. Green light (λ=540nm) was used so that most of the absorbtion occurred within the depletion layer, thus avoiding lateral diffusion of photo-generated charge (which takes place in field-free regions below the depletion layer).

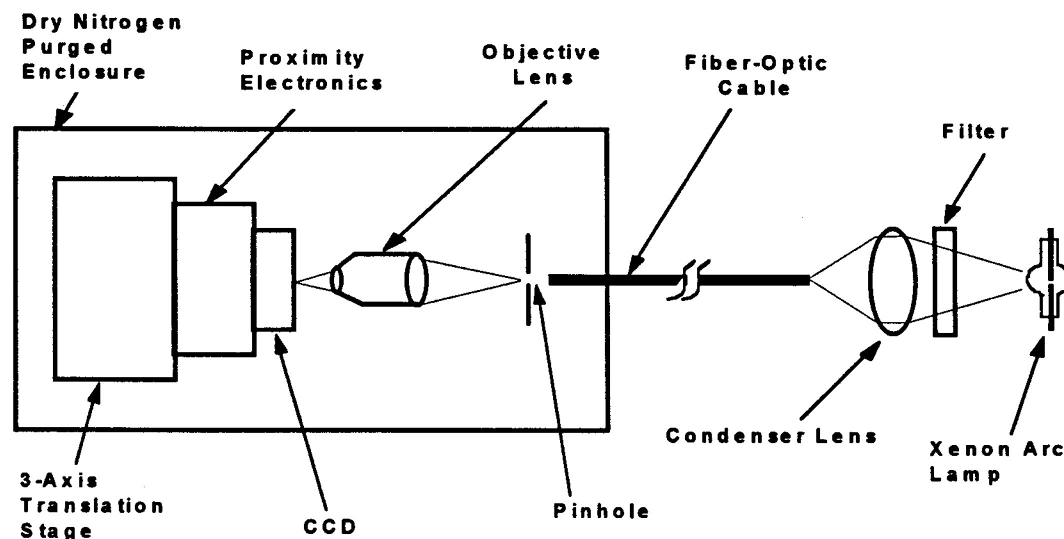

Fig. 7.1-1 Schematic diagram of the spot projection system.

The CCD, daughter board and Peltier cooler were mounted on a three-axis translation stage so as to remotely control the focus and position of the light spot. It was found that the spot could be projected and centred onto a pixel with less than 1% of the intensity blurred into adjacent pixels. This blurred charge acts as a small background signal but was not significant compared with the background levels used in this study (particularly as it is only present within a given pixel for one line move time - unlike dark current background which is always present). The signal amplitude of the spot was sensitive to its position relative to the electrode structure of the CCD. Some care was needed to avoid vibrations and so keep the amplitude constant. The optical bench (excluding the arc lamp) was placed inside a dark enclosure, purged with dry

Copyright © Sira Ltd 1995

nitrogen gas so as to allow the CCD to be operated at temperatures down to -25°C. Since microscope objectives can be obtained with long working distances (up to several cm) it would be possible, in an alternative arrangement, to illuminate the CCD through the window of a cryostat or other hermetic enclosure.

After integrating the signal from the spot illumination, the charge was frame-transferred into the CCD storage region, which was shielded from light. Further transfer regimes were then carried out within the storage region to measure the emission time constant of the dominant CTI defect and the effects on CTI of dose, temperature, signal size and clock waveform.

The parallel CTI was found by first clocking the charge in a backwards direction (away from the serial register) a total of 50 pixels, then changing direction and clocking 50 pixels back again. This movement takes a time T given by

$$T = 100 \times \text{line move time} \qquad (7\text{-}1)$$

and was performed a number of times so as to achieve a large number of transfers (and so improve the accuracy). The time between line moves could be varied and, for CTI measurements, it was always ensured that T was appreciably larger than the emission time constant - so that traps were empty by the time signal charge returned. Typical line move times were 2μs at around 15°C and 20μs at -15°C. The CTI was found from a plot of the fractional charge loss from the spot versus the number of pixel transfers (provided that the number of transfers was not so large that a linear relation was no longer obtained). A typical plot is shown in figure 7.1-2. Serial CTI was measured in a similar way, except that charge was first transferred into the serial register before charge shuffling. The serial transfer time was 1μs per pixel.

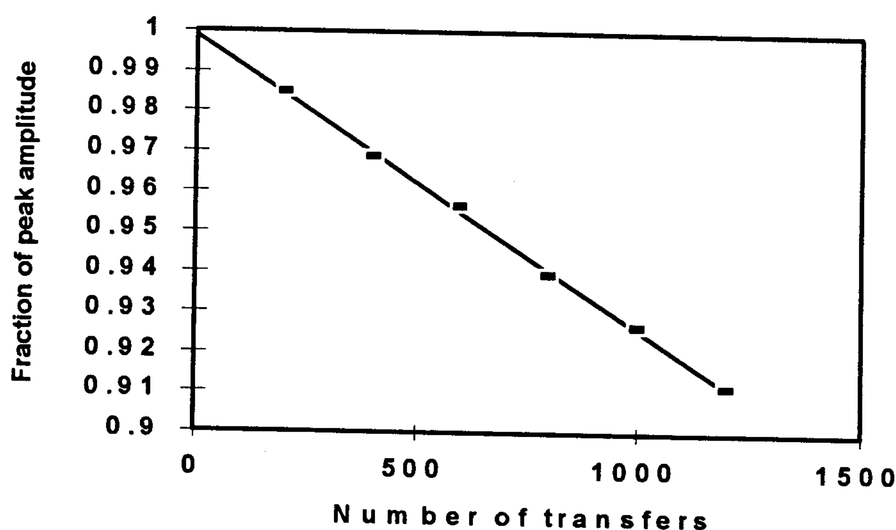

Fig 7.1-2. Typical plot of fractional charge loss versus number of pixel transfers, for spot illumination.

Background charge was provided by the dark current. Low backgrounds (down to 150 electrons/pixel at -20°C after 4krad of 10MeV protons) could be achieved using a combination of fast dumping of unwanted parts of the image (to reduce the integration time) and operation with surface inversion (by dither clocking or using MPP mode). Since the CCDs were proton

Copyright © Sira Ltd 1995

damaged, even with the suppression of the interface trap component, the bulk displacement dark current remains. However it will be seen that the CTI damage did not change appreciably for backgrounds below 500 electrons per pixel.

7.1.1 Theory

We assume that radiation-induced CTI in buried channel CCDs is caused by the trapping of signal charge at defect centres within the buried channel. Since the buried channel is within the depletion layer, the only important mechanisms are the capture of signal electrons from the conduction band to the trap level and their subsequent emission back to the conduction band. The time constants for these processes (τ_c and τ_e, respectively) are:

$$\tau_c = 1/\sigma_n v_{th} n_s \qquad (7\text{-}2)$$

$$\tau_e = \exp(E/kT)/\sigma_n X_n v_{th} N_c \chi \qquad (7\text{-}3)$$

where

- n_s = electron density within the buried channel
- σ_n = capture cross section for mobile electrons
- v_{th} = average thermal velocity for electrons
- N_c = effective density of states in the conduction band
- T = absolute temperature
- k = Boltzmann's constant
- X_n = the 'entropy factor' associated with the entropy change for electron emission from the trap
- χ = field enhancement factor
- E = energy level of the trap below the conduction band.

We have included a field enhancement factor, χ, in the expression for τ_e to allow for any enhanced emission due to the Poole-Frenkel effect or to phonon assisted tunneling, both of which occur in regions with an electric field greater than about 10^4 V/cm.

It can be seen that τ_C depends on the local charge density. It is useful to distinguish between signal charge which is only found in a few sparsely separated pixels (for example signals from x-ray events, spot illuminations or from the 'highlights' of an otherwise flat image) and background charge (from dark current or a slowly varying illumination) which is present in all pixels (and is present under a storage electrode for the majority of the time). The background charge acts so as to keep a proportion of the traps in the buried channel permanently filled. Figure 7.1-3 shows the structure of a typical CCD and the volumes occupied by a background and a signal charge packet. A consequence of the n-buried channel structure is that there is a minimum in the electrical potential (a potential well) located about 1μm below the silicon surface. At this location the signal density will have a maximum value. As a first approximation it can be assumed that the potential (and so n_s) does not change much in the lateral direction until we reach the pixel edges (defined by the channel stops and the electrodes). However the signal density decreases (and τ_C increases) rapidly for depths either side of the potential minimum

Copyright © Sira Ltd 1995

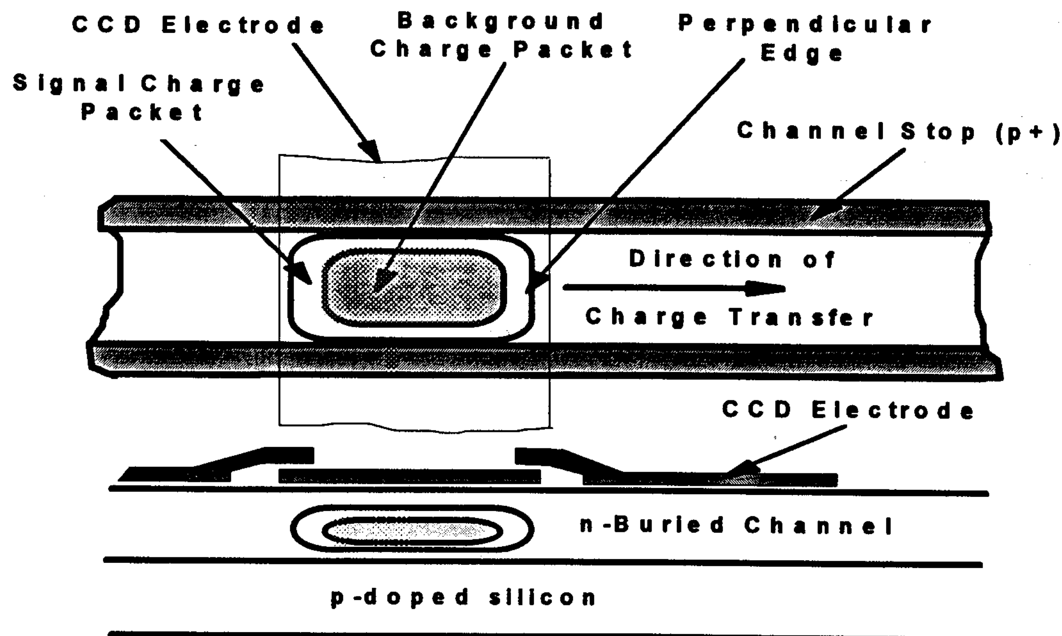

Fig. 7.1-3 Volumes occupied by a signal and a background charge packet in a buried channel CCD. Note that, in reality, the packets do not have hard edges.

First we calculate the signal charge which is trapped under an electrode. This will be zero when charge is first transferred in and will steadily increase thereafter. If n_t is the number of traps which are empty (out of a total N_t), then:

$$\frac{dn_t}{dt} = \frac{(N_t - n_t)}{\tau_c} - \frac{n_t}{\tau_e} \qquad (7\text{-}4)$$

The solution is:

$$n_t = n_\infty [1 - \exp(-t/\tau_c).\exp(-t/\tau_e)] \qquad (7\text{-}5)$$

where

$$n_\infty = N_t /(1 + \tau_c /\tau_e) \qquad (7\text{-}6)$$

A steady state is reached for dwell times, t, large compared with either τ_c or τ_e. In a region where the signal density is low, τ_c will be large, however the charge trapped will carry on increasing up until dwell times comparable with either τ_c or τ_e, whichever is the smaller. Background charge is effectively present within a pixel for the whole time it takes to transfer a frame. Hence charge can be trapped from an extended region of the buried channel where the capture time is particularly long (though the steady state fraction of traps filled will be small if τ_c is greater than τ_e). It will be seen that this gives an enhanced effectiveness in the filling of traps by background charge and so a reduction in CTI.

7.2 RESULTS FOR CCD02 DEVICES

In this section we discuss results for 385 (horizontal) x 288 (vertical) devices. These are manufactured using the same technology and approximately the same pixel size (22 μm x 22 μm rather than 22.5 μm x 22.5 μm) as the MERIS CCD25-20 devices . Hence the results should be fully representative of effects for the MERIS (and the GOMOS DMSA/B) CCDs. This is borne out by measurements on CCD25-20 devices in paragraph 7.3.

Copyright © Sira Ltd 1995

7.2.1. Measurements of Emission Time Constant

Because of the exponential dependence of τ_e on energy level in equation (7-2) and the possibility that capture cross sections may be temperature dependent, there can be large errors in extrapolating low temperature measurements to the range of interest here (-30°C to 30°C). Hence a first step was to measure τ_e for room temperature conditions. This was done by repeatedly transferring the spot into an adjacent pixel, holding it there for a delay time Δt and then moving it back again (and waiting for Δt). For delay times comparable to, or less than, τ_e the trapped charge will not be fully emitted by the time the signal packet returns. When a steady state is reached under these conditions, all the traps within a pixel, less those which emit in a time Δt, will be filled. This charge will then be the amount lost from the spot. Before the steady state is reached, a smaller charge will be trapped (because some of the traps will be located in regions where the charge density is low and the capture time long). However since some of this charge remains trapped after Δt, the trap occupancy gradually increases until the steady state is reached. If the spot signal is $S(\Delta t)$ (S_0 without the extra transfers before readout) then:

$$S(\Delta t) = S_0 - N_t \exp(-\Delta t/\tau_e) \qquad (7\text{-}7)$$

Note that this is not the situation described by equation (7-4) (which will be used in the next section) since that applies to the case where $\Delta t >> \tau_e$. Now if the steady state charge lost is plotted logarithmically against delay time, τ_e can be found from the slope of the resulting straight line. A typical plot is shown in figure 7.2-1. The emission time constant was measured for a range of temperatures between -20 and 20°C at high signal level (100,000 electrons) and backgrounds ~10,000 electrons, with the following results:

Temp. (°C)	20	7	-5	-20
τ_e (μs)	22	64.5	120	430

Figure 7.2-2 shows these values plotted against 1000/T. The T^2 term in the ordinate follows from the temperature dependence of $v_{th}N_c$ (= $4.11 \times 10^{25} (T/77)^2$ cm^{-2} s^{-1}).

The slope of the line yields an energy level of 0.416 ± 0.029 eV. The intercept, together with equation (7-2), $X_n = 1.7$ and $\chi = 1$, gives a capture cross section (σ_n) of order 10^{-15} cm^2. These values are consistent with the dominant trap defect being the phosphorus-vacancy (Si-E) centre. An accurate determination of σ_n cannot be made because of the sensitivity to the assumed value of the trap energy level. Choosing the generally accepted value for the P-V center (=0.44eV) gives a σ_n of 1.5×10^{-15} cm^2. The measurements were made for pixels in both parallel and serial registers with similar results.

Note that the values of τ_e given above may be underestimated by as much as 10-20%. This is because equation (7-7) is an approximation. In fact it was found that in going to the lower temperatures (and longer delay times) the total trapped charge (which we assumed to be constant at N_t) increased by a factor ~1.5. This is probably because the long delay time allows capture by a larger volume of silicon. It is therefore possible that the longer times used in each τ_e measurement also give higher charge loss.

Copyright © Sira Ltd 1995

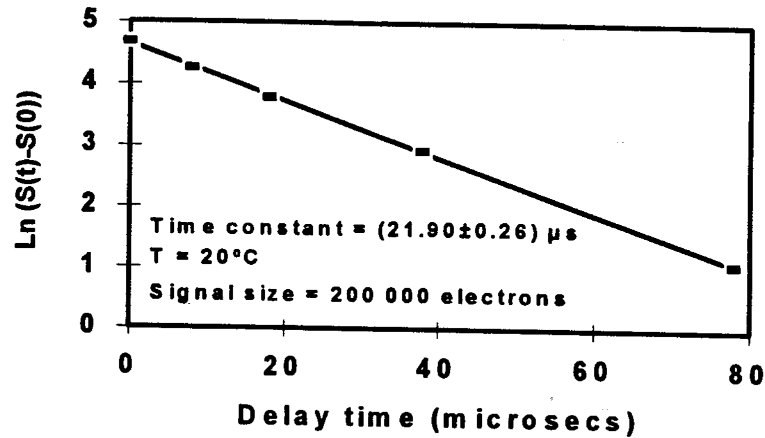

Fig. 7.2-1 The trap emission time constant is derived from plots of spot amplitude versus delay time between line moves.

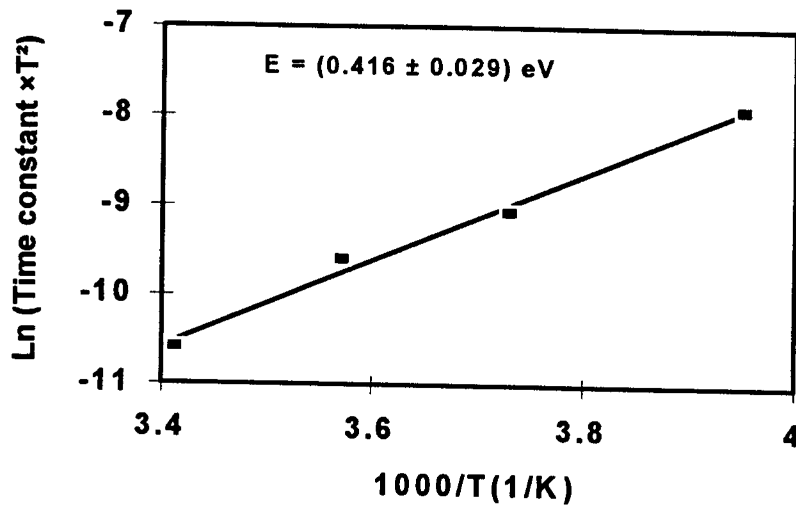

Fig. 7.2-2 Plots of $\ln(\tau_e.T^2)$ versus inverse temperature yield the energy level of the dominant trap.

This will tend to give a higher gradient in plots such as figure 7.2-1 and so an underestimated τ_e. However allowing a factor 1.5 change in the total trapped charge only results in a 10% change in τ_e. Measurements of charge deferred into trailing pixels are consistent with the above values for τ_e..

7.2.2. Effect of Signal Size and Background on CTI

CTI measurements were made after 4krad 10 MeV protons using the method described above for a variety of dark charge backgrounds and signal sizes (these could be varied separately by changing the integration time and the spot brightness). Parallel CTI was measured for a range of signals from close to full well capacity (~3. 10^5 electrons) down to a few hundred electrons. The errors were larger for small signal sizes but were acceptable for cases where the noise on the background was low.

Copyright © Sira Ltd 1995

The presence of a dark charge background radically affects the CTI behavior. The change in CTI with signal size, for three levels of background charge is given in figure 7.2-3, and CTI for different backgrounds at two signal sizes is shown in figure 7.2-4. It was found that for backgrounds of 500 electrons or less (the lowest value used being 150 electrons) the CTI values lay on a single curve which was a strong function of signal size, but that for backgrounds of 16,000 electrons or higher the CTI was roughly 0.00008 per pixel transfer, independent of signal size.

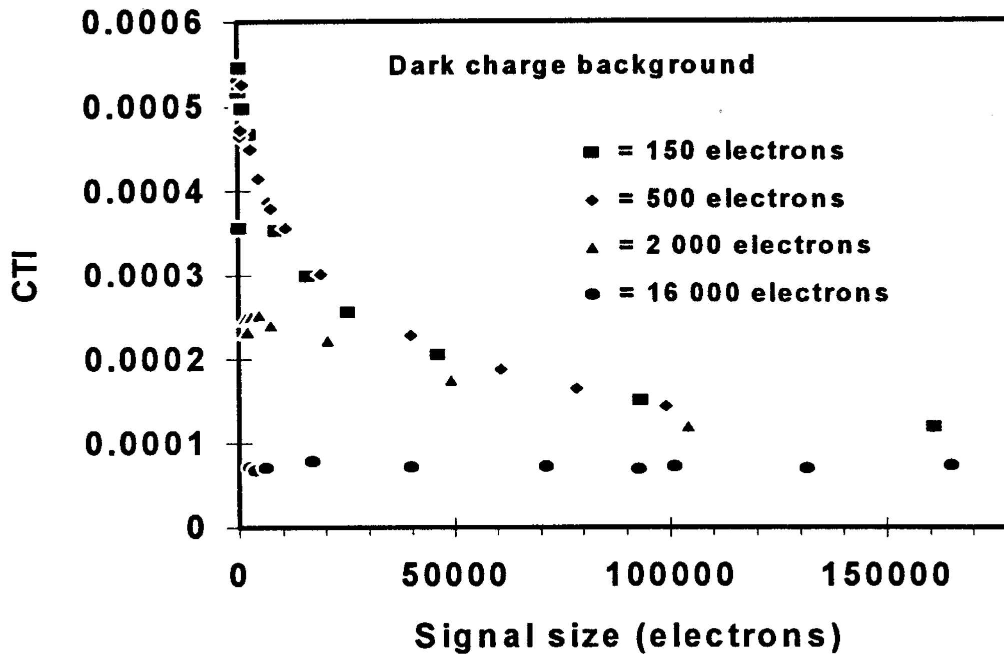

Fig. 7.2-3 CTI after 4krad 10 MeV protons for various signal sizes and backgrounds. The dwell time per phase was 2/3μs.

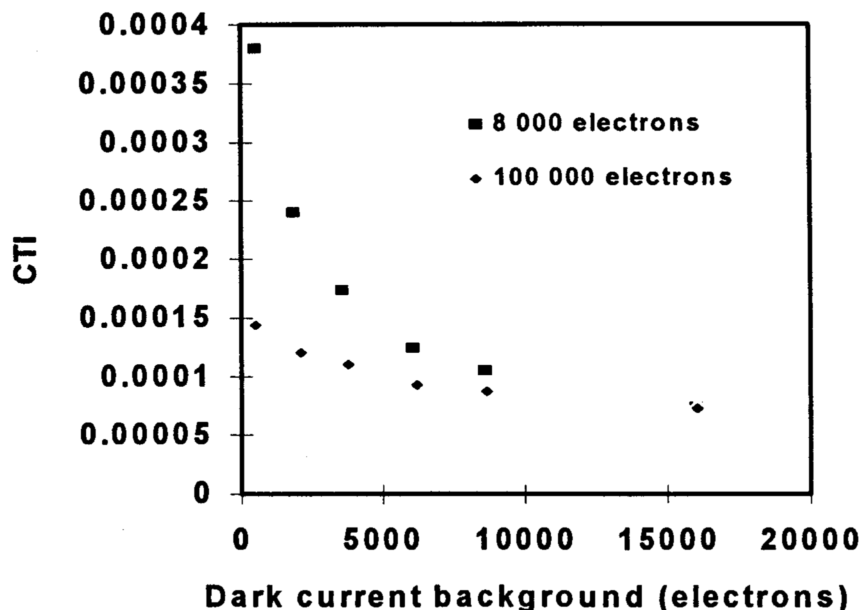

Fig. 7.2-4 As figure 7.2-3, but showing CTI as a function of background at two signal sizes..

Copyright © Sira Ltd 1995

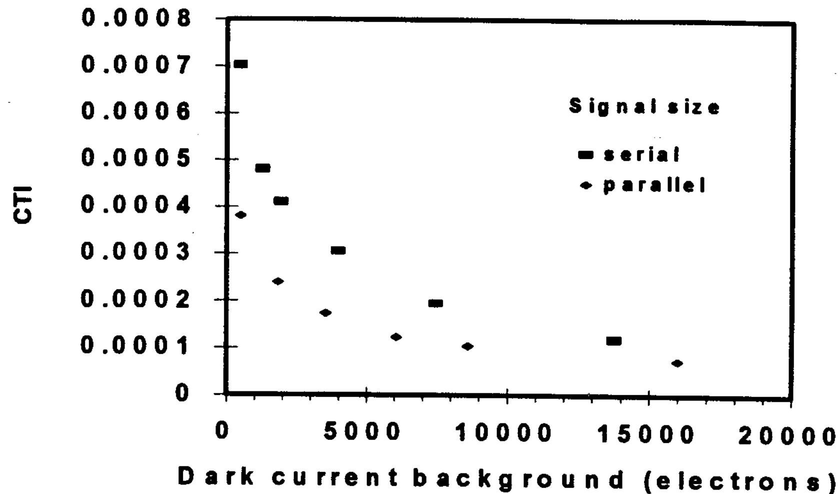

Fig. 7.2-5 Serial and parallel CTI for the same device

Measurements of serial CTI were also made. These are compared with parallel CTI in figure 7.2-5. The results converge for high backgrounds, but for low levels the serial CTI is about twice as large as the parallel. This may be related to the fact that, in these devices, the pixels in the serial register have twice the area of those in the image or storage regions.

The charge loss (= CTI x signal size) as a function of signal size is given in figure 7.2-6. This charge loss corresponds to those traps seen by the signal which have not been filled by the background charge. Assuming that the traps are evenly distributed, the charge loss corresponds to an extra effective volume occupied by the signal above that taken up by the background. It should therefore be possible to calculate the charge loss, Δq, for a given signal size and background from the curve for charge loss at low background. An analytical function of the form

$$\Delta q(S) = 6.6\mathrm{x}10^{-5}\,S + 8.5\mathrm{x}\{1 - \exp(-3.15\mathrm{x}10^{-5}\,S)\} \qquad (7\text{-}8)$$

was fitted to the lowest background (150 electron) CTI data set shown in figure 7.2-6. It might be expected that the charge lost for any signal (S) and background (B) would be:

$$\Delta q(S,B) = \Delta q(S + B) - \Delta q(B) \qquad (7\text{-}9)$$

However this was found to give a poor fit to the data. A much better fit (shown in figure 7.2-6 - and also fitting the data of figure 7.2-4) assumed that the background was *more effective* in filling traps than the signal - in fact by a factor 5, so that:

$$\Delta q(S,B) = \Delta q(S + 5\mathrm{x}B) - \Delta q(5\mathrm{x}B) \qquad (7\text{-}10)$$

Thus, even a small background level can dramatically reduce the CTI.

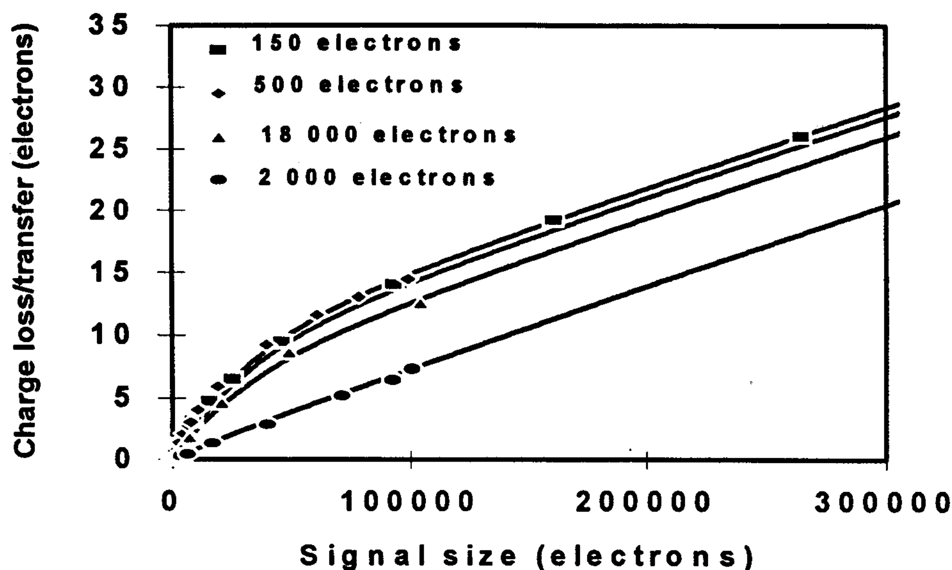

Fig. 7.2-6 Charge loss (derived from Fig. 7.2-3) versus signal size for four values of background charge. The theoretical fit assumes that background charge is 5 times more effective in filling traps than signal.

7.2.3. Effect of Line Move Rate on the Trapped Charge

It has not been possible to calculate an accurate charge density distribution, but figure 7.2-7, which is based on Gaussian profiles and typical values for the peak density can be used as an illustration of roughly how the signal density varies with depth (we take it as uniform in the lateral dimensions). From these distributions the capture time can be calculated as a function of depth from equation (7-2). This can then be substituted in equation (7-5) to give the percentage of traps filled (versus depth) for a given dwell time under an electrode (the line move time being 3 times this for a 3-phase CCD). Figure 7.2-8 shows the trap occupancy for dwell times of - typical of those used for signal transfer in this study, and for a much longer dwell time of - typical of that expected for the background. The curves are for the same total charge (electrons). Clearly the background fills more traps in total than the same sized signal packet and this agrees qualitatively with the results of the previous section. Using Gaussian density profiles does not however lead to a close fit to the data - the best fit we have obtained corresponds to the empirical relation given in equation (7-10). It should be borne in mind that the lateral charge distribution will play a part and there will also be charge trapping in the perpendicular edges of the charge packet (figure 7.1-3). Hence a detailed model will require a three dimensional simulation of the charge distribution within the buried channel.

Copyright © Sira Ltd 1995

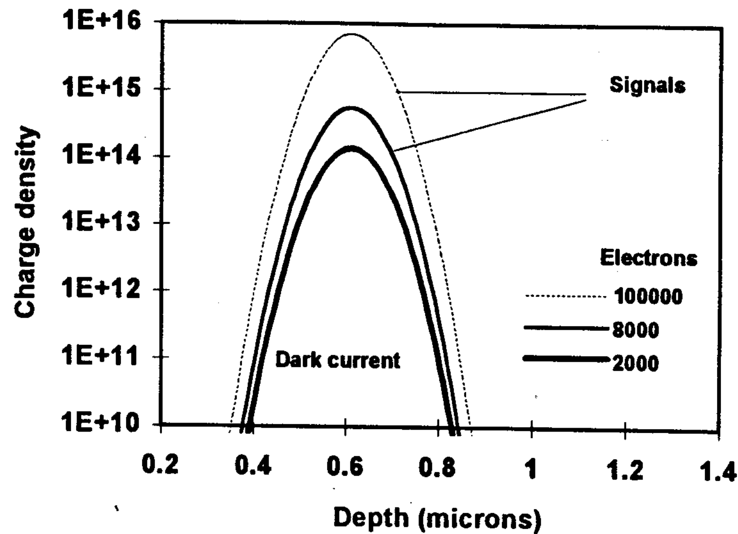

Fig. 7.2-7 Approximations to signal density distributions for different signal sizes.

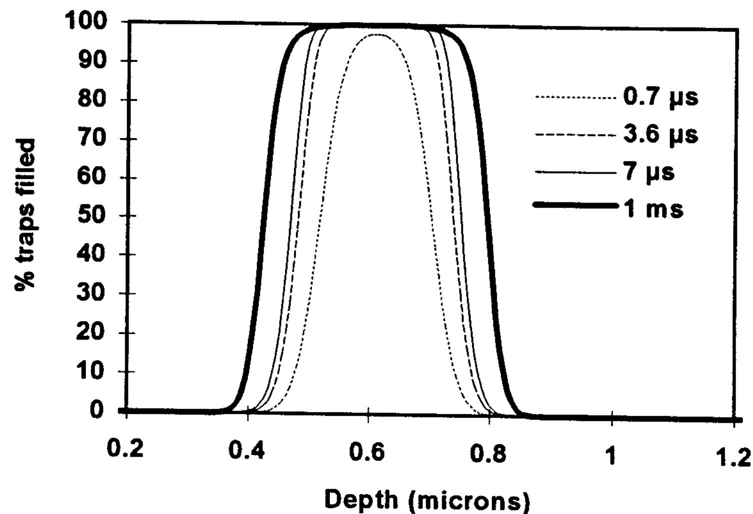

Fig. 7.2-8 Trap occupancy versus depth in the buried channel for different pixel dwell times.

Measurements were also made of CTI for different signal dwell times, and results are shown in figure 7.2-9. It is seen that CTI does degrade as the dwell time increases, indicating that charge is indeed being trapped in a greater volume of silicon. The simple model illustrated in figures 7.2-7 and 7.2-8 predicts that the CTI saturates (i.e. ceases to increase) for dwell times greater than τ_c. Unfortunately the experimental conditions cannot easily cover this region because long dwell times inevitably result in high dark charge backgrounds - using lower temperatures merely increases τ_c so that even longer dwell times are needed. However the results of figure 7.2-9 are important in that they imply that dwell times of several hundred microseconds (a typical line move time during readout at 1µs/pixel) gives a CTI increased by a factor 2 compared with line rates of a few µs (typical of frame transfer or fast line dump rates).

Copyright © Sira Ltd 1995

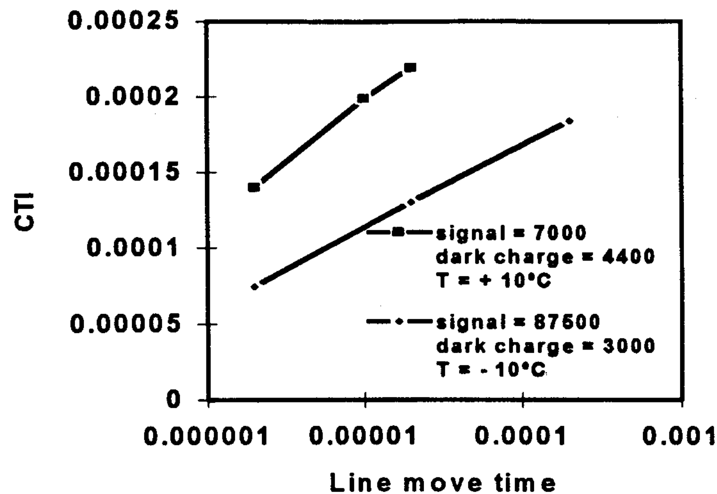

Fig. 7.2-9 CTI versus dwell time under an electrode, for constant signal size and background.

7.2.4. CTI Versus Proton Fluence (or Total Dose)

Figure 7.2-10 shows CTI versus dose (in krad(Si) - 1 krad being equivalent to $1.8x10^9$ 10MeV protons/cm^2). This data was obtained from different fluence regions (obtained by masking during irradiation) on each of two CCDs. High signal levels (~10^5 electrons) were used so that the results were not sensitive to background dark charge (which otherwise would give a reduced CTI for the higher fluence regions). Similar results were obtained in all cases and a damage factor (change in CTI per pixel transfer, divided by 10MeV proton fluence) of $1.1x10^{-14}$ cm^2 can be derived.

X-ray measurements using a Cd^{109} radioactive source are given in figure 7.2-11 for the same CCDs. These correspond to signal sizes of ~6000 electrons, but high backgrounds were used so as to minimize the effects of background variation (c.f. figure 7.2-3). Such backgrounds should give the same CTI as for the optical measurements (figure 7.2-11), if it were not for the fact that the x-ray results were obtained with frame transfer operation (and line moves every 400μs during readout) in contrast to the optical results for line moves every 2μs. It is seen from figure 7.2-10 that these differences can cause a factor ~2 change in CTI. It is unfortunate that, due to experimental constraints, the two methods cannot be compared for exactly the same conditions; however if the differences are allowed for then the errors in either approach appear to be less than 30%. If the differences in readout and background are taken into account, the present x-ray measurements give a damage factor very similar to the value $3.4x10^{-14}$ cm^2 found in the previous study [RD5].

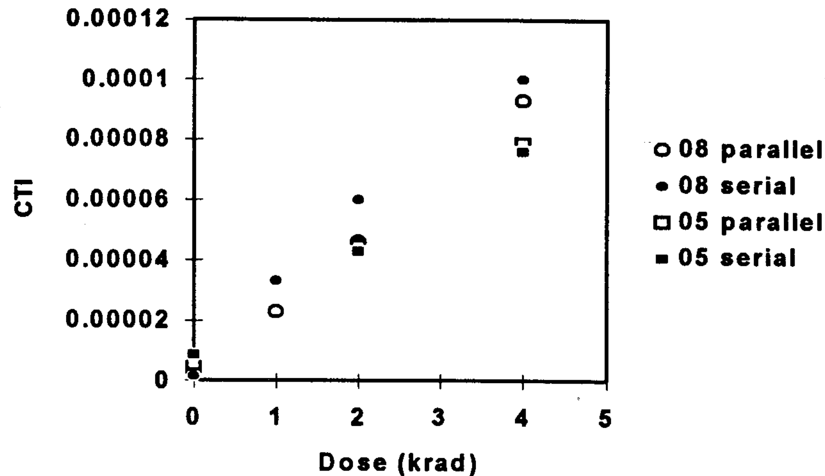

Fig. 7.2-10 Serial and parallel CTI versus dose for high signals.

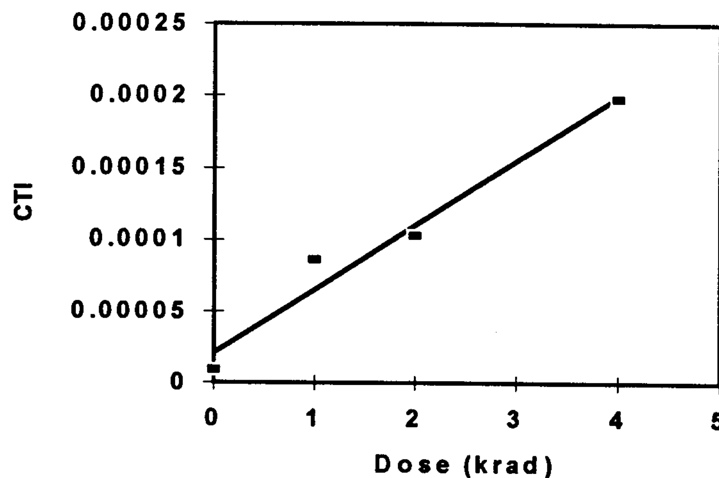

Fig. 7.2-11 X-ray results for CTI at high backgrounds.

7.2.4. Change in CTI With Clock Waveform

Though not the main object of this study, the effect of varying the clock voltages and the overlaps between clock phases was briefly investigated. It was found that clock voltage swing had little effect for serial or parallel transfers and that clock overlap had none for parallel transfers. However, for serial clocking, low CTI was only obtained if clock phases 1 and 2, and 3 and 1 were overlapped (the overlap between 2 and 3 not being significant). However this seems to be an effect more related to the dynamics of charge flow than to radiation damage (since the effect of proton bombardment appears to be to add a roughly constant CTI component to all the pre-irradiation measurements).

Copyright © Sira Ltd 1995

7.3 RESULTS FOR CCD25-20 AND TH7895M DEVICES

Figure 7.3-1 shows parallel CTI versus total dose (of 10 MeV protons, 1 krad being equivalent to 1.79E9 p/cm^2) for CCD25-20 device #03. The data was obtained for a signal size of 3.1 x 10^4 electrons and for moderate background (90-900 electrons), the temperature was -20°C.

The CTI (i.e. the fractional charge loss per pixel transfer) after 4 krad of 10 MeV protons is ~1 E-4. For the CCD02 devices studied in the previous section (figure 7.2-3 and figure 6 of paper RD6) for the same signal and background the CTI is ~2E-4, in fairly good agreement, though it is interesting that the CTI is lower.

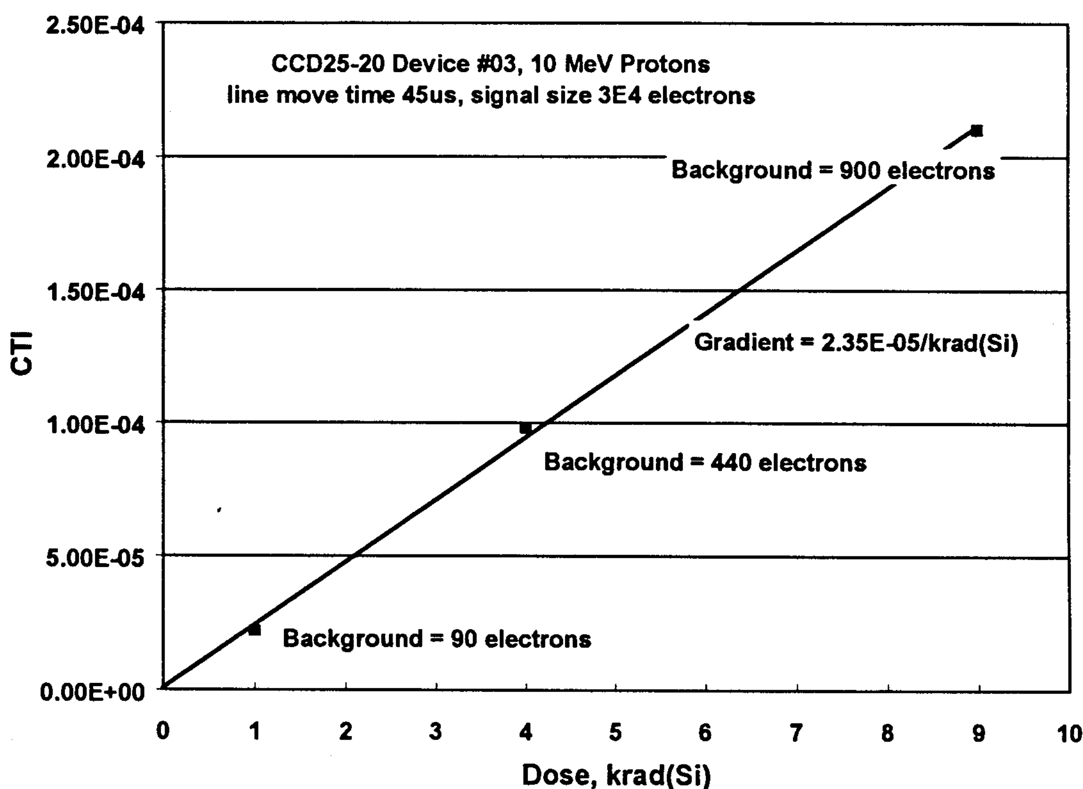

Figure 7.3-1 CTI versus total dose (10 MeV protons) for a CCD25-20

As a check on the above results, CCD25-20 #03 was operated in a representative MERIS mode with appropriate binning and charge dumping. A spot of light was imaged onto the 8 krad region of the CCD so that it fell on one of the readout bands (with x2 binning). The spot amplitude was as large as possible whilst keeping within the full well capacity. In this situation the deferred charge was as large as could be achieved. The CCD temperature was -20°C. A vertical slice down the image is shown in figure 7.3-1a. This shows the spot illumination and the positions of the pixels which are binned and readout (microbands) and the pixels which are dumped. For the lines readout before the spot, there is no deferred charge. For lines readout after, there is additional charge in the microbands for pixels in the same column as the spot due to degraded CTE. Note that the data in the figure is affected by readout noise, by averaging over all available pixels the results can be improved. After averaging it was found that the deferred charge per binned pixel was 15 ADC units, and the deferred charge divided by the

Copyright © Sira Ltd 1995

signal amplitude was 0.000667. Hence, allowing for the binning, the 8krad level and the fact the charge is being lost during both frame transfer and readout, we should divide this number by 8 so as to get a CTI per pixel transfer of 8.33E-05 for 4 krad 10MeV protons. This agrees very well with the above results. Though, in view of the differences between the CCD02 and CCD25-20 devices and the errors involved in comparing results for different background, signal and clocking conditions, it should not be expected that effects can be predicted to better than a factor ~2.

Note that no other effects were seen, indicating that the charge binning and dumping were working as expected.

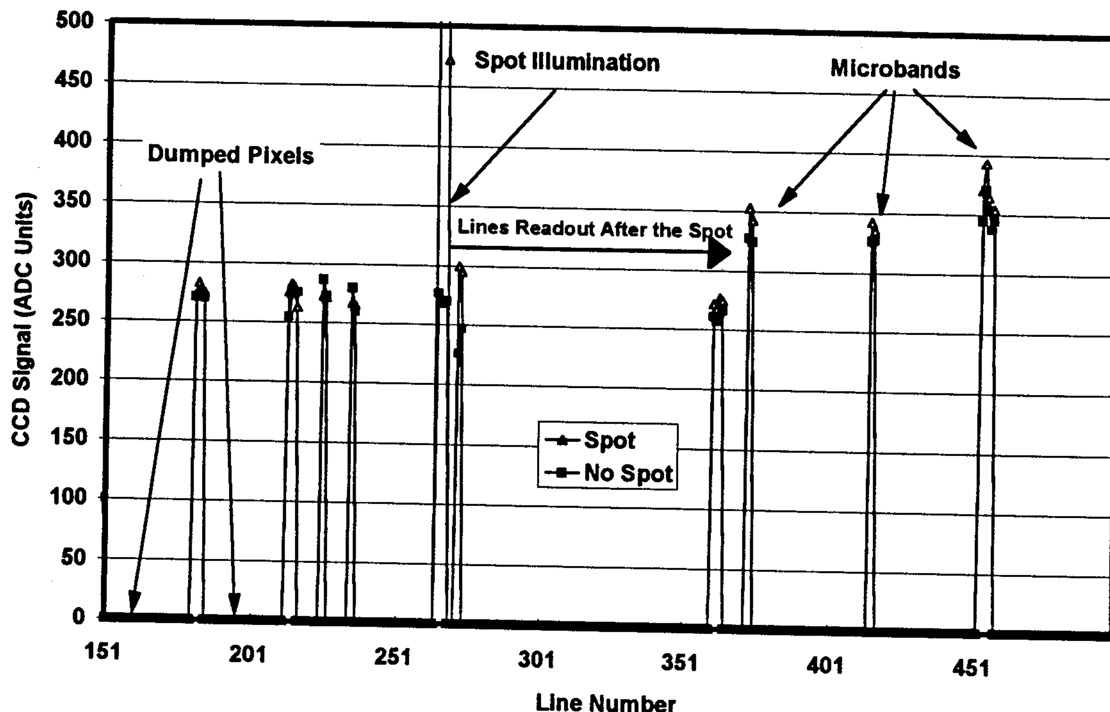

Figure 7.3-1a Results of spot illumination on CCD25-20 device #03, for lines readout after the spot there is additional charge due to proton-induced CTI

Figure 7.3-2 shows a similar plot to figure 7.3-1 but for a TH7895M CCD (device #09) and for a higher signal (1E5 electrons) and higher background (360-2,800 electrons) after 4 krad the CTI was 6.3 E-5 , again in good agreement with figure 7.2-3, figure 6 of RD6). Note that because the dark current varies with total dose (or, more correctly, proton fluence) the background level also changes (as shown in the plots). Hence the plots are slightly curved (but the effect is small since at high signals the CTI is not sensitive to background).

Figure 7.3-3 shows CTI versus signal size for the TH7895M, the form of the curve is very similar to that for the EEV device.

Copyright © Sira Ltd 1995

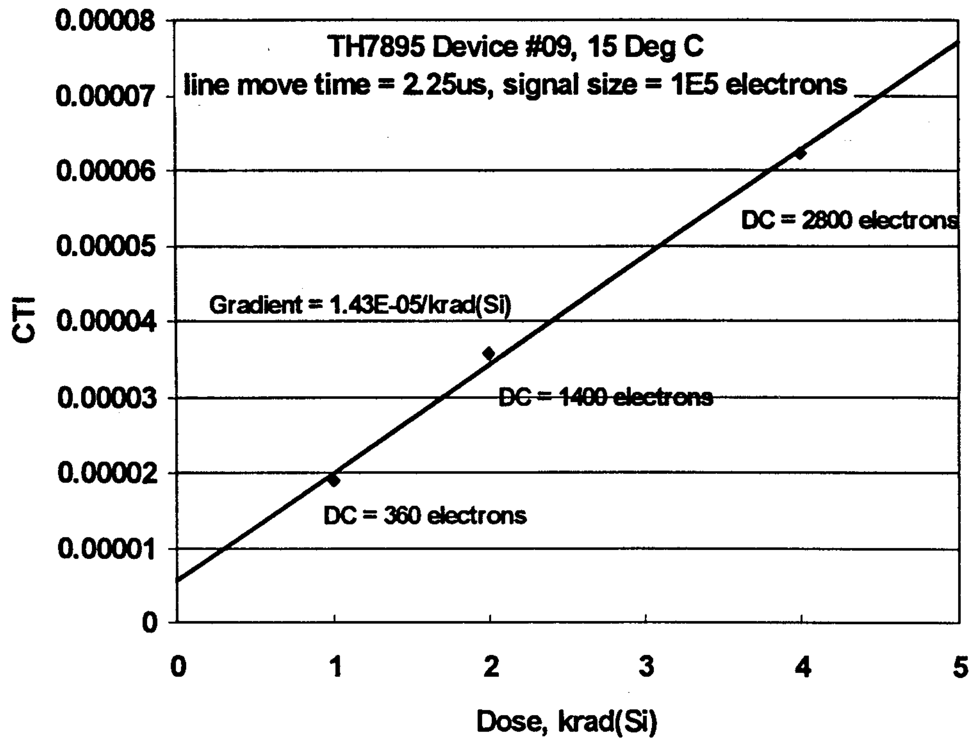

Figure 7.3-2 CTI versus total dose (10 MeV protons) for a TH7895M device

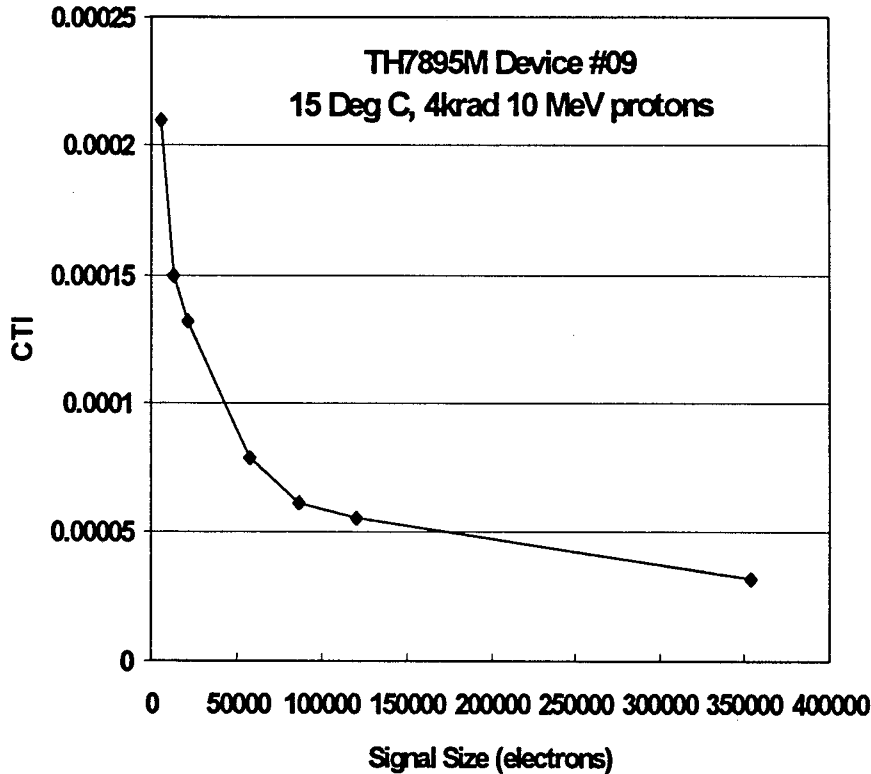

Figure 7.3-3 CTI versus signal size for a TH7895M device (high background)

7.4 CONCLUSIONS

The strong dependencies on signal size and background and the variations with signal dwell time (and, indirectly, on temperature), indicate that the prediction of CTI performance and the effect on acquired image data will not be straightforward. The ideal situation would be to have a CTI simulation model which would transport charge packets from a given scene integration through a 'virtual' CCD to give the readout image. The empirical relations (equations (7-8) and (7-10)) are a first step in developing such a model, but more work is needed. In the meantime, we make some suggestions on the prediction of CTI effects. Firstly it is necessary to classify the scene in terms of the presence of a background (perhaps slowly varying) and occasional signal 'highlights' - this is simple for star images or for x-ray events but is otherwise more complex. Also it is necessary to separate effects for different readout conditions - e.g. frame transfer or charge dumping (at typical line transfer times of a few μs) or slow readout (line transfer times of a few hundred μs). The charge loss can then be predicted, knowing the signal size and background. If during charge transfer the signal highlights are separated in time (t_0) by less than τ_e (which can be estimated from equation (7-3), knowing the operating temperature) then there also a reduction in CTI by a factor ($1-\exp[-t_o/\tau_e]$): this can be very beneficial at low temperatures where τ_e is long (~1ms at -100°C). The effect on the image will also depend on the spreading of the trapped charge into adjacent pixels. During frame transfer the trapped charge will usually be released over tens of trailing pixels (since τ_e = several line times). In contrast, during readout, τ_e can be less than the line time so that charge is only deferred to one trailing pixel.

Copyright © Sira Ltd 1995

8 OUTPUT WAVEFORM MEASUREMENTS

An HP 54522A digital oscilloscope was used to measure and record the CCD output waveforms. The feature most likely to be affected by irradiation is the settling time of the CCD output amplifier. Figures 8-1 to 8-4 show that there was no noticeable change in the waveforms for any of the devices after the maximum dose used (4krad).

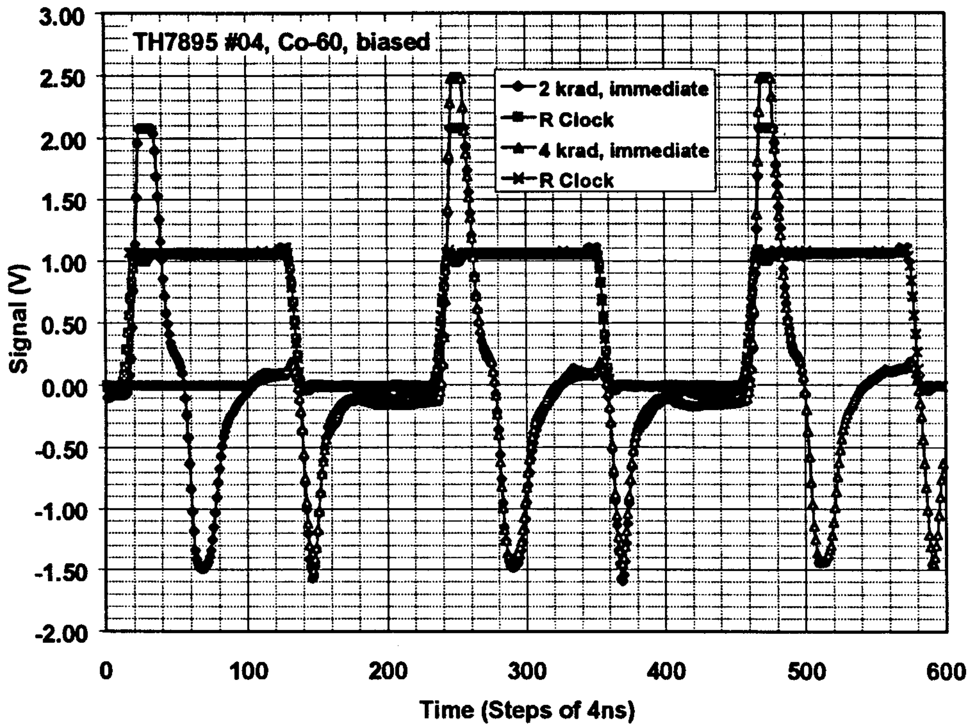

Figure 8-1 Output waveforms for a TH7895M device.

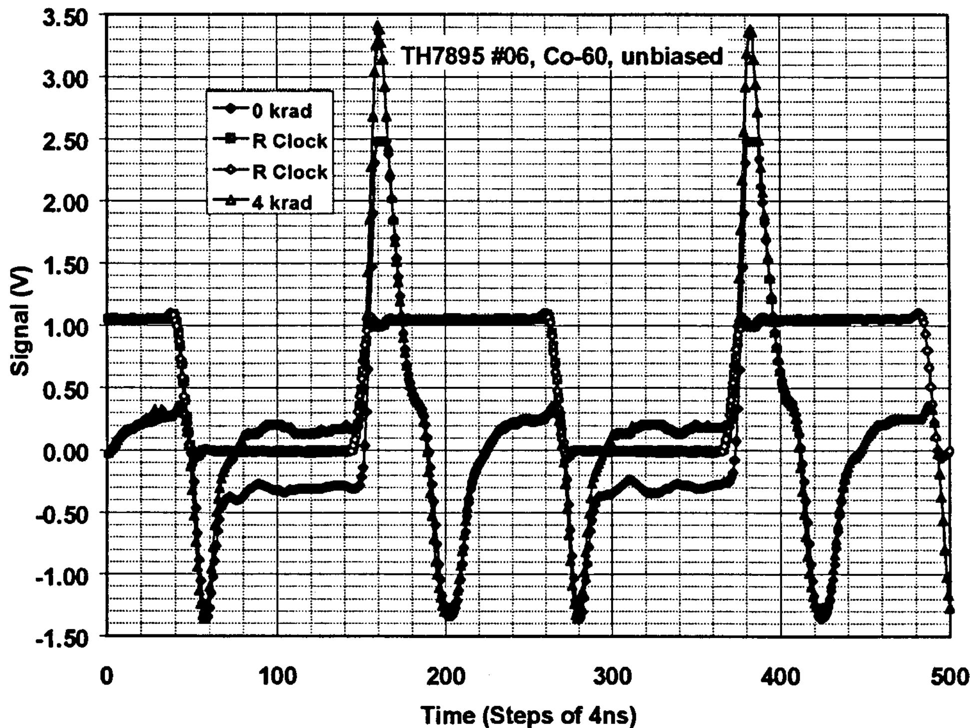

Figure 8-2 Output waveforms for a TH7863B device.

Copyright © Sira Ltd 1995

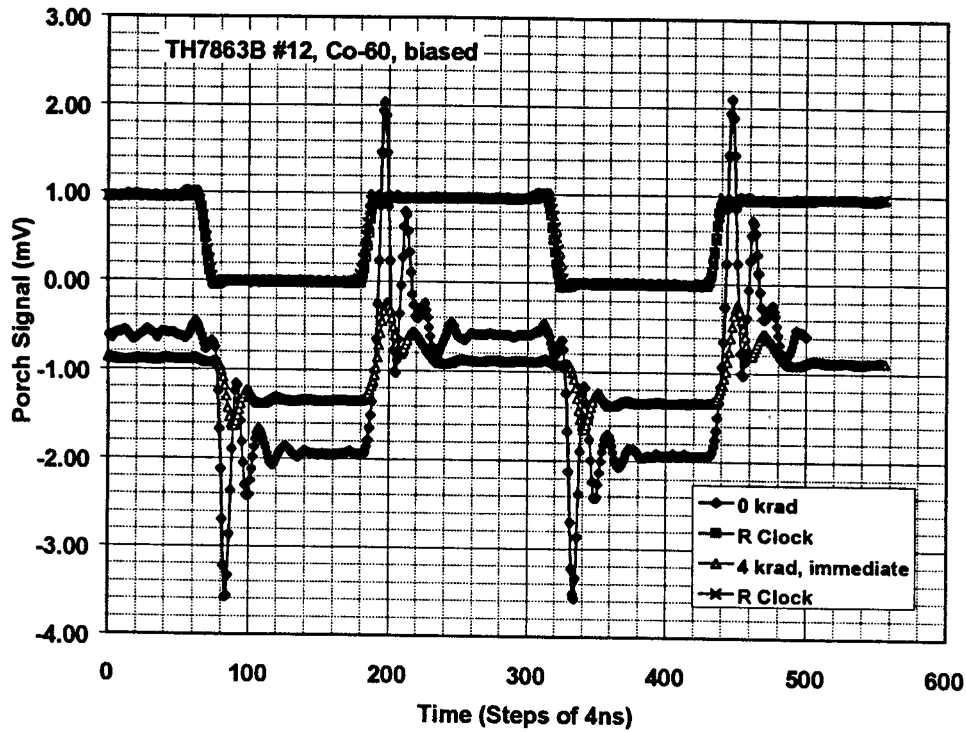

Figure 8-3 Output waveforms for a TH7863B device.

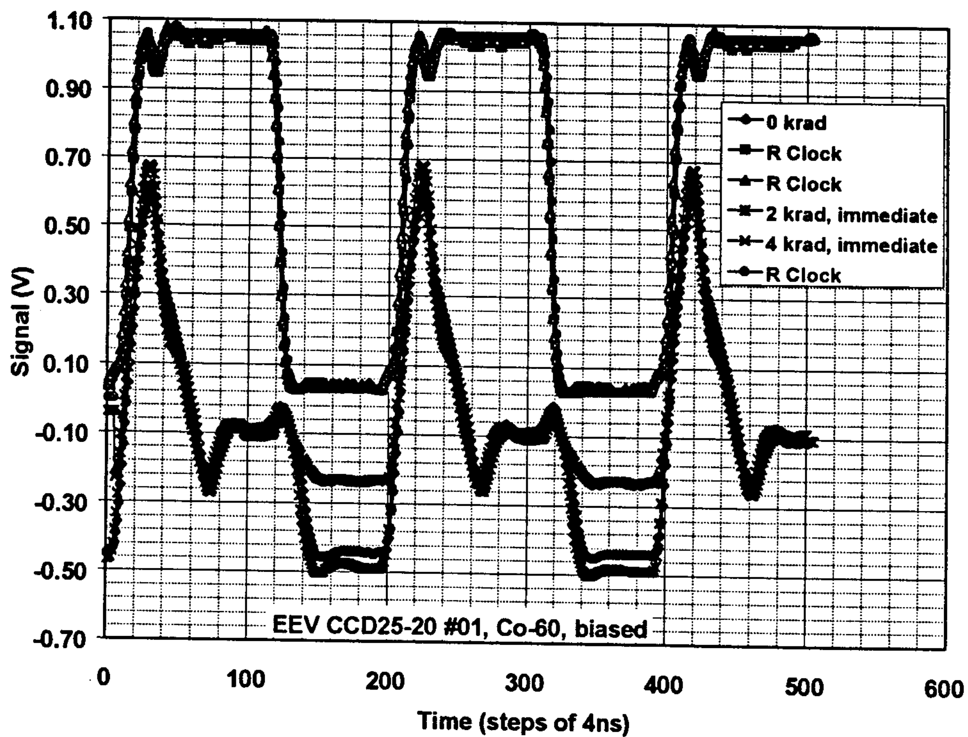

Figure 8-4 Output waveforms for a CCD25-20 device.

Copyright © Sira Ltd 1995

9 THRESHOLD VOLTAGE SHIFTS

9.1 DC OUTPUT VOLTAGE

Figures 9.1-1 and 9.1-2 show the dc value of the CCD output voltage for CCD25-20 and TH7895 devices. Variations in this parameter reflect threshold voltage shifts in the output amplifier stage. The data is probably influenced by spurious offsets involved in different cabling arrangements, prior, during and after irradiation and also due to noise pickup, but there is a general increase in output voltage of order 0.02 to 0.04 V for biased devices and ~0.07-0.1 V for biased devices per krad. For the TH7863B devices there was little change in DC output voltage, values remained in the range 9.5±0.1 V throughout.

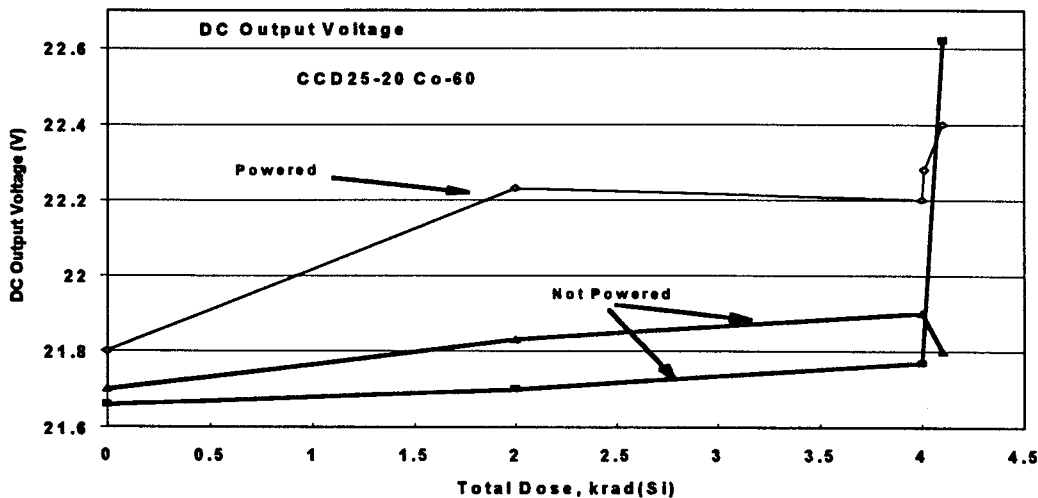

Figure 9.1-1 DC Output voltage for Co-60 irradiated CCD25-20s

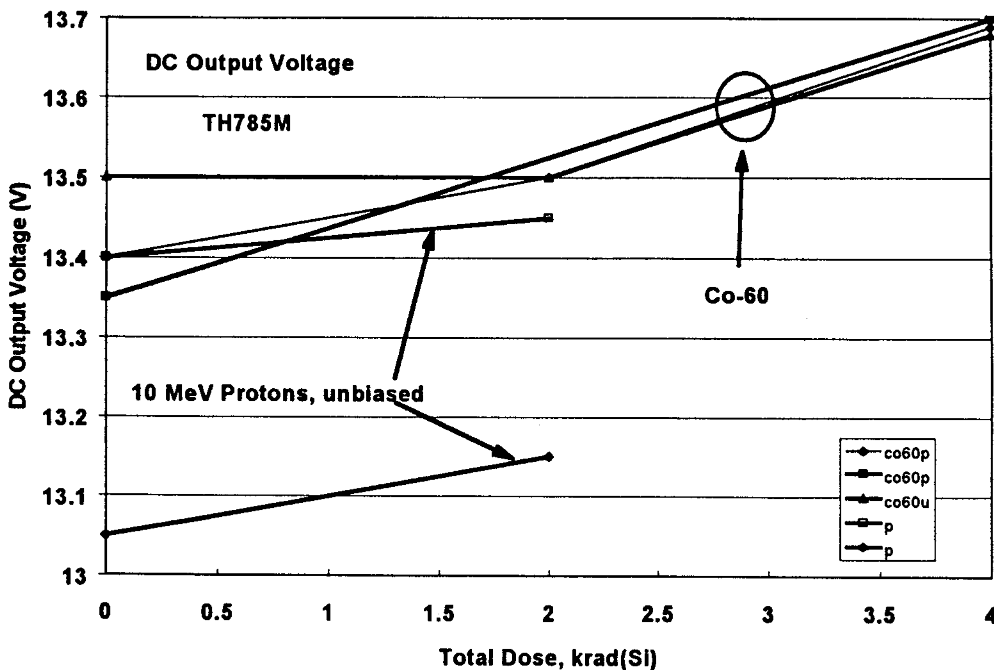

Figure 9.1-2 DC Output voltage for TH7895M CCDs

Copyright © Sira Ltd 1995

9.2 OTHER MEASUREMENTS OF THRESHOLD SHIFTS

Measurements of the output signal (from over scanned - or 'porch' pixels) were made as a function of the following voltages:

- rest drain (Vrd)
- reset clock high level (V resh)
- reset clock low level (Vresl)
- output gate voltage (Vog)

Depending on the CCD type, it was found that one or more of these measurements yielded a plot with features from which the change in threshold voltage could be deduced. Note that, the measured shifts, although related to shifts in flatband voltage, may not be identical because of differences in the on-chip circuits involved. By also looking at the signal size (the difference beween active and overscanned pixel levels) it was also possible to estimate the voltage regions for which the devices were operational (i.e. had signal gain essentially independent of bias voltage).

The variation of output signal with bias (or clock) voltage also depends on the shape of the output waveform and on the bandwidth of the signal processing circuits. Hence, although the shifts measured here (i.e.relative changes) should be representative, the exact shape of the plots (i.e. the absolute values) will not necessarily be the same for other designs of off-chip CCD electronics. As discussed in section 3, measurements at the start of the programme (and whilst at Harwell) were made with a low bandwidth in the signal processing system. The bandwidth was increased for later measurements.

A general feature of the results for all devices was that there was no noticeable change in threshold voltages after irradiation. That is, there was no annealing. This is noted now and will not be discussed again for individual cases.

9.2.1 CCD25-20 Devices

Figures 9.2.1-1 to 9.2.1-4 show plots of output signal versus Vrd and Vresh for Co-60 (biased) and 10MeV proton (unbiased) irradiated CCD25-20s. The following results were found:

Change in theshold voltage/krad (ΔV/krad) for CCD25-20s

	Co-60, biased (#01)	10MeV proton, unbiased (~03)
Vrd	0.05 V	<0.05 V
Vresl	0.15 V	<0.05 V

These results are broadly in line with previous work [RD5] which found threshold voltage shifts ~0.04 V/krad for unbiased devices and ~0.08 V/krad for biased devices.

Figure 9.2.1-5 shows results for varying reset high level. There is a sharp feature at the end of the useful voltage range which could be used for threshold voltage determination, but measurements were not made on all devices over the full voltage range in this case.

The effect of varying the output gate voltage is shown in figures 9.2.1-6 and 9.2.1-7. There are no obvious features with which to identify threshold voltage shifts with this parameter.

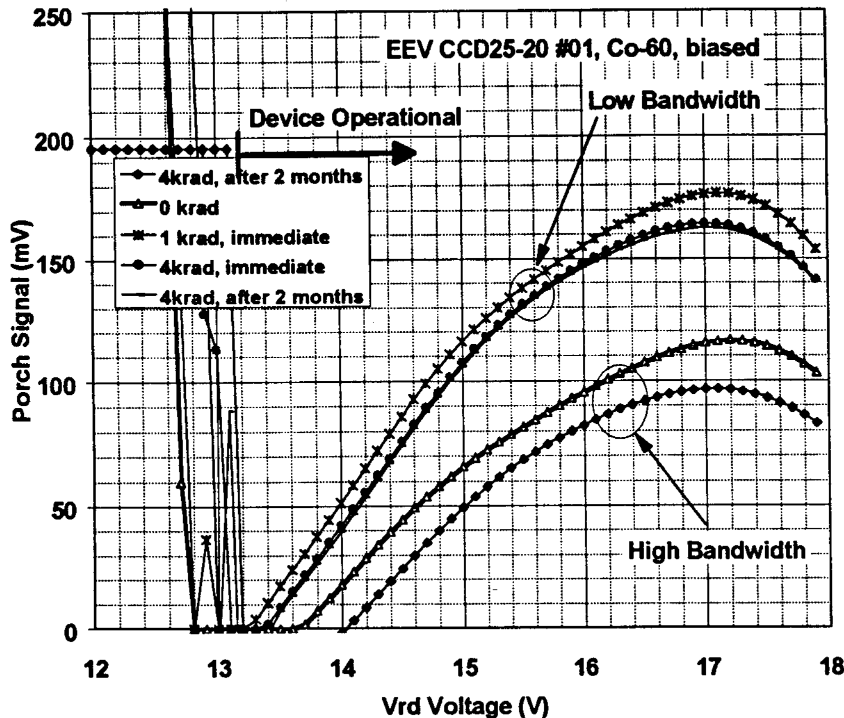

Figure 9.2.1-1 Output signal versus Vrd for a Co-60 (biased) irradiated CCD25-20

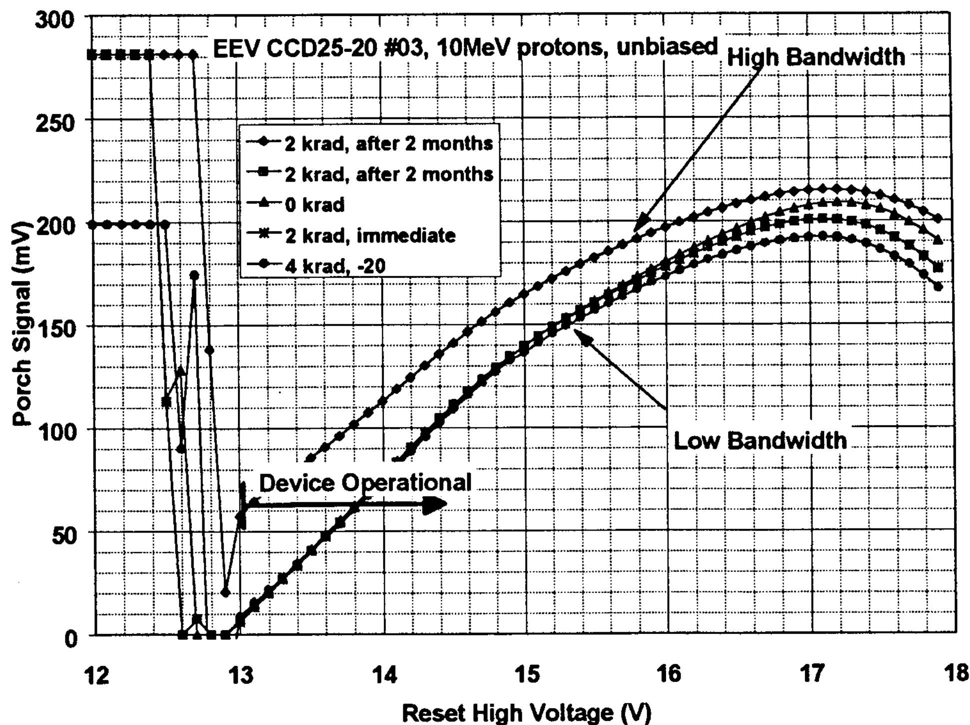

Figure 9.2.1-2 Output signal versus Vrd for a 10MeV proton (unbiased) irradiated CCD25-20

Copyright © Sira Ltd 1995

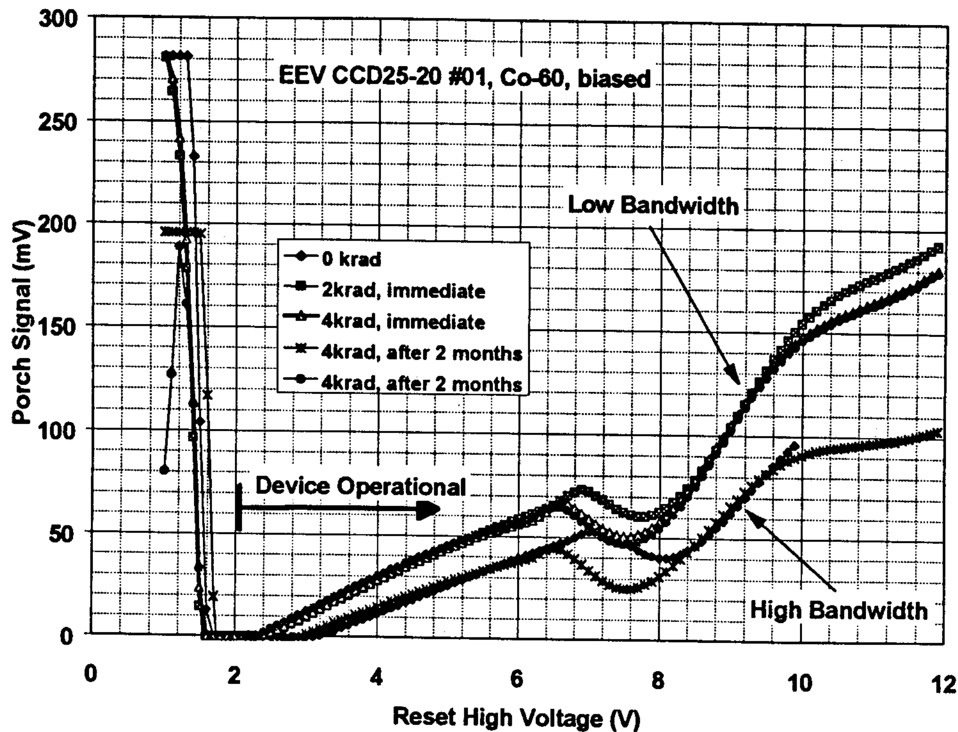

Figure 9.2.1-3 Output signal versus Vresh for a Co-60 (biased) irradiated CCD25-20

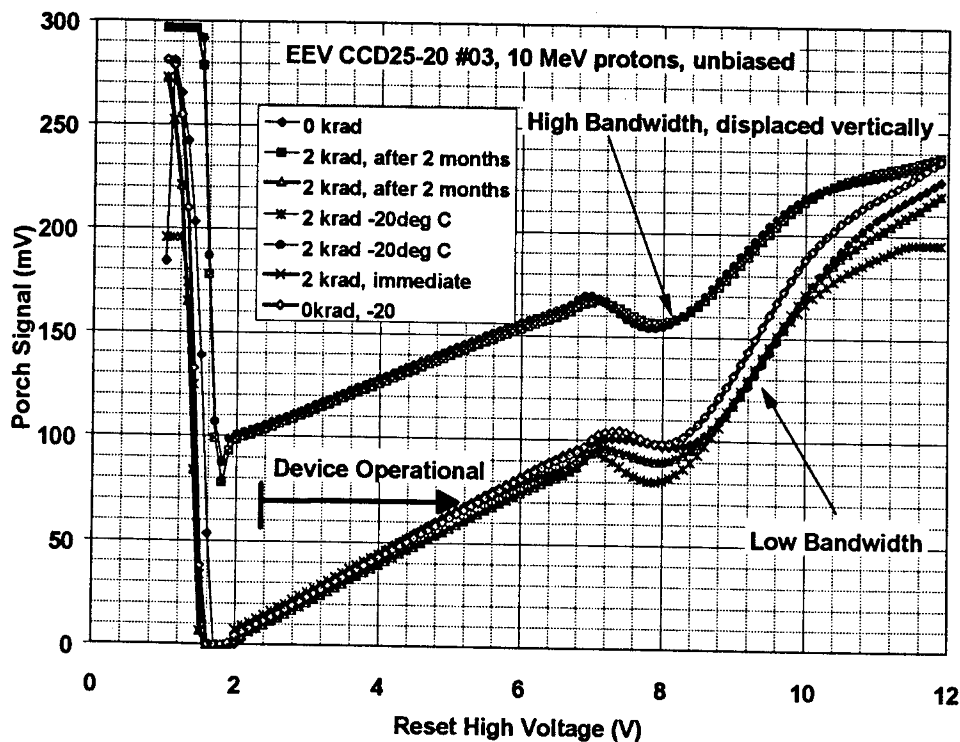

Figure 9.2.1-4 Output signal versus Vresh for a 10MeV proton (unbiased) irradiated CCD25-20

It can be seen from the above plots that there is an effect of the irradiations on the shape of the curves. This can result in a change in offset voltage with total dose. It appears that with these devices shifts ~10mV after 4krad can be expected depending on conditions, though the effects are generally reduced (on the order of a few mV) for high signal bandwidths (as would normally be used). There is also a small change in offset voltage with temperature. Figure

9.2.1-8 shows this for two devices (high bandwidth). Changes of a few mV can be expected over the range 20 to -20°C.

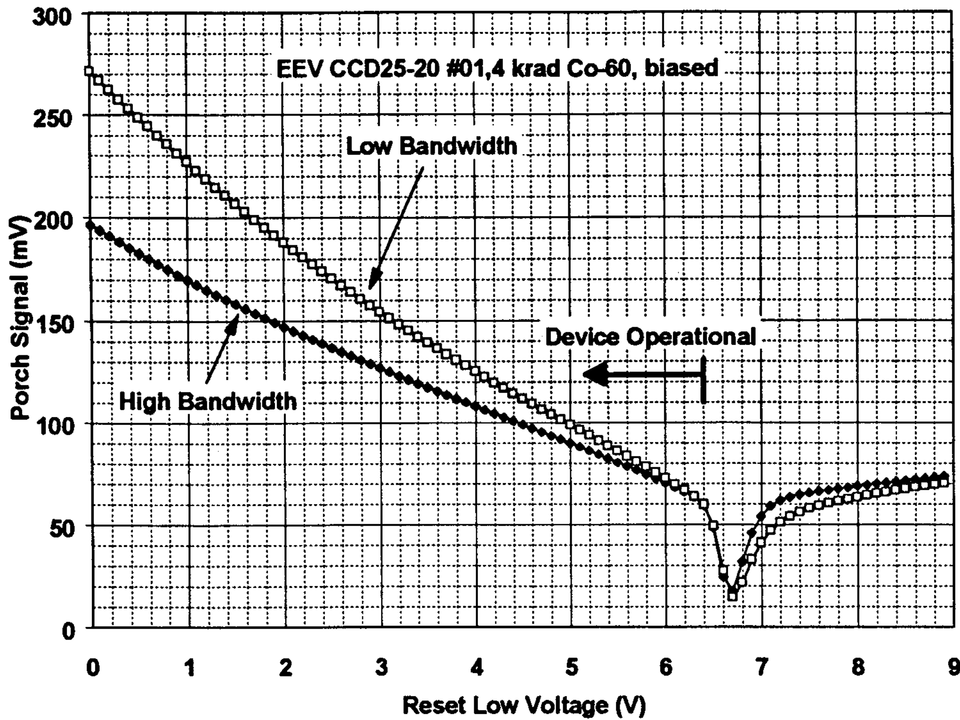

Figure 9.2.1-5 Output signal versus Vresl for a Co-60 (biased) irradiated CCD25-20

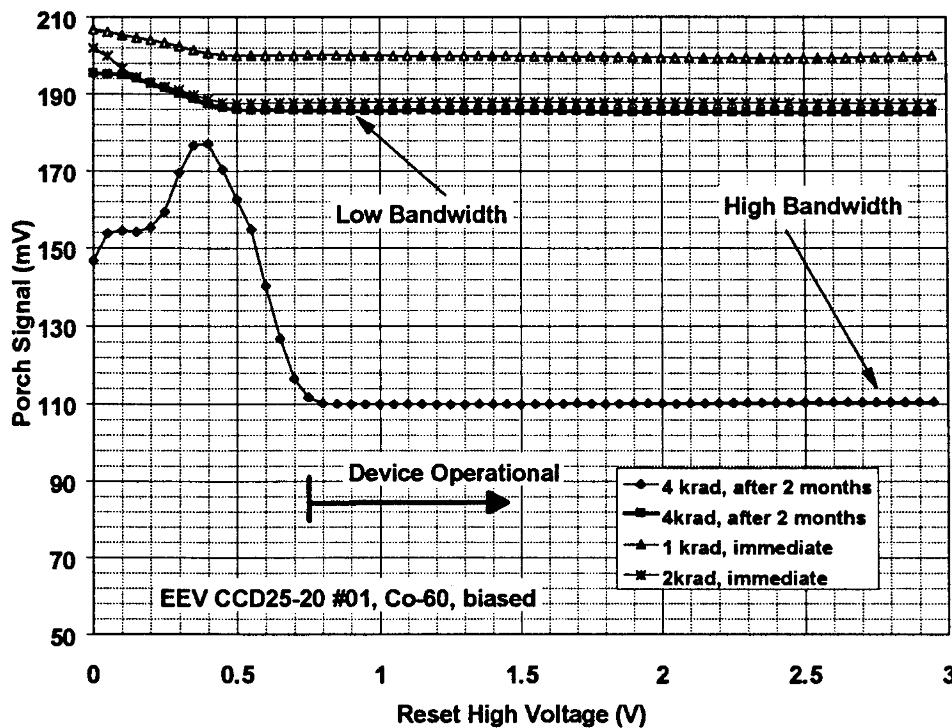

Figure 9.2.1-6 Output signal versus Vog for a CO-60 (biased) irradiated CCD25-20

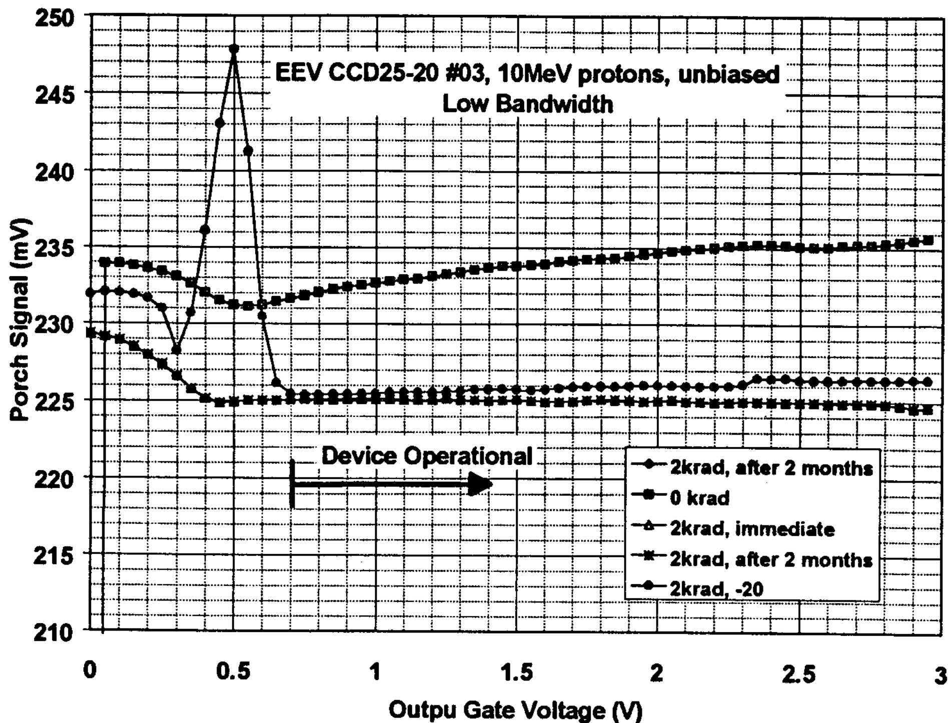

Figure 9.2.1-7 Output signal versus Vog for a 10MeV proton (unbiased) irradiated CCD25-20

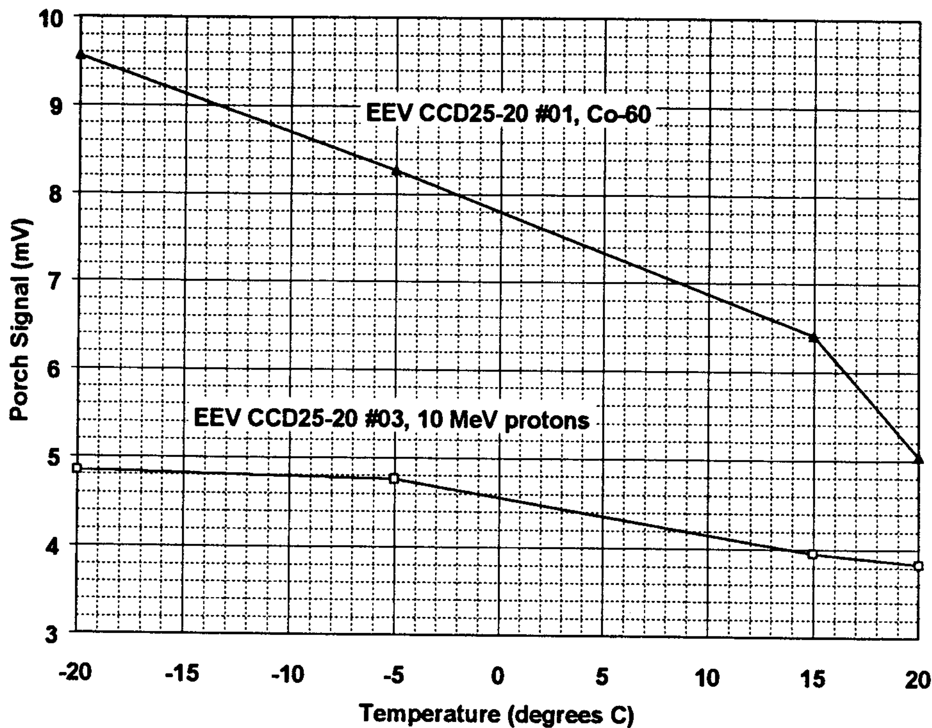

Figure 9.2.1-8 Offset votage versus temperature for two CCD25-20 devices

For applications such as MERIS it was particularly important to check the efficiency of dump gate operation after irradiation. Figures 9.2.1-9 and 9.2.1-10 show plots of signal remaining after a large number of line dumps versus dump gate high voltage. If the dump gate is below a certain threshold voltage then charge is not dumped and the signal in the line readout after line dumping becomes large (and eventually overflows). This threshold voltage depends on the R

Copyright © Sira Ltd 1995

clock high voltage (not surprisingly) and dump gate high must be ≥ R clock high -0.8 V for dumping to be effective. The figures show that irradiation seems to have little effect on dump gate operation. Hence for MERIS this does not seem to be a critical issue.

To check the residual signal left behind after dump gate operation the signal in the line readout after a sequence of 30 line dumps was averaged 64 times. Device #03 was measured at -20 °C. This had 8 krad and 0 krad regions and the average signal in both regions was compaired for the line. It was found that the average difference was 0.9 electrons for a signal size (per pixel) of 2.8E4 electrons. This is likely to be an upper limit and the residual charge may be less than this.

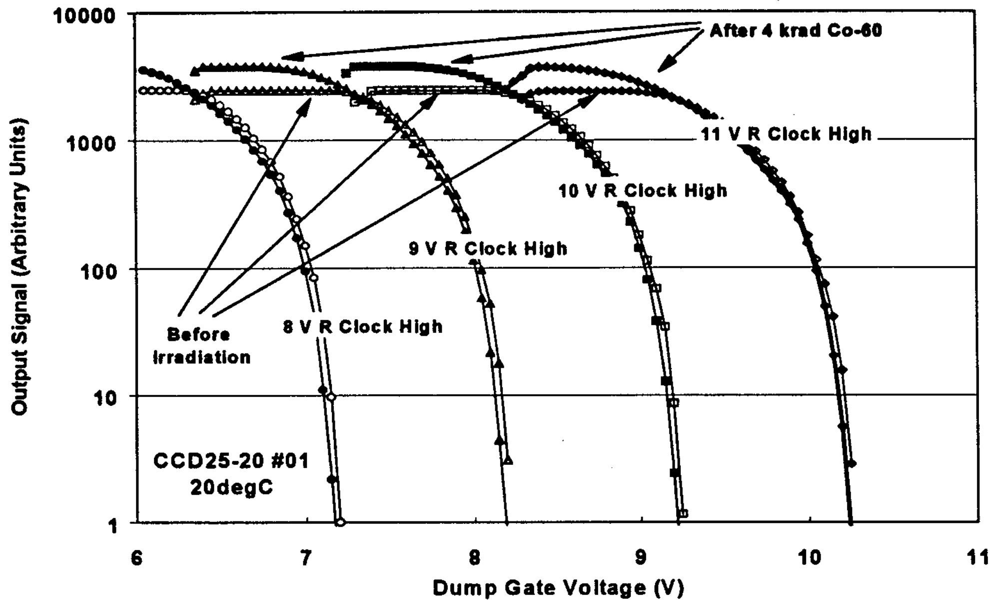

Figure 9.2.1-9 Output signal versus dump gate voltage

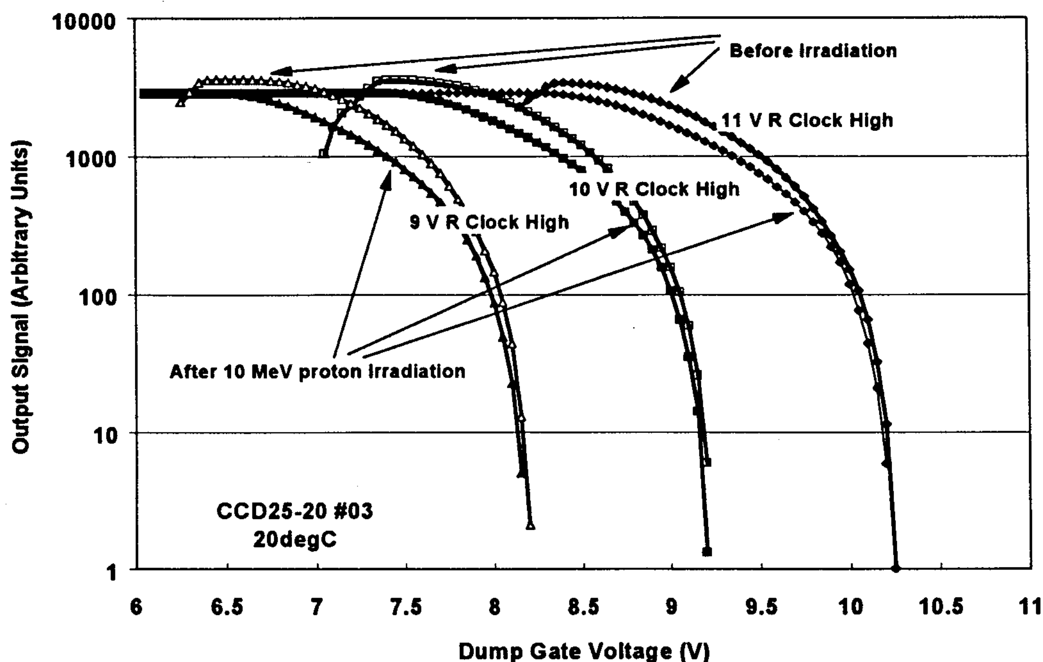

Figure 9.2.1-10 Output signal versus dump gate voltage

9.2.2 TH7895M Devices

Measurements were made of output signals for varying Vrd, Vresl, Vresh and Vog voltages. Figures 9.2.2-1 to 9.2.2-8 show that there are sharp transitions in functionality for TH7895 devices. For example Vrd needs to be greater than ~10 V for the device to be functional (and optional performance occurs at ~12.5 V according to the manufacturer). Likewise the reset low voltage needs to be less than ~5.5 V for functionality (and usually $R\phi_{low}$ would be 0 V). Figure 9.2.2-9 shows the change with reset high voltage and figure 9.2.2-10 shows that there was no significant change in offset voltage with irradiation.

From the changes in the transition points the threshold voltage shift can be measured quite accurately. For example we have:

device	irradiation	ΔVrd (V) 2 krad	ΔVrd (V) 4 krad	ΔVrd (V) 4 krad, after 2 months
#04	Co-60 biased	0.18	0.33	0.36
#06	Co-60 unbiased	0.06	0.10	0.12
#uv	46 MeV proton, unbiased	0.04V after 1.2 krad		

device	irradiation	ΔVreset low 2 krad	ΔVreset low 4 krad	ΔVreset low 4 krad, after 2 months
04	Co-60 biased	-0.125	-0.25	-0.25
05	Co-60 biased	-	-0.25	-0.25
06	Co-60 unbiased	-0.075	-0.15	-0.2
07	10 MeV proton, unbiased	-	-	-0.1
08	10 MeV proton, unbiased	-	-	0.1
09				

Note that bias during irradiation appears to be worst case and the shift per krad is

	ΔV (V/krad)
Vdr, biased	0.08
Vdr, unbiased	0.03
Vresetlow, biased	0.06
Vresetlow, unbiased	~0.04

Copyright © Sira Ltd 1995

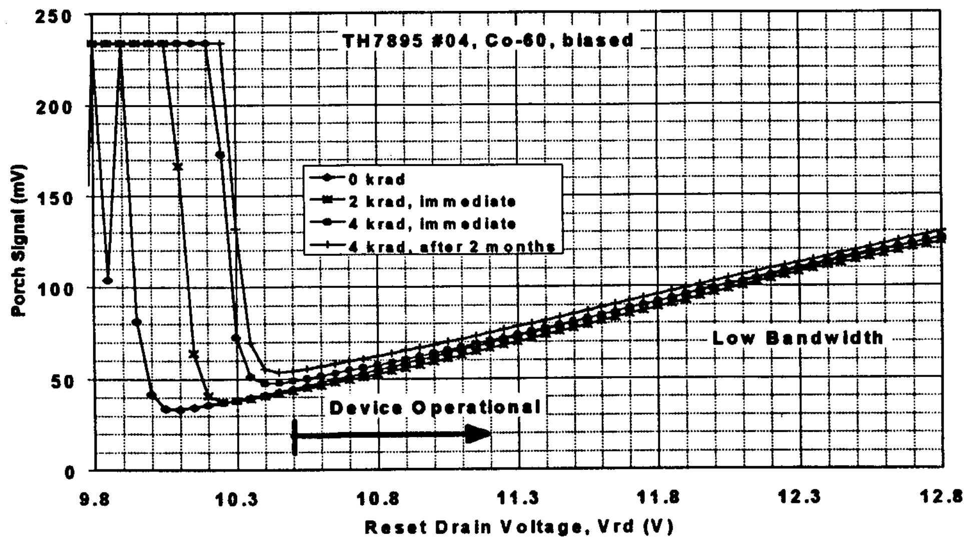

Figure 9.2.2-1 Output signal versus Vrd for a Co-60 irradiated TH7895M device

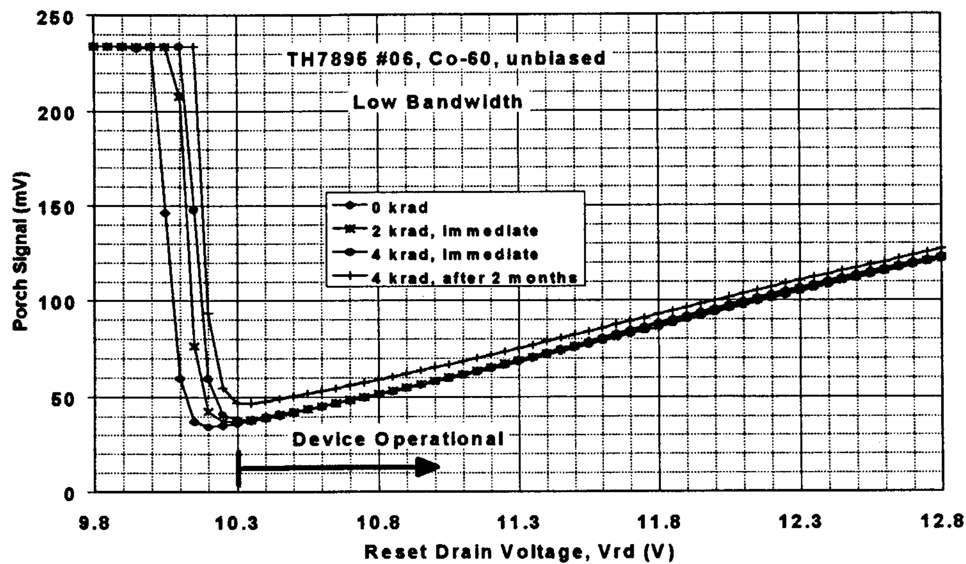

Figure 9.2.2-2 Output signal versus Vrd for a Co-60 irradiated TH7895M device

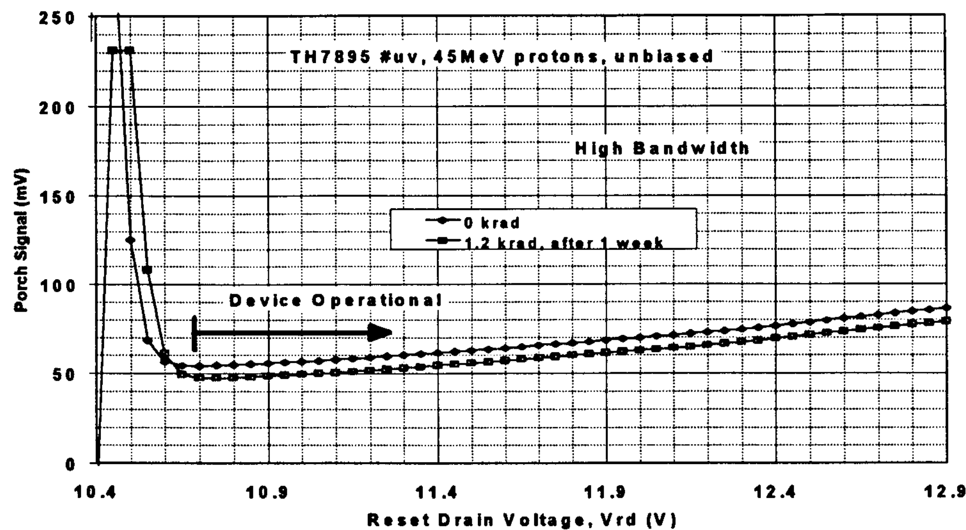

Figure 9.2.2-3 Output signal versus Vrd for a 46MeV irradiated TH7895M device

Copyright © Sira Ltd 1995

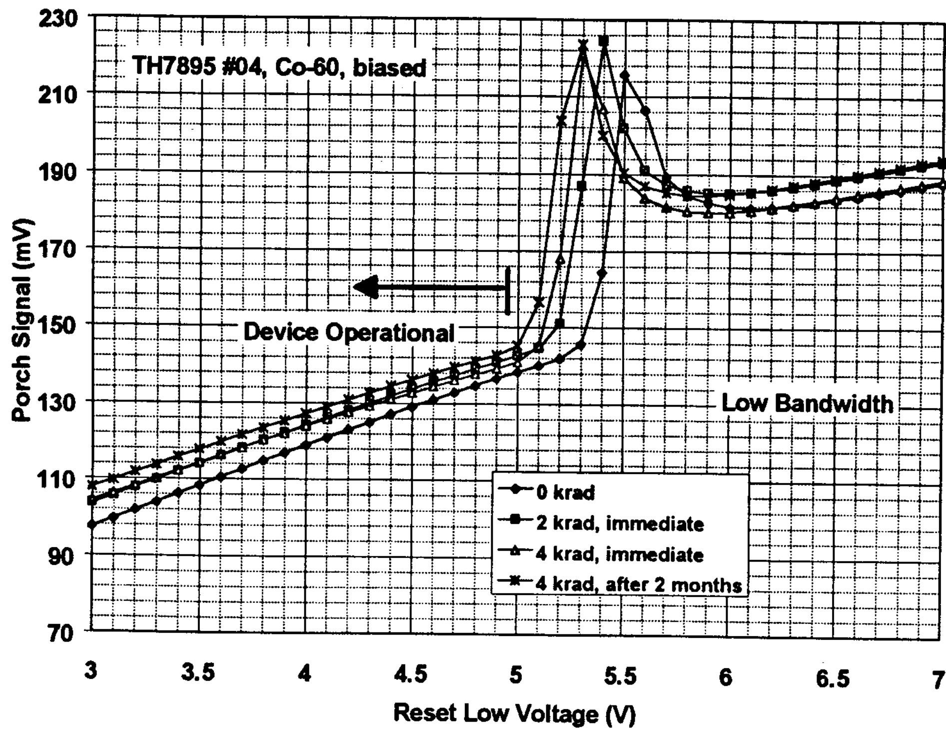

Figure 9.2.2-4 Output signal versus Vresl for a Co-60 irradiated TH7895M device

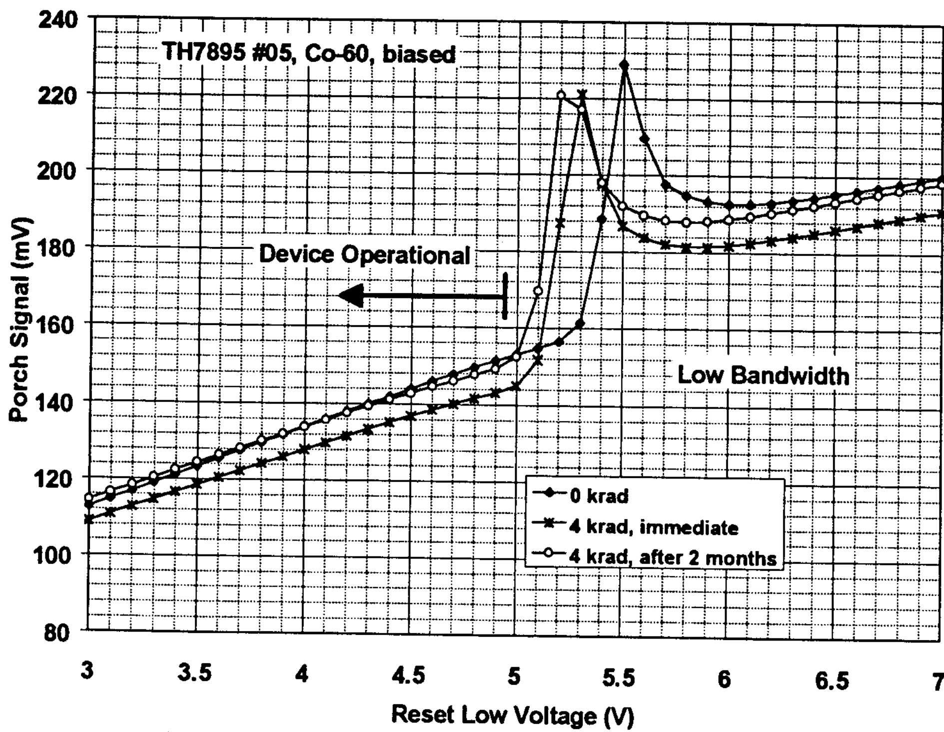

Figure 9.2.2-5 Output signal versus Vresl for a Co-60 irradiated TH7895M device

Copyright © Sira Ltd 1995

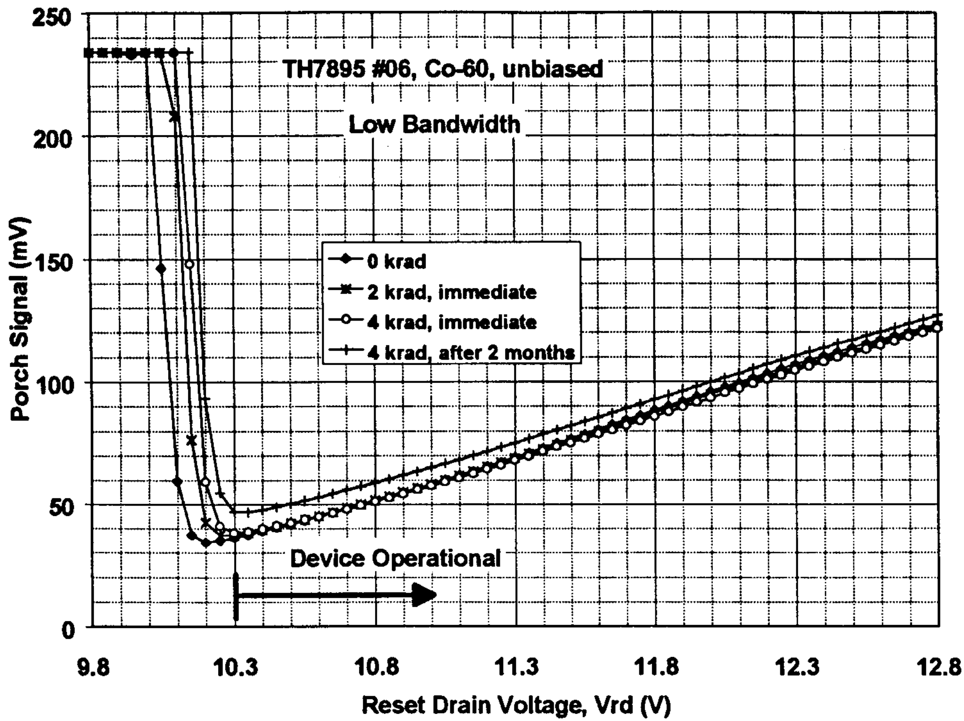

Figure 9.2.2-6 Output signal versus Vresl for a Co-60 irradiated TH7895M device

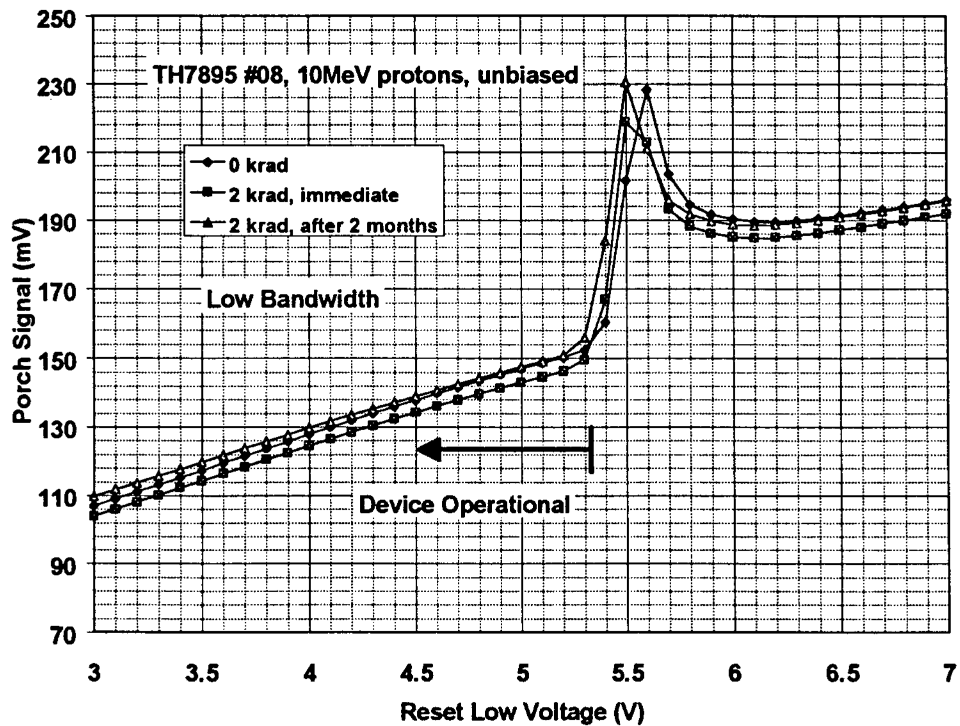

Figure 9.2.2-7 Output signal versus Vresl for a 10MeV irradiated TH7895M device

Copyright © Sira Ltd 1995

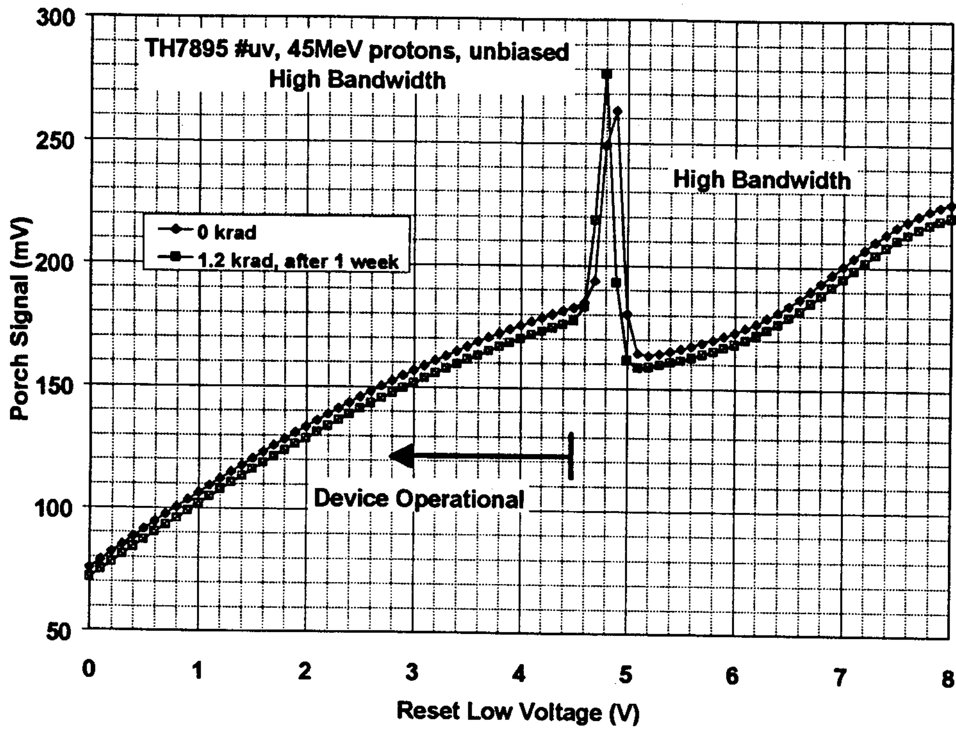

Figure 9.2.2-8 Output signal versus Vresl for a 10MeV irradiated TH7895M device

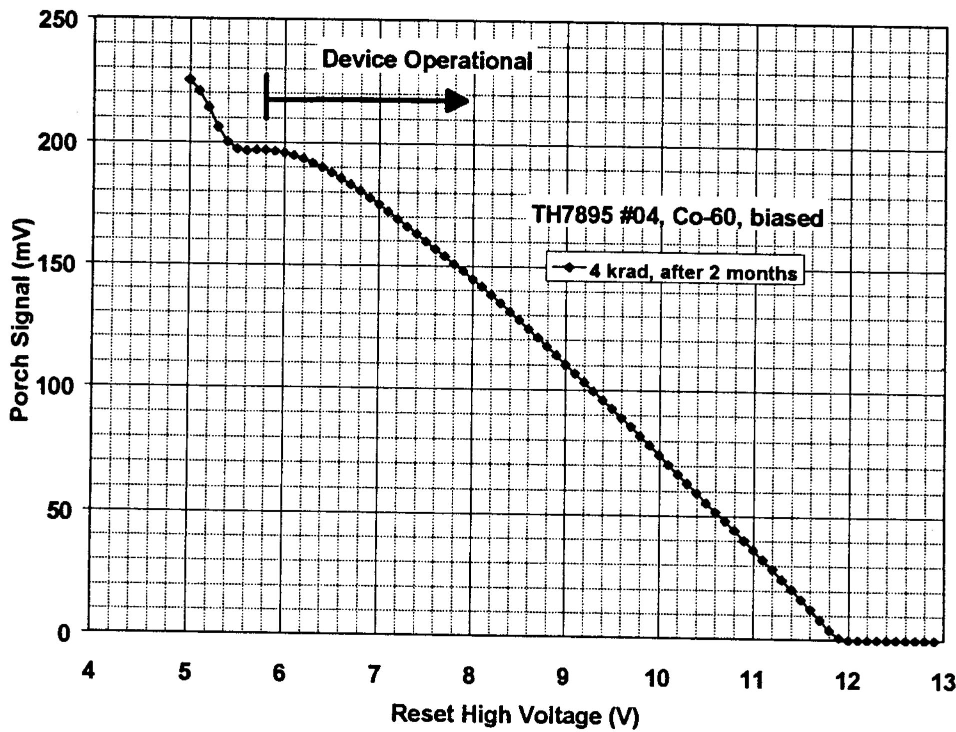

Figure 9.2.2-9 Output signal versus Vrd for a Co-60 irradiated TH7895M device

Copyright © Sira Ltd 1995

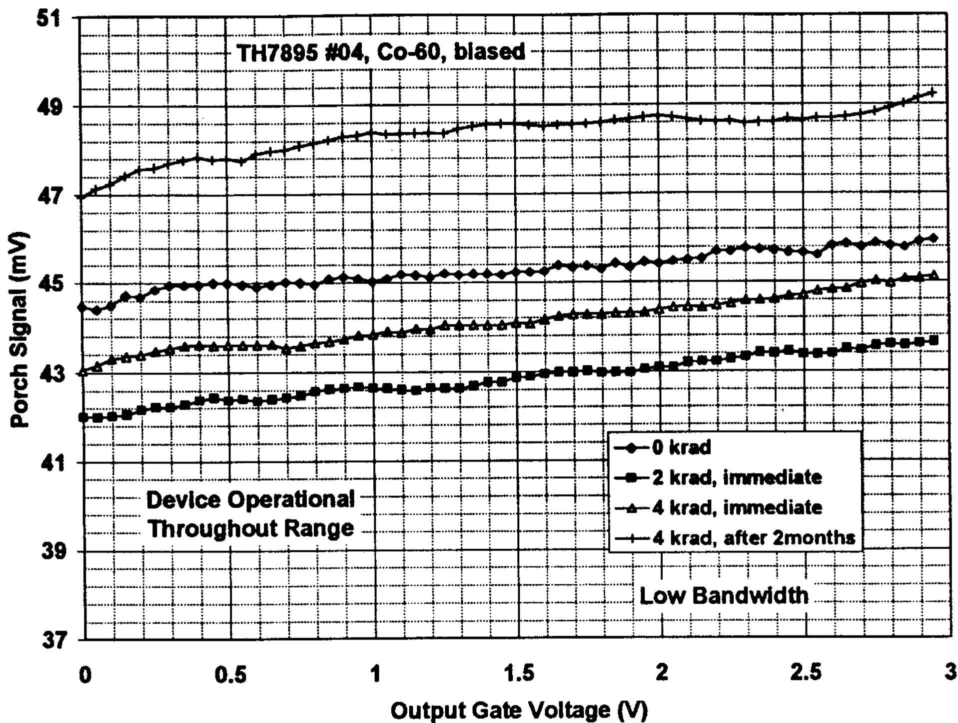

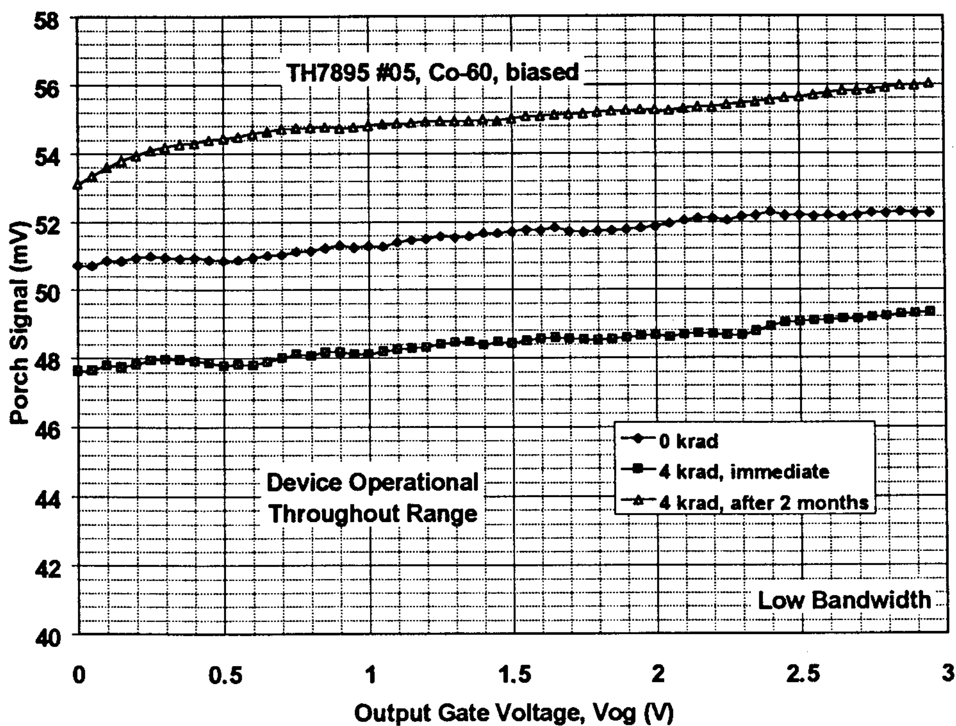

Figure 9.2.2-10 Output signal versus Vog for Co-60 irradiated TH7895M devices

Copyright © Sira Ltd 1995

9.2.3 TH7395 Devices

Figures 9.2.3-1 and 9.2.3-2 show plots of output signal versus Vrd and Vresl for device #01. This received 4krad Co-60 whilst biased and it is seen that the threshold shift is between 0.36 and 0.2 V. so we have

Threshold voltage shift /krad (biased)~0.07V/krad

Figure 9.2.3-3 shows the variation with Vresh. There were no sharp features with which to determine threshold shifts. Figure 9.2.3-4 shows a plot agaoinst output gate voltage. There is very little change in offset voltage with irradiation.

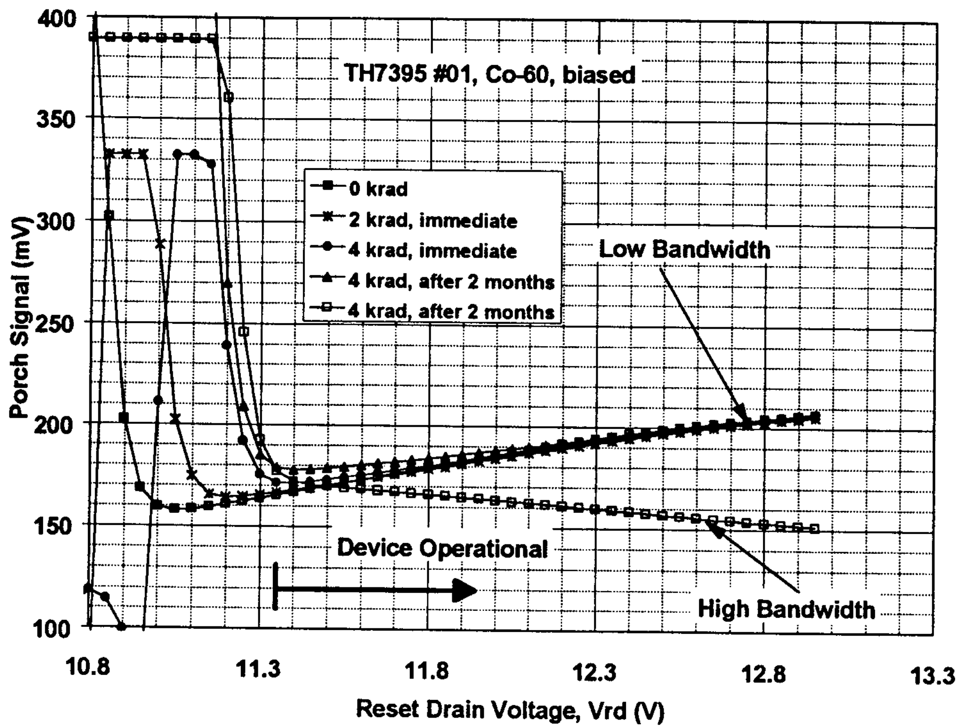

Figure 9.2.3-1 Output signal versus Vrd for a Co-60 irradiated TH7395 device

Copyright © Sira Ltd 1995

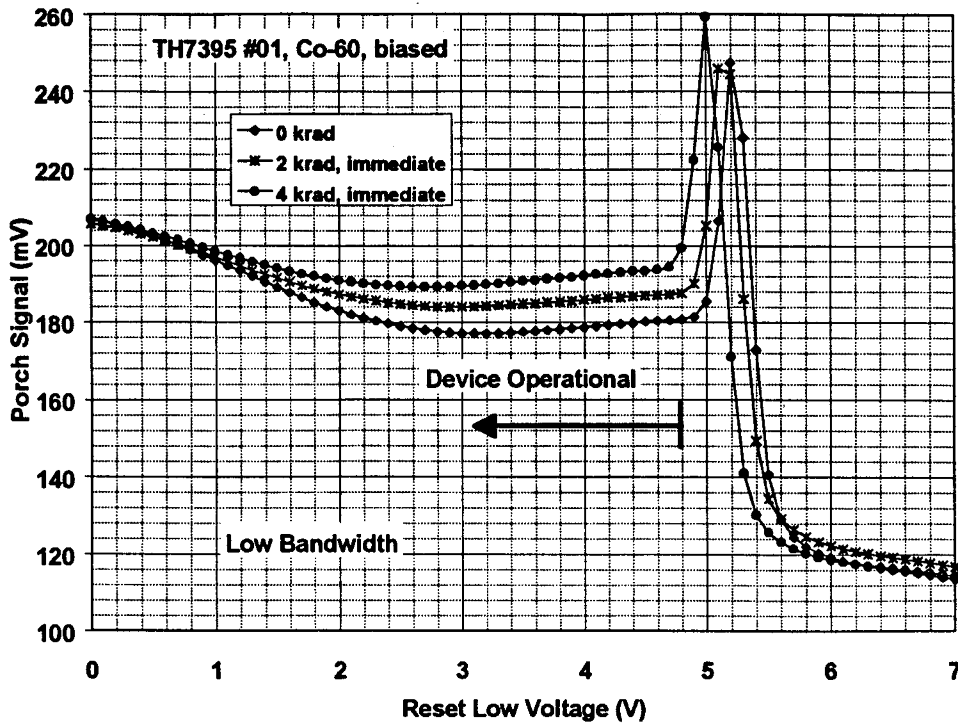

Figure 9.2.3-2 Output signal versus Vresl for a Co-60 irradiated TH7395 device

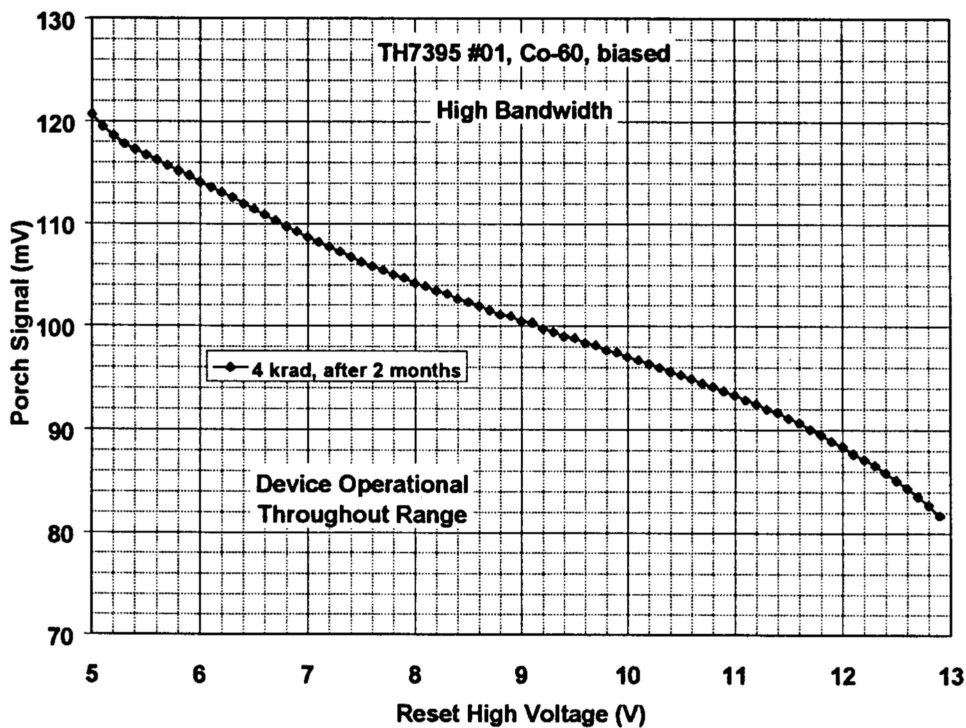

Figure 9.2.3-3 Output signal versus Vresh for a Co-60 irradiated TH7395 device

Copyright © Sira Ltd 1995

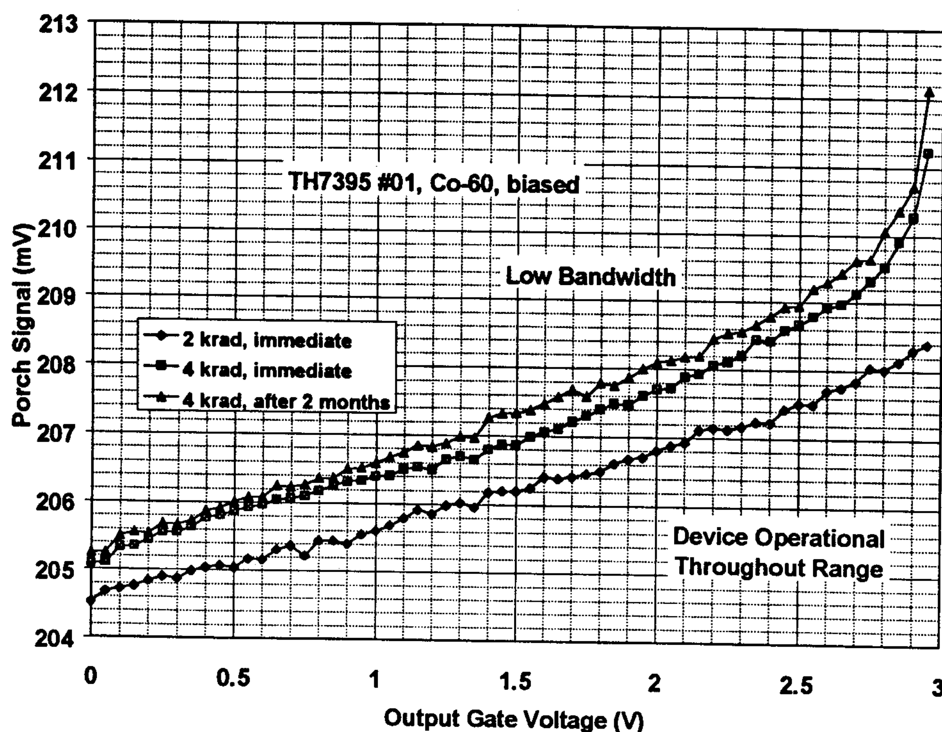

Figure 9.2.3-4 Output signal versus Vog for a Co-60 irradiated TH7395 device

9.2.4 TH7863B Devices

Figures 9.2.4-1 to 9.2.4-6 show output signal as a function of Vrd, Vresl and Vresh for biased and unbiased devices. The threshold shifts were as follows

TH7863B Threshold shifts after 4krad

Biased devices	0.4 V
Unbiased devices	0.15 V

So this gives shifts/krad of approximatetly 0.1V and 0.04V/krad for devices biased and unbiased, respectively, during irradiation.

Figure 9.2.4-7 shows that, as with the other Thomson devices there is little change in offset voltage with irradiation.

Copyright © Sira Ltd 1995

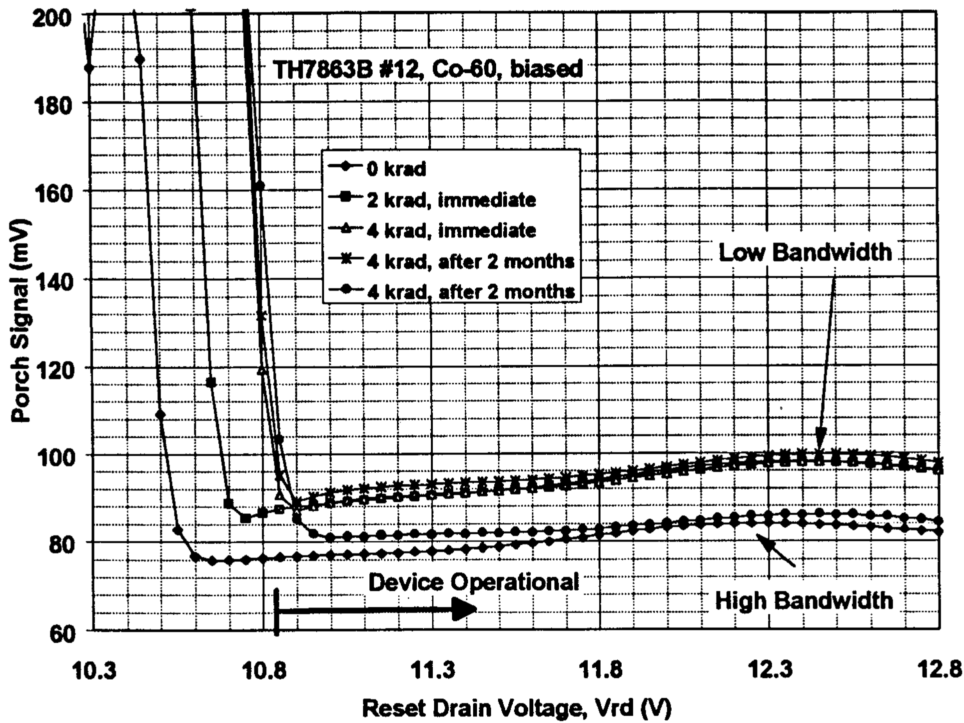

Figure 9.2.4-1 Output signal versus Vrd for a Co-60 irradiated TH7863B device

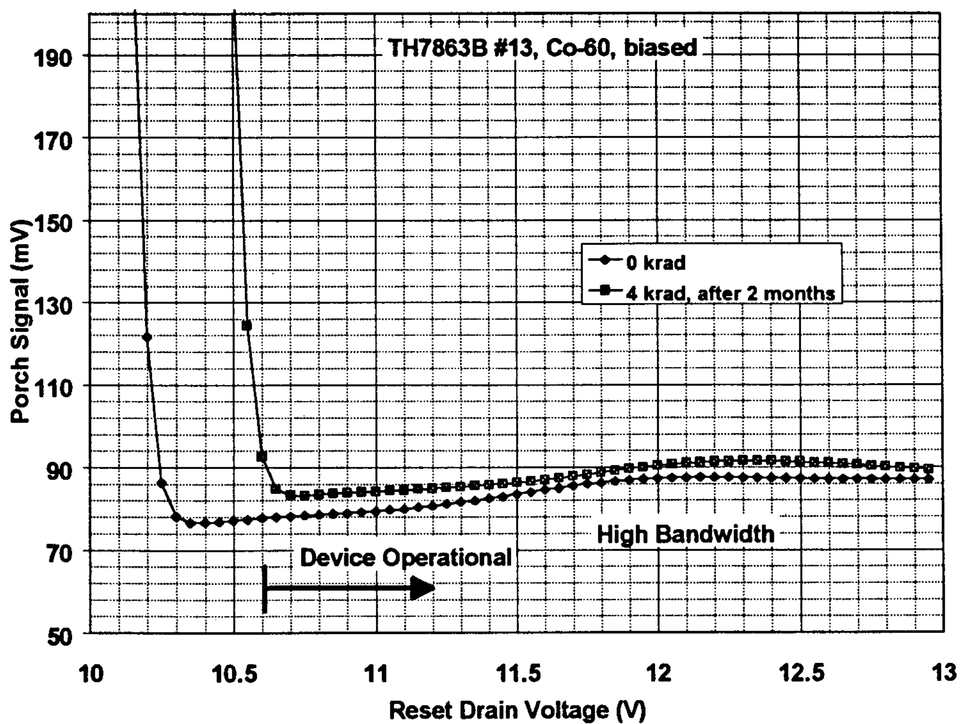

Figure 9.2.4-1 Output signal versus Vrd for a Co-60 irradiated TH7863B device

Copyright © Sira Ltd 1995

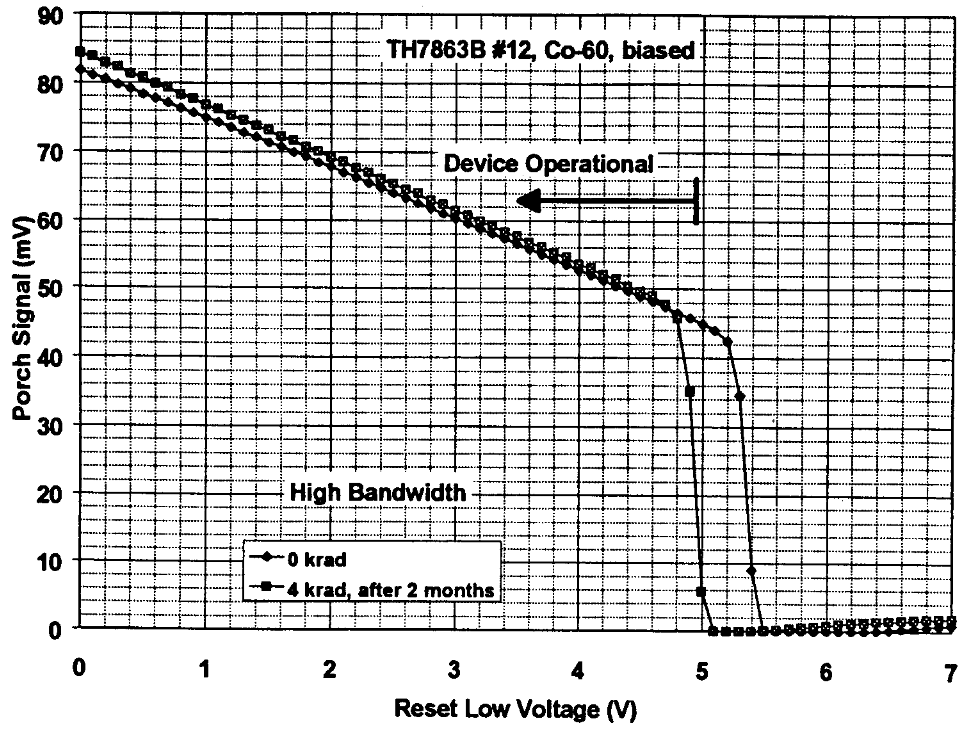

Figure 9.2.4-2 Output signal versus Vresl for a Co-60 irradiated TH7863B device

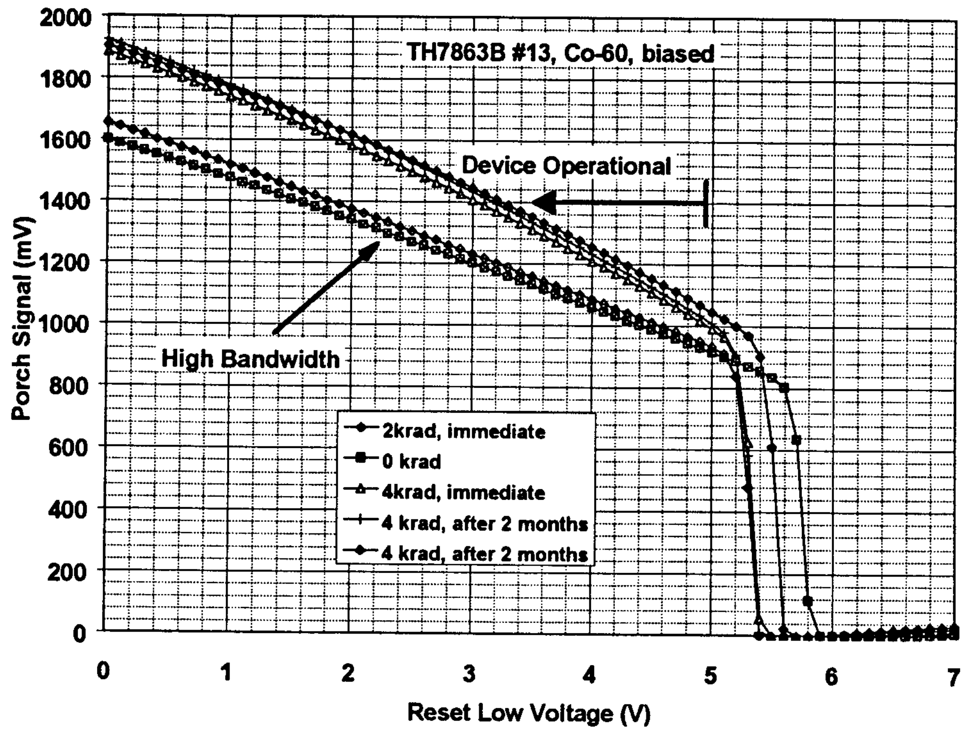

Figure 9.2.4-3 Output signal versus Vresl for a Co-60 irradiated TH7863B device

Copyright © Sira Ltd 1995

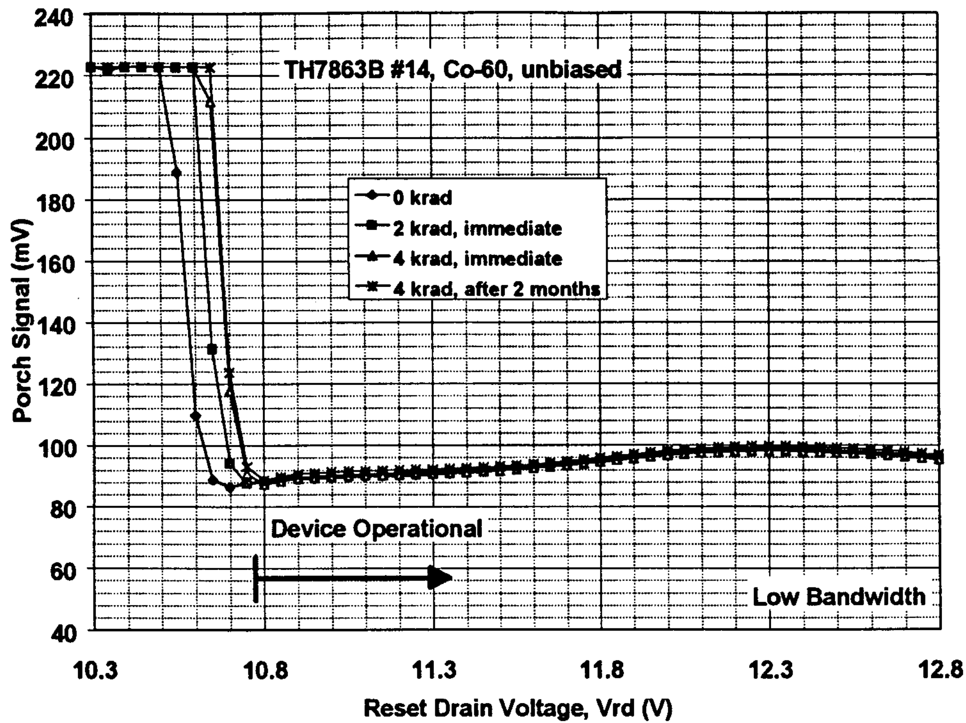

Figure 9.2.4-4 Output signal versus Vrd for a Co-60 irradiated TH7863B device

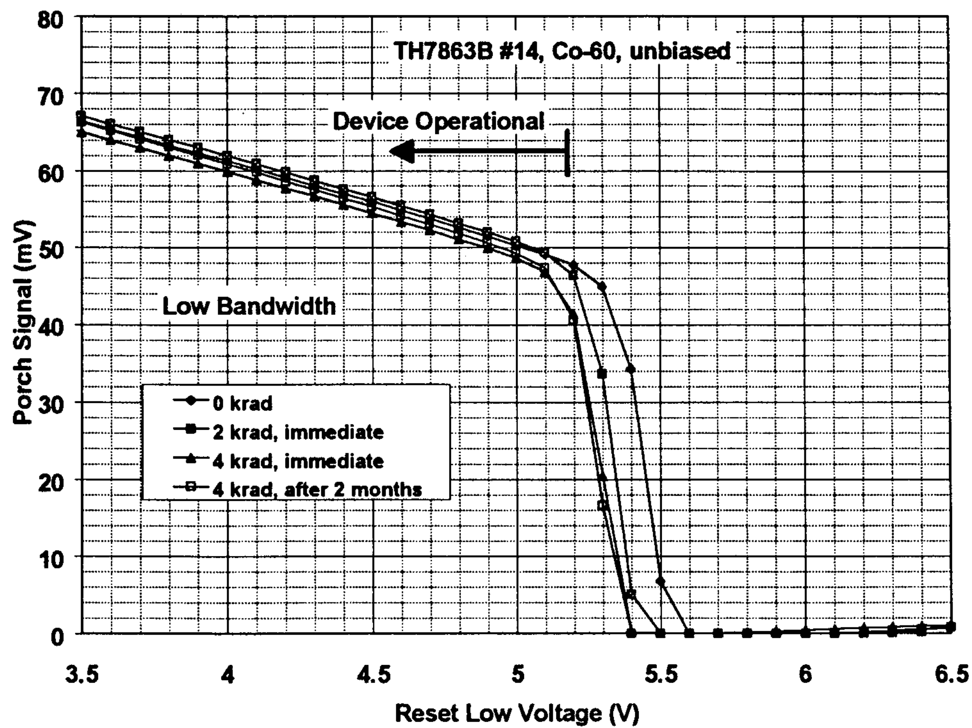

Figure 9.2.4-5 Output signal versus Vresl for a Co-60 irradiated TH7863B device

Copyright © Sira Ltd 1995

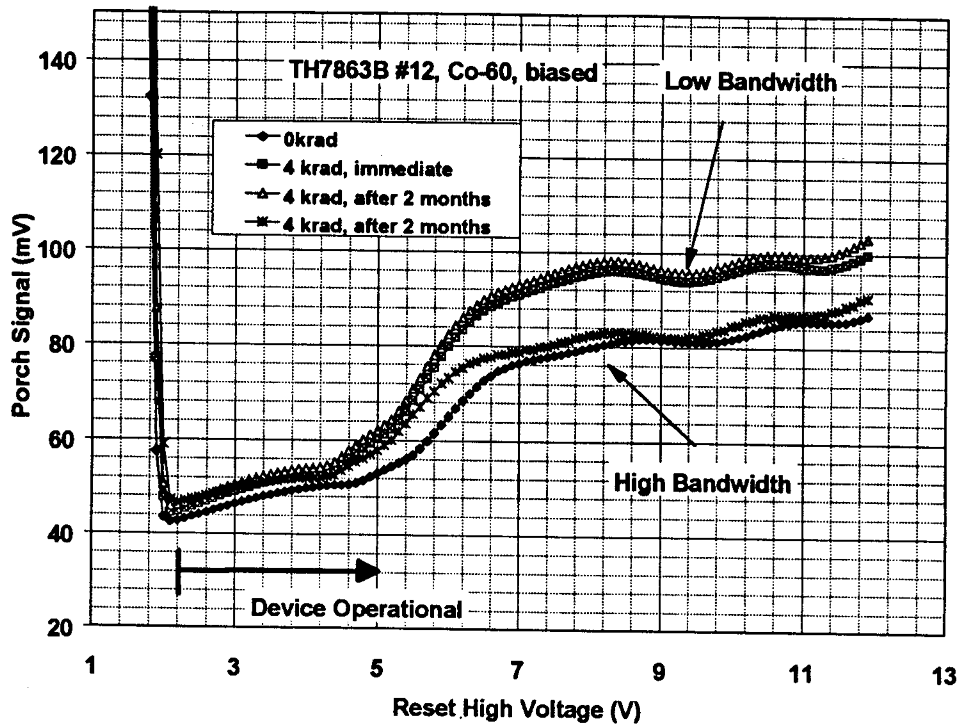

Figure 9.2.4-6 Output signal versus Vresh for a Co-60 irradiated TH7863B device

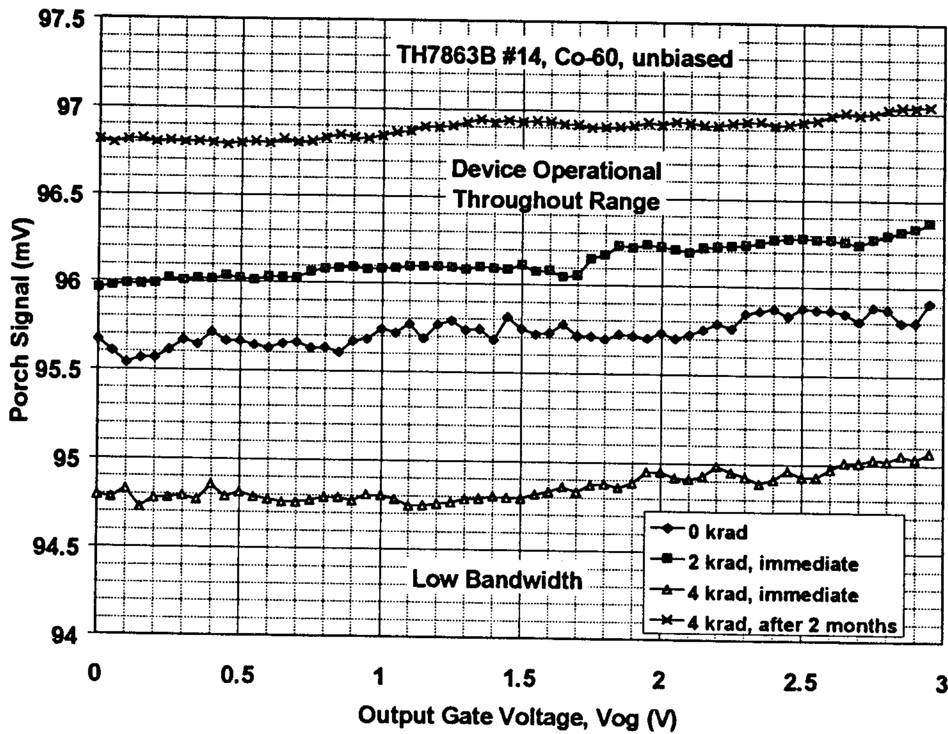

Figure 9.2.4-7 Output signal versus Vog for a Co-60 irradiated TH7863B device

Copyright © Sira Ltd 1995

10 OUTPUT AMPLIFIER SUPPLY CURRENTS

The current in the output drain bias line was measured in darkness for each device as a function of total dose. Plots of the data are shown in figures 10-1 to 10-4. It can be seen that some annealing takes place after irradiation, particularly for the CCD25-20 devices. The TH7863B devices give the largest change (and the most consistent data - probably because the changes are larger and errors smaller) and also very little annealing. Below is a table of starting values and the average change per krad. Measurements were also made with devices illuminated to approximately Vsat/2. In all cases the current was reduced on illumination, but by less than 1%, hence this effect is not thought to be significant and will not be discussed further.

Table 10-1 Otput amplifier currents

Vod currents	Pre-irradiation value (mA)	Drift (mA/krad)
TH 7863B, biased	6.7 to 7.4	0.113
TH 7863B, unbiased	6.7 to 7.4	0.05
TH 7395, unbiased	3.4 to 3.6	0.01
TH 7895, biased	0.94 to 0.96	0.004
TH 7895, unbiased	0.94 to 0.96	0.015
CCD25-20, unbiased	2.25 to 2.28	0.003

Apart from the 7863B results, the increases in Iod are very small.

The values for the TH7863B are very similar to those from a previous study of the TH7863A (final report on ESTEC contract 7787/88/NL/DG, March 1991, "Co60 radiation testing of THX31160 and TH7863 CCDs for the Silex programme [RD3].

	Drift in Iod (mA/krad)	
	biased	unbiased
This study	0.11	0.05
Co-60 results for 7863A	0.12	0.04

Also the ΔIod for the EEV CCDs is similar to that found previously for CCD02 and CCD05 devices (in RD5 ΔIod is given as ~0.004 mA/krad). As in that study there is a suggestion that the shift is higher for the Co60 irradiated device (#01) compared with the two that were irradiated with 10 MeV protons, however the statistics are not good enough to make a definite statement.

Copyright © Sira Ltd 1995

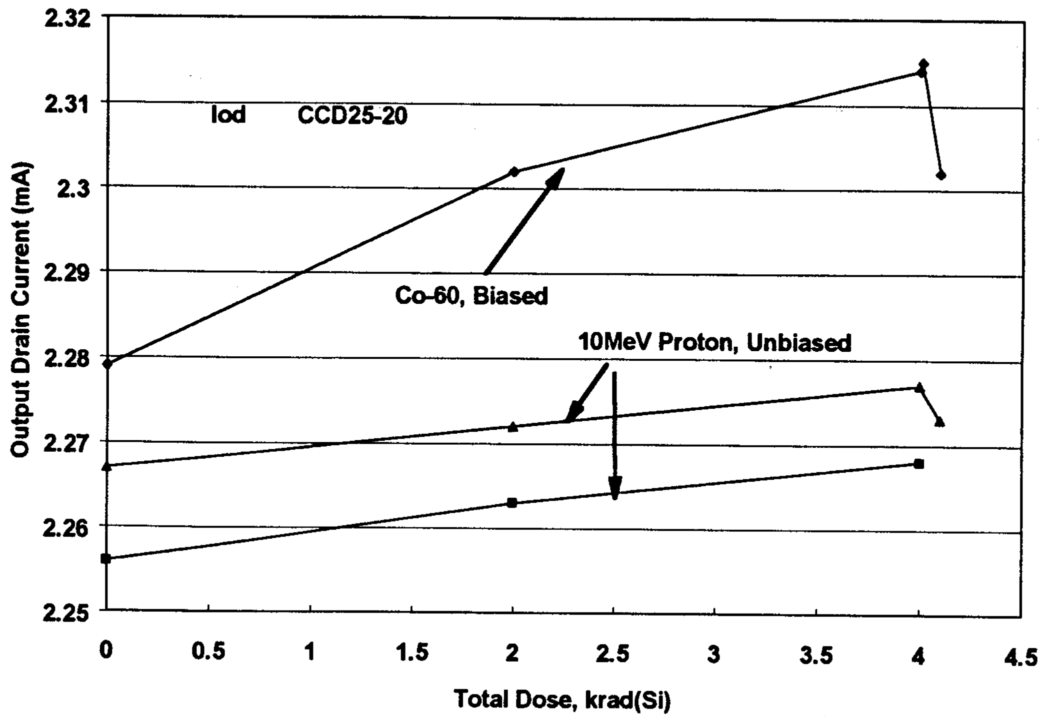

Figure 10-1 Output amplifier currents for CCD25-20 devices

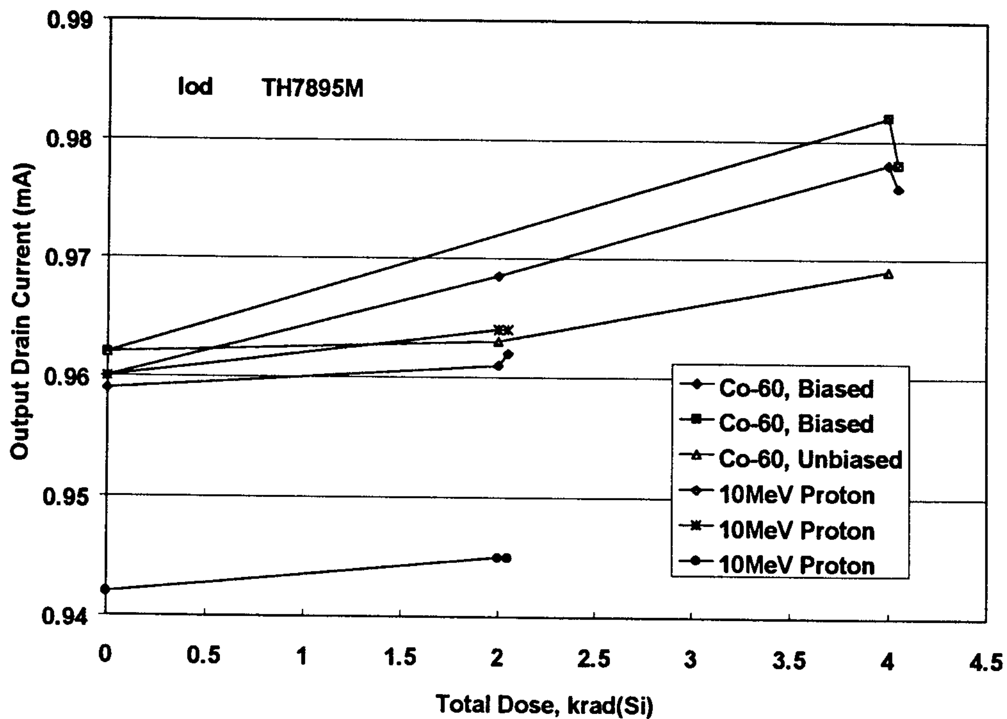

Figure 10-2 Output amplifier currents for TH7895M devices

Copyright © Sira Ltd 1995

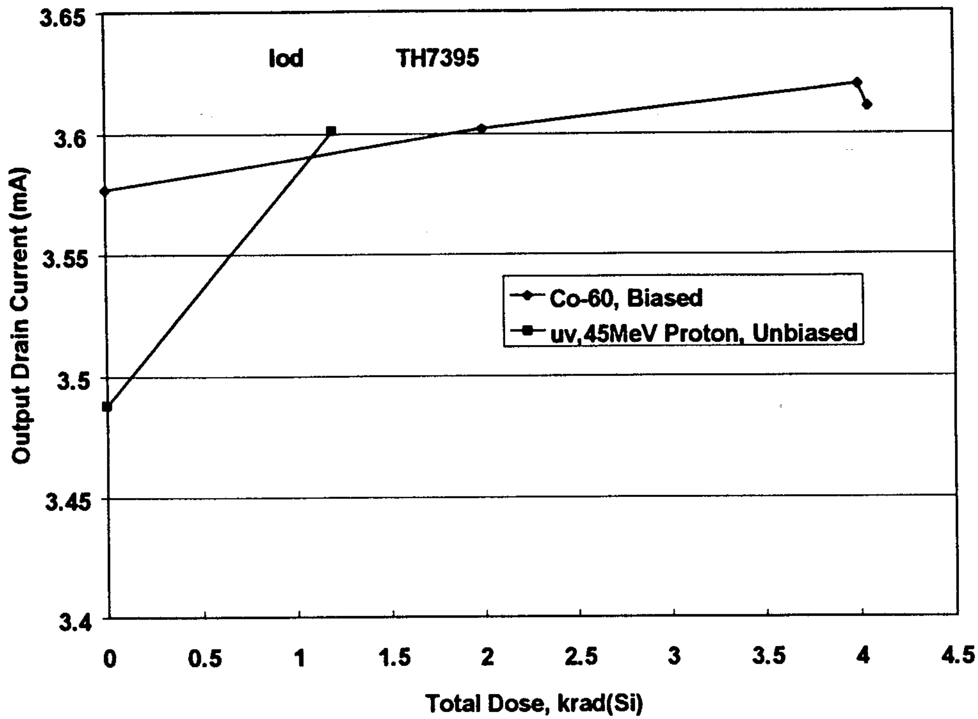

Figure 10-3 Output amplifier currents for TH7395 devices

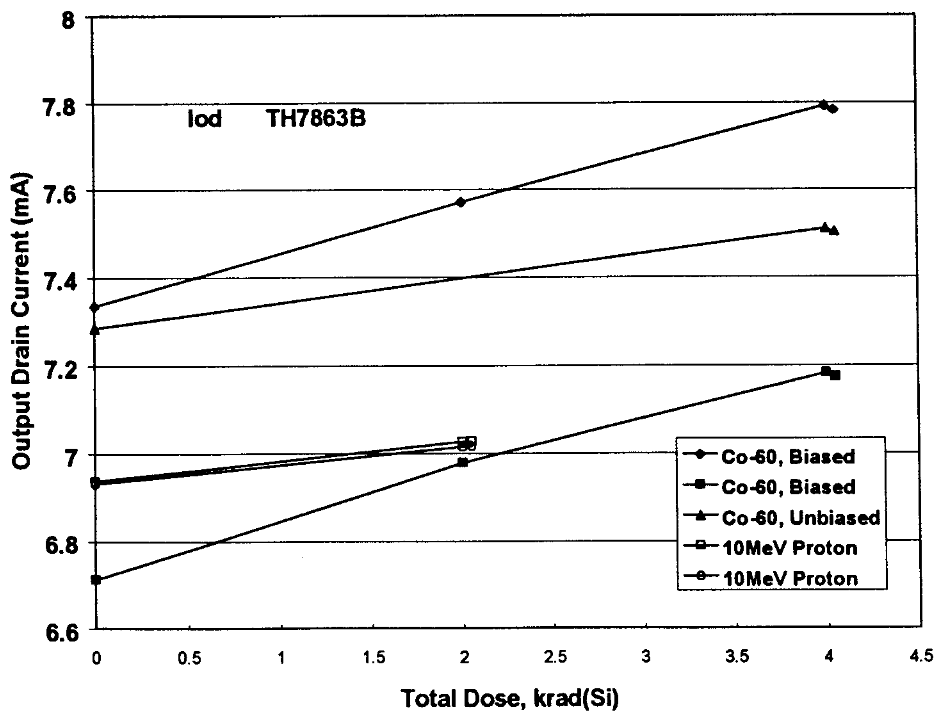

Figure 10-4 Output amplifier currents for TH7863B devices

Copyright © Sira Ltd 1995

11 DISCUSSION

11.1 EXAMPLES FOR MISSION ANALYSES

As an example of the effects to be expected for a particular mission, we take a reference level of **3 krad(Si)** total ionizing dose. This is equivalent to a fluence of 5.4 x10^9 10MeV protons/cm^2. We then have the following table of parameter changes, taking Co-60 data after annealing - or proton data, whichever gives the worst case. The values are given at 20°C. Apart from dark current spikes, it was found that over the range 20°C to -20°C the dark current changed according to an Arrhenius relation (i.e. expE/kT) with an activation energy of ~0.64eV, hence results can be extrapolated to other temperatures. For dark current spikes which experience field enhancement the activation energy is lowered, to ~0.4eV as a worst case. Dark current non-uniformity and random telegraph signals are discussed below. Other parameters, such as threshold voltage shift or full well capacity, have not been found to change over the present temperature range.

Table 11-1 CCD parameter changes after 3krad (at 20°C)

Parameter	Unit	CCD25-20	TH7863B	TH7895M	TH7395
Image region dark current at 20°C not dithered dithered	nA/cm^2	6.6 (3) [1] ~2 (0.9)	3	0.2, protons	~9 (biased) [2] ~2 (unbiased)
Storage region dark current at 20°C	nA/cm^2	1.6 (0.9)	~24 (biased) ~9 (unbiased)	Too small to measure when inverted [4]	~4 (biased) [4] ~2 (unbiased) [4]
CVF	% change	<4%	<4%	<4%	<4%
Full well capacity	% change	~4% (unbiased) probably ~10%(biased)	~25%(biased) ~12%(unbiased)	<5%	<5% [3]
PRNU		no change	no change	no change	no change
CTI		~1E-4 for signals ~ 3E4 electrons and background ~ 500 electrons	Not Measured	~5E-5 for signals ~ 1E5 electrons and background ~ 1E3 electrons	Not Measured
Waveform features		no change	no change	no change	no change
Threshold voltage shift	V	~0.2V(biased) ~0.1V(unbiased)	0.3V(biased) 0.1V(unbiased)	0.2V(biased) 0.1V(unbiased)	~0.2V(biased)
Output amplifier supply current	mA	~0.01mA	0.3mA(biased) 0.15(unbiased)	no change	no change

Copyright © Sira Ltd 1995

Notes:

1 Values in parentheses are for typical EEV CCD02 and CCD05 devices measured in [RD5]

2 Co-60 data on the sample TH7395 device gave high dark current. The reasons are not known.

3 For the TH7395 the full well capacity was greater at the edges of the CCD (i.e. the irradiated parts) than the middle (unirradiated). This may be due to the effect of the distributed resistance and capacitance of the CCD electrodes on the drive waveforms.

4 When not inverted the storage region component increases at ~1nA/cm^2/krad at 20°C for Co-60 irradiated TH7895M and TH7395N devices, irrespective of bias during irradiation.

RANDOM TELEGRAPH SIGNALS

For 10 MeV proton irradiation, the probability of creation of an RTS defect was found to be ~1.8E-5/incident proton and this probability scales with elastic NIEL. The RTS defects appear to give dark current density amplitudes roughly in the range 0.01-0.1nA/cm^2 at 20°C. With our limited understanding (at present) of the mechanisms for RTS behaviour and the effect of changing temperature, it may be prudent to scale the amplitudes with an activation energy typical for field enhanced spikes (i.e. ~0.4eV). To obtain the time constants near room temperature it has been found that an activation energy of 0.9eV can be used (with time constants ~5 minutes at 20°C). At -20°C, however, many defects are still swithcing on time scales of several hours.

DARK SIGNAL NON-UNIFORMITY

With proton irradiation it has been found that there are isolated spikes with amplitudes up to 8nA/cm^2 at 20°C. Histograms for a typical MPP device at 20°C are shown in figure 11.1-1. Also shown are empirical fits assuming the distribution is made up of a Gaussian main peak plus an exponential tail. For a bin size (BS) of 0.00144 nA/cm^2 (as in the figure), the following expression was used, with N the bin number:

$$\text{Counts}(N) = b\,\exp[-(\{N*BS\}-f)^2/c^2] + d\,\exp[-e*\text{abs}[(N*BS)-f] \qquad (11\text{-}1)$$

where

b is a scaling parameter on the total number of counts in the main peak
c is related to the half-width of the main peak, in nA/cm^2 (which increases with fluence)
d gives the number of counts in the tail and increases with proton fluence
e is related to the slope of the exponential tail
f is the position of the main peak (in nA/cm^2) which increases with fluence due to the increased mean dark current level

Copyright © Sira Ltd 1995

the values used in the fit were:

	1 krad	2 krad	3 krad
b	250	600	1300
c	0.018	0.015	0.012
d	170	85	42.5
e	7.5	7.5	7.5
f	0.097	0.045	0.03

As expected the slope of the exponential tail is independent of fluence, but the nuber of counts in the tail varies linearly with fluence. Though further work (outside the scope of this study) will be needed to fully understand the detailed shape of the dark current histograms, the above relation can be used as a first attempt for scaling to other mission fluences. Note that if (as in the CCD25-20 devices studied here) there is a significant ionization-induced surface dark current then the main peak in the histograms will be broadened.

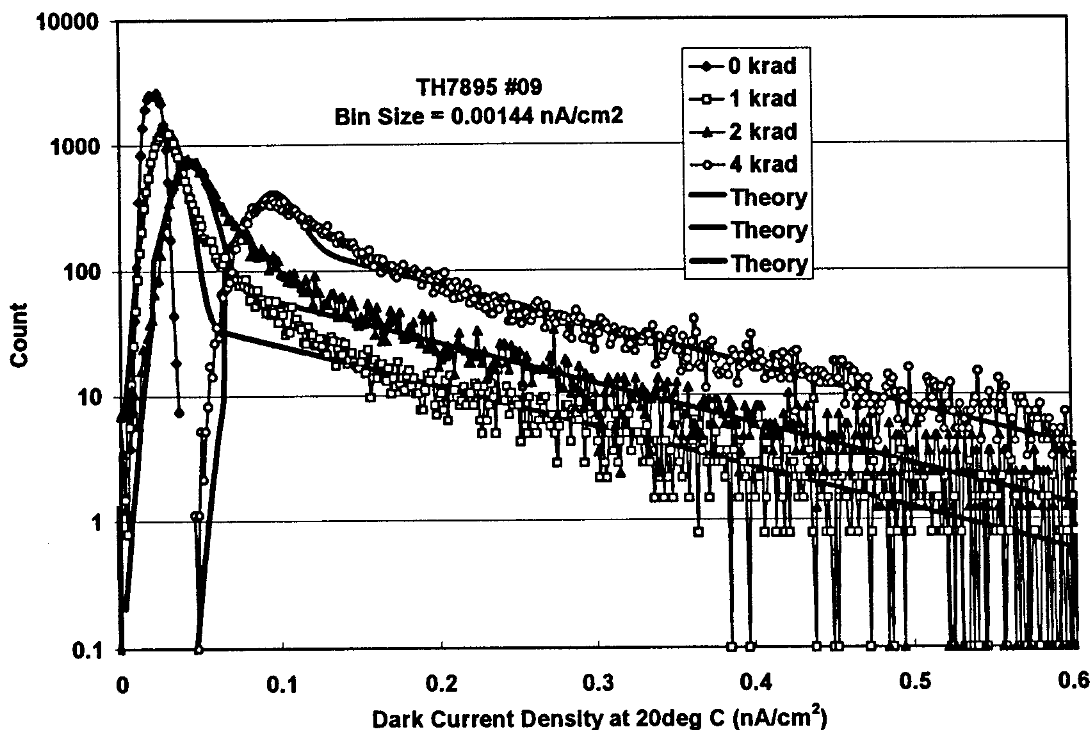

Figure 11-1 Histograms of dark current density for a proton-irradiated TH7895M device at20°C.

11.2 IMPACT REVIEW

It is likely that the major impact on the performance of instruments, which use CCDs similar to those tested here, operated at near room temperature (say +30 to -30 °C) and in low Earth orbits, will be the increase in dark current (and non-uniformity) and loss of CTE. Other parameters will be affected but are not expected to have a large impact. In this section we refer to a mission dose of 3 krad, but at the low total doses discussed here effects are linear with total dose and extrapolations can be easily made. first we deal with some of the more minor issues and then return to dark charge and CTE.

Copyright © Sira Ltd 1995

i) Threshold voltage shifts differ somewhat from device to device and also depend on the way they are measured (for example, not all bias lines show the same shift in threshold). However as a rough guide the shift is ~0.08 V/krad for biased devices and ~0.04 V/krad when not biased. Apart from changes in CVF (discussed below), this is not likely to cause problems for device performance for total doses <5 krad since there should be sufficient margin on bias voltages for near-optimal operation.

ii) From the present measurements it appears that changes in charge to voltage conversion faction (CVF) are <4%. Some missions require stability of CVF to 1% or better, this can still not be verified. In view of the shifts in threshold voltage for normal commercial CCDs (~0.08 V/krad for powered devices), it is inevitable that the operating points of the output stage will shift, at least to some extent. A firm requirement for better than 1% gain stability is likely to dictate use of a hardened oxide (and the development of an accurate measurement procedure).

iii) Full well capacity appears to be a parameter which is degraded by total ionizing dose. It is likely that biased operation is the worst case. The device most affected seems to be the TH7863B which showed ~30% change after 4 krad. It is recommended that there be some margin, (say 10-20%) allowed for decrease in full well capacity when using CCDs in a LEO environment. The antiblooming function provided by dither clocking may be a definite advantage for some programmes.

iv) Increases in power consumption are modest for the CCDs tested and probably arise from changes in the operating point (and hence drain current) of the output stage. Since no CMOS circuits are involved there are no parasitic transistors structures and no dramatic increases in power consumption are to be expected As found in previous studies the drain current for TH7863 devices is a readily measured indicator of total dose.

v) There were no significant changes in output waveform shape, PRNU or responsivity. Also the were no obvious effects attributed to the UV coating on the two such devices studied.

vi) Dark current for devices operated in inversion (by use of MPP implants) will be dominated by the bulk component from proton-induced displacement damage. For the EEV CCDs, where dither clocking can be used, the situation is not so clear cut. For the CCD25-20s studied here, large reductions in surface dark current were not achieved, especially since a high value of substrate voltage could not be used (or full well capacity was sacrificed). For the MERIS devices operated at -20 °C or below the dark current should be less than 50 electrons (2 krad) or 100 electrons (4 krad). Non-uniformity at low temperatures is dominated by proton dark spikes and black/white pairs from dither clocking. The latter non-uniformity is signal dependent (and hence difficult to calibrate) and is likely to affect at least one pixel per line at the 20 electron level. An Arrhenius relation with an activation energy in the range 0.63 - 0.65 eV can be used for extrapolating mean dark current (either surface or bulk) to other temperatures.

Random telegraph signals have been detected at -20 °C with switching periods of several hours. These may have an effect on dark current calibration philosophy.

vii) The pre-irradiation dark current and the change/krad were higher for the thinned TH7395 devices than for the unthinned TH7895 CCDs. This may be due to the effects of the

Copyright © Sira Ltd 1995

thinning process, however only two devices were studied and one of these was a set-up grade device. It is recommended that further work be carried out if the performance of these devices is important for a particular application.

viii) Charge transfer efficiency has been found to be strongly signal and background dependent. If we take a best case example situation where the signal (or the background) is high, the CTE after 4 krad is likely to be ~0.0001 per pixel transfer during frame transfer (and probably x2 higher during readout). Serial and parallel CTI are similar at high charge levels so, after 600 transfers (say, 300 vertical and 300 horizontal) this gives a 6% charge loss which is likely to have a significant effect on absolute accuracy (note though, that charge is only lost from the 'highlights of an image). The lost charge is spread over several pixels. At -20 °C the emission time is ~400 µs so that during frame transfer or line dumping readout (at 2 µs line move time) the trapped charge is spread out over ~200 pixels.

If we have a large signal of say 10^5 electrons followed by a much lower one (e.g. during frame transfer in the MERIS instrument, were the larger signal is at the blue end of the spectrum and is readout last) then say, 3% of the 10^5 electrons will be trapped and released over the following 200 pixels - the signal in each being 15 electrons - this is likely to be the level at which a large signal will 'contaminate' a lower one.